

RILEM State-of-the-Art Reports

Masayasu Ohtsu *Editor*

Innovative AE and NDT Techniques for On-Site Measurement of Concrete and Masonry Structures

State-of-the-Art Report of the RILEM
Technical Committee 239-MCM



@Seismicisolation  Springer

RILEM State-of-the-Art Reports

@Seismicisolation

RILEM STATE-OF-THE-ART REPORTS

Volume 20

RILEM, The International Union of Laboratories and Experts in Construction Materials, Systems and Structures, founded in 1947, is a non-governmental scientific association whose goal is to contribute to progress in the construction sciences, techniques and industries, essentially by means of the communication it fosters between research and practice. RILEM's focus is on construction materials and their use in building and civil engineering structures, covering all phases of the building process from manufacture to use and recycling of materials. More information on RILEM and its previous publications can be found on www.RILEM.net.

The RILEM State-of-the-Art Reports (STAR) are produced by the Technical Committees. They represent one of the most important outputs that RILEM generates—high level scientific and engineering reports that provide cutting edge knowledge in a given field. The work of the TCs is one of RILEM's key functions.

Members of a TC are experts in their field and give their time freely to share their expertise. As a result, the broader scientific community benefits greatly from RILEM's activities.

RILEM's stated objective is to disseminate this information as widely as possible to the scientific community. RILEM therefore considers the STAR reports of its TCs as of highest importance, and encourages their publication whenever possible.

The information in this and similar reports is mostly pre-normative in the sense that it provides the underlying scientific fundamentals on which standards and codes of practice are based. Without such a solid scientific basis, construction practice will be less than efficient or economical.

It is RILEM's hope that this information will be of wide use to the scientific community.



More information about this series at <http://www.springer.com/series/8780>

@Seismicisolation

Masayasu Ohtsu
Editor

Innovative AE and NDT Techniques for On-Site Measurement of Concrete and Masonry Structures

State-of-the-Art Report of the RILEM
Technical Committee 239-MCM



@Seismicisolation

Editor

Masayasu Ohtsu
Graduate School of Engineering
Kyoto University
Kyoto
Japan

ISSN 2213-204X
RILEM State-of-the-Art Reports
ISBN 978-94-017-7605-9
DOI 10.1007/978-94-017-7606-6

ISSN 2213-2031 (electronic)
ISBN 978-94-017-7606-6 (eBook)

Library of Congress Control Number: 2016937349

© RILEM 2016

No part of this work may be reproduced, stored in a retrieval system, or transmitted in any form or by any means, electronic, mechanical, photocopying, microfilming, recording or otherwise, without written permission from the Publisher, with the exception of any material supplied specifically for the purpose of being entered and executed on a computer system, for exclusive use by the purchaser of the work. Permission for use must always be obtained from the owner of the copyright: RILEM.

Printed on acid-free paper

This Springer imprint is published by Springer Nature
The registered company is Springer Science+Business Media B.V. Dordrecht

@Seismicisolation

RILEM Publications

The following list is presenting the global offer of RILEM Publications, sorted by series. Each publication is available in printed version and/or in online version.

RILEM Proceedings (PRO)

PRO 1: Durability of High Performance Concrete (ISBN: 2-912143-03-9); *Ed. H. Sommer*

PRO 2: Chloride Penetration into Concrete (ISBN: 2-912143-00-04); *Eds. L.-O. Nilsson and J.-P. Ollivier*

PRO 3: Evaluation and Strengthening of Existing Masonry Structures (ISBN: 2-912143-02-0); *Eds. L. Binda and C. Modena*

PRO 4: Concrete: From Material to Structure (ISBN: 2-912143-04-7); *Eds. J.-P. Bournazel and Y. Malier*

PRO 5: The Role of Admixtures in High Performance Concrete (ISBN: 2-912143-05-5); *Eds. J. G. Cabrera and R. Rivera-Villarreal*

PRO 6: High Performance Fiber Reinforced Cement Composites—HPFRCC 3 (ISBN: 2-912143-06-3); *Eds. H. W. Reinhardt and A. E. Naaman*

PRO 7: 1st International RILEM Symposium on Self-Compacting Concrete (ISBN: 2-912143-09-8); *Eds. Å. Skarendahl and Ö. Petersson*

PRO 8: International RILEM Symposium on Timber Engineering (ISBN: 2-912143-10-1); *Ed. L. Boström*

PRO 9: 2nd International RILEM Symposium on Adhesion between Polymers and Concrete ISAP '99 (ISBN: 2-912143-11-X); *Eds. Y. Ohama and M. Puterman*

PRO 10: 3rd International RILEM Symposium on Durability of Building and Construction Sealants (ISBN: 2-912143-13-6); *Ed. A. T. Wolf*

PRO 11: 4th International RILEM Conference on Reflective Cracking in Pavements (ISBN: 2-912143-14-4); *Eds. A. O. Abd El Halim, D. A. Taylor and El H. H. Mohamed*

PRO 12: International RILEM Workshop on Historic Mortars: Characteristics and Tests (ISBN: 2-912143-15-2); *Eds. P. Bartos, C. Groot and J. J. Hughes*

PRO 13: 2nd International RILEM Symposium on Hydration and Setting (ISBN: 2-912143-16-0); *Ed. A. Nonat*

PRO 14: Integrated Life-Cycle Design of Materials and Structures—ILCDES 2000 (ISBN: 951-758-408-3); (ISSN: 0356-9403); *Ed. S. Sarja*

PRO 15: Fifth RILEM Symposium on Fibre-Reinforced Concretes (FRC)—BEFIB'2000 (ISBN: 2-912143-18-7); *Eds. P. Rossi and G. Chanvillard*

PRO 16: Life Prediction and Management of Concrete Structures (ISBN: 2-912143-19-5); *Ed. D. Naus*

PRO 17: Shrinkage of Concrete—Shrinkage 2000 (ISBN: 2-912143-20-9); *Eds. V. Baroghel-Bouny and P.-C. Aïtcin*

PRO 18: Measurement and Interpretation of the On-Site Corrosion Rate (ISBN: 2-912143-21-7); *Eds. C. Andrade, C. Alonso, J. Fullea, J. Polimon and J. Rodriguez*

PRO 19: Testing and Modelling the Chloride Ingress into Concrete (ISBN: 2-912143-22-5); *Eds. C. Andrade and J. Kropp*

PRO 20: 1st International RILEM Workshop on Microbial Impacts on Building Materials (CD 02) (e-ISBN 978-2-35158-013-4); *Ed. M. Ribas Silva*

PRO 21: International RILEM Symposium on Connections between Steel and Concrete (ISBN: 2-912143-25-X); *Ed. R. Elsgehausen*

PRO 22: International RILEM Symposium on Joints in Timber Structures (ISBN: 2-912143-28-4); *Eds. S. Aicher and H.-W. Reinhardt*

PRO 23: International RILEM Conference on Early Age Cracking in Cementitious Systems (ISBN: 2-912143-29-2); *Eds. K. Kovler and A. Bentur*

PRO 24: 2nd International RILEM Workshop on Frost Resistance of Concrete (ISBN: 2-912143-30-6); *Eds. M. J. Setzer, R. Auberg and H.-J. Keck*

PRO 25: International RILEM Workshop on Frost Damage in Concrete (ISBN: 2-912143-31-4); *Eds. D. J. Janssen, M. J. Setzer and M. B. Snyder*

PRO 26: International RILEM Workshop on On-Site Control and Evaluation of Masonry Structures (ISBN: 2-912143-34-9); *Eds. L. Bindu and R. C. de Vekey*

PRO 27: International RILEM Symposium on Building Joint Sealants (CD03); *Ed. A. T. Wolf*

PRO 28: 6th International RILEM Symposium on Performance Testing and Evaluation of Bituminous Materials—PTEBM'03 (ISBN: 2-912143-35-7; e-ISBN: 978-2-912143-77-8); *Ed. M. N. Partl*

PRO 29: 2nd International RILEM Workshop on Life Prediction and Ageing Management of Concrete Structures (ISBN: 2-912143-36-5); *Ed. D. J. Naus*

PRO 30: 4th International RILEM Workshop on High Performance Fiber Reinforced Cement Composites—HPFRCC 4 (ISBN: 2-912143-37-3); *Eds. A. E. Naaman and H. W. Reinhardt*

PRO 31: International RILEM Workshop on Test and Design Methods for Steel Fibre Reinforced Concrete: Background and Experiences (ISBN: 2-912143-38-1); *Eds. B. Schnütgen and L. Vandewalle*

PRO 32: International Conference on Advances in Concrete and Structures 2 vol. (ISBN (set): 2-912143-41-1); *Eds. Ying-shu Yuan, Surendra P. Shah and Heng-lin Lü*

PRO 33: 3rd International Symposium on Self-Compacting Concrete (ISBN: 2-912143-42-X); *Eds. Ó. Wallevik and I. Nielsson*

PRO 34: International RILEM Conference on Microbial Impact on Building Materials (ISBN: 2-912143-43-8); *Ed. M. Ribas Silva*

PRO 35: International RILEM TC 186-ISA on Internal Sulfate Attack and Delayed Ettringite Formation (ISBN: 2-912143-44-6); *Eds. K. Scrivener and J. Skalny*

PRO 36: International RILEM Symposium on Concrete Science and Engineering—A Tribute to Arnon Bentur (ISBN: 2-912143-46-2); *Eds. K. Kovler, J. Marchand, S. Mindess and J. Weiss*

PRO 37: 5th International RILEM Conference on Cracking in Pavements—Mitigation, Risk Assessment and Prevention (ISBN: 2-912143-47-0); *Eds. C. Petit, I. Al-Qadi and A. Millien*

PRO 38: 3rd International RILEM Workshop on Testing and Modelling the Chloride Ingress into Concrete (ISBN: 2-912143-48-9); *Eds. C. Andrade and J. Kropf*

PRO 39: 6th International RILEM Symposium on Fibre-Reinforced Concretes—BEFIB 2004 (ISBN: 2-912143-51-9); *Eds. M. Di Prisco, R. Felicetti and G. A. Plizzari*

PRO 40: International RILEM Conference on the Use of Recycled Materials in Buildings and Structures (ISBN: 2-912143-52-7); *Eds. E. Vázquez, Ch. F. Hendriks and G. M. T. Janssen*

PRO 41: RILEM International Symposium on Environment-Conscious Materials and Systems for Sustainable Development (ISBN: 2-912143-55-1); *Eds. N. Kashino and Y. Ohama*

PRO 42: SCC'2005—China: 1st International Symposium on Design, Performance and Use of Self-Consolidating Concrete (ISBN: 2-912143-61-6); *Eds. Zhiwu Yu, Caijun Shi, Kamal Henri Khayat and Youjun Xie*

PRO 43: International RILEM Workshop on Bonded Concrete Overlays (e-ISBN: 2-912143-83-7); *Eds. J. L. Granju and J. Silfwerbrand*

PRO 44: 2nd International RILEM Workshop on Microbial Impacts on Building Materials (CD11) (e-ISBN: 2-912143-84-5); *Ed. M. Ribas Silva*

PRO 45: 2nd International Symposium on Nanotechnology in Construction, Bilbao (ISBN: 2-912143-87-X); *Eds. Peter J. M. Bartos, Yolanda de Miguel and Antonio Porro*

PRO 46: ConcreteLife'06—International RILEM-JCI Seminar on Concrete Durability and Service Life Planning: Curing, Crack Control, Performance in Harsh Environments (ISBN: 2-912143-89-6); *Ed. K. Kovler*

PRO 47: International RILEM Workshop on Performance Based Evaluation and Indicators for Concrete Durability (ISBN: 978-2-912143-95-2); *Eds. V. Baroghel-Bouny, C. Andrade, R. Torrent and K. Scrivener*

PRO 48: 1st International RILEM Symposium on Advances in Concrete through Science and Engineering (e-ISBN: 2-912143-92-6); *Eds. J. Weiss, K. Kovler, J. Marchand, and S. Mindess*

PRO 49: International RILEM Workshop on High Performance Fiber Reinforced Cementitious Composites in Structural Applications (ISBN: 2-912143-93-4); *Eds. G. Fischer and V.C. Li*

PRO 50: 1st International RILEM Symposium on Textile Reinforced Concrete (ISBN: 2-912143-97-7); *Eds. Josef Hegger, Wolfgang Bramshuber and Norbert Will*

PRO 51: 2nd International Symposium on Advances in Concrete through Science and Engineering (ISBN: 2-35158-003-6; e-ISBN: 2-35158-002-8); *Eds. J. Marchand, B. Bissonnette, R. Gagné, M. Jolin and F. Paradis*

PRO 52: Volume Changes of Hardening Concrete: Testing and Mitigation (ISBN: 2-35158-004-4; e-ISBN: 2-35158-005-2); *Eds. O. M. Jensen, P. Lura and K. Kovler*

PRO 53: High Performance Fiber Reinforced Cement Composites—HPFRCC5 (ISBN: 978-2-35158-046-2); *Eds. H. W. Reinhardt and A. E. Naaman*

PRO 54: 5th International RILEM Symposium on Self-Compacting Concrete (ISBN: 978-2-35158-047-9); *Eds. G. De Schutter and V. Boel*

PRO 55: International RILEM Symposium Photocatalysis, Environment and Construction Materials (ISBN: 978-2-35158-056-1); *Eds. P. Baglioni and L. Cassar*

PRO 56: International RILEM Workshop on Integral Service Life Modelling of Concrete Structures (ISBN 978-2-35158-058-5); *Eds. R. M. Ferreira, J. Gulikers and C. Andrade*

PRO 57: RILEM Workshop on Performance of cement-based materials in aggressive aqueous environments (e-ISBN: 978-2-35158-059-2); *Ed. N. De Belie*

PRO 58: International RILEM Symposium on Concrete Modelling—CONMOD'08 (ISBN: 978-2-35158-060-8); *Eds. E. Schlangen and G. De Schutter*

PRO 59: International RILEM Conference on On Site Assessment of Concrete, Masonry and Timber Structures—SACoMaTiS 2008 (ISBN set: 978-2-35158-061-5); *Eds. L. Binda, M. di Prisco and R. Felicetti*

PRO 60: Seventh RILEM International Symposium on Fibre Reinforced Concrete: Design and Applications—BEFIB 2008 (ISBN: 978-2-35158-064-6); *Ed. R. Gettu*

PRO 61: 1st International Conference on Microstructure Related Durability of Cementitious Composites 2 vol., (ISBN: 978-2-35158-065-3); *Eds. W. Sun, K. van Breugel, C. Miao, G. Ye and H. Chen*

PRO 62: NSF/ RILEM Workshop: In-situ Evaluation of Historic Wood and Masonry Structures (e-ISBN: 978-2-35158-068-4); *Eds. B. Kasal, R. Anthony and M. Drdácký*

PRO 63: Concrete in Aggressive Aqueous Environments: Performance, Testing and Modelling, 2 vol., (ISBN: 978-2-35158-071-4); *Eds. M. G. Alexander and A. Bertron*

PRO 64: Long Term Performance of Cementitious Barriers and Reinforced Concrete in Nuclear Power Plants and Waste Management—NUCPERF 2009 (ISBN: 978-2-35158-072-1); *Eds. V. L'Hostis, R. Gens, C. Gallé*

PRO 65: Design Performance and Use of Self-consolidating Concrete—SCC'2009 (ISBN: 978-2-35158-073-8); *Eds. C. Shi, Z. Yu, K. H. Khayat and P. Yan*

PRO 66: 2nd International RILEM Workshop on Concrete Durability and Service Life Planning—ConcreteLife'09 (ISBN: 978-2-35158-074-5); *Ed. K. Kovler*

PRO 67: Repairs Mortars for Historic Masonry (e-ISBN: 978-2-35158-083-7); *Ed. C. Groot*

PRO 68: Proceedings of the 3rd International RILEM Symposium on ‘Rheology of Cement Suspensions such as Fresh Concrete (ISBN 978-2-35158-091-2); *Eds. O. H. Wallevik, S. Kubens and S. Oesterheld*

PRO 69: 3rd International PhD Student Workshop on ‘Modelling the Durability of Reinforced Concrete’ (ISBN: 978-2-35158-095-0); *Eds. R. M. Ferreira, J. Gulikers and C. Andrade*

PRO 70: 2nd International Conference on ‘Service Life Design for Infrastructure’ (ISBN set: 978-2-35158-096-7, e-ISBN: 978-2-35158-097-4); *Ed. K. van Breugel, G. Ye and Y. Yuan*

PRO 71: Advances in Civil Engineering Materials—The 50-year Teaching Anniversary of Prof. Sun Wei’ (ISBN: 978-2-35158-098-1; e-ISBN: 978-2-35158-099-8); *Eds. C. Miao, G. Ye, and H. Chen*

PRO 72: First International Conference on ‘Advances in Chemically-Activated Materials—CAM’2010’ (2010), 264 pp., ISBN: 978-2-35158-101-8; e-ISBN: 978-2-35158-115-5, *Eds. Cajun Shi and Xiaodong Shen*

PRO 73: 2nd International Conference on ‘Waste Engineering and Management—ICWEM 2010’ (2010), 894 pp., ISBN: 978-2-35158-102-5; e-ISBN: 978-2-35158-103-2, *Eds. J. Zh. Xiao, Y. Zhang, M. S. Cheung and R. Chu*

PRO 74: International RILEM Conference on ‘Use of Superabsorbent Polymers and Other New Additives in Concrete’ (2010) 374 pp., ISBN: 978-2-35158-104-9; e-ISBN: 978-2-35158-105-6; *Eds. O.M. Jensen, M.T. Hasholt, and S. Laustsen*

PRO 75: International Conference on ‘Material Science—2nd ICTRC—Textile Reinforced Concrete—Theme 1’ (2010) 436 pp., ISBN: 978-2-35158-106-3; e-ISBN: 978-2-35158-107-0; *Ed. W. Brameshuber*

PRO 76: International Conference on ‘Material Science—HetMat—Modelling of Heterogeneous Materials—Theme 2’ (2010) 255 pp., ISBN: 978-2-35158-108-7; e-ISBN: 978-2-35158-109-4; *Ed. W. Brameshuber*

PRO 77: International Conference on ‘Material Science—AdIPoC—Additions Improving Properties of Concrete—Theme 3’ (2010) 459 pp., ISBN: 978-2-35158-110-0; e-ISBN: 978-2-35158-111-7; *Ed. W. Brameshuber*

PRO 78: 2nd Historic Mortars Conference and RILEM TC 203-RHM Final Workshop—HMC2010 (2010) 1416 pp., e-ISBN: 978-2-35158-112-4; *Eds J. Válek, C. Groot, and J. J. Hughes*

PRO 79: International RILEM Conference on Advances in Construction Materials Through Science and Engineering (2011) 213 pp., e-ISBN: 978-2-35158-117-9; *Eds Christopher Leung and K.T. Wan*

PRO 80: 2nd International RILEM Conference on Concrete Spalling due to Fire Exposure (2011) 453 pp., ISBN: 978-2-35158-118-6, e-ISBN: 978-2-35158-119-3; *Eds E.A.B. Koenders and F. Dehn*

PRO 81: 2nd International RILEM Conference on Strain Hardening Cementitious Composites (SHCC2-Rio) (2011) 451 pp., ISBN: 978-2-35158-120-9, e-ISBN: 978-2-35158-121-6; *Eds R.D. Toledo Filho, F.A. Silva, E.A.B. Koenders and E.M.R. Fairbairn*

PRO 82: 2nd International RILEM Conference on Progress of Recycling in the Built Environment (2011) 507 pp., e-ISBN: 978-2-35158-122-3; *Eds V.M. John, E. Vazquez, S.C. Angulo and C. Ulsen*

PRO 83: 2nd International Conference on Microstructural-related Durability of Cementitious Composites (2012) 250 pp., ISBN: 978-2-35158-129-2; e-ISBN: 978-2-35158-123-0; *Eds G. Ye, K. van Breugel, W. Sun and C. Miao*

PRO 85: RILEM-JCI International Workshop on Crack Control of Mass Concrete and Related issues concerning Early-Age of Concrete Structures—ConCrack 3—Control of Cracking in Concrete Structures 3 (2012) 237 pp., ISBN: 978-2-35158-125-4; e-ISBN: 978-2-35158-126-1; *Eds F. Toutlemonde and J.-M. Torrenti*

PRO 86: International Symposium on Life Cycle Assessment and Construction (2012) 414 pp., ISBN: 978-2-35158-127-8, e-ISBN: 978-2-35158-128-5; *Eds A. Ventura and C. de la Roche*

PRO 87: UHPFRC 2013—RILEM-fib-AFGC International Symposium on Ultra-High Performance Fibre-Reinforced Concrete (2013), ISBN: 978-2-35158-130-8, e-ISBN: 978-2-35158-131-5; *Eds F. Toutlemonde*

PRO 88: 8th RILEM International Symposium on Fibre Reinforced Concrete (2012) 344 pp., ISBN: 978-2-35158-132-2, e-ISBN: 978-2-35158-133-9; *Eds Joaquim A.O. Barros*

PRO 89: RILEM International workshop on performance-based specification and control of concrete durability (2014) 678 pp, ISBN: 978-2-35158-135-3, e-ISBN: 978-2-35158-136-0; *Eds. D. Bjegović, H. Beushausen and M. Serdar*

PRO 90: 7th RILEM International Conference on Self-Compacting Concrete and of the 1st RILEM International Conference on Rheology and Processing of Construction Materials (2013) 396 pp, ISBN: 978-2-35158-137-7, e-ISBN: 978-2-35158-138-4, *Eds. Nicolas Roussel and Hela Bessaias-Bey*

PRO 91 draft: CONMOD 2014—RILEM International Symposium on Concrete Modelling (2014), ISBN: 978-2-35158-139-1; e-ISBN: 978-2-35158-140-7

PRO 92: CAM 2014—2nd International Conference on advances in chemically-activated materials (2014) 392 pp., ISBN: 978-2-35158-141-4; e-ISBN: 978-2-35158-142-1, *Eds. Caijun Shi and Xiadong Shen*

PRO 93: SCC 2014—3rd International Symposium on Design, Performance and Use of Self-Consolidating Concrete (2014) 438 pp., ISBN: 978-2-35158-143-8; e-ISBN: 978-2-35158-144-5, *Eds. Caijun Shi, Zhihua Ou, Kamal H. Khayat*

PRO 94 (online version): HPFRCC-7—7th RILEM conference on High performance fiber reinforced cement composites, e-ISBN: 978-2-35158-146-9, *Eds. H. W. Reinhardt, G.J. Parra-Montesinos, H. Garrecht*

PRO 95: International RILEM Conference on Application of superabsorbent polymers and other new admixtures in concrete construction, ISBN: 978-2-35158-147-6; e-ISBN: 978-2-35158-148-3, *Eds. Viktor Mechcherine, Christof Schroefl*

PRO 96 (online version): XIII DBMC: XIII International Conference on Durability of Building Materials and Components, e-ISBN: 978-2-35158-149-0, *Eds. M. Quattrone, V.M. John*

PRO 97: SHCC3—3rd International RILEM Conference on Strain Hardening Cementitious Composites, ISBN: 978-2-35158-150-6; e-ISBN: 978-2-35158-151-3, *Eds. E. Schlangen, M.G. Sierra Beltran, M. Lukovic, G. Ye*

PRO 98: FERRO-11—11th International Symposium on Ferrocement and 3rd ICTRC—International Conference on Textile Reinforced Concrete, ISBN: 978-2-35158-152-0; e-ISBN: 978-2-35158-153-7, *Ed. W. Brameshuber*

PRO 99 (online version): ICBBM 2015—1st International Conference on Bio-Based Building Materials, e-ISBN: 978-2-35158-154-4, *Eds. S. Amziane, M. Sonebi*

PRO 100: SCC16—RILEM Self-Consolidating Concrete Conference, ISBN: 978-2-35158-156-8; e-ISBN: 978-2-35158-157-5

PRO 101 (online version): III Progress of Recycling in the Built Environment, e-ISBN: 978-2-35158-158-2, *Eds. M. Quattrone, V.M. John*

PRO 102: FRC-CREEP 2016—International RILEM Workshop on Creep Behaviour in Cracked Sections of Fibre Reinforced Concrete, ISBN: 978-2-35158-159-9, e-ISBN: 978-2-35158-160-5, *Eds Pedro Serna, Aitor Llano-Torre and Sergio H. P. Cavalaro*

PRO 103 (online version): ACESC'16—International Conference on Advances in Civil Engineering and Sustainable Construction, e-ISBN: 978-2-35158-161-2, *Eds.T.Ch. Madhavi, G. Prabhakar, Santhosh Ram, and P.M. Rameshwaran*

RILEM Reports (REP)

Report 19: Considerations for Use in Managing the Aging of Nuclear Power Plant Concrete Structures (ISBN: 2-912143-07-1); *Ed. D. J. Naus*

Report 20: Engineering and Transport Properties of the Interfacial Transition Zone in Cementitious Composites (ISBN: 2-912143-08-X); *Eds. M. G. Alexander, G. Arliguie, G. Ballivy, A. Bentur and J. Marchand*

Report 21: Durability of Building Sealants (ISBN: 2-912143-12-8); *Ed. A. T. Wolf*

Report 22: Sustainable Raw Materials—Construction and Demolition Waste (ISBN: 2-912143-17-9); *Eds. C. F. Hendriks and H. S. Pietersen*

Report 23: Self-Compacting Concrete state-of-the-art report (ISBN: 2-912143-23-3); *Eds. Å. Skarendahl and Ö. Petersson*

Report 24: Workability and Rheology of Fresh Concrete: Compendium of Tests (ISBN: 2-912143-32-2); *Eds. P. J. M. Bartos, M. Sonebi and A. K. Tamimi*

Report 25: Early Age Cracking in Cementitious Systems (ISBN: 2-912143-33-0); *Ed. A. Bentur*

Report 26: Towards Sustainable Roofing (Joint Committee CIB/RILEM) (CD 07) (e-ISBN 978-2-912143-65-5); *Eds. Thomas W. Hutchinson and Keith Roberts*

Report 27: Condition Assessment of Roofs (Joint Committee CIB/RILEM) (CD 08) (e-ISBN 978-2-912143-66-2); *Ed. CIB W 83/RILEM TC166-RMS*

Report 28: Final report of RILEM TC 167-COM ‘Characterisation of Old Mortars with Respect to Their Repair (ISBN: 978-2-912143-56-3); *Eds. C. Groot, G. Ashall and J. Hughes*

Report 29: Pavement Performance Prediction and Evaluation (PPPE): Interlaboratory Tests(e-ISBN: 2-912143-68-3); *Eds. M. Partl and H. Piber*

Report 30: Final Report of RILEM TC 198-URM ‘Use of Recycled Materials’ (ISBN: 2-912143-82-9; e-ISBN: 2-912143-69-1); *Eds. Ch. F. Hendriks, G. M. T. Janssen and E. Vázquez*

Report 31: Final Report of RILEM TC 185-ATC ‘Advanced testing of cement-based materials during setting and hardening’ (ISBN: 2-912143-81-0; e-ISBN: 2-912143-70-5); *Eds. H. W. Reinhardt and C. U. Grosse*

Report 32: Probabilistic Assessment of Existing Structures. A JCSS publication (ISBN 2-912143-24-1); *Ed. D. Diamantidis*

Report 33: State-of-the-Art Report of RILEM Technical Committee TC 184-IFE ‘Industrial Floors’ (ISBN 2-35158-006-0); *Ed. P. Seidler*

Report 34: Report of RILEM Technical Committee TC 147-FMB ‘Fracture mechanics applications to anchorage and bond’ Tension of Reinforced Concrete Prisms—Round Robin Analysis and Tests on Bond (e-ISBN 2-912143-91-8); *Eds. L. Elfgrén and K. Noghabai*

Report 35: Final Report of RILEM Technical Committee TC 188-CSC ‘Casting of Self Compacting Concrete’ (ISBN 2-35158-001-X; e-ISBN: 2-912143-98-5); *Eds. Å. Skarendahl and P. Billberg*

Report 36: State-of-the-Art Report of RILEM Technical Committee TC 201-TRC ‘Textile Reinforced Concrete’ (ISBN 2-912143-99-3); *Ed. W. Brameshuber*

Report 37: State-of-the-Art Report of RILEM Technical Committee TC 192-ECM ‘Environment-conscious construction materials and systems’ (ISBN: 978-2-35158-053-0); *Eds. N. Kashino, D. Van Gemert and K. Imamoto*

Report 38: State-of-the-Art Report of RILEM Technical Committee TC 205-DSC ‘Durability of Self-Compacting Concrete’ (ISBN: 978-2-35158-048-6); *Eds. G. De Schutter and K. Audenaert*

Report 39: Final Report of RILEM Technical Committee TC 187-SOC ‘Experimental determination of the stress-crack opening curve for concrete in tension’ (ISBN 978-2-35158-049-3); *Ed. J. Planas*

Report 40: State-of-the-Art Report of RILEM Technical Committee TC 189-NEC ‘Non-Destructive Evaluation of the Penetrability and Thickness of the Concrete Cover’ (ISBN 978-2-35158-054-7); *Eds. R. Torrent and L. Fernández Luco*

Report 41: State-of-the-Art Report of RILEM Technical Committee TC 196-ICC ‘Internal Curing of Concrete’ (ISBN 978-2-35158-009-7); *Eds. K. Kovler and O. M. Jensen*

Report 42: ‘Acoustic Emission and Related Non-destructive Evaluation Techniques for Crack Detection and Damage Evaluation in Concrete’—Final Report of RILEM Technical Committee 212-ACD (e-ISBN: 978-2-35158-100-1); *Ed. M. Ohtsu*

Contents

1	Introduction	1
	M. Ohtsu	
2	Concrete Structures	5
	Christian U. Grosse, Dimitrios G. Aggelis and Tomoki Shiotani	
3	Masonry Structures	27
	Giuseppe Lacidogna, Federico Accornero and Alberto Carpinteri	
4	Computerized AE Tomography	47
	Yoshikazu Kobayashi and Tomoki Shiotani	
5	Acoustic Emission Analysis for NDE in Concrete	69
	Dimitrios G. Aggelis	
6	Cross-Sectional Visualization of Defects by SIBIE	89
	Takeshi Watanabe, Ninel Alver and Masayasu Ohtsu	
7	3D Visualization of Crack Kinematics by AE-SiGMA	105
	Kentaro Ohno and Masayasu Ohtsu	
8	Hybrid NDE for Rebar Corrosion in Concrete	133
	Yuma Kawasaki, Yuichi Tomoda and Masayasu Ohtsu	
9	On-Site Damage Evaluation by AE and CT in Concrete	157
	Tetsuya Suzuki and Masayasu Ohtsu	
10	Overview of Visualized NDE for On-Site Measurement	173
	Masayasu Ohtsu	

Chapter 1

Introduction

M. Ohtsu

Abstract Technical committee TC-239 MCM “On-Site Measurement of Concrete and Masonry Structures by Visualized NDT” has been completed in March, 2016. Thus, historical development and research activities of the committee are summarized as the introduction. The objective of the state-of-the-art report is stated.

Keyword Nondestructive testing • Concrete, Masonry • On-site measurement • Infra-dock

Development of NDT (nondestructive testing) techniques for inspection is very active all over the world. In particular, one-site measurement of existing concrete and masonry structures is in heavy demand, because many structures are aged and deteriorated. For example, assessing the safety of the emblematic masonry buildings and masonry towers that characterize the World’s Cultural Heritage is an important problem. In order to formulate predictions on their stability and to estimate the safety, it is necessary to be able to identify damage signals and to determine their causes. In this regard, development and establishment of innovative and highly advanced NDT are necessary.

Acoustic emission (AE) and related NDE (nondestructive evaluation) techniques have been extensively studied in the previous TC 212-ACD (acoustic emission and related NDE techniques for crack detection and damage evaluation in concrete). The committee was set up in 2004, and was successfully finalized in 2009. Based on achievement of this TC, a follow-up committee is proposed and approved as TC-239 MCM, “On-Site Measurement of Concrete and Masonry Structures by Visualized NDT”. A list of TC-members is given in Table 1.1.

All meetings have been held in conjunction with the international symposia, which was organized by one of members of TC-239 MCM. The 1st, 5th and 7th meetings were offered by Prof. M.C. Forde, in conjunction with the International

M. Ohtsu (✉)

Graduate School of Engineering, Kyoto University, Kyoto, Japan
e-mail: ohtsu.masayasu.4v@kyoto-u.ac.jp

Table 1.1 List of active members

Name	Affiliation	e-mail address
Masayasu Ohtsu (Chairman)	Graduate School of Engineering, Kyoto University	ohtsu.masayasu.4v@kyoto-u.ac.jp
Tomoki Shiotani (Secretary)	Graduate School of Engineering, Kyoto University	shiotani@df7.so-net.ne.jp shiotani.tomoki.2v@kyoto-u.ac.jp
Michael C. Forde	University of Edinburgh	m.forde@ed.ac.uk
Mitsuhiro Shigeishi	Graduate School of Science and Technology, Kumamoto University	shigeishi@civil.kumamoto-u.ac.jp
Toshiro Kamada	Division of Global Architecture, Graduate School of Engineering, Osaka University	kamada@civil.eng.osaka-u.ac.jp
Thomas Vogel	Swiss Federal Institute of Technology (ETH) Zurich	vogel@ibk.baug.ethz.ch
Andrej Moczeko	Wroclaw University of Technology, Institute of Building Engineering	andrzej.moczeko@pwr.wroc.pl
Christian U. Grossé	Department of Non-Destructive Testing, Centre for Building Materials at the Technische Universität München	grossé@cbm.bv.tum.de
Tetsuya Suzuki	Department of Agricultural and Environmental Engineering, Faculty of Agriculture	suzuki@agr.niigata-u.ac.jp
Takeshi Watanabe	Department of Civil Engineering, The University of Tokushima	watanabe@ce.tokushima-u.ac.jp
Aljosa Sajna	Laboratory for Concrete Slovenian National Building and Civil Engineering Institute	aljosa.sajna@zag.si
Giuseppe Lacidogna	Department of Structural, Geotechnical and Building Engineering, Politecnico di Torino	giuseppe.lacidogna@polito.it
Dimtrios G. Aggelis	Department of Mechanics of Materials and Construction, Vrije Universiteit Brussel	daggelis@vub.ac.be
Markus Krüger	Institute of Construction Materials University of Stuttgart	markus.krueger@mpa.uni-stuttgart.de
Julia Summers	Associate-Civil Structures, Infrastructure Group, Arup	Julia.summers@arup.com
Simona Fontul	LNEC, Transportation Department	simona@lnec.pt
Hwa Kian Chai	Dept Civil Engineering, University of Malaya	hwakian.chai@gmail.com
Shigenori Yuyama	Nippon Physical Acoustics	yuyama@pacjapan.com

(continued)

Table 1.1 (continued)

Name	Affiliation	e-mail address
Kentaro Ohno	Tokyo Metropolitan University	ohno@tmu.ac.jp
T.E. Matikas	Department of Materials Science and Engineering, University of Ioannina	matikas@cc.uoi.gr
Yoshikazu Kobayashi	Department of Civil Engineering Nihon University	kobayasi@civil.cst.nihon-u.ac.jp

Conference on Structural Faults and Repair (SFR). The 2nd meeting was organized by the chairman, Prof. M. Ohtsu in conjunction with the 20th International AE Symposium (IAES-20). The 3rd meeting was offered by Prof. D. Aggelis in conjunction with the 5th International Conference on Emerging Technologies in NDT. The 4th meeting was offered by Prof. T. Shiotani in conjunction with AEWG-54 Meeting. The 6th meeting was organized by Prof. M. Ohtsu in conjunction with the 6th Kumamoto International Workshop on Fracture, Acoustic Emission and NDT in Concrete (KIFA-6). The 7th meeting is held in conjunction with the 6th Conference on Emerging Technologies in Non-Destructive Testing, Free University of Brussel, Belgium, May 27–29, 2015.

So far, applications of NDT techniques to on-site measurements have been marginally successful, because each technique requires a particular analysis. In this regard, visualization and imaging of results are in great demand for practitioners and engineers for inspection. Accordingly, on-site measurements of concrete and masonry structures by NDT techniques are comprehensively studied, focusing on visualization procedure of the results measured.

From the TC 212-ACD, one damage evaluation technique by AE, DeCAT procedure is being under review. In addition, AE application to corrosion detection in reinforced concrete is known to be promising. As a visualized technique of AE, SiGMA analysis is intensely studied in two institutes in Japan and Italy. So, these three techniques are investigated for visualization of the results. Recently, SIBIE analysis of the impact-echo technique is in progress. It can visually identify locations of delamination and void, depths of surface cracks and imperfectly grouted tendon-ducts. So, establishment of SIBIE technique is of concern, based on round-robin tests at members' institutes. A computer tomography (CT) of ultrasonic pulse-velocity also allows visualization of internal defects in the structures and has been employed very successfully by members of the proposed committee. The radar technique is well known to be available for visualization of internal defects. Accordingly, these visualized NDT techniques are surveyed and summarized in this state-of-the art report.

Here, the state-of-the-art report (STAR) has been updated, since the following the objective is taken into account.

(Objective)

Toward the sustainable society in the world, long service life of infrastructure is going to be an evolutional target. Aging and disastrous damages due to recent earthquakes in concrete structures have updated the urgent demand for continuing maintenance of the structures in service. This is a critical demand for the sustainable infrastructure. To this end, a variety of NDT techniques and evaluation methods for diagnosis are under development.

With respect to human body, the medical dock is systematized in Japan. In order to extend the service life of the concrete structure, an “infra-dock”, so-called as similar to the medical dock for human body is to be established. For prognosis of structures, visualization and imaging of NDT results are in great demand for practitioners and engineers for inspection. Accordingly, on-site measurements of concrete and masonry structures by NDT techniques are comprehensively surveyed, focussing on visualization procedures and prognostic techniques for the infra-dock.

Chapter 2

Concrete Structures

Christian U. Grosse, Dimitrios G. Aggelis and Tomoki Shiotani

Abstract Implementation of Non-destructive Evaluation (NDE) procedures in concrete structures seems to be the only way towards a safe and economic infrastructure management. Since concrete structures have reasonably ceased to be regarded as maintenance-free, periodic inspection is deemed necessary. Although destructive techniques can provide information on the strength of the material, this is only based on sampling and cannot be performed in a wide basis. Therefore, NDE methodologies, especially with the capability of visualizing the interior of the structure, have been developed and applied in structures to answer a question that cannot be addressed destructively. This chapter focuses on the current trends of elastic wave and general techniques that are used and new trends with some examples of how NDE assists in the identification of damage and maintenance of concrete structures are highlighted.

Keywords NDT devices • Transducers • Radar • Thermography • AE • Data processing

C.U. Grosse (✉)

Department of Non-destructive Testing, Centre for Building Materials, Technische Universität München, Munich, Germany
e-mail: grosse@tum.de

D.G. Aggelis

Faculty of Engineering Sciences, Department of Mechanics of Materials and Constructions (MeMC), Vrije Universiteit Brussel, Brussels, Belgium
e-mail: daggelis@vub.ac.be

T. Shiotani

Graduate School of Engineering, Kyoto University, Kyoto, Japan
e-mail: shiotani@df7.so-net.ne.jp; shiotani.tomoki.2v@kyoto-u.ac.jp

2.1 Introduction

Concrete is a material used to create the infrastructure supporting nearly all fields of human activity. Residential buildings, bridges, highways, dams and other structures are made of concrete. The long expected life span involves continuous deteriorating actions by own weight, external loads, temperature cycles, chemical degradation and earthquakes. The optimal performance of concrete structures is crucial for economic reasons but more importantly for human safety. Concrete structures should be inspected regularly in order to evaluate their vulnerabilities and apply proper repair action. Maintenance schemes of the structures should be based on the importance of the structure and its damage condition. Therefore, economic, fast and reliable on-site measurement techniques are in high demand.

2.2 Material and Structural Conditions for Measurements

Concrete is a special material. For construction purposes cementitious materials are nowadays the most widely used materials replacing traditional building materials like stone, masonry and wood for many applications. Considering that the worldwide consumption of cement was in 2012 approximately 3.7 Billion tons [51] demonstrates the importance of concrete for every national economy. The success of this material class is mainly due to the composite structure and the flexibility is given at the construction site. However, this causes also a problem due to materials heterogeneities since concrete consists usually of the cementitious matrix as well as of aggregates (of different size), pores, water and several additives. On the same structural macro or meso level, metallic materials exhibit a much more homogeneous structure than concrete. The large variety of concrete mixes used in practice is leading to very different behavior concerning the applicability of NDT. Moreover, a mixture out of the same ingredients (qualitatively and quantitatively) can perform differently due to the boundary condition during casting (temperature, segregation, compaction, etc.). Since concrete alone is unable to accept higher tensile loads, it is usually reinforced using steel bars for example. This makes a steel-reinforced concrete (SRC) structure tougher and broadens the application range but it further enhances the degree of heterogeneity of the individual structural components.

NDT techniques are affected by various material components (water, reinforcement, voids) in a different way. NDT methods based for example on electro-magnetic waves (like RADAR) are more affected by the reinforcement and by water compared to methods based on elastic waves like ultrasound. The latter interfere vice versus extensively with air pores leading to higher attenuation and scattering. The situation is even more difficult due to the geometrical boundary condition. At real constructions, the accessibility limits the types of NDT in most cases, allowing one-sided access only. The geometry of the structural parts is

complex since they consists of the slabs, beams or columns a structure, has often dimensions in the range a typical wavelength of NDT or affect the results by side reflections that can camouflage the desired signal. This is certainly also true for different types of reinforcement (bars, wires, tendons and fibers). In addition, the surface conditions (rough concrete surface due to the formwork), coatings and covers may have an influence on NDT methods or at least on the efficiency. All of these complex conditions are somehow limiting the applicability and success of modern test methods.

2.3 Requirements by the Stakeholders

NDT techniques are mainly used as tools for quality control of concrete structures—either during the building process or in form of maintenance applications (monitoring or inspection) during the lifetime of a structure. However, NDT applications in civil engineering are still in its infancy compared to other fields. While in most mechanical engineering applications the number of similar objects or its similarity, respectively, is high, this is not the case for concrete structures. It is a feature of civil engineering to create unique objects being the best suitable for the local needs in regard to the owner, climate, topography and so on. A stakeholder of today asks even more for a specialized construction including new compositions of material components, for a more robust and durable construction and finally also for the most cost-efficient way of construction. These optimization requirements lead to new high-tech materials including for example new fiber reinforcements, self-compacting, lightweight or high-strength concrete. A stakeholder expects that NDT is capable to handle all these materials reliably. Existing structures and older constructions can be even more difficult if (what happens often) no or little information about the design and its materials is available. To summarize this point one can state that considering the uniqueness of objects and compared to other industries like automotive and aeronautical traditional NDT methods are less efficient. Although a big percentage of a gross domestic production of a nation goes into buildings of the infrastructure applications of quality control techniques including NDT are limited. This is a surprise since in a modern economy maintenance of the infrastructure should have a high priority. It is certainly a big task to enhance the efficiency of NDT techniques for applications in civil engineering and to give stakeholders modern tools at hand to keep the value of their properties. This certainly requires the development of new devices and data processing techniques that will be addressed in the next section. Others topics are as important as this. Training of the experts should be further improved including even teaching of NDT basics in the civil engineering curricula at universities. The training of specialists should be standardized similar to the level certifications required in other industries. Standardization should be enhanced regarding test equipment and data processing techniques as well. All of these could lead to a modern quality management that is not yet existing in most countries. Stakeholders finally require a clear result of NDT

measurement. Still missing are modern NDT tools being used in the construction phase of a building in terms of quality assurance. Without the application of NDT for quality assurance in such an early phase the application of inspection and monitoring techniques later on during the service life of a structure is more difficult since a complete assessment of a building have to be done then prior to NDT applications. A certified inspection right after finishing a construction could lead to a more solid and reliable quality control since only deviation of an initial status have to be detected. Such a certificate (like a “birth certificate”) could be given to the stakeholder enhancing also the value of a construction. Such a procedure is well known in other industrial branches for objects with a much lower total value and briefer lifetime.

Nevertheless, NDT has values also being applied during service life. Modern test methods have the potential to deliver data for the prognosis of the residual lifetime for civil engineering structures. Semi-probabilistic or full-probabilistic techniques can enable for a reduction of safety factors and slender constructions and a much more efficient maintenance procedure what is both of immediate value for a stakeholder. However, these techniques are not yet fully developed and need more attention in future.

2.4 New Developments on Devices

In the past NDT techniques for probing CE structures have not been developed to the same high level compared to applications in the field of medical diagnoses or testing power plant components, automotive or aeronautical parts. One reason is the before mentioned variation of different materials in CE (concrete, wood, stone, masonry, steel, polymers etc.) leading to complexity. Considering concrete alone, one can see a significant improvement of NDT methods in the last decade [23]. Former drawbacks of NDT applications at concrete structures are handled and new sensors and devices have been established as a workaround. This includes the time-consuming setup of sensors and devices as well as implementing flexibility to the measuring system and more sophisticated data processing algorithms. Some of the recent developments are addressed in the following sub-sections.

2.4.1 *Improvement of Devices and Sensors*

The major task of sensors and NDT devices is to use waves and wave fields in a way that changes of the signal can be related to deteriorations inside opaque materials like concrete or SRC. Other tasks concerning material properties or the quality of a component are also addressed by NDT. It is the benefit of developments in micro-electronics in the last years to enable for sophisticated NDT techniques

adjusted to the needs of CE applications. Most of these techniques certainly still need more involvement but the basic concepts can already be found in the literature.

2.4.2 Calibration of Equipment and Transfer Functions of Transducers

The signal that any NDT device display as an “output” is certainly influenced by the whole recording system, where each individual part of the measuring chain (emitter, medium/structure in which the signal propagates, sensor/receiver, recording and storing unit, data processing, Fig. 2.1) can be considered as a filter altering the original signal. As a filter system we indicate something that can manipulate, change, record, or transmit signals. For example such a system can transform the displacement of a ground motion into equivalent velocity or acceleration or restrict the frequency content. In this regard the concept of transfer functions (TF) is useful.

According to Fig. 2.1 each system is represented by its individual transfer function and the resulted post-processed recording (“output”) can be seen as a convolution of all these influences onto the originating signal. This process is also known as *linear filter theory*, where the output is treated as a sequence of more or less linear filters. To apply filter theory, all of the known influences are assigned by a different transfer function. In most NDT applications it is important to know or guess the weight of these functions as a precondition to eliminate their influence and to reveal one desired “filter function”, i.e. the medium or the source. While the intention of non-destructive testing methods is the investigation of material parameters or material failure and not the characterization of the measuring system, one has to reduce the effects related to sensors, coupling or the recording system with care. An ideal sensing system acts as a zero filter producing only little distortions to the data transmitting the information more or less unaltered. In the worst case the data are distorted by the sensing filter so much that the original information is completely camouflaged or even erased.

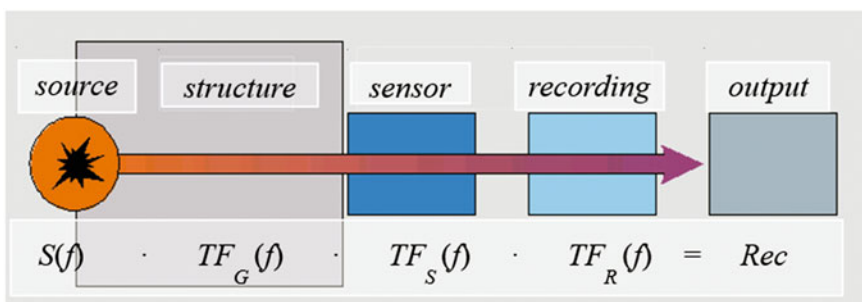


Fig. 2.1 Concept of transfer functions [12]

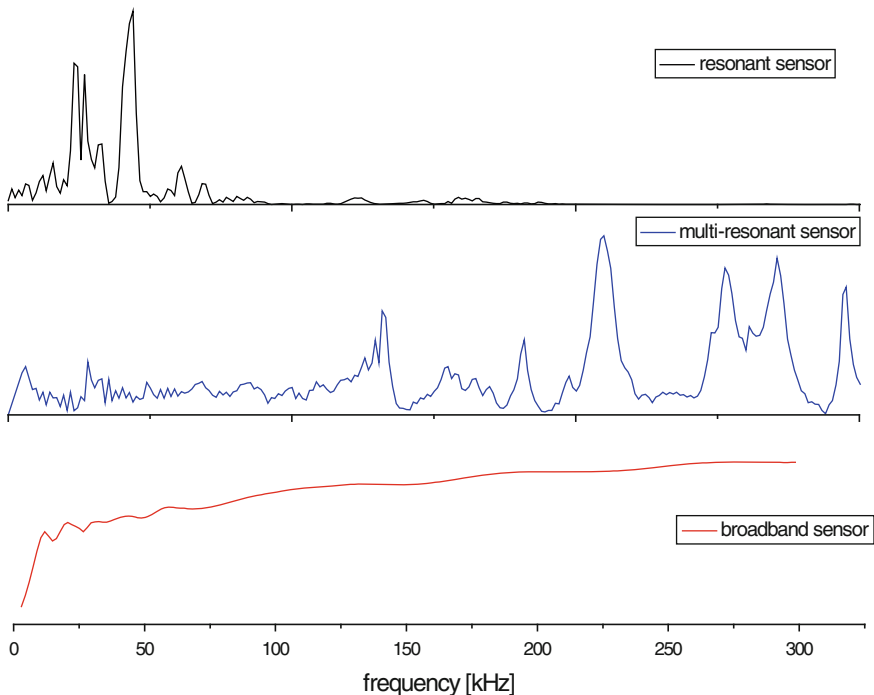


Fig. 2.2 Typical frequency response functions of resonance (*top*), multi-resonance (*middle*) and high-fidelity broadband (*bottom*) piezo-electric transducers

The type of sensors used in Ultrasonic Testing (UT) or Acoustic Emission Technique (AET) almost exclusively are sensors that exploit the piezoelectric effect of lead zirconate titanate (PZT). While piezoelectric sensors and their design are described in numerous books and papers (e.g., [17, 19, 20]), some characteristics play an influential role in measurements. These features are important in regard to sensitivity (and therefore, the detectability of signals) and the analysis of the signals with (frequency response).

To enhance the detection radius of piezoelectric sensors to AE signals [9], they are usually operated in their resonance, i.e. the signals are recorded within a small frequency range due to the frequency characteristics of the transducer as shown in Fig. 2.2. The disadvantage is that an analysis of the frequencies present in the signal is of limited range. Very well damped sensors, such as those used for vibration analysis, are operated outside of their resonant frequency allowing broadband analyses to be performed, but are usually less sensitive to acoustic emission signals. For many years a NIST (National Institute for Standards and Technology) conical transducer developed by Proctor [32, 33] was used as a reference for AE measurements.

To overcome the disadvantages of limited bandwidth transducers showing several particular resonances were developed. These sensors, which are called

multi-resonance transducers (Fig. 2.2, middle), have a higher sensitivity than sensors with a backward mass used outside of their resonance frequency. However, such sensors should not be considered as high-fidelity broadband sensors and it is essential to know their frequency response functions. Otherwise, signal characteristics from the source are not distinguishable from artifacts introduced by incorrect knowledge of the frequency response. A calibration of the sensors' frequency response, as well as understanding of the directional sensitivity, is important for many applications in non-destructive testing. It was a goal for many years to develop sensors for non-destructive testing purposed that exhibit a so-called high-fidelity behavior. The problem is similar to sound systems where in the 1960s standards were developed for music equipment (loudspeaker, microphone, amplifier, vinyl and later on tape recording) to minimize the amount of noise and distortions and providing an accurate frequency response. High-fidelity sensors for different applications (e.g., AET: [25]; Fig. 2.2, bottom) are under development to establish recording systems as a “zero-phase filter”.

Essential to determine the limits of a sensor (or a measuring device) is the launch of proper calibration standards. In the AET literature (e.g., Hsu and Breckenridge [16, 26, 54]) different methods of calibrating sensors and determining their transfer functions are described. Measurements used in sensor calibration should include the frequency, as well as the phase response function and the direction sensitivity (i.e. angle of incidence of the wave). Concerning the frequency response, techniques have been proposed using a reference source (capillary) on a large steel block [16], the face-to-face technique [15] or a laser-vibrometer [53]. All these methods have drawbacks in relation to the used physical techniques (measurement of free oscillations of the sensor instead of the coupled system) or the effort needed (steel block calibration). New techniques are under development and first results are already published [24, 25, 28].

2.4.3 Coupling of Transducers

Non-destructive testing techniques in engineering can be subdivided into methods used at a laboratory scale or in situ. Challenges are—in addition to the above mentioned—related to coupling problems. Measurements at structures like buildings, facilities or bridges are in particular challenging since they are usually large compared to the aperture of NDT signals. The coupling problem is dominating some of the NDT techniques and this is the reason why so much effort was put into methods to speed up data acquisition and to overcome the coupling problem. Contact-free techniques are the first choice; among them are RADAR (Fig. 2.3, left) and Infrared-Thermography (Fig. 2.3, right). While near-field problems can be handled using for example far-field airborne RADAR [30, 55], such problems are of less importance using IR-Thermography.

Although ultrasound is the method of choice in many applications including medical diagnosis or the inspection of welded joints, its applications concerning



Fig. 2.3 Contact-free NDT applications like Radar (*left*) and IR-Thermography (*right*) enhancing the measurement speed (*right picture*) by courtesy of Dr. J. Frick)



Fig. 2.4 Ultrasound techniques like air-coupled transducers (*left*) or point-contact transducers (*right*) are developed to speed up NDT measurements

concrete structures was limited. Traditional ultrasound techniques required a coupling agent being used at the surface to avoid voids trapped between the sensor and the surface. Ultrasound is sensitive to such voids even if they are of small diameter since ultrasound waves are almost totally reflected at boundaries to air. However, the use of coupling agents is often disturbing the optical appearance of a structure and leftovers of the agents can disturb further NDT applications. More important is that measurements using such coupling agents at large structures are costly and time consuming. Some new developments like air-coupled transducers (Fig. 2.4, left) or point-contact arrays (Fig. 2.4, right) are therefore promising techniques that will certainly be further considered but need to be optimized for measurements at large concrete structures [14].

2.5 Data Processing Techniques

2.5.1 Examples of Present Applications

Despite the inarguable fact that wave propagation techniques are far from reaching their potential [2], results have already started to be implemented in SHM high impact applications. An example is given below in Fig. 2.5, where the elastic waves emitted by an impact hammer and recorded by low frequency accelerometers through-the-thickness of concrete helped to visualize the initial problematic areas of the dam pier. Furthermore, after the repair by grout injection it was possible to quantify the improvement [44, 46]. Since pulse velocity depends on the material's elastic properties and remaining void content, it can be used as deterministic parameter of the mechanical status in addition to the visible signs and the experience of the site engineers. Attenuation coefficients of elastic waves, Q-values being regarded as an intrinsic parameter irrespective to the frequency is also used in the latest studies [47, 48] and the Q-value has been correlated to the damage parameter Ω .

In any case, apart from the evaluation of the damage status, it is essential for an NDT technique or methodology to be capable of evaluating the condition after repair in order to confirm if the mechanical integrity has been enhanced or more action is necessary [57].

Applications based on more delicate wave features like frequency dispersion have the potential to characterize surface deterioration due to carbonation, or visualize hidden defects in concrete members. They have started to be used in

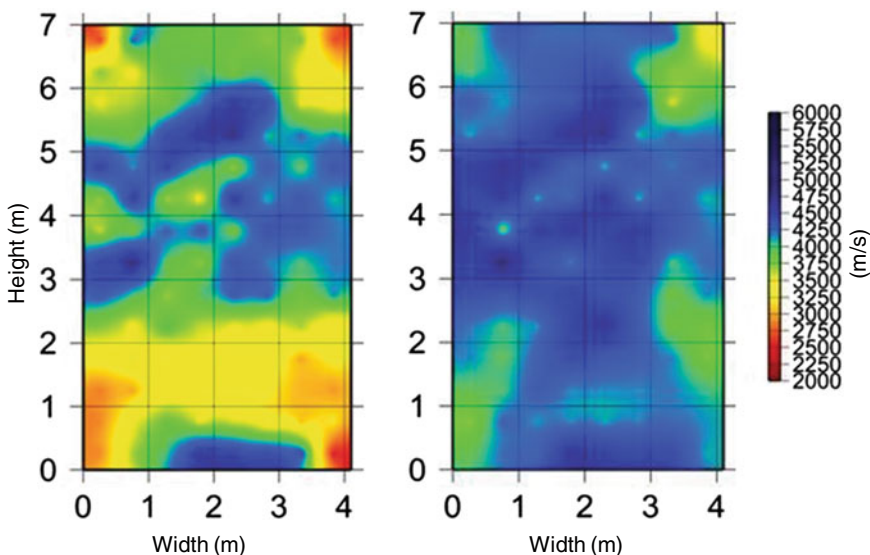


Fig. 2.5 Velocity distribution in a cross section of concrete pier: before (left) and after (right) repair by grout injection

structures but are still not widespread due to the sensitivity to experimental conditions other than the damage degree (e.g., coupling, surface roughness) [1, 31].

In the “sister” field of AE, the aforementioned difficulties again apply. Still, specific conclusions can be drawn even in large scale, mainly in the direction of quantifying the damage degree by specialized indices based on the incoming activity [44, 46] or characterizing the fracture mode [27, 45] (e.g., concrete crack, cable rupture, deboning). This supplies useful information for the remaining life of the structure. As for the other notable addresses, sensitive NDT is not always effectively in any structures. As mentioned already the structures shall be maintained according to their importance and the corresponding critical scale of defect/damage should be determined. To implement this procedure, systematic studies relating damage scale to the NDT resolution or wavelength shall be carried out more intensively.

2.5.2 Automation and Combination of Techniques

The coupling problem leads to another point related to automation. It is often required in practice to investigate a large area of a structure. Moreover, the accessibility of a structure is limited either due to geometry (e.g., bridge cable) or in time due to traffic or other time constraints. Autonomous measuring units working independently from an operator can be beneficial in such cases, like robots which use magnetic flux for assessment in cable-supported bridges or in other cases apply a mechanical excitation for testing the dynamic response by accelerometers [56]. Concerning inspection techniques first devices have been developed [34] that can handle practical problems related to rough surfaces and geometrical boundary conditions *in situ*. The benefit of these devices is in addition the ability to use different NDT techniques simultaneously including for example RADAR, ultrasound, microwave, impact-echo, rebar detection and other methods. The combination of different techniques is advantageous for traditional non-automatized NDT applications. Every NDT technique has its own advantages and disadvantages and is more or less suited for a certain application and boundary condition [5, 52]. NDT inherent ambiguities can significantly be reduced using a combination of techniques. In many cases the combination is enhanced by “data fusion” methodologies aiming at the accurate evaluation of concrete properties including the prediction of *in situ* strength [4, 38], a subject that concentrates serious efforts of the engineering community [36]. Unfortunately, these advantages have to be tradeoff for a dramatic increase of data, what have to be seen in the context of the “big data” discussion and general issues related to the data-enabled techniques in engineering and the handling of many Gigabyte of data (e.g., for AET discussed in [35]). Autonomous and automated NDT inspection devices will probably be more successful in future as soon as the total price of such a system is reduced.

A combination of data from different sensing techniques is beneficial not only for a one time inspection but for a continuous monitoring of concrete structures.



Fig. 2.6 Example of a wireless sensor mote (www.smartmote.de) and measurement of acoustic emission and strain data at a concrete structure [10, 11]

Structural health monitoring (SHM) can provide data that allow a better understanding of its structural performance, and in turn allows prediction of its durability and remaining lifetime. To function properly and cost-efficient, a monitoring procedure must be reliable, inexpensive and simple to be implemented. The techniques used should be easy to adapt to different types of structures and structural elements. Given these facts, the development and application of wireless sensor pods (often referred to as Motes), incorporating micro-electromechanical systems-based microsensors (MEMS), is a powerful solution to SHM ([8, 20]; Fig. 2.6, left). Lynch [22] presents a thorough overview of wireless sensor platforms. From past work, wireless monitoring system equipped with accurate yet low cost sensors can reduce structural monitoring costs dramatically but also wired systems like fiber optical sensors have some advantages [13]. A correlation of the data obtained by different sensors (AET, GPR, vibrations, temperature, humidity, strain, etc.) will lead to a further understanding of structural behavior, as typically done in bridges [3] or other structures like the concrete transition piece in wind turbine towers [18, 50]. For example, a cross-check of AE activity (Fig. 2.6, right) with increasing strain or with a sudden or abnormal increase of the ambient or inner structure temperature can give further insight into structural state. Such sensor data correlations will also decrease the amount of data transmitted after implementing intelligent data processing and correlation algorithms. Devices for the structural health monitoring (SHM) of constructions have been numerously assembled lately and it is nearly impossible to refer to all of them here.

2.6 Improvement of Data Processing Techniques

A pre- or post-processing of measurement data is very often required. Referring to the concept of transfer functions earlier a data processing can be required to eliminate the influences of other systems (coupling, sensor characteristics, etc.) than the one under consideration (material properties, source function, etc.). Besides, it is

the challenge of all applications to get the maximum of information out of the limited number of observations available. In almost all cases, the number of sensors is either limited or the number of events or the time or space for further observations. To deal with these limitations scientists of all disciplines have developed methods to increase the significance of the observation for example by enhancing the signal to noise ratio. While it is impossible to describe all the different developments, concerning data processing tools one example will be given.

2.6.1 New Inversion Techniques for Ultrasound

The collection of data (e.g., using ultrasound) is very often done along lines where either several (or many) sensors are placed or where a sensor-receiver pair is moved along to perform a B-Scan. Concerning the B-Scans the data obtained will contain always some redundancy, e.g., by containing information of common reflectors in the depth. Methods to make advantage of this redundancy to enhance the signal to noise ratio and to determine the real depth of the reflectors are called migration techniques (time or depth migration) in geophysical prospecting. A simple way to perform such a migration is the use of common depth point techniques as illustrated in Fig. 2.7, left.

Techniques that are more sophisticated are the Kirchhoff migration, the Reverse Time Migration (RTM) or Gaussian Beam Migrations. Based on these geophysical developments methods called in ultrasonic applications Synthetic Aperture Focusing Techniques (SAFT) [7, 50, 41] were established a few years ago. B-Scan measurements with a single transmitter-receiver pair in pulse-echo along lines can be reconstructed with SAFT algorithms enhancing the signal quality subjected to scattering or attenuation ([40], Fig. 2.8). Phased array techniques in ultrasonic or RADAR applications can be considered the hardware equivalent to migration and SAFT techniques. Ultrasonic phased array probes consists usually of many individual crystals. One can distinguish between linear, linear curved and 2D matrix

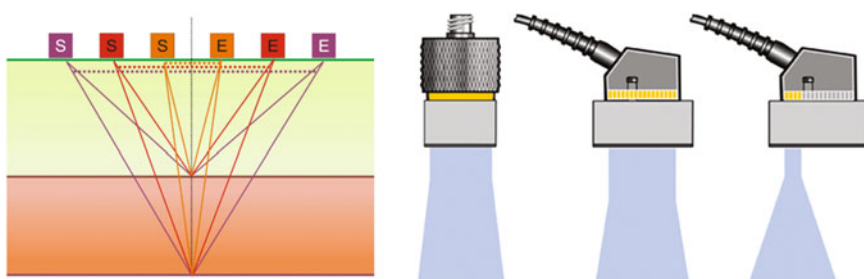


Fig. 2.7 Transmitter/receiver configuration (*left*) to perform common depth point migration in Geophysics. Comparison of the aperture of conventional and phased array transducers (*right*) with 16 elements (all or 4 are pulsing)—*Source Olympus*

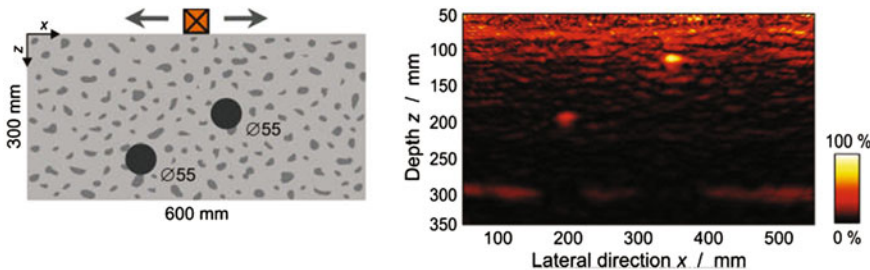


Fig. 2.8 Ultrasonic pulse-echo measurements at a concrete block with two inhomogeneities (*left*) and the SAFT reconstruction after measurement [40]

composite transducers. Instead of calculating the time delays in respect to the reflector these probes are able to steer a narrow beam focusing to a certain depth point (Fig. 2.8, right). However, the physics of migration is applicable in this case as well. Successful applications are described in the literature [37] and several applications for concrete structures have been reported.

These techniques have recently pushed forward. The main difference between seismic migration and ultrasound phased array techniques (UPAT) is the directivity pattern of the beam. In UPAT the beam is steered in a certain direction by using a time delay technique resulting in a constructive addition of signal amplitudes in a certain angle or to a certain depth point. This is causing a “blind region” underneath the surface, where objects are not detectable (near field effect). Moreover is the effort of beam steering on the hardware relatively high. As a consequence (and following seismic prospection methods of today), UPAT was developed towards transducers emitting the excited waves concentrically, what was called “sampling phased array” [6, 29]. The receiving sensing elements have a much larger aperture and no blind spots occur. More importantly are the facts that this technique is on the hardware side more easy to be implemented and probing is significantly faster. While the technique was until now mainly applied at metallic materials and those out of fiber-reinforced polymers an implementation for concrete structures is yet to be done.

2.6.2 Reliability Analysis for NDT Methods and the Effect of a Defect

It is standard nowadays to include an error analysis along with the presentation of NDT data. As all measurement data, these data are subjected to both, systematical and statistical errors. Quantification of these errors including procedures like Gauss’ Propagation of Uncertainty technique and standard deviations are usually given. However, this is no proof of reliability of NDT techniques. A simple question may illustrate this. If, as a result of an application of such a NDT technique, no flaw is

detected, what does that mean? Does it mean that the object contains no flaw or is the used NDT method unable to detect it? Will the flaw be detected by a change of a certain measuring parameter or by repetitive measurements? In recent years methods determining the *Probability of Detection* (PoD) have been developed that can include also the *Receiver Operating Characteristic* (ROC). It is a surprise that these methods are not already widely applied in the NDT of concrete structures. A clear description of the capability of the applied NDT techniques should always be included in a report delivered to a customer. It can already be concluded out of several applications of PoD and ROC analyses that such techniques are probably leading back to a more original question. What type of defects and which dimensions of deterioration are acceptable for the customer; required is a guess of the *Effect of a Defect* (EoD). The NDT expert in the field can often give no answer to these questions. Prior to measurements it should be analyzed, e.g., by static analyses, what effect a certain defect has for the structure of interest.

Moreover, NDT techniques will be more and more required in future to perform a detailed failure prognosis for a structure using full-probabilistic calculations. Knowing the properties of all material and components as well as the effective load history (my means of NDT and SHM) uncertainties can be reduced and the construction can be assessed on the basis of true exposures and loads. This can lead to a reduction of safety factors (β -value). As input parameters the results of NDT techniques can be used, e.g.:

- determination of geometrical properties (e.g., thickness) to calculate the dead load
- measurement of the concrete cover
- positioning of pre-stressing elements to determine the lever arm of a force
- detection of wire breaks and missing reinforcement
- detection and localization of voids (honeycombing) in the concrete matrix.

Using NDT technique to help with the assessment of a structure in some of these problems a probability analysis using PoD and ROC techniques is required.

2.7 Numerical Simulation and Forward Modeling

Numerical simulations that are using for example finite elements, finite differences or boundary element methods are common today to investigate the fracture behavior of materials. A more or less accurate model of the material and the component under the test is required and the failure of such a component under a certain load can be predicted. These techniques are increasingly used to reduce the efforts of empirical destructive tests or to derive more details about the failure process.

Non-destructively derived information—that are more and more available from NDT methods—can be compared to the results of these simulations what leads to a more solid model and usually a more precise setting of the start parameters.

The interaction between destructive tests, numerical simulations and NDT methods is becoming a very efficient way to obtain information about material parameters and the behavior of structural components under different type of loads.

It is obvious that the numerical simulation of the NDT part of the experiments itself can further enhance the benefits. With the use of proper simulation tools, the interaction between a measureable NDT parameter (e.g., the potential field, elastic wave, electro-magnetic field) and the deterioration process in a component can be predicted. Using for example forward modeling tools to predict numerically the interaction of an elastic wave (ultrasound) with a crack can be important to find out, if an ultrasound device can detect a crack of a certain dimension and in a certain depth. It will enable the user to determine, if the setup, the sensors or their frequencies have to be changed. Knowing the EoD (see above) and the PoD as required by the customer, the measurement parameters could be optimized prior to do the first measurement in situ. This is clearly a much more efficient way to use NDT techniques and in particular required for complex materials (like concrete) and difficult boundary conditions (geometries, composites) as we usually have in civil engineering applications.

This can be demonstrated by an example from experiments at the Eidgenössische Technische Hochschule Zürich in Switzerland [39, 43]. One of the major problems concerning pre-stressed concrete elements (as we can found them in bridge girders) are un-grouted ducts, what can lead to corrosion and failure. For many years, it was challenging to find a setup and a NDT technique being able to detect the voids in the duct. In the mentioned study, it was investigated, if AET is able to help. The girder was loaded in 4P-bending and had a length of 4.5 and a cross-section of 0.44×0.44 meter as shown in Fig. 2.9.

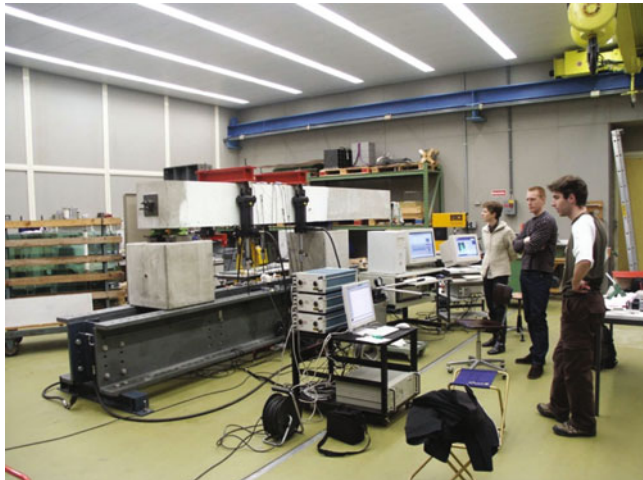


Fig. 2.9 Setup of AET during the 4-Point-Bending load of a pre-stressed concrete beam

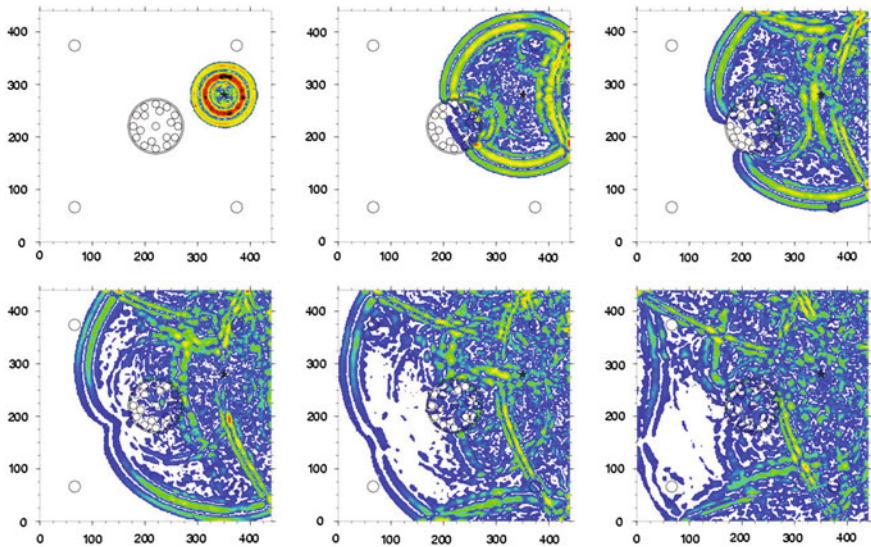


Fig. 2.10 Forward simulation of elastic wave propagation in the beam depicted in Fig. 2.8 with steel reinforcement in the corners and a PE-duct containing steel wires [39]; snap shots in time intervals of 15 μ s

Figure 2.10 depicts the results of a forward modelling of AE waves travelling from a certain point inside a girder propagating through the beam to AE sensors placed at the surface. Cross-sections are shown in time steps of 15 μ s computed using an elasto-dynamic finite integration technique (EFIT) code developed by Schubert [42]. EFIT enable for a correct simulation of the elastic wave propagation in highly complex composites with pores, voids, free surfaces and anisotropic changes of materials properties. Wave phenomena like mode conversion or scattering can be simulated. With unknown source or receiver functions, the simulation describes just the interaction of the waves with the material. It is noticed that the interaction of the waves (compressional and shear waves) with the heterogeneous concrete (aggregates, pores), the reinforcement bars and the duct leads to highly scattered waves. It is difficult to discriminate effects of voids in the duct from other scatterers. With given dimensions and sensor characteristics it will be difficult to detect an un-grouted part of a duct.

The model used in these calculations consisted of 918×918 points and this 2D model alone required a significant calculation time on a standard computer. This is certainly one of the drawbacks since complex models and highly accurate forward modeling codes require some computer power. With advances in micro-computing and optimization of such codes the technique becomes more and more available for public. Codes are already available not only for elastic but also for electro-magnetic waves (RADAR) and for potential field techniques. It seems to be feasible in near future to test first, what PoD can be achieved with a certain NDT technique and

sensor setup, before any expert conduct time-consuming and costly practical measurements. This has the potential to increase significantly the efficiency of NDT applications in CE in future.

2.8 Temporal and Spatial Evaluation of PC Cable Breakage

Due to un-grouted PC ducts, corrosion-induced cables' breakage is reported frequently in post-tensioned PC structures, leading to eventual failure in the worst case. However, the specific failure mechanism as well as deterministic investigation techniques for cables' breakage have yet to be clarified. When the cable is ruptured, elastic energy is released accompanying elastic waves namely acoustic emission (AE) [49]. Identification of the breakage could be carried out by this AE activity, followed by specifying the source location. While as for the existent PC breakage, the area of breakage could be determined by examining secondary AE activity generated due to the friction between fractured grout agent and tendons, which is resulted from re-anchoring around the breakage. These AE activities are experimentally produced using a full-scale PC beam being subjected to four-point bending ([45], Fig. 2.11), where the cables' breakages are simulated by stress reduction of each of PC cables in turn and the breakage areas as well as the failure areas of grout material are quantitatively identified with AE activities. As a result of careful observation of AE activity in terms of failure types, it became obvious that the failure progress due to cables' breakage and following re-anchoring were readily identified by the AE activity (Fig. 2.12). In addition, the existent breakage with re-anchoring area could be specified by AE sources as they had peculiar frequencies than others.

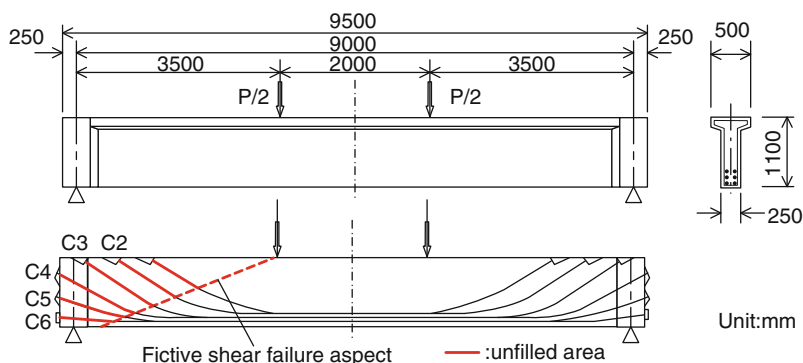


Fig. 2.11 PC beam specimen simulating step-wise cable rupture

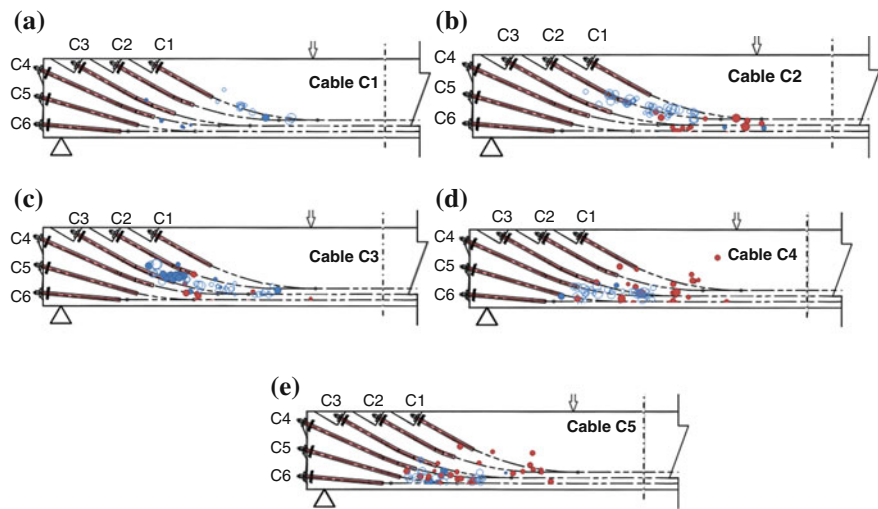


Fig. 2.12 2D AE sources after stress release depicting open circles and ones showing solid circles during cyclic load after each stress release of cable. **a** After stress release of C1. **b** After stress release of C1–C2. **c** After stress release of C1–C3. **d** After stress release of C1–C4. **e** After stress release of C1–C5

2.9 Concluding Remarks

The present chapter intents to address issues related to the NDE monitoring of concrete structures. The importance and special characteristics of concrete make it a challenging material for the usual NDE techniques. However, due to the advancement of technology, the capabilities of testing continuously increase. Improvement of devices and new technologies like wireless sensors simplify monitoring, while tomography algorithms enable accurate visualization of the damage pattern within the structure. The developments in NDE are matching the increased needs of contemporary construction, like better control during manufacturing and operation, as well as reliable condition assessment when is judged necessary. These hopefully meet the highest quality standards, satisfy the requirements of the stakeholders and ensure a safe management of the infrastructure for the public namely infra-asset management.

References

- Aggelis, D.G., Shiotani, T., Polyzos, D.: Characterization of surface crack depth and repair evaluation using Rayleigh waves. *Cem. Concr. Compos.* **31**(1), 77–83 (2009)
- Aggelis, D.: Wave propagation through engineering materials; assessment and monitoring of structures through non-destructive techniques. *Mater. Struct.* **46**, 519–532 (2013)

3. Alani, A.M., Aboutalebi, M., Kilic, G.: Integrated health assessment strategy using NDT for reinforced concrete bridges. *NDT&E Int.* **61**, 80–94 (2014)
4. Balayssac, J.-P., Laurens, S., Arliguie, G., Breysse, D., Garnier, V., Dérobert, X., Piwakowski, B.: “Description of the general outlines of the French project SENSO—Quality assessment and limits of different NDT methods. *Constr. Build. Mater.* **35**, 131–138 (2012)
5. Breccolotti, M., Bonfigli, M.-F., Materazzi, A.-L.: Influence of carbonation depth on concrete strength evaluation carried out using the SonReb method. *NDT&E Int.* **59**, 96–104 (2013)
6. Bulavinov, A., et al.: Sampling phased array a new technique for signal processing and ultrasonic imaging. *ECNDT*, Berlin (2006)
7. Doctor S.R., Hall, T.E., Reid, L.D.: SAFT—the Evolution of a signal processing technology for ultrasonic testing. *NDT Int.* **19**, 163–167 (1986)
8. Glaser, S.D., Tolman, A.: Sense of sensing. *J. Infrastruct. Syst.* **14**(1), 4–14 (2008)
9. Grosse, C.U., Ohtsu, M. (eds.): *Acoustic Emission Testing in Engineering—Basics and Applications*, 404 p. Springer, Heidelberg (2008). ISBN: 978-3-540-69895-1
10. Grosse, C.U., Krüger, M., Bachmaier, S.: Wireless sensing techniques for an efficient monitoring of structures and plants. In: Proceedings 35th MPA Seminar “Materials & Components Behavior in Energy & Plant Technology”, pp. 5.1–5.21, Stuttgart (2009)
11. Grosse, C.U., Glaser, S.D., Krüger, M.: Initial development of wireless acoustic emission sensor motes for civil infrastructure state monitoring. *J. Smart Struct. Syst.* **6**(3), 197–209 (2010)
12. Grosse, C.U.: Evolution of NDT methods for structures and materials: some successes and failures. In: *Non-destructive Testing of Materials and Structures*, pp. 3–18, Springer (2012). ISBN: 978-94-007-0723-8
13. Grosse, C.U.: Wired and wireless structural health monitoring of bridges. In: *Proceedings of the 10th Japanese German Bridge Symposium*, Muenchen (2014)
14. Kim, G., In, C.-W., Kim, J.-Y., Kurtis, K.E., Jacobs, L.J.: Air-coupled detection of nonlinear Rayleigh surface waves in concrete—application to microcracking detection. *NDT&E Int.* **67**, 64–70 (2014)
15. Hatano, H., Mori, E.: Acoustic-emission transducer and its absolute calibration. *J. Acoust. Soc. Am.* **59**(2), 344–349 (1976)
16. Hsu, N.N., Breckenridge, F.R.: Characterization and calibration of acoustic emission sensors. *Mater. Eval.* **39**, 60–68 (1981)
17. Hykes, D.L., Hedrick, W.R., Starchman, D.E.: *Ultrasound Physics and Instrumentation*. Mosby-Year Book, 2. edn (1992)
18. Iliopoulos, A.N., Devriendt, C., Iliopoulos, S.N., Van Hemelrijck, D.: Continuous fatigue assessment of offshore wind turbines using a stress prediction technique. In: *Proceedings of the SPIE 9064, Health Monitoring of Structural and Biological Systems*, 90640S (2014). doi:[10.1117/12.2045576](https://doi.org/10.1117/12.2045576)
19. Kino, G.S.: *Acoustic Waves: Devices, Imaging, and Analog Signal Processing*. Prentice Hall (1987)
20. Krautkrämer, J., Krautkrämer, H.: *Werkstoffprüfung mit Ultraschall*. Springer, Berlin (1986)
21. Krüger, M., Grosse, C.U., Reinhardt, H.W.: Structural health monitoring with wireless sensors to enhance sustainability in structural engineering. In: *IABSE Symposium Weimar 2007 “Improving Infrastructure Worldwide”*. Weimar Symposium Report, vol. 93, pp. 202–211 (2007). ISBN: 978-385748-116-1
22. Lynch, J.P.: An overview of wireless structural health monitoring for civil structures. *Phil. Trans. R. Soc. Lon. A., Math. Phys. Sci. Roy. Soc. Lon.* **365**(1851), 345–372 (2007)
23. Maierhofer, C., Reinhardt, H.W., Dobmann, G. (Eds.): *Non-destructive Testing Methods*. vol. 1 + 2, Woodhead Publishing (2010). ISBN 1-84569-950-5
24. Manthei, G.: “Characterisation of acoustic emission sensors”, EWGAE Vienna, NDT.net. e-J. Nondestr. Test. 9. <http://www.ndt.net>
25. McLaskey, G.C., Glaser, S.D.: Acoustic emission sensor calibration for absolute source measurements. *J. Nondestr. Eval.* **31**(2), 157–168 (2012)

26. Miller, R.K., McIntire, P. (Eds.): Acoustic emission testing. Nondestructive testing handbook, vol. 5, p. 603. American Society for Nondestructive Testing. 2 edn. (1987)
27. Mpalkas, A.C., Vasilakos I., Matikas T.E., Chai, H.K., Aggelis, D.G.: Monitoring of the fracture mechanisms induced by pull-out and compression in concrete. Eng. Fract. Mech. (2014). doi:[10.1016/j.engfracmech.2014.07.020](https://doi.org/10.1016/j.engfracmech.2014.07.020)
28. Ono, K., Cho, H., Matsua, T.: “Bar- and plate-wave characterization of AE sensors”, EWGAE Vienna, NDT.net. e-J. Nondestr. Test. 9 (2010). www.ndt.net
29. Osman, A.: Automated evaluation of three dimensional ultrasonic datasets. PhD Thesis, University Erlangen/Nuernberg, 185 p (2013)
30. Pieraccini, M.: Monitoring of civil infrastructures by interferometric radar: a review. Sci. World J. Article ID 786961 (2013). <http://dx.doi.org/10.1155/2013/786961>
31. Piwakowski, B., Fnine, A., Goueygou, M., Buyle-Bodin, F.: Generation of Rayleigh waves into mortar and concrete samples. Ultrasonics **42**(2004), 395–402 (2004)
32. Proctor, T.M.: Some details on the NBS conical transducer. J. Acoust. Em. **1**(3), 173–178 (1982)
33. Proctor, T.M.: More recent improvements on the NBS conical transducer. J. Acoust. Em. **5**(4), 134–142 (1986)
34. Raupach, M., Reichling, K., Wiggenhauser, H., Stoppel, M., Dobmann, G., Kurz, J.: BETOSCAN—An instrumented mobile robot system for the diagnosis of reinforced concrete floors. In: Alexander, M. (ed.) Proceedings 2nd International Conference on Concrete Repair, Rehabilitation and Retrofitting (ICCRRR). Taylor & Francis, London, pp. 651–655 (2009)
35. Qi, G., Wayne, S.F.: A framework of data-enabled science for evaluation of material damage based on acoustic emission. J. Nondestr. Eval. (2014). doi:[10.1007/s10921-014-0255-7](https://doi.org/10.1007/s10921-014-0255-7)
36. Rilem: Technical Committee 249-ISC Non destructive in situ strength assessment of concrete (2014). http://rilem.net/gene/main.php?base=8750&gp_id=295
37. Ritter, J.: “Ultrasonic Phased Array probes for non-destructive examinations using composite crystal technology”, DGZfP, NDTnet—December 1996, vol. 1, no. 12 (1996)
38. Sbartaï, Z.M., Laurens, S., Elachachi, S.M., Payan, C.: Concrete properties evaluation by statistical fusion of NDT techniques. Constr. Build. Mater. **37**, 943–950 (2012)
39. Schechinger, B.: Schallemissionsanalyse zur Überwachung der Schädigung von Stahlbeton. PhD Thesis, ETH Zürich, Switzerland, IBK-Bericht Nr. 295, vdf Hochschulverlag, 149 p (2006)
40. Schickert, M.: Progress in Ultrasonic SAFT-Imaging of Concrete. In: NDT-CE, Berlin: Deutsche Gesellschaft für Zerstörungsfreie Prüfung (DGZfP), BB 85-CD, vol. 63, 11 p (2003)
41. Schickert, M., Hillger, W.: Ein Ultraschall-Multikanal-Messsystem mit SAFT-Rekonstruktion für die Abbildung von Betonbauteilen. In: DGZfP-Jahrestagung, Münster, 18.-20.5.2009. Berlin: Deutsche Gesellschaft für Zerstörungsfreie Prüfung (DGZfP), CD-ROM, pp. 1–10 (2009)
42. Schubert, F.: Ausbreitungsverhalten von Ultraschallimpulsen in Beton und Schlussfolgerungen für die zerstörungsfreie Prüfung. PhD Thesis, TU Dresden, 310 p (2000)
43. Schubert, F., Schechinger, B.: Numerical modeling of acoustic emission sources and wave propagation in concrete. NDT.net. e-J. Nondestr. Test. **7**(9), (2002). <http://www.ndt.net>
44. Shiotani, T., Momoki, S., Chai, H.-K., Aggelis, D.G.: Elastic wave validation of large concrete structures repaired by means of cement grouting. Constr. Build. Mater. **23**(7), 2647–2652 (2009)
45. Shiotani, T., Oshima, Y., Goto, M., Momoki, S.: Temporal and spatial evaluation of grout failure process with PC cable breakage by means of acoustic emission. Constr. Build. Mater. **48**, 1286–1292 (2013)
46. Shiotani, T., Aggelis, D.G., Makishima, O.: Global monitoring of large concrete structures using acoustic emission and ultrasonic techniques. J. Bridge Eng.-ASCE **14**(3), 188–192 (2009)
47. Shiotani, T., Takada, Y., Watanabe, T., Ohtsu, H.: Damage evaluation of heterogeneous materials by Q-value analysis of AE waveforms, pp. 1–6. JSNDI, Progress in Acoustic Emission XV (2012)

48. Shiotani, T., Takada, Y., Ishitusuka, K., Momoki, K.: Damage assessment of concrete structures by using ultrasonic Q-value. Engineering Technics Press, Proceedings of Structural Faults & Repair 2014, #1336, CD-ROM (2014)
49. Shiotani, T., Shigeishi, M., Ohtsu, M.: Damage evaluation of prestressed concrete-piles by acoustic emission. JSCE J. Mater. Conc. Struct. Pavements **48**(655), 133–141 (2000)
50. Tong, J.-H., Chiu, C.-L., Wang, C.-Y., Liao, S.-T.: Influence of Rebars on elastic-wave-based synthetic aperture Focusing technique Images for detecting Voids in concrete Structures. NDT&E Int. (2014). doi:[10.1016/j.ndteint.2014.08.001](https://doi.org/10.1016/j.ndteint.2014.08.001)
51. USGS: Mineral Commodity Summaries, January 2013. United States Geological Survey, pp. 38–39 (2013). <http://minerals.usgs.gov/minerals/pubs/commodity/cement/mcs-2013-cemen.pdf>
52. Verma, S.K., Bhaduria, S.S., Akhtar, S.: Review of nondestructive testing methods for condition monitoring of concrete structures. J. Constr. Eng. Article ID 834572 (2013). <http://dx.doi.org/10.1155/2013/834572>
53. Weiler, B., Grosse, C.U.: Calibration of Ultrasonic transducers—a comparative study of different methods. Otto Graf J. **6**, 153–167 (1995)
54. Wood, B.R.A., Harris, R.W.: An evaluation of the breaking pencil lead calibration technique, pp. 423–439. Jap. Soc. NDI. Progress in acoustic emission VI, Tokyo (1982)
55. Yu, T.Y., Büyükköztürk, O.: A far-field airborne radar NDT technique for detecting debonding in GFRP-retrofitted concrete structures. NDT&E Int. **41**, 10–24 (2007)
56. Yun, H.-B., Kim, S.-H., Wu, L., Lee, J.-J.: Development of inspection robots for bridge cables. Sci. World J. Article ID 967508 (2013). <http://dx.doi.org/10.1155/2013/967508>
57. Zoidis, N., Tatsis, E., Vlachopoulos, C., Gotzamanis, A., Clausen, J.S., Aggelis, D.G., Matikas, T.E.: Inspection, evaluation and repair monitoring of cracked concrete floor using NDT methods. Constr. Build. Mater. **48**, 1302–1308 (2013)

Chapter 3

Masonry Structures

Giuseppe Lacidogna, Federico Accornero and Alberto Carpinteri

Abstract Historical masonry buildings often show diffused crack patterns due to different causes in relation to original function, construction technique and loading history. Non-destructive testing methods, and especially the Acoustic Emission (AE) technique, applied as in situ monitoring systems allow reliable evaluation of the state of conservation of these structures and its evolution in time. In this chapter three different case studies are presented to show the AE technique capability on the assessment of damage evolution in ancient brick and stone artworks. All the analyzed structures are located in remarkable Italian sites from the Architectural Heritage point of view.

Keywords Acoustic emission · Cracking evolution · Damage localization · Masonry constructions · Structural assessment

3.1 Introduction

Acoustic emission (AE) is a non-invasive and non-destructive monitoring technique and therefore is ideally suited for use in the assessment of historic and monumental structures that are subjected to high, long-term or cyclic loads, or, more in general, are exposed to seismic risk [19, 28]. Having identified the fractured or damaged portion of a structure, it is possible to evaluate its stability from the evolution of damage, which may either gradually come to a halt or propagate at an increasingly fast rate [11, 35, 42, 53]. Moreover, if the position of the defects is not known to begin with, it can be located by making use of a multiplicity of sensors and by triangulation, prior to assessing the stability of a structure based on the evolution of damage phenomena [17, 18, 34, 52].

G. Lacidogna (✉) · F. Accornero · A. Carpinteri
Department of Structural, Geotechnical and Building Engineering,
Politecnico di Torino, Turin, Italy
e-mail: giuseppe.lacidogna@polito.it

Using the AE technique, the authors have acquired considerable experience in the monitoring of historical buildings and monuments [6, 11–14, 22, 23, 40]. In this chapter three different case studies are presented to show the AE technique capability on the assessment of damage evolution in ancient brick and stone artworks. All the analyzed structures are located in remarkable Italian sites from the Architectural Heritage point of view.

As a first example, an interesting study is focused on the structural stability of the medieval towers of Alba, a characteristic town in Piedmont. The impact of earthquakes on damage evolution was assessed for all the towers, whereas for the “Sineo Tower”, characterized by a leaning of about 1 % on the north side, the stability under the influence of dead loads was also investigated [11, 12].

Therefore, the case of the Syracuse Athena Temple monitoring—actually the Syracuse Cathedral—located in Sicily is shown [22, 23, 40]. The Cathedral, placed in the higher zone of the Ortigia island, has been included in the UNESCO World Heritage List since 2005. It presented different evidence of criticism in correspondence to the ancient pillars situated in the central nave of the monument. The Cathedral in fact, is the result of the transformation of the ancient Athena’s Greek Temple (fifth century BC), with modifications that have also been the consequence of the damage caused by earthquakes. In this study, the AE technique was used to determine the damage level in a pillar that is part of the vertical bearing structure of the Cathedral.

Another original application of the AE technique, is on the evaluation of the state of conservation of mural paintings and their structural supports. This study in particular is still in progress on the painting surfaces of the Monte Tabor Chapel, in the UNESCO Renaissance Complex of the Sacred Mountain of Varallo, in Piedmont [28]. While the first two cases are briefly presented, a detailed description of the AE monitoring is performed in the last section.

3.2 AE Monitoring of Historical Buildings and Monuments

As it has been mentioned in the Introduction the AE technique is very usefully adopted by the authors to investigate a wide series of structural problems related to masonry structures. In particular, it has been used to assess the damage evolution in important Italian monuments, to analyze the residual capability of ancient brick masonry under loading, or to evaluate the reliability of reinforcing techniques employed in historical bearing structures.

The leading-edge equipment adopted by the authors consists of six “Units for Storage Acoustic emission Monitoring” (USAM) that can be synchronized for multichannel data processing [6, 11, 12, 22, 23, 27, 40]. The most relevant parameters acquired from the AE signals (frequencies in a range between 50 and 800 kHz, arrival time, amplitude, duration, number of events and oscillations) are

stored in the USAM memory and then downloaded to a PC for multi-channel data processing. Microcracks localization can be performed from this elaboration and the damaging condition of the monitored specimen can be determined [17, 18, 52]. Of course, in the analyses, which also could include the cracks classification methods [1, 26, 43–45], must be taken in account the effects of distortion of the ultrasonic waves on the AE parameters [2, 27].

3.3 The Medieval Towers of Alba

The medieval towers of Alba have been monitored by the AE technique. These masonry buildings from the XIIIth century are among the tallest and mightiest medieval towers preserved in Piedmont (Fig. 3.1).

Sineo Tower is square, 39 m high, and leans to a side by about 1 %. Wall thickness ranges from 2 m at the foundation level to 0.8 m at the top. The bearing walls are “a sacco”, that is, consist of brick faces enclosing a mixture of rubble and bricks bonded with lime and mortar. Over a height of 15 m, the tower is incorporated in a later building. Astesiano Tower has a similar structure, but has a rectangular base. The total height is about 36 m and the tower does not lean on any side.

Torre Bonino, just under 35 m high, is the least imposing of the towers analysed, but the square-shaped structure has been incorporated in a valuable building from the Italian Art Nouveau period.



Fig. 3.1 Astesiano, Sineo and Bonino Towers in the skyline of the city of Alba

For the Sineo Tower, through AE monitoring, two cracks were detected in the inner masonry layer at the seventh floor level (Fig. 3.2a, b). The monitoring process revealed an ongoing damaging process, characterized by slow crack propagation inside the brick walls. In the most damaged zone, crack spreading had come to a halt, the cracks having achieved a new condition of stability, leading towards compressed zones of the masonry. In this particular case, it can be seen that, in the monitored zone, each appreciable crack advancement is often correlated to a seismic event. In the diagram shown in Fig. 3.2d, the cumulative AE function relating to the area monitored is overlaid with the seismic events recorded in the Alba region during the same time period; the relative intensity of the events is also shown [11, 12].

A similar behaviour was observed for the Astesiano Tower. This structure was monitored by means of two transducers applied to the inner masonry layer of the tower, at the fourth floor level near the tip of a large vertical crack. The results obtained during the monitoring period are summarized in Fig. 3.2e. It can be seen how the damage to the masonry and the propagation of the cracks, as reflected by the cumulative number of AE counts, evolved progressively over time. A seismic event of magnitude 4.7 on the Richter scale occurred during the monitoring period: from the diagram we can see how the cumulative function of AE counts grew rapidly immediately after the earthquake. For Torre Bonino, monitored at first floor level, a progressive release of energy is observed under constant loading, this is due to a pseudo-creep phenomenon in the material. A seismic event of magnitude 3.0 on the Richter scale occurred during the monitoring period (Fig. 3.2f).

During the observation period, the towers behaved as sensitive earthquake receptors. Thus, as can be seen, the AE technique is able to analyse state variations in a certain physical system and to identify, well in advance, the premonitory signals that precede a ‘catastrophic’ event [32, 33, 40].

3.4 The Cathedral of Syracuse

The AE technique was also used to assess the structural stability of the Cathedral of Syracuse (Fig. 3.3a), that shows in different parts of its structures traces of the destructive earthquake that struck the City of Syracuse in 1542 (see Fig. 3.3b). In the sixth century AD, the fifth century BC Greek temple of Athena in Syracuse, was transformed into a Catholic Church, and later became the Cathedral of the City; the building was frequently modified along the centuries until the present configuration (Fig. 3.3c) [3, 7, 46, 49]. The internal pillars have a peculiar interest; they had been obtained from the stonework walls of the internal cell of the Greek temple. The pillars show several repaired areas and replacements, but also several cracks. In order to evaluate their state of preservation, the extension and the depth of the replacements and the presence of internal defects, an investigation programme was planned by the Superintendence of Syracuse and the Politecnico of Milan [7].

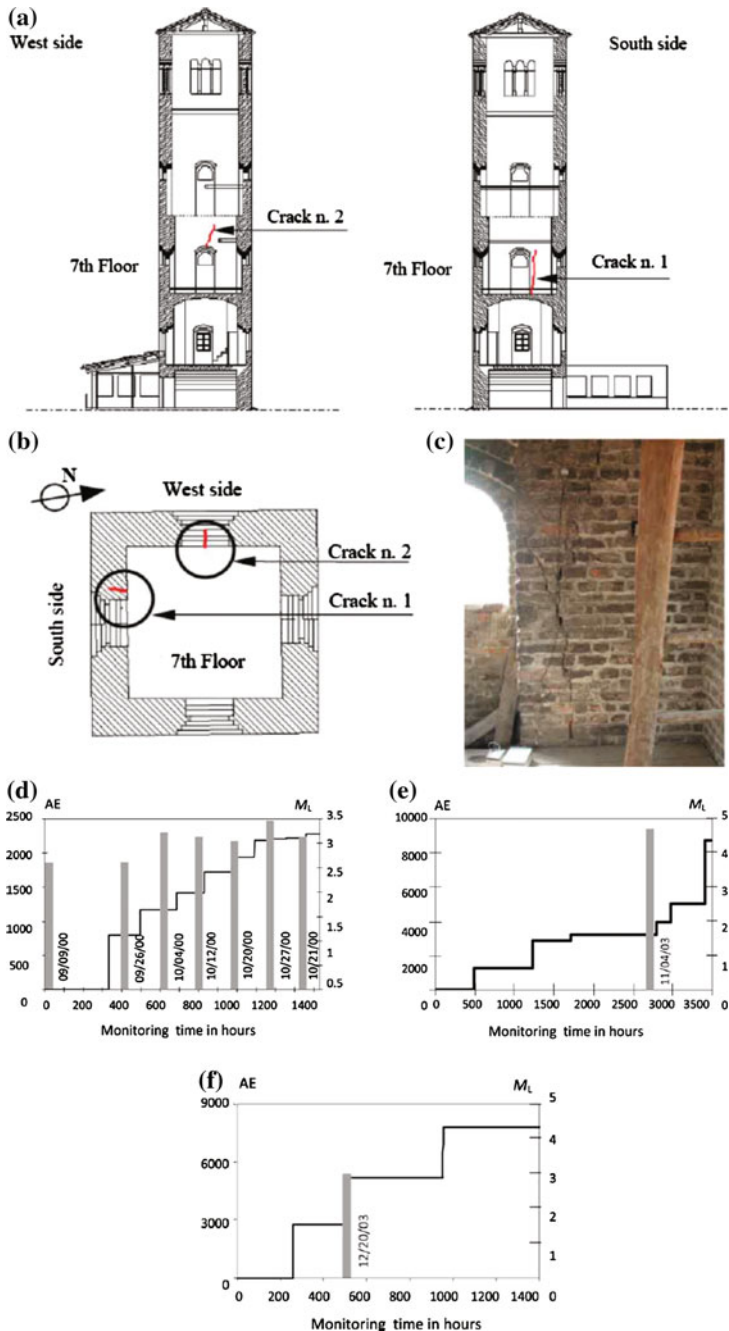


Fig. 3.2 Cross-sections of the Sineo Tower (a), plan of the monitored zone (b), photo taken during the monitoring of crack no. 1 (c). AE counting number and seismic events in local Richter scale magnitude (M_L). Torre Sineo (d), Torre Astesiano (e) and Torre Bonino (f)

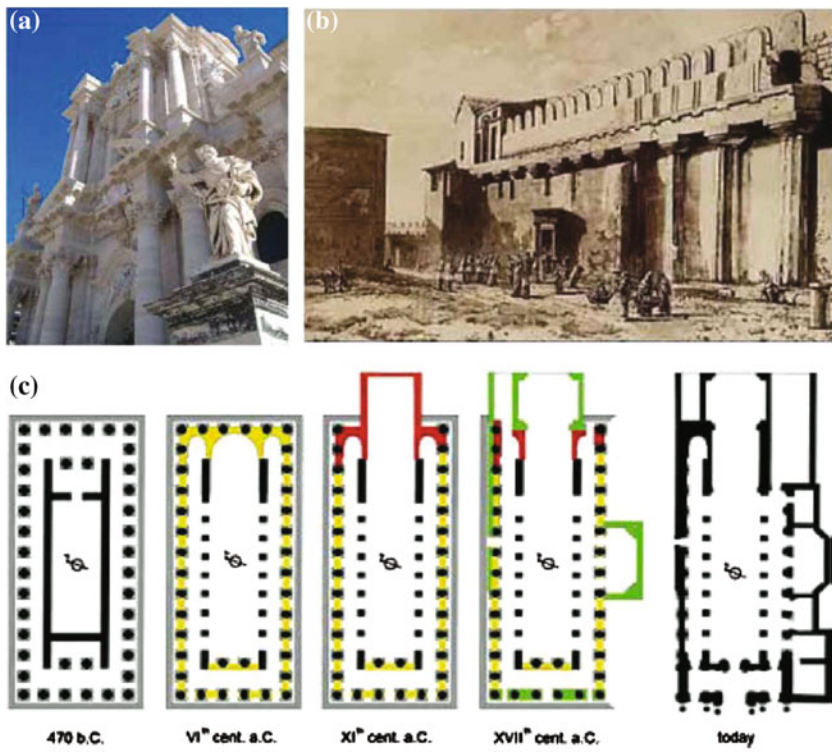


Fig. 3.3 The façade of the Syracuse Cathedral (a). A historical view after the 1542 earthquake (b). The evolution of the plan along centuries (c) [3, 7, 46, 49]

The crack pattern was classified and accurately documented and reported on the geometrical survey. Furthermore, a monitoring of the cracks development carried out for approximately 2 years showed an evident trend to increase their size in some cracks of the pillars positioned at the end of the central nave, which suggested a further check of the damage by acoustic emission [22, 23, 40].

The AE monitoring process was performed on a pillar of the central nave (Fig. 3.4a, c). The temple had 14 columns along the sides and 6 at front, and some of them, belonging to the peristyle and the stylobate, can still be identified. In the layout of the Cathedral, shown in Fig. 3.4a, the pillar selected for the application of the AE monitoring technique is indicated by a circle. On this element, situated towards the altar, serious damage was observed. It is important to stress the effects of the 1542 earthquake, which produced a great deformation of the perimeter wall close to the pillar.

The pillar, save for a few strengthening works performed—according to the Syracuse Superintendence for Cultural Heritage—during a restoration process in 1926 (see Fig. 3.4d) was thought to be made of limestone blocks, probably

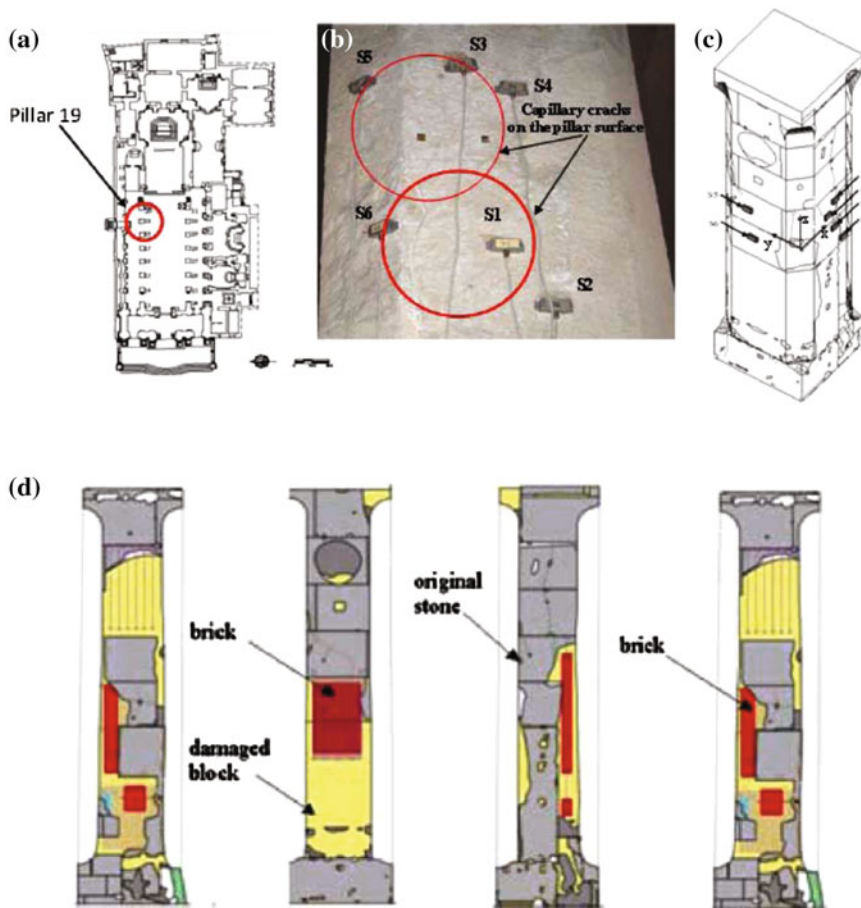


Fig. 3.4 Plan of the Syracuse Cathedral with the indication of the monitored pillar (a). The AE sensors were applied on the external surface of the pillar at a height of about 4 m (b, c). View of the four sides of the monitored pillar. In the figure various materials making the pillar are reported (d) [7, 23]

installed during the initial construction of the temple dedicated to Athena in the fifth century BC.

The AE equipment adopted by the authors consisted of six units, USAM, synchronized for multi-channel data processing [6, 11–14]. The six AE sensors have been applied on the middle zone of the pillar [22, 23, 40] (see Fig. 3.4b, c).

The monitoring process began at 11:00 a.m. of 19 September 2006 and ended at 12:20 p.m. of 21 January 2007. The data collected were analysed in order to interpret the evolution of damage and determine the position of AE sources within the pillar.

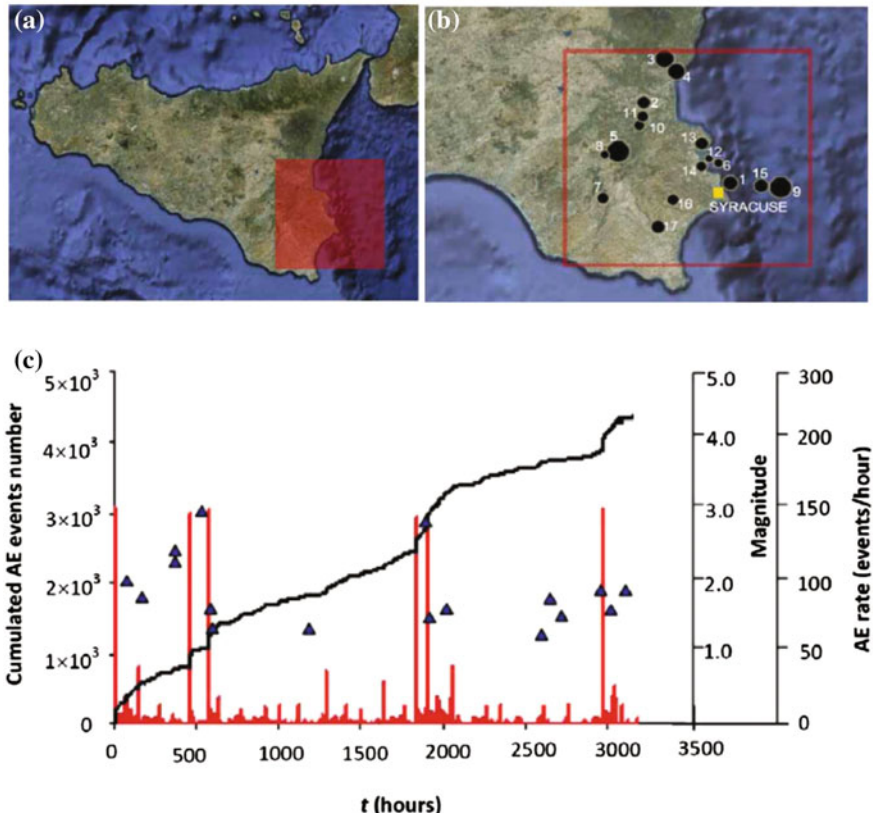


Fig. 3.5 Map of Sicily showing the location of the monitored site (yellow square) and epicenters (black circles) of nearby earthquakes that occurred during the monitoring period (a, b). Cumulated AE events number, instantaneous AE rate averaged over 1 h in the temple pillar and nearby earthquake occurrence (triangles) as functions of time. The most relevant seismic events, with the local magnitude value, occurring during the same period are indicated in graph (c)

Cumulated AE events number, instantaneous AE rate averaged over 1 h in the temple pillar and nearby earthquake occurrence (triangles) as functions of time are reported in Fig. 3.5, considering a region within a radius of ca 50 km around the City of Syracuse (Fig. 3.5a, b). The most relevant seismic events, with the local magnitude value, occurring during the same period are indicated in the graph.

If we examine the chart illustrating the differential function of AE counts, we can see sudden increases in the oscillation peaks occurring at certain intervals over time. It should be also noted that during the monitoring period, strong seismic actions were recorded in the area (see Fig. 3.5c). Earthquake data for the period were obtained from the website: www.ct.ingv.it/Sismologia/GridSism.asp published by the Seismic Data Analysis Group of Catania (Gruppo di Analisi Dati Sismici—INGV-CT). From the wealth of data available, we selected the seismic events with a

local magnitude (ML) greater than 1.2 that occurred during the monitoring period. These events are illustrated in Fig. 3.5c, where the relative magnitudes are also given [22, 23]. The chart in Fig. 3.5c, showing AE monitoring and regional earthquake data, reveals an interesting correlation between the AE activities determined experimentally and seismic events: the timing of the energy peaks measured by means of the AE differential counts is seen to coincide almost invariably with seismic shocks [40]. This correspondence seems to show how the pillar monitored behaves in a pseudo-stable manner when subject to the vertical loads alone, but has a meagre capacity to respond elastically to horizontal or oscillatory actions.

3.5 The Monte Tabor Chapel in Varallo

As aforementioned, the authors have also successfully applied the AE technique, not only to evaluate the stability of the historical structures, but also to assess the state of conservation of mural painting and their structural supports.

The preservation of the mural painting heritage is a complex problem that requires the use of non-destructive investigation methodologies to assess the integrity of decorated artworks without altering their state of conservation [41]. The physical-chemical decay and the damage evolution of materials constituting the decorated surfaces and the structural masonry supports can be caused by infiltrations of water, thermo-elastic stresses, or seismic and environmental vibrations. The physical-chemical degradation has to be dealt with Materials Science and Chemical Engineering techniques [29]. On the other hand, the instability and the dynamic behaviour of the decorated surfaces, induced also by seismic and environmental vibrations, can be investigated by the AE technique, using monitoring systems to control continuously and simultaneously different structural supports [28].

The data collected during the in situ experimental tests can be interpreted with Fracture Mechanics models and methodologies [8, 9, 19, 24].

A complete diagnosis of crack pattern regarding not only the external decorated surface but also the internal support is of great importance due to the criticality of internal defects and damage phenomena, which may suddenly degenerate into irreversible failures [6, 25].

The Sacred Mountain of Varallo is the most ancient Sacred Mountain of Piedmont and Lombardy and it is located among the green of the forests at the top of a rocky spur right above the City of Varallo (Fig. 3.6). It consists in 45 Chapels, some of which are isolated, while others are part of monumental groups. They contain over 800 life-size wooden and multicoloured terracotta statues, which represent the Life, the Passion and the Death of Christ [41].

As the first object of investigation with the AE technique, the Chapel XVII of the Sacred Mountain of Varallo was chosen (Fig. 3.7). This Chapel houses the scene of the Transfiguration of Christ on Mount Tabor. This Chapel was also foreseen in the “Book of Mysteries” by Alessi (1565–1569) [5, 30], from which the group of



Fig. 3.6 The Sacred Mountain of Varallo: view of the square of Tribunals



Fig. 3.7 External view of Chapel XVII (a); internal view of the Mount Tabor installation (b)

sculptures located high on the mountain take inspiration. The relative foundations were already begun in 1572, but the chapel was not completed until the 1660s.

3.5.1 Scaling Laws for AE Monitoring

From a physical point of view, investigations with AE technique of micro-fracture processes have revealed power-law distributions and critical phenomena [31, 36, 51] characterized by intermittency of AE event avalanches [56], fractal distributions of AE event locations, and complex space-time coupling [55]. Localization of cracks distribution within the specimen volume by means of AE technique has permitted to confirm that the energy is dissipated over preferential bands and surfaces during the damage evolution [20, 21]. Moreover, after the work of Scholz on the b -value [50], Aki [4] was the first to show in an empirical way that the seismic b -value is related to the fractal dimension D , and that usually $2b = D$. This assumption, and its implication with the damage release rate and time dependent mechanisms, both at the laboratory and at the Earth's crust scale, has been pointed out in [18, 39].

In this framework, AE data have been interpreted by means of statistical and fractal analysis, considering the multiscale aspect of cracking phenomena [19]. Consequently, a multiscale criterion to predict the damage evolution has been formulated.

Recent developments in fragmentation theories [15] have shown that the energy W during microcrack propagation is dissipated over a fractal domain comprised between a surface and the specimen volume V .

The following *size-scaling* law has been assumed during the damage process:

$$W \propto N \propto V^{D/3}. \quad (3.1)$$

In Eq. (3.1) D is the so-called fractal exponent comprised between 2 and 3, and N is the cumulative number of AE signals that the structure provides during the damage monitoring.

The authors have also shown that energy dissipation, as measured with the AE technique during the damaging process, follows the *time-scaling* law [16]:

$$W \propto N \propto t^{\beta_t}, \quad (3.2)$$

where β_t is the time-scaling exponent for the dissipated energy in the range (0, 3) and N is the number of AE signals.

By working out the exponent β_t from the data obtained during the observation period, we can make a prediction on the structure's stability conditions: if $\beta_t < 1.0$ the structure evolves toward stability conditions; if $\beta_t \approx 1.0$ the process is metastable; if $\beta_t > 1.0$ the process is unstable.

Moreover, a statistical interpretation to the variation in the b -value during the evolution of damage detected by AE has been proposed, which is based on a treatment originally proposed by Carpinteri et al. [10, 21]. The proposed model captures the transition from the condition of diffused criticality to that of imminent failure localisation.

3.5.2 *b*-Value Analysis for AE Monitoring

By analogy with seismic phenomena, in the AE technique the magnitude may be defined as follows:

$$m = \log_{10} A_{\max} + f(r), \quad (3.3)$$

where A_{\max} is the amplitude of the signal expressed in volts, and $f(r)$ is a correction factor taking into account that the amplitude is a decreasing function of the distance r between the source and the sensor.

In seismology the empirical Gutenberg-Richter's law [47]:

$$\log_{10}N(\geq m) = a - bm, \text{ or } N(\geq m) = 10^{a-bm}, \quad (3.4)$$

expresses the relationship between magnitude and total number of earthquakes with the same or higher magnitude in any given region and time period, and it is the most widely used statistical relation to describe the scaling properties of seismicity. In Eq. (3.4), N is the cumulative number of earthquakes with magnitude $\geq m$ in a given area and within a specific time range, whilst a and b are positive constants varying from a region to another and from a time interval to another. Equation (3.4) has been used successfully in the AE field to study the scaling laws of AE wave amplitude distribution. This approach evidences the similarity between structural damage phenomena and seismic activities in a given region of the Earth's crust, extending the applicability of the Gutenberg-Richter's law to Structural Engineering. According to Eq. (3.4), the b -value changes systematically at different times in the course of the damage process and therefore can be used to estimate damage evolution modalities.

Equation (3.4) can be rewritten in order to draw a connection between the magnitude m and the size L of the defect associated with an AE event. By analogy with seismic phenomena, the AE crack size-scaling entails the validity of the relationship:

$$N(\geq L) = cL^{-2b}, \quad (3.5)$$

where N is the cumulative number of AE signals generated by source defects with a characteristic linear dimension $\geq L$, c is a constant of proportionality, and $2b = D$ is the fractal dimension of the damage domain.

It has been evidenced that this interpretation rests on the assumption of a dislocation model for the seismic source and requires that $2.0 \leq D \leq 3.0$, i.e., the cracks are distributed in a fractal domain comprised between a surface and the volume of the analysed region [4, 48, 54].

The cumulative distribution (3.5) is substantially identical to the cumulative distribution proposed by Carpinteri [10], which gives the probability of a defect with size $\geq L$ being present in a body:

$$P(\geq L) \propto L^{-\gamma}. \quad (3.6)$$

Therefore, the number of defects with size $\geq L$ is:

$$N^*(\geq L) = cL^{-\gamma}, \quad (3.7)$$

where γ is a statistical exponent measuring the degree of disorder, i.e. the scatter in the defect size distribution, and c is a constant of proportionality. By equating distributions (3.5) and (3.7) it is found that: $2b = \gamma$. At the collapse, the size of the maximum defect is proportional to the characteristic size of the structure. As shown

by Carpinteri et al. [21], the related cumulative defect size distribution (referred to as self-similarity distribution) is characterized by the exponent $\gamma = 2.0$, which corresponds to $b = 1.0$. It was also demonstrated by Carpinteri et al. [21] that $\gamma = 2.0$ is a lower bound which corresponds to the minimum value $b = 1.0$, observed experimentally when the load bearing capacity of a structural member has been exhausted.

Therefore, by determining the b -value it is possible to identify the energy release modalities in a structural element during the monitoring process. The extreme cases envisaged by Eq. (3.1) are $D = 3.0$, which corresponds to the critical condition $b = 1.5$, when the energy release takes place through small defects homogeneously distributed throughout the volume, and $D = 2.0$, which corresponds to $b = 1.0$, when energy release takes place on a fracture surface. In the former case diffused damage is observed, whereas in the latter two-dimensional cracks are formed leading to the separation of the structural element.

In the following, the data obtained from the monitoring are mainly interpreted by Eqs. (3.2) and (3.4).

3.5.3 Monitoring Results

As described in [28] also this structure has shown itself sensitive to seismic events occurring within a radius of about 100 km from the City of Varallo, and to moisture infiltration that have the effect of detaching the mural paintings from their supports.

As regards the structural integrity, Chapel XVII shows a vertical crack of about 3.00 m in length and a detachment of frescos both on the North wall, which are the object of the monitoring campaign by means of AE. Six USAM AE sensors are employed to monitor the damage evolution of the structural support of the decorated surfaces of the Chapel: four are positioned around the vertical crack while two are positioned near the frescos detachment (Fig. 3.8). For the sensor pasting on decorated surfaces, a suitable methodology was applied.

The monitoring period of the structural supports of the chapel began on April 28, 2011 and ended on June 4, 2011, it lasted about 900 h. The results obtained by the application of the AE sensors are presented in Figs. 3.9 and 3.10. For the vertical crack (Fig. 3.9), approximately 550 AE signals were analyzed, while for the frescos detachment (Fig. 3.10) 1200 AE signals were considered. The cumulated AE signals, AE rates, β_t parameters and b -values are shown in Figs. 3.9 and 3.10. In particular, to calculate the β_t parameters and the b -values represented in Fig. 3.9, about 200 data for time were used, while about 400 data for time were used for the same parameters reported in Fig. 3.10. More specifically, the three b -values calculated for the vertical crack (Fig. 3.9) are shown in Fig. 3.11 with the corresponding coefficients of determination R^2 .

As can be seen from Fig. 3.9, the vertical crack monitored on the North wall of the chapel presents a stable condition during the acquisition period ($0.5 < \beta_t < 1.0$) and a distribution of cracks on a surface domain is clearly proved by the b -value in

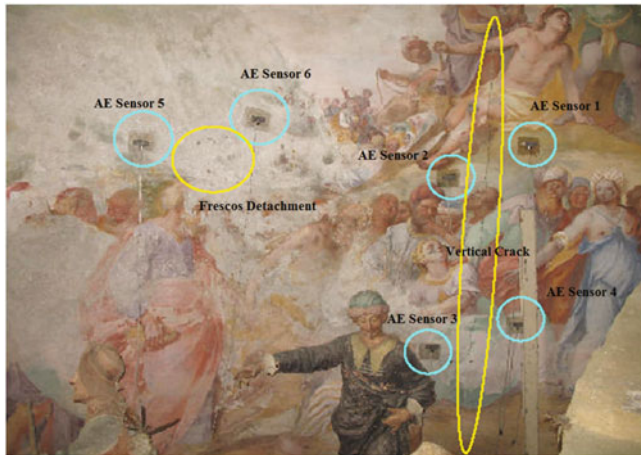


Fig. 3.8 Chapel XVII: View of the monitored damages and position of the AE sensors

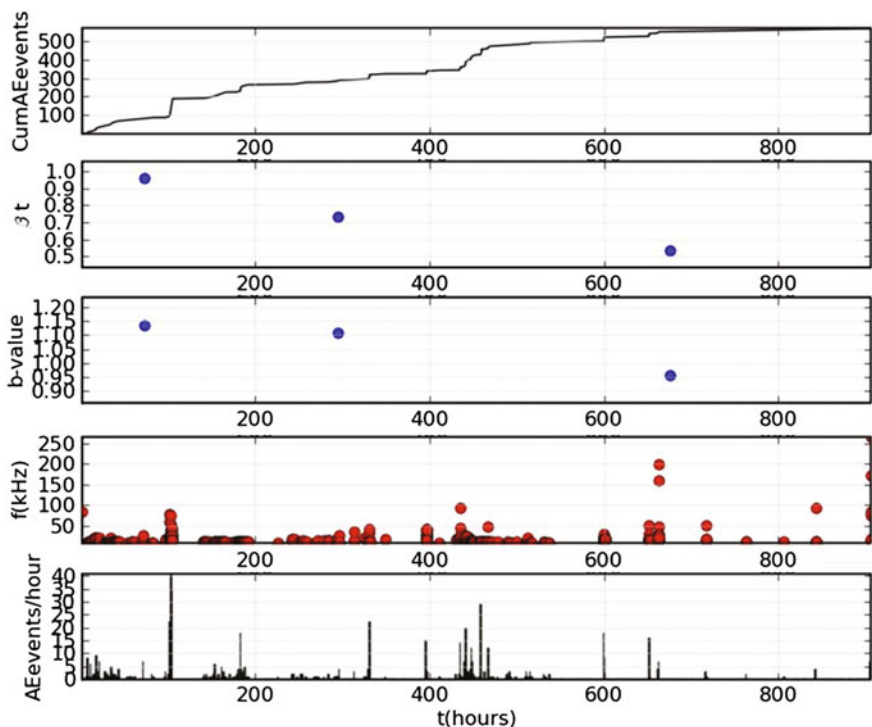


Fig. 3.9 Chapel XVII: AE from the vertical crack monitoring

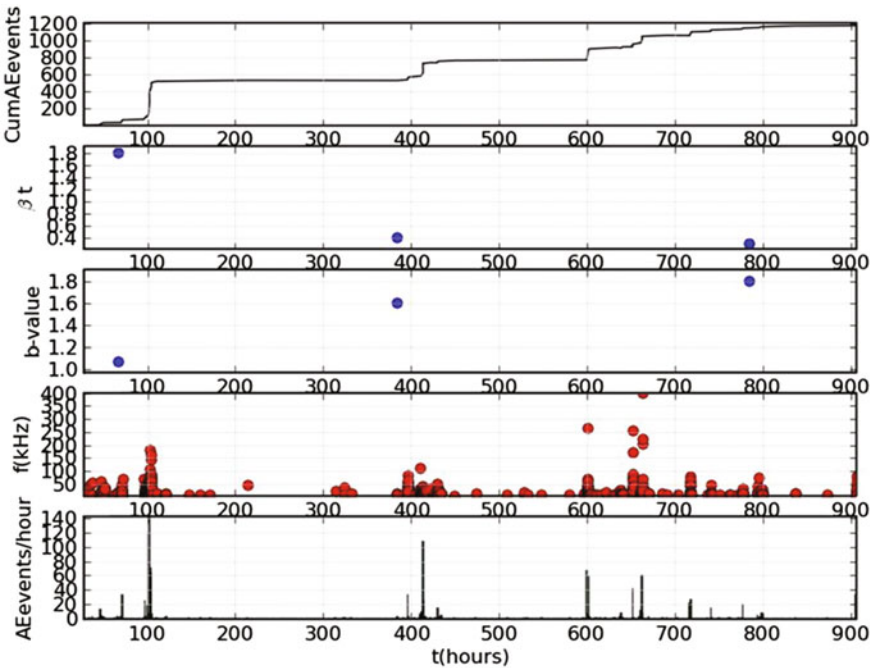


Fig. 3.10 Chapel XVII: AE from frescos detachment monitoring

the range (0.95, 1.15). In this case, it is interesting to note that, since the monitored wall is of large dimensions, a b -value approaching to 1 does not imply a substantial loss of load-bearing capacity of the entire wall, but rather the coalescence of the microcracks along the surface of the vertical crack, which can continue to advance without substantially compromising the structure bearing capacity. Further evidence for the presence of the crack is offered by the low frequency signals registered (<200 kHz): as a matter of fact, considering the velocity as a constant and applying the Lamb ratio [37], the wavelength needs to be larger than the size of the maximum inhomogeneity in order for the wave to pass through without significant modifications in its waveform. It is reasonable to assume that for a high frequency wave it is possible only to propagate through a small inhomogeneity; on the contrary for a low frequency wave it is possible also to propagate through a large inhomogeneity [19, 38]. Concerning the monitored frescos detachment (Fig. 3.10), the decorated surface tends to evolve towards metastable conditions ($0.5 < \beta_t < 1.8$) and the signals acquired show high frequency characteristics (<400 kHz); therefore a distribution of microcracks in the volume is assumed for the analysed region.

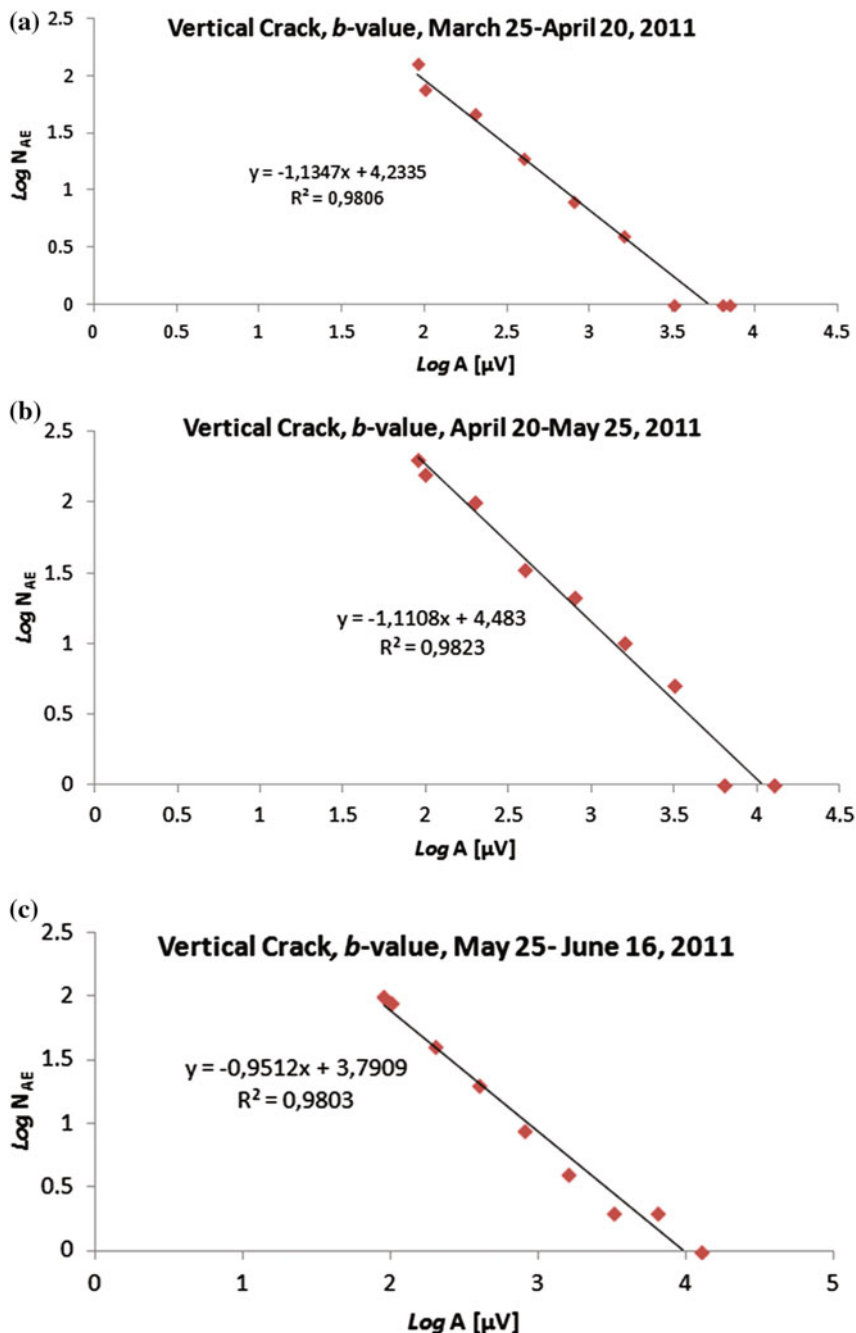


Fig. 3.11 Chapel XVII: *b*-values computed for the vertical crack with the corresponding coefficients of determination R^2 ; from March 25 to April 20, 2011 (a); from April 20 to May 25, 2011 (b); from May 25 to June 16, 2011 (c)

3.6 Conclusions

Three case studies have been presented to show the AE technique capability on damage assessment of masonry historical structures. The collected data were analyzed in order to interpret the evolution of damage by means of Fracture Mechanics. Thanks to this method, it is possible to estimate the amount of energy released during the fracture process and to obtain information on the criticality of ongoing processes.

The first case study focused on the structural stability of three medieval towers rising in the centre of Alba, a characteristic town in Piedmont. Then, the evolution of damage in a pillar that is part of the vertical bearing structure of the Syracuse Cathedral has been evaluated. From the charts plotted for differential or cumulative functions of the AE signal counts, it has been seen that these structures are subjected to a damage process mainly due to the seismic actions. This suggests that AE structural monitoring coupled to the analysis of local earthquake activity can be a tool of crucial importance in earthquake damage mitigation.

Finally, the Chapel XVII of the Sacred Mountain of Varallo has been presented. It shows some structural concern due to large cracks and a degradation of the high valuable frescos, which tend to detach from the masonry support. In order to assess the evolution of those phenomena, the results of the AE monitoring program have been provided. The monitoring results show that the large cracks are stable, while the process of detachment of the frescos is evolving cyclically.

The proposed non-destructive monitoring approach allows for analyze cracks evolution, and in general damage propagation. Therefore it is useful to derive the optimal priority for interventions directed to preservation, safeguard and valorization of the masonry architectural heritage.

Acknowledgments The Town Council of Alba, the Cultural Heritage Superintendence of Syracuse, and the Special Nature Reserve of Varallo are gratefully acknowledged.

The authors are also grateful to Prof. Luigia Binda, for having provided the historical data on the Syracuse Cathedral. Special thanks are also due to Dr. Gianni Niccolini, and Dr. Amedeo Manuello for the collaboration in the AE data analysis on the same monument.

References

1. Aggelis, D.G.: Classification of cracking mode in concrete by acoustic emission parameters. *Mech. Res. Commun.* **39**, 153–157 (2011)
2. Aggelis, D.G., Mpalkas, A.C., Ntalakas, D., Matikas, T.E.: Effect of wave distortion on acoustic emission characterization of cementitious materials. *Constr. Build. Mater.* **35**, 183–190 (2012)
3. Agnello, G.: Il Duomo di Siracusa e i suoi Restauri. Ediprint, Siracusa (1996). (in Italian)
4. Aki, A.: A probabilistic synthesis of precursory phenomena. In: Simpson, D.W., Richards, P. G. (Eds.) *Earthquake Prediction: An International Review*, vol. 4, pp. 566–574 (1981)
5. Alessi, G.: Libro dei Misteri. Anastatic Copy, Bologna (1974). (in Italian)

6. Anzani, A., Binda, L., Carpinteri, A., Lacidogna, G., Manuello, A.: Evaluation of the repair on multiple leaf stone masonry by acoustic emission. *Mater. Struct.* **41**, 1169–1189 (2008)
7. Binda, L., Casolo, S., Petrini, V., Saisi, A., Sanjust, C.A., Zanzi, L.: Evaluation of the seismic vulnerability of the Syracuse Cathedral: investigation and modeling. In: Proceedings of International Symposium Studies on Historical Heritage. Yildiz Technical University, Istanbul, Turkey, pp. 683–690 (2004)
8. Botvina, L.R., Shebalin, P.N., Oparina, I.B.: A mechanism of temporal variation of seismicity and Acoustic Emission prior to macrofailure. *Dokl. Phys.* **46**, 119–123 (2001)
9. Botvina, L.R.: Damage evolution on different scale levels. *Phys. Solid Earth* **47**, 859–872 (2011)
10. Carpinteri, A.: Scaling laws and renormalization groups for strength and toughness of disordered materials. *Int. J. Solids Struct.* **31**, 291–302 (1994)
11. Carpinteri, A., Lacidogna, G.: Structural monitoring and integrity assessment of medieval towers. *J. Struct. Eng. (ASCE)* **132**, 1681–1690 (2006)
12. Carpinteri, A., Lacidogna, G.: Damage evaluation of three masonry towers by acoustic emission. *Eng. Struct.* **29**(7), 1569–1579 (2007)
13. Carpinteri, A., Lacidogna, G.: *Earthquakes and Acoustic Emission*. Taylor & Francis, London (2007)
14. Carpinteri, A., Lacidogna, G.: *Acoustic Emission and Critical Phenomena: From Structural Mechanics to Geophysics*. CRC Press, Boca Raton (2008)
15. Carpinteri, A., Pugno, N.: Fractal fragmentation theory for shape effects of quasi-brittle materials in compression. *Mag. Concr. Res.* **54**, 473–480 (2002)
16. Carpinteri, A., Lacidogna, G., Pugno, N.: Time-scale effects on acoustic emission due to elastic waves propagation in monitored cracking structures. *Phys. Mesomech.* **8**, 77–80 (2005)
17. Carpinteri, A., Lacidogna, G., Niccolini, G.: Critical behaviour in concrete structures and damage localization by acoustic emission. *Key Eng. Mater.* **312**, 305–310 (2006)
18. Carpinteri, A., Lacidogna, G., Pugno, N.: Richter's laws at the laboratory scale interpreted by Acoustic Emission. *Mag. Concr. Res.* **58**, 619–625 (2006)
19. Carpinteri, A., Lacidogna, G., Pugno, N.: Structural damage and life-time assessment by Acoustic Emission monitoring. *Eng. Fract. Mech.* **74**, 273–289 (2007)
20. Carpinteri, A., Lacidogna, G., Puzzi, S.: Prediction of cracking evolution in full scale structures by the *b*-value analysis and Yule statistics. *Phys. Mesomech.* **11**, 260–271 (2008)
21. Carpinteri, A., Lacidogna, G., Niccolini, G., Puzzi, S.: Critical defect size distributions in concrete structures detected by the acoustic emission technique. *Meccanica* **43**, 349–363 (2008)
22. Carpinteri, A., Lacidogna, G., Manuello, A.: The *b*-value analysis for the stability investigation of the ancient Athena Temple in Syracuse. *Strain* **47**, 243–253 (2009)
23. Carpinteri, A., Lacidogna, G., Invernizzi, S., Manuello, A., Binda, L.: Stability of the vertical bearing structures of the Syracuse Cathedral: experimental and numerical evaluation. *Mater. Struct. (RILEM)* **42**, 877–888 (2009)
24. Carpinteri, A., Lacidogna, G., Puzzi, S.: From criticality to final collapse: Evolution of the *b*-value from 1.5 to 1.0. *Chaos, Solitons Fractals* **41**, 843–853 (2009)
25. Carpinteri, A., Invernizzi, S., Lacidogna, G.: Historical brick-masonry subjected to double flat-jack test: Acoustic emissions and scale effects on cracking density. *Constr. Build. Mater.* **23**, 2813–2820 (2009)
26. Carpinteri, A., Corrado, M., Lacidogna, G.: Heterogeneous materials in compression: Correlations between absorbed, released and acoustic emission energies. *Eng. Fail. Anal.* **33**, 236–250 (2013)
27. Carpinteri, A., Lacidogna, G., Accornero, F., Mpalkas, A.C., Matikas, T.E., Aggelis, D.G.: Influence of damage in the acoustic emission parameters. *Cement Concr. Compos.* **44**, 9–16 (2013)
28. Carpinteri, A., Lacidogna, G., Invernizzi, S., Accornero, F.: The Sacred Mountain of Varallo in Italy: Seismic risk assessment by Acoustic Emission and structural numerical models. *Sci. World J. Special Issue* (2013)

29. De Filippis, E., Tulliani, J.M., Sandrone, R., Scarzella, P., Palmero, P., Lombardi, Sertorio C., Zerbiniatti, M.: Analisi degli intonaci della Cappella del Calvario al Sacro Monte di Varallo. *ARKOS* **12**, 38–45 (2005)
30. De Filippis, E.: Sacro Monte of Varallo. Borgosesia (2009). (in Italian)
31. Garcimartin, A., Guarino, A., Bellon, L., Ciliberto, S.: Statistical properties of fracture precursors. *Phys. Rev. Lett.* **79**, 3202 (1997)
32. Gregori, G.P., Paparo, G.: Acoustic emission (AE): A diagnostic tool for environmental sciences and for non destructive tests (with a potential application to gravitational antennas). In: W. Schroeder, ed. Meteorological and geophysical fluid dynamics (A book to commemorate the centenary of the birth of Hans Ertel), 417 pp., Arbeitkreis Geschichte der Geophysik und Kosmische Physik, Wilfried Schröder/Science, Bremen, pp. 166–204 (2004)
33. Gregori, G.P., et al.: Acoustic emission and released seismic energy. *Nat. Hazards Earth Syst. Sci.* **5**(6), 777–782 (2005)
34. Grosse, C.U., Reinhardt, H.W., Dahm, T.: Localization and classification of fracture types in concrete with quantitative acoustic emission measurement techniques. *NDT Int.* **30**(4), 223–230 (1997)
35. Grosse, C.U., Ohtsu, M.: Acoustic Emission Testing. Springer, Heidelberg (2008)
36. Lu, C., Mai, Y.-W., Shen, Y.-G.: Optimum information in crackling noise. *Phys. Rev. Lett.* **E 72**, 027101–1 (2005)
37. Lamb, H.: On waves in an elastic plate. *Proc. Roy. Soc. A* **93**, 114–128 (1917)
38. Landis, E.N., Shah, S.P.: Frequency-dependent stress wave attenuation in cement-based materials. *J. Eng. Mech.* **121**, 737–743 (1995)
39. Main, I.G.: Damage mechanics with long-range interactions: Correlation between the seismic *b*-value and the two-point correlation dimension. *Geophys. J. Int.* **111**, 531–541 (1992)
40. Niccolini, G., Carpinteri, A., Lacidogna, G., Manuello, A.: Acoustic emission monitoring of the Syracuse Athena Temple: Scale invariance in the timing of ruptures. *Phys. Rev. Lett.* **106**:108503/1–4 (2011)
41. Niccolini, G., Borla, O., Accornero, F., Lacidogna, G., Carpinteri, A.: Scaling in damage by electrical resistance measurements: An application to the terracotta statues of the Sacred Mountain of Varallo Renaissance Complex (Italy). *Rend. Lincei Sci. Fisiche Nat.* **26**, 203–209 (2014)
42. Ohtsu, M.: The history and development of acoustic emission in concrete engineering. *Mag. Concr. Res.* **48**, 321–330 (1996)
43. Ohtsu, M., et al.: Recommendation of RILEM TC212-ACD: Acoustic Emission and related NDE techniques for crack detection and damage evaluation in concrete: Measurement method for acoustic emission signals in concrete. *Mater. Struct.* **43**, 1177–1181 (2010)
44. Ohtsu, M., et al.: Recommendation of RILEM TC212-ACD: Acoustic Emission and related NDE techniques for crack detection and damage evaluation in concrete: Test method for damage qualification of reinforced concrete beams by Acoustic Emission. *Mater. Struct.* **43**, 1183–1186 (2010)
45. Ohtsu, M., et al.: Recommendation of RILEM TC212-ACD: Acoustic Emission and related NDE techniques for crack detection and damage evaluation in concrete: Test method for classification of active cracks in concrete by Acoustic Emission. *Mater. Struct.* **43**, 1187–1189 (2010)
46. Privitera, S.: Illustrazioni sull'Antico Tempio di Minerva. Oggi il Duomo di Siracusa. Memoria del Parroco Serafino Privitera, Tipografia La Fenice Musumeci, Catania (1863). (in Italian)
47. Richter, C.F.: Elementary Seismology. In: W.H. Freeman, San Francisco and London (1958)
48. Rundle, J.B., Turcotte, D.L., Shcherbakov, R., Klein, W., Sammis, C.: Statistical physics approach to understanding the multiscale dynamics of earthquake fault systems. *Rev. Geophys.* **41**, 1–30 (2003)
49. Russo, S.: La Cattedrale di Siracusa. Archivio Storico Siracusano **III**(V), 35–62 (1991). (in Italian)

50. Scholz, C.H.: The frequency-magnitude relation of microfracturing in rock and its relation to earthquakes. *Bull. Seismol. Soc. Am.* **58**, 399–415 (1968)
51. Sethna, J.P., Dahmen, K.A., Myers, C.R.: Crackling noise. *Nature* **410**, 242 (2001)
52. Shah, S.P., Li, Z.: Localization of microcracking in concrete under uniaxial tension. *ACI Mater. J.* **91**(4), 372–381 (1994)
53. Shiotani, T., Fujii, K., Aoki, T., Amou, K.: Evaluation of progressive failure using AE sources and improved b-value on slope model tests. *VII Prog. Acoust. Emission* **7**, 529–534 (1994)
54. Turcotte, D.L.: *Fractals and Chaos in Geology and Geophysics*. Cambridge University Press, New York (1997)
55. Turcotte, D.L., Shcherbakov, R.: Damage and self-similarity in fracture. *Theoret. Appl. Fract. Mech.* **39**, 245–258 (2003)
56. Weiss, J., Marsan, D.: Three-dimensional mapping of dislocation avalanches: Clustering and space/time coupling. *Science* **299**, 89–92 (2003)

Chapter 4

Computerized AE Tomography

Yoshikazu Kobayashi and Tomoki Shiotani

Abstract Newly developed Computerized Acoustic Emission Tomography (AE Tomography) is summarized, which could identify elastic wave velocity distribution and source locations of AE events. Starting with theory of AE Tomography based on ray-trace technique, two- and three-dimensional problems are stated, and capability of AE Tomography is discussed by performing a series of numerical investigations. Furthermore, AE Tomography is applied for evaluation of existing structures as well as laboratory tests to verify an applicability of AE Tomography.

Keywords Computerized tomography · Ray-trace · 2D AE tomography · 3D AE tomography

4.1 Introduction

Accidents of concrete structures are frequently reported world-wide due to disasters, damages and deteriorations. Considering the unexpected growth of construction investment, it is important to maintain the structures with the limited budget to extend their service lives. To sustain these aging infrastructures, the preventive maintenance shall be taken rather than the reactive maintenance [2]. However, the assessment techniques, sensitive to the tiny or early damage for the preventive maintenance, are not yet to be well established. The techniques to diagnose early internal damages of infrastructures is thus in high demand.

For diagnosis of internal damages in concrete structures, ultrasonic- or seismic-wave tomography and acoustic emission (AE) measurement have been widely applied to evaluate the structural integrity. The ultrasonic-wave tomography

Y. Kobayashi (✉)
Department of Civil Engineering, Nihon University, Tokyo, Japan
e-mail: kobayashi.yoshikazu@nihon-u.ac.jp

T. Shiotani
Graduate School of Engineering, Kyoto University, Kyoto, Japan
e-mail: shiotani@df7.so-net.ne.jp; shiotani.tomoki.2v@kyoto-u.ac.jp

is a technique to reconstruct the velocity distribution from travel times of ray-paths among excitations and receivers. Since the travel times must contain information of the location and the excitation time, the excitation shall be made at the designated point with an accurate time of excitation records. For AE measurement, in contrast, AE sources could be identified from arrival time differences among AE sensors, assuming a homogeneous velocity in the material of interest.

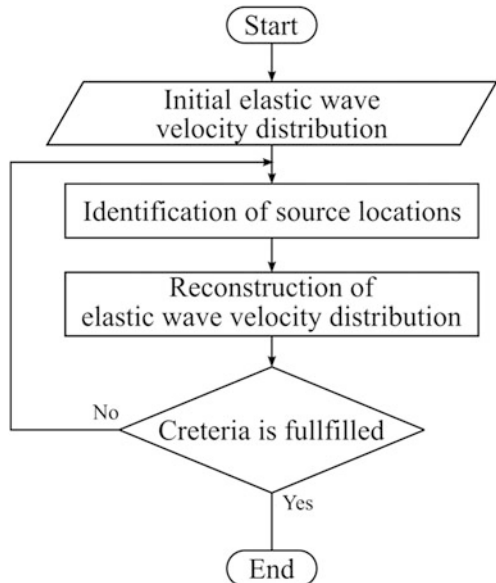
With respect to the issue on propagation velocity, the source location in AE measurement is based on an opposite idea to the velocity reconstruction in tomography. So far as pioneering works, simultaneous implementation of AE source location and the velocity reconstruction was proposed [8, 9]. These studies adopted an assumption that the wave ray-paths among sources and receivers are straight to simplify the computational procedure. As a result, the velocity distribution reconstructed would contain errors due to its insufficient treatment of the ray-paths. The authors have been studying the algorithm which can implement such wave ray-traces as to determine the velocity distribution and to locate AE sources. In this chapter, newly proposed AE source-location algorithm and the tomography to determine the velocity distribution are stated. The details of ray-trace technique and tomography procedure can be found elsewhere [3].

4.2 Computational Flow of AE Tomography

The algorithm, which can implement both wave ray-traces to determine the velocity distribution and to locate AE sources, is named AE tomography. Thus, the locations of AE sources and the velocity distributions are simultaneously estimated. In the actual procedure, the estimation is iteratively performed one another because the former depends on the latter vice versa. Locations of AE sources are computed with an assumed elastic-wave velocity, and then the velocity structure is reconstructed by using the first arrival time travelling between sources and receivers in the tomography. It should be noted that the first travel times are obtained as differences between arrival times of AE waves at receivers and emission times at AE sources. Then, AE source locations are revised on the basis of the velocity distribution of the cells of which velocity is updated.

With regards to required information on the both estimations, such a crucial dependency is found that simultaneous implementation of the two procedures would be difficult. The fact results in a strategy, in which an initial velocity distribution is assumed for AE source locations, following determination of emission times and then the conventional elastic-wave tomography is performed. A computational flow is summarized in Fig. 4.1. The algorithm consists of two stages. At the first stage, the source locations are computed by using arrival times based on the initial elastic-wave velocity distribution. The emission times of AE signals are also estimated from locations of receivers. It is noteworthy that this process is executed with consideration of inhomogeneity of the elastic-wave velocity distribution on the basis of ray-trace technique. At the second stage, theoretical arrival times at the receivers are

Fig. 4.1 Analytical flow of AE tomography



calculated as the sum of the estimated emission times and travel times from the estimated source location to the receivers on the basis of the ray-trace technique, as well as the identification of the source locations. The velocity distribution is reconstructed and updated, by minimizing the differences between the theoretical arrival times and the measured arrival times. These two stages are iteratively executed until the criterion on convergence is fulfilled. Eventually, the elastic-wave velocity structure and the source locations are determined simultaneously.

4.3 Source Location Technique

In present algorithm, the source locations are computed on heterogeneous velocity distribution. On the basis of the ray-trace technique, the accuracy of resultant source locations is improved. At first, the velocity distribution is assumed in the medium of interest. Thus, arrival times of AE at locations of receivers are known. The ray-trace is respectively conducted from individual receivers on a mesh that covers the medium of interest to compute travel times from the receiver to the nodal points. Here, the potential emission time at the nodal points, P'_{ik} , can be computed as,

$$P'_{ik} = A_i - \Delta T_{ik}, \quad (4.1)$$

where i indicated the i th receiver, k denotes k th nodal point to be arrived, A_i is the arrival time at the receiver i , ΔT_{ik} is the travel time from the receiver i to the nodal point k and P'_{ik} is the potential emission time at the point k . The potential emission

time implies the time when AE event is to be emitted at the nodal point k in the case where the arrival time is observed as A_i at the receiver i on the given elastic-wave velocity structure. This procedure is executed for every receiver on an individual event. Thus, if n receivers are installed in the medium, every nodal point has n potential emission times for the individual event. It should be noted that the potential emission times must be identical to AE generations at the source location, if the ray-paths and the elastic-wave velocity distribution are correct. However, because the accuracy of the velocity distribution is generally insufficient, the nodal point that gives the minimum variance of the potential emission times is chosen in this source location algorithm.

The advantage of this source location technique is to take into account the effect of heterogeneity of the elastic-wave velocities for the computation of the source location. Since this technique is supposed to be applied to evaluation of structural integrity and the heterogeneity of velocity distribution is frequently found in practice, the proposed procedure is quite effective. Especially, the heterogeneity would be stronger if the medium is seriously deteriorated. It might result in severe miscalculation of the source locations in the conventional source location technique. By employing AE-Tomography, source locations could be obtained with the reasonable accuracy even in the case of severe heterogeneity of the elastic-wave velocities, in particular, in the degraded medium. For the reliable evaluation of structural integrity, the advantage of the source location technique presented would play a significant role.

It is noteworthy that the relay point introduced [3] shall be another candidate in this algorithm. The resolution of the source location is controllable by changing the density of relay points. This helps to increase the accuracy of the identified source location even in the case that the mesh is coarse. In contrast, the computational cost highly rises if the relay points installed densely on the mesh. Hence, the cost and benefit on the accuracy of the source location should be considered to decide the density of the relay points prior to computing the source location. Additionally, while the emission times of the individual events are necessary for the reconstruction of elastic-wave velocity structure, the average of the potential emission times at the source location is adopted as the emission time O'_k of the event as,

$$O'_k = \frac{1}{n} \sum_{i=1}^n P'_{ik}. \quad (4.2)$$

In following section, the algorithm of reconstruction is presented.

4.4 Elastic-Wave Tomography with Estimation of Source Location

The elastic-wave velocity distribution is to be reconstructed by iteratively updating to minimize the differences between observed arrival times and computed arrival times. The differences are formalized by using observation equations. Since the

emission time is estimated as the average of the potential emission times at the source location, the theoretical arrival time A'_i at receiver i is obtained, as follows;

$$A'_i = O'_k + \Delta T_{ik}. \quad (4.3)$$

Because cells that are crossed by the ray-path from the source location k to receiver i and the length of segment in the cells are already computed in the ray-trace procedure, observation equations of the arrival times are written, as following;

$$\begin{Bmatrix} A'_1 \\ A'_2 \\ \vdots \\ A'_n \end{Bmatrix} = \begin{Bmatrix} O'_k \\ O'_k \\ \vdots \\ O'_k \end{Bmatrix} + \begin{bmatrix} \ell_{11} & \ell_{12} & \dots & \ell_{1m} \\ \ell_{21} & \ell_{22} & \dots & \ell_{2m} \\ \vdots & \vdots & \ddots & \vdots \\ \ell_{n1} & \ell_{n2} & \dots & \ell_{nm} \end{bmatrix} \begin{Bmatrix} S_1 \\ S_2 \\ \vdots \\ S_n \end{Bmatrix}. \quad (4.4)$$

This is the observation equation of one AE event. The equation is rewritten as,

$$\{A'_i\} = \{O'_k\} + [\ell_{ij}] \{S_j\}. \quad (4.5)$$

Although this equation looks like linear, it is actually nonlinear with slowness S_j , since the computed source location and the ray-path vary with the velocity distribution. Hence, the observation equation is linearized by ignoring the nonlinearity, and it might cause errors on the reconstruction. However, the errors become negligible in the proposed procedure of the reconstruction, although the correction of errors is given below. Equation 4.5 is arranged for individual AE events, and renamed by serially numbering as,

$$\{A'\}_l = \{A'_i\}, \quad (4.6)$$

$$\{O'\}_l = \{O'_k\}, \quad (4.7)$$

$$[\ell_{ij}]_l = [\ell_{ij}], \quad (4.8)$$

in which l is a serialized AE event number. Thus, entire observation equations are described, as follows;

$$\begin{Bmatrix} \{A'\}_1 \\ \{A'\}_2 \\ \vdots \\ \{A'\}_{en} \end{Bmatrix} = \begin{Bmatrix} \{O'\}_1 \\ \{O'\}_2 \\ \vdots \\ \{O'\}_{en} \end{Bmatrix} + \begin{bmatrix} [\ell_{ij}]_1 \\ [\ell_{ij}]_2 \\ \vdots \\ [\ell_{ij}]_{en} \end{bmatrix} \begin{Bmatrix} S_1 \\ S_2 \\ \vdots \\ S_n \end{Bmatrix}, \quad (4.9)$$

in which en is number of AE events. The equation is rewritten as,

$$\{A'\} = \{O'\} + [\ell]\{S\}. \quad (4.10)$$

Eventually, the difference between the observed and computed arrival time $\{\Delta A\}$ is obtained,

$$\{\Delta A\} = \{A\} - \{A'\} = (\{A\} - \{O'\}) + [\ell]\{S\} = \{T\} - \{T'\}. \quad (4.11)$$

where $\{T\}$ is the travel time vector that is estimated from the observed arrival times and the computed occurrence times, and $\{T'\}$ is the travel time vector that is computed by applying the ray-trace technique between the computed source location and the receivers. Thus, reconstruction of the elastic-wave velocity structure in AE-Tomography algorithm is performed by minimizing the difference between $\{T\}$ and $\{T'\}$. The emission times and the source locations that are computed by the source location technique are applied to obtaining $\{T\}$ and $\{T'\}$, respectively. The observation equation is written by changing the observation vector, as follows;

$$\{T\} = [\ell]\{S\}. \quad (4.12)$$

It is noteworthy that this observation equation is identical to the observation equations for the conventional elastic-wave velocity tomography. This implies that the first travel times observed are also applicable as observation data in this algorithm. This fact is quite beneficial in practice. The number of observation data can be increased, if preliminary surveys to measure the first travel times are performed. The observation equations obtained from the computed emission times are less accurate than those from the first travel times measured. Thus, the use of the first travel times could upgrade the reconstruction of the velocity distribution, whereas the travel time vector that is computed from the computed emission time involves “estimation”.

The reconstruction of the elastic-wave velocity distribution is an identification problem, and many techniques are available. SIRT (Simultaneous Iterative Reconstruction Technique) is well known, because of its simplicity and robustness. The procedure distributes the differences between the observed travel time and computed travel time on cells in the ray-path as,

$$\Delta T_{ij} = \frac{\Delta T_i \ell_{ij}}{\sum_j \ell_{ij}}. \quad (4.13)$$

Here i is the number of observation equation and j is the cell number. ℓ_{ij} is a element of matrix $[\ell]$, and i and j correspond to row number and column number of

matrix $[\ell]$, respectively. For minimizing the distributed travel time error ΔT_{ij} in the cell j , the slowness at the cell j is updated as

$$S'_{ij} = S_j + \Delta S'_{ij} \quad (4.14)$$

in which

$$\Delta S_{ij} = \frac{\Delta T_{ij}}{\ell_{ij}} = \frac{\Delta T_i}{\sum_j \ell_{ij}} \quad (4.15)$$

This represents an update of slowness of cell j by only one ray-path. Thus, final updates of the slowness are computed as weighted average of ΔS_{ij} with ℓ_{ij} in the individual cells, and updated slowness of cell j is described as,

$$S'_j = S_j + \frac{\sum_i \Delta S_{ij} \ell_{ij}}{\sum_i \ell_{ij}}. \quad (4.16)$$

Since the algorithm reconstructs the elastic-wave velocity distribution, two-dimensional AE tomography is executed by combining with the source location technique.

4.5 Numerical Verification of Two-Dimensional AE Tomography

4.5.1 Source Location Technique in Two-Dimensional Problem

An applicability of the present algorithm is verified in two-dimensional problems [4]. Figure 4.2 shows a two-dimensional numerical model which represents a cross-section of the model. The cross-section consists of two regions, colored orange and colored blue. The orange and blue regions represent the sound and the damaged regions, respectively, of which elastic-wave velocities are set to 4000 and 3000 m/s. Artificial 100 AE sources are randomly generated in the cross-section. Travel times from AE sources to the receivers that are installed on the apexes of the cross-section are computed by the ray-trace technique. The computed travel times are employed as the observed arrival times of AE events, and the source locations are performed.

Additionally, for evaluating the effects of the relay points on the accuracy of the source locations identified, two cases of $N = 1$ and $N = 4$ are studied. Here, the parameter “N” means the number of the relay points in individual cells. Namely, the case $N = 1$ implies that the relay points are not installed. In the case $N = 4$, the cell is divided into 4 in horizontal and vertical directions and a lattice is made, as the

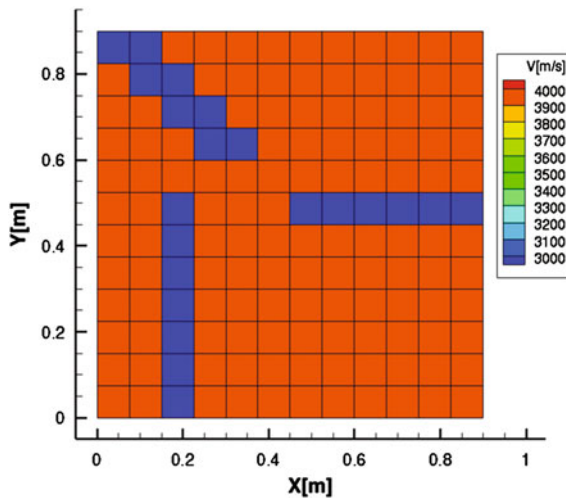


Fig. 4.2 A two-dimensional model for the source location technique

relay points are installed at nodal points of the lattice. Thus, the relay points are densely installed with the increase in the parameter N .

Figure 4.3 shows results of the source locations. It is found that the source locations are accurately estimated even in the heterogeneous velocity field. In the case $N = 1$, the source locations are identified at the nodal points of the mesh. This is because the relay points are not installed, although the real source locations randomly distribute in the cross-section. This implies that the resolution of the source location is depend on the mesh size and the identified source locations could contain intervals of the nodal points as the maximum errors. In the case $N = 4$, the resolution of the source location is drastically improved due to the installation of the relay points. Since 4 relay points are installed on the individual cells, the resolution

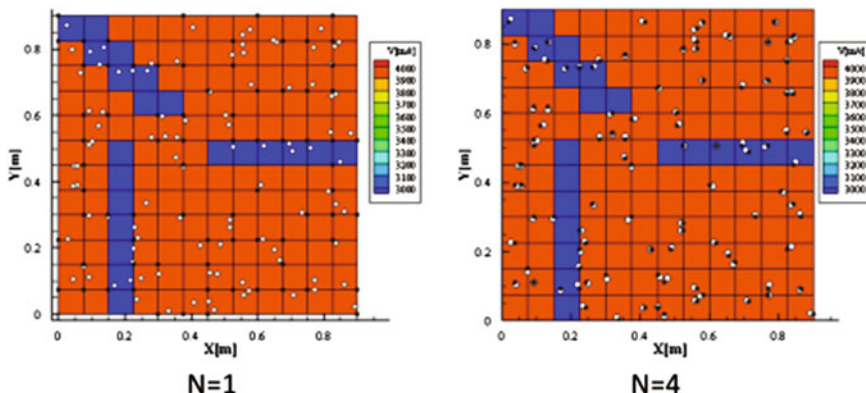


Fig. 4.3 Identified source locations

of the source location is performed with 1/4 interval of the nodal points. Hence, the identified source locations can be closer to the real source locations than the case of $N = 1$. This result suggests the mesh dependency of the resolution of the source location.

4.5.2 AE Tomography in Two-Dimensional Problem

The presented algorithm of AE Tomography is applied to a two-dimensional problem. A numerical model is shown in Fig. 4.4, as one crack is modeled. This through-thickness crack corresponds to a low-velocity area. Artificial 100 AE events are randomly generated in this cross section, and arrival times of AE signals at receivers that are installed at apexes of the cross-section are computed by conducting the ray-trace from the artificial sources. In the computation, the ray-path across the crack is ignored to model the through-thickness crack. It should be noted the first travel times are applied to numerical verification. Here, arrival times of AE are handled, as emission times of AE are unknown quantities. The condition corresponds to the case that all of the emission times are zero by chance. This is because the procedure of AE tomography is applicable to all the cases where arrival times are identical. Thus, without information on the emission times, the velocity distribution is to be readily constructed. Here, initial elastic wave velocity distribution is assumed as uniform, in which elastic wave velocity is 4000 m/s.

Figure 4.5 shows the elastic-wave velocity distribution reconstructed and identified source locations by the presented AE tomography algorithm. A low velocity area is found in the vicinity of the crack, whereas the identified area is spreading at the bottom of the cross section rather than representing the shape of the crack. The reconstruction of the elastic-wave velocity structure is an identification problem and its accuracy depends on the conditions of the observation. Generally, sparse installation of the receivers limits the number of the ray-paths. Thus, the accuracy of the reconstructed velocity structure is degraded at the areas where the ray-paths is poorly arranged. In this example, only four receivers are installed on the apexes of the cross section, and thus the ray-paths mostly head from the center of the cross

Fig. 4.4 A crack model for two-dimensional AE tomography

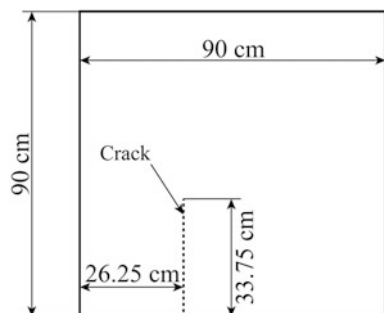
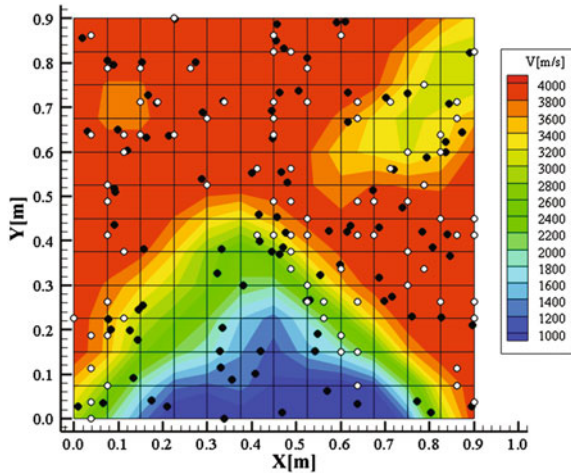


Fig. 4.5 Reconstructed elastic wave velocity structure and the identified source locations

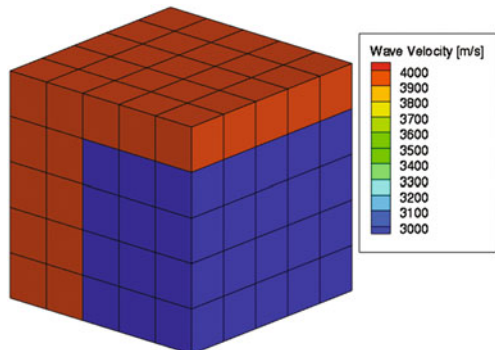
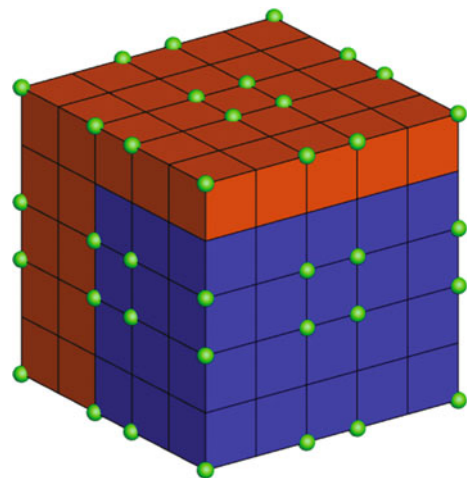


section to the apexes. As a result, the crack is visualized as the low velocity area on the lower half of the cross section. Since the cracked area could be found as the low velocity area even in the sparse receiver installation, the present technique would be sufficient for screening of the anomalies.

4.6 Numerical Examples of Three-Dimensional AE Tomography

4.6.1 Source Location Technique in Three-Dimensional Problem

An applicability of the presented algorithm is verified in three-dimensional problem as well [5]. A three-dimensional (3D) model is shown in Fig. 4.6. The model consists of two regions, colored orange and colored blue, which represent the sound and damaged regions. Here, elastic-wave velocities are set to 4000 and 3000 m/s, respectively. Travel times from AE sources assumed that are randomly generated in the volume are computed by the ray-trace technique, and are employed as the observed arrival times of AE events and then their source locations are identified. The verification is executed by comparing identified and true source locations. 56 receivers are illustrated as green spheres shown in Fig. 4.7. These are installed on the surfaces. Figure 4.8 illustrates identified source locations that are shown as white spheres, while true source locations are shown as black spheres. It is noteworthy that there exist slight differences between the identified and true source locations, because of a limitation on resolution of the source locations. The present algorithm assigns the source locations on nodal or relay points in the volumetric

Fig. 4.6 3D model**Fig. 4.7** Locations of dense installation of receivers for source location

meshes, and it is not guaranteed that the true source locations exist on the points. These errors are reduced by adopting more dense setting of nodal or relay points in the volume although the computational cost rises.

The receivers are densely set on the volume in Fig. 4.6. Obviously, it is difficult to use many receivers in practical applications. Hence, another case is studied by using a few numbers of receivers as illustrated in Fig. 4.9. Only eight receivers are installed at apexes of the volume as shown, and the source locations are identified by using the velocity distribution in Fig. 4.6. According to the results in Fig. 4.10, it is realized that the present algorithm could identify the source locations with reasonable accuracy, even with the less number of receivers than the case of Fig. 4.8.

Fig. 4.8 Source locations in dense installation of receivers

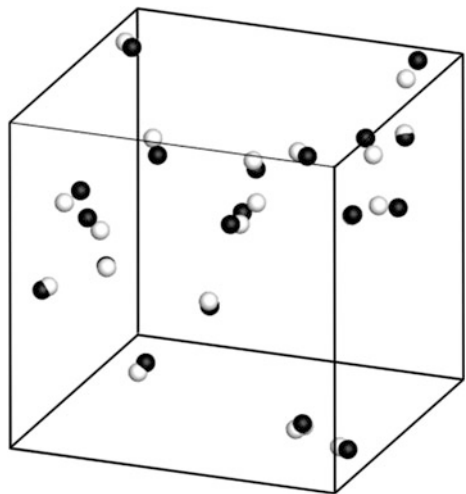
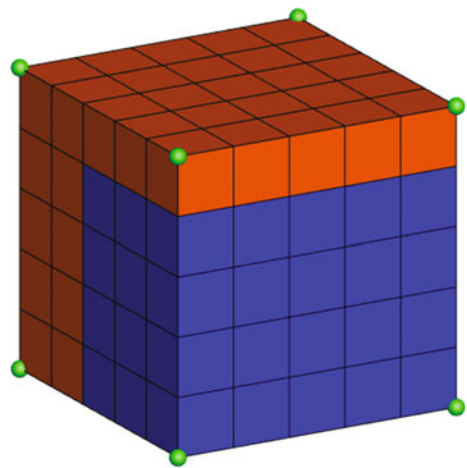


Fig. 4.9 Locations of sparse installation of receivers for source location



4.6.2 AE Tomography in Three-Dimensional (3D) Problem

Figure 4.11 shows a model for 3D AE tomography. Eight receivers are installed at the apexes of the volume, and data collections are conducted as the same as the source location. 20 events are generated in this case, and elastic-wave velocity distribution is updated 10 times by using SIRT. It is noted that observations are generated by using the elastic-wave velocity distribution of the model in Fig. 4.6, where homogeneous velocity distribution with the elastic-wave velocity of 4000 m/s is specified as its initial velocity. Reconstructed elastic wave velocity distribution and identified source locations are shown in Fig. 4.12. The velocity

Fig. 4.10 Source locations in sparse installation of receivers

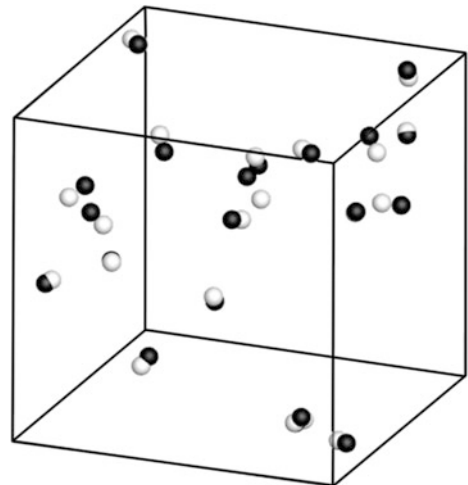


Fig. 4.11 Initial model for AE-Tomography

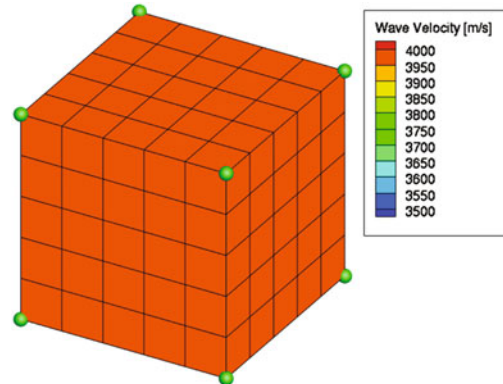


Fig. 4.12 Identified source locations and elastic wave velocity distribution (Number of events = 20, Number of updates = 10)

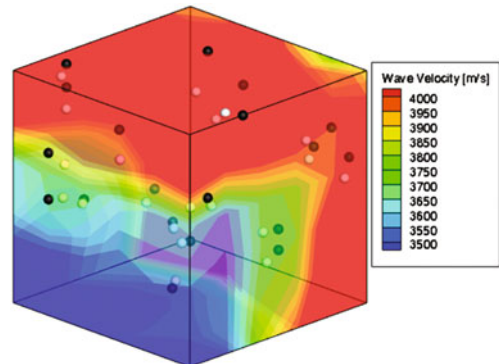
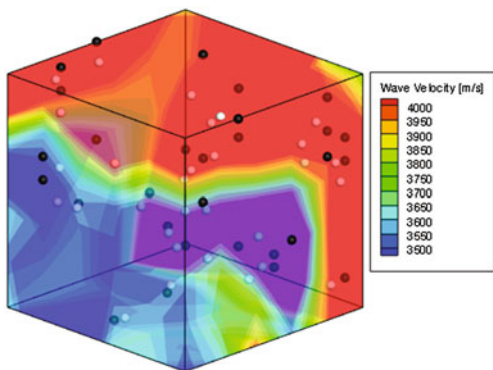


Fig. 4.13 Identified source locations and elastic wave velocity distribution (Number of events = 30, Number of updates = 40)



distribution reconstructed is so similar to that in Fig. 4.6 as that the identified source locations are similar as well. Concerning the accuracy of source locations, there exist a little differences from the result of the verification of the source location technique. This is because the velocity distribution is unknown in this case, and thus the reconstructed distribution is not identical to that of Fig. 4.6. The source locations are to be determined by applying the reconstructed velocity distribution. It eventually leads to the errors of identified source locations. As a result, the source locations identified show the approximate locations.

AE tomography is verified in another observation condition. The number of events and the number of iteration is increased into 30 and 40, respectively. Figure 4.13 shows that the identified source locations and the elastic-wave velocity distribution reconstructed. The results are improved by employing more number of events and iterations. It implies that the reconstructed elastic wave-velocity distribution and the source locations become more accurate by upgrading observation conditions.

4.7 Applications

4.7.1 Planar Structure

AE tomography was applied to a deteriorated reinforced concrete (RC) bridge deck of the bullet train [12]. At the investigation site, some exfoliations were found in the shallow areas by impact acoustics and then are identified as shown in Fig. 4.14. Since the damage near the surface doesn't always reflect the degree of internal damages, the surface-wave tomography was performed. An area investigated is 2400 mm × 2400 mm on the bottom surface of RC bridge deck. As shown in Fig. 4.15, 13 AE sensors are arranged for AE tomography. In addition, the array of

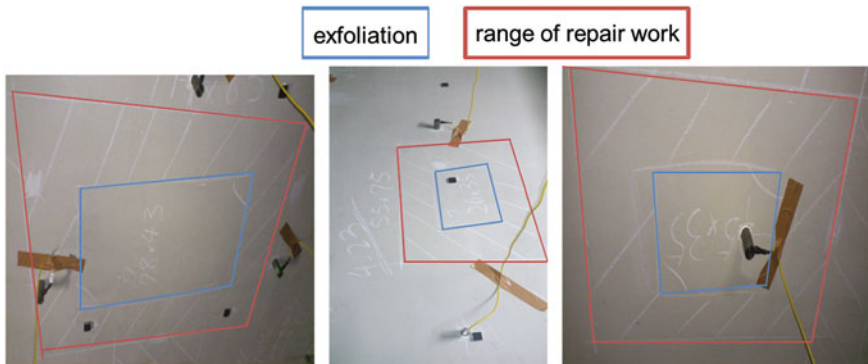


Fig. 4.14 Exfoliations and range of repair work in the surface of RC bridge deck

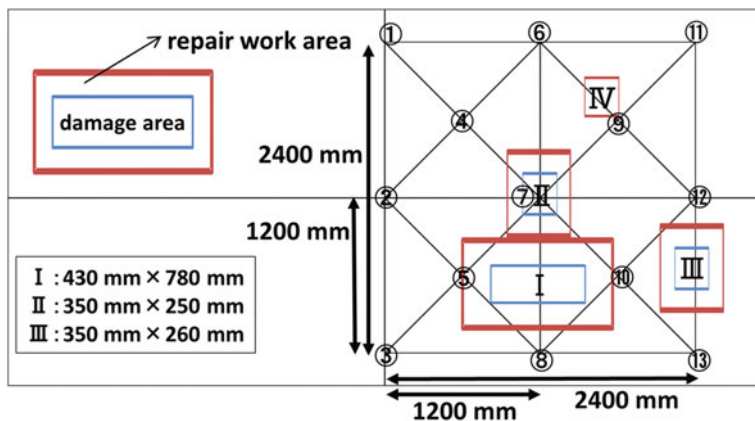


Fig. 4.15 Sensor array of AE tomography

16-accelerometer is found in Fig. 4.16 for the surface-wave tomography. As can be seen in these figures, four damage areas (I, II, III and IV) have been already estimated by impact acoustics. It is noted that damage area IV could not be confirmed by impact acoustics, prior to AE measurement.

It is known that surface wave or Rayleigh wave propagates along the surface with rotating motions of elliptic orbit inside. In particular, surface wave exhibits the largest energy which accounts for 70 % of the whole energy, with lower attenuation rate than those of other waves. Based on these characteristics, surface wave tomography has been proposed as to diagnose inside the structures from the surface [1, 6]. Figure 4.17 illustrates a concept of the surface wave tomography. At first, surface waves have been excited with hammering. In the case that such internal defects as cracks and voids exist in the shallow layer, reflection and dispersions of surface wave result in the longer propagation distance than those of non-defect

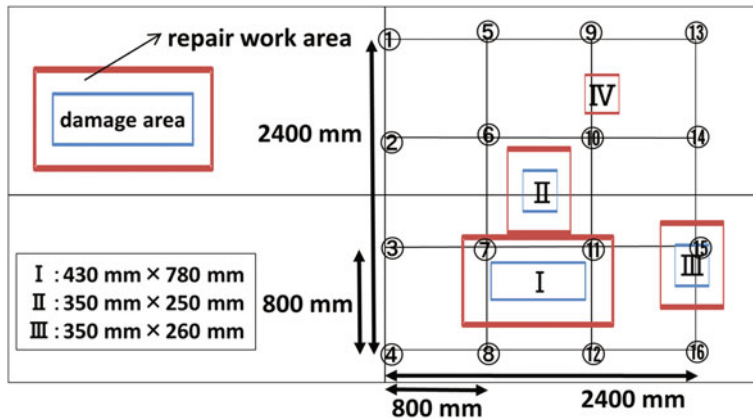


Fig. 4.16 Sensor array of Rayleigh-wave tomography

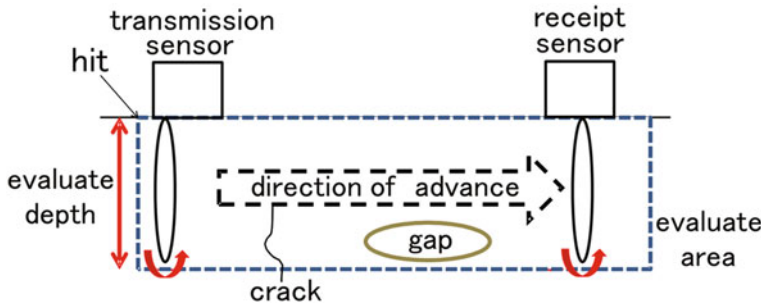


Fig. 4.17 Rayleigh wave tomography

layer. As a result, the propagation velocity becomes smaller than that of intact. Accordingly it is possible to evaluate the inner damages by estimating the propagated velocity obtained from the dominant frequency of surface wave in the tomography procedure. In this case, the maximum depth to be estimated corresponds to the wavelength calculated from the dominant frequency of the surface wave. In addition, the diameter of a hammer head may change the frequency as to adjust the measurement depth. Still the depth to be evaluated is, in principle, limited to a half of the thickness.

Results of Rayleigh wave tomography are shown in Fig. 4.18, where results of impact acoustics are superimposed. The damage areas from I to IV are reasonably identified. In advance, the areas from I to III were evaluated by the impact acoustics, while no information could be obtained for the damage area IV. It is found that several damaged areas are located near the lower right, corresponding to area III and the central area, corresponding to areas I and II. It is noted that impact acoustics and Rayleigh wave tomography only evaluate the shallow layer. As a

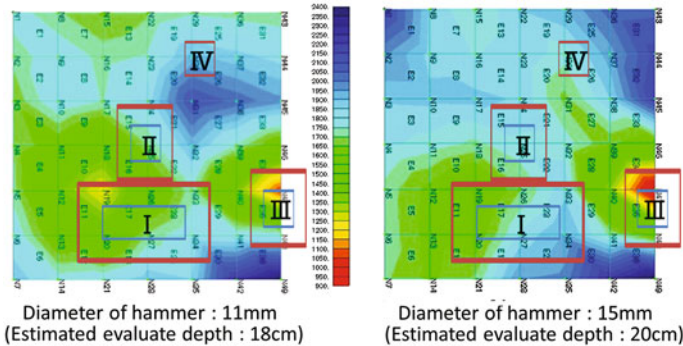


Fig. 4.18 Results of Rayleigh wave tomography

result, the damage areas identified in Fig. 4.18 represent the damages located shallower than the evaluation depth.

AE measurement was conducted repeatedly 10 times during the passage of bullet trains. Because AE waves obtained from the measurement included background noises, mechanical vibrations caused by trains passage and secondary AE activity, it was necessary to extract only the secondary AE activity generated from existing damages. This is because only the secondary AE activity must be applied to AE tomography analysis. It has been already reported that AE waves associated with the background noises have small energy levels. Thus, the noise-related AE waves were eliminated by filtering small-energy waves. Then AE waves due to vibrations were filtered. Figure 4.19a shows AE wave detected by the train vibration, while AE wave generated from the existent damage, namely due to secondary AE activity is shown in Fig. 4.19b. It is observed that AE wave from the existent damage has a short rise time and exponential attenuation over the time. In contrast,

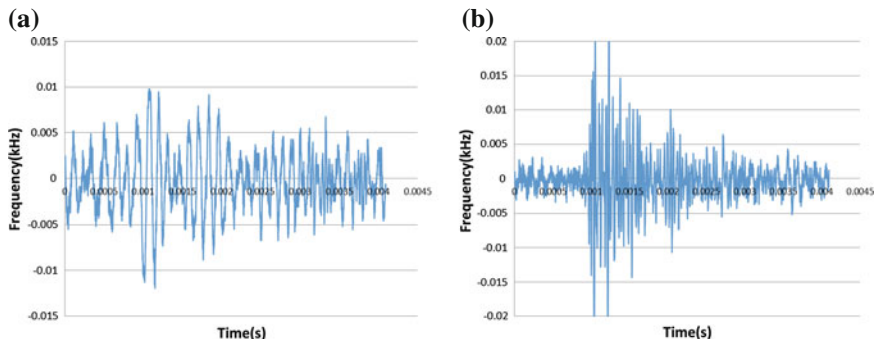


Fig. 4.19 Waveforms detected in AE measurement. **a** Vibration-induced AE waveform. **b** AE waveform induced by existent damage

Table 4.1 Characteristic AE parameters due to different causes (*Energy unit relative and frequency unit kHz*)

Passage		Energy	Average FRQ	Center FRQ	Peak FRQ
First	AE wave	30.6	14.3	32.8	18.4
	Vibration wave	54.125	6.875	33	6.75
Second	AE wave	101	13.75	28.91667	21.66667
	Vibration wave	95	10	29.36364	7.181818
Third	AE wave	117.1667	11.83333	31.66667	21.83333
	Vibration wave	100.2	9.9	30.8	7

vibration-induced AE wave has a longer rise time and lower frequency in comparison to the secondary AE wave. This fact accords well with the previous reports [10, 11].

Based on these qualitative characteristics of waveform features, 10 waves of two types were selected and averaged for each parameter as shown in Table 4.1. This process was applied to AE waves detected with three times passages of bullet trains. From Table 4.1, it is realized that a dominant difference between two types of AE waves is obtained with respect to the peak frequency. Therefore, the peak frequency was employed for classifying the two types of AE waves. In particular, AE waveforms with higher peak frequency were extracted as the secondary AE waves, and applied to AE tomography.

Results of AE tomography is found in Fig. 4.20a. Based on results in Table 4.1, high-pass filter of 7 kHz is applied. Surprisingly the damage area IV, which could not be evaluated by other inspections, is to be identified. In order to extract mechanical noises further, visual discrimination was implemented. Results are given in Fig. 4.20b. Although the damage area III could not well visualized, the

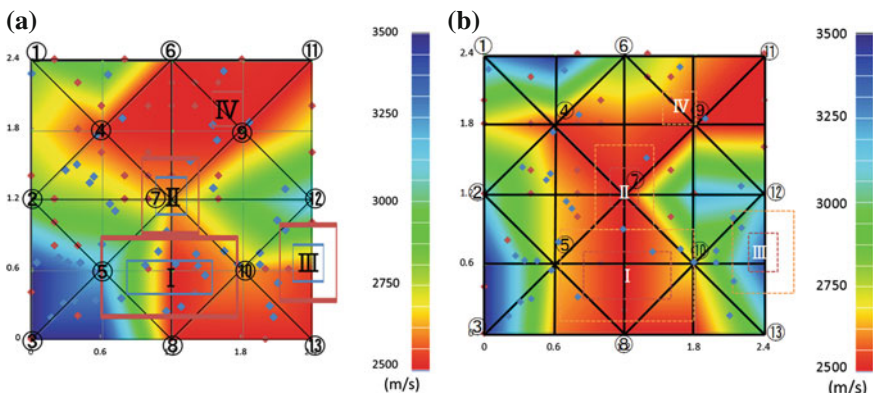


Fig. 4.20 Characteristic AE parameter with different causes. **a** AET result with using high-pass filter of 7 kHz. **b** AET result with both HP filter and visual filter

damage areas I and II are successfully identified. Considering the maximum depth of Rayleigh wave tomography, the deeper defects than 25 cm cannot be evaluated in the case of 50 cm thick plate. Thus, the damage area IV evaluated by AE tomography might be located deeper than 25 cm in depth.

4.7.2 Cylindrical Specimens

Cylindrical tuff specimens were sampled at the site of rock slope failure monitoring in Hokkaido in Japan [8]. The specimen has 100 mm in diameter and 200 mm in height. The array of AE sensor for AE tomography is shown as in Fig. 4.21a. Eight AE sensors of 60 kHz resonant are placed on the surface. Four strain gauges are installed onto the central surface of the specimen. Triaxial compression tests were conducted under consolidated drained condition for measuring AE activity in the specimen. The confining pressure was set at 294 kPa and the loading rate was kept constant by 1 kN/min. Figure 4.21b shows photos of the specimen during and after the test. As can be seen, shear fracture is observed in the specimen after recording 907 AE events.

In Fig. 4.22, accumulated numbers of AE events and transversal strain are shown with elapsing time. The accumulated number of AE events is increasing along with the increase in transversal strain. Focusing on the relation between the elapsed time and the accumulated number of AE events, fracture process can be divided into three stages. The stage from Step-0 to Step-1 is regarded as the progress stage of the microscopic failure. Then the stage from Step-1 to Step-2 is considered as of a steady stage of mesoscopic failure and the stage from Step-2 to Step-3 is the stage of final macroscopic failure. In order to verify the change of velocity structure at these three stages, 3D AE tomography analysis was conducted.

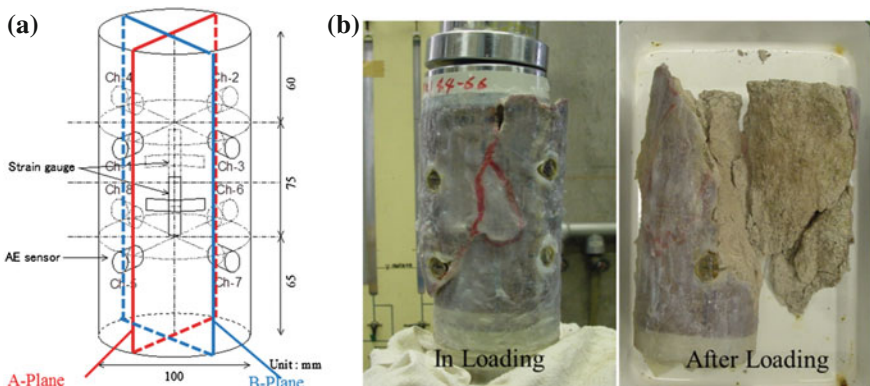


Fig. 4.21 Experimental conditions. **a** Array of AE sensors. **b** Photos of specimens after the test

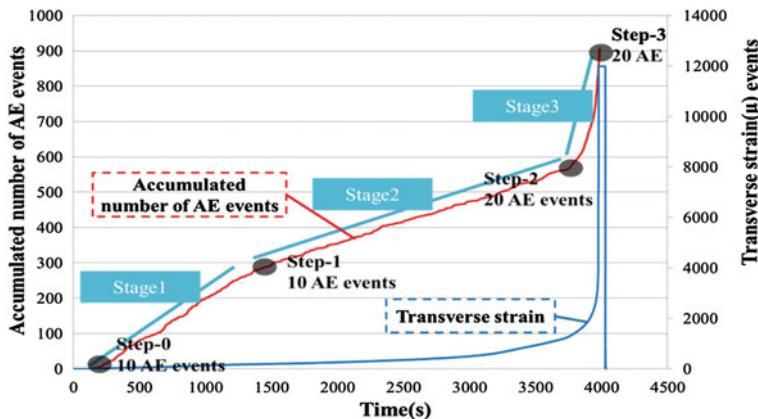
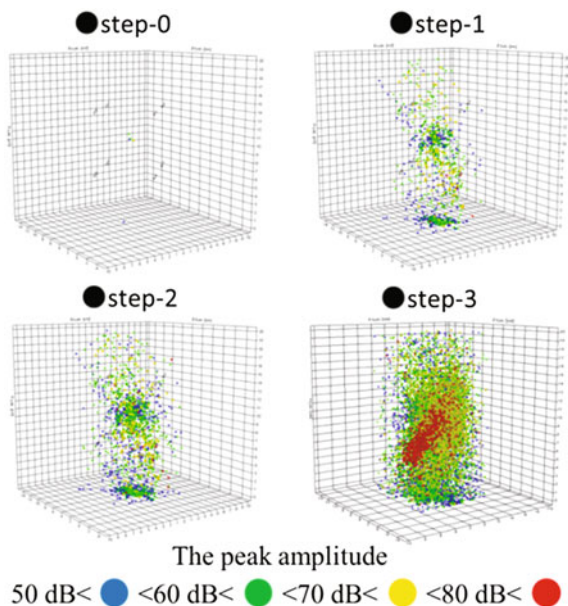


Fig. 4.22 Cumulative AE events with transverse strain

To examine the damage distribution in each stage, AE tomography was implemented by using only the latest AE data at the end of each stage to be examined. For example, 10 AE events generated at around Step-1 were employed for the analysis of AE tomography.

3D AE source locations in the specimen are shown at each step in Fig. 4.23. The blue plots show AE source locations which have the peak amplitude larger than 50 dB, in the same manner, the green and yellow ones show AE sources between

Fig. 4.23 Evolution of 3D AE sources with steps



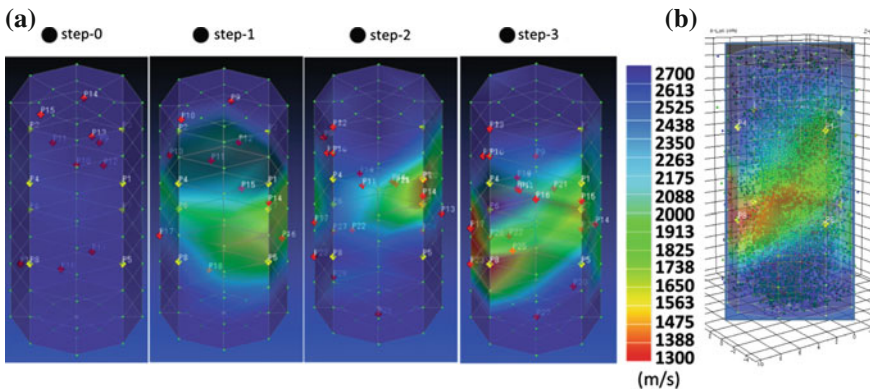


Fig. 4.24 Results of AE tomography. **a** Step-wise tomogram with used AE sources (see red +). **b** Tomogram with AE sources at Step 3

60 and 70 dB, between 70 and 80 dB respectively, and red ones show AE sources larger than 80 decibel. It is obvious that the number of AE sources is increasing in accordance with the loads. Especially the plane comprised of red points at Step-3 could be identified as the shear failure plane, because it closely corresponds to the shear plane observed in Fig. 4.21b.

Results of 3D AE tomography are shown in Fig. 4.24a. The areas of low elastic-wave velocity are not found at Step-0, implying that no remarkable damages progress. At Step-1 and Step-2, the low elastic-wave velocity area is confirmed in the central zone. From Step-0 to Step-1, the progress of damage could be expected. However, from Step-1 to Step-2, obvious damage progress can't be observed, probably due to the stress re-distribution. At Step-3, the large scale of damage evolution is identified, since low elastic-wave velocity areas are found from the upper right area to the lower left area in the specimen, which is in good agreement with the area of final shear failure (see Fig. 4.21b).

4.8 Concluding Remarks

Theory of AE tomography is briefly reviewed. This is a novel procedure as the advanced computerized tomography of the elastic-wave measurement. As discussed here, both the velocity distribution of elastic waves and the source locations of AE events are simultaneously obtained. Starting with two-dimensional cases, the capability of AE Tomography is discussed by performing a series of numerical investigations. Furthermore, in the three-dimensional problems, AE Tomography is applied to evaluation of existing structures as well as laboratory tests to verify an applicability of AE Tomography.

References

1. Chai, H.K., Aggelis, G.D., Momoki, S., Kobayashi, Y., Shiotani, T.: Single-side access tomography for evaluating interior defect of concrete. *Constr. Build. Mater.* **24**, 2411–2418 (2010)
2. Frangopol, M.D., Kai-Yung, Lin, Estes, C.E.: Life-cycle cost design of deteriorating structures. *J. Struct. Eng.* **123**(10), 1390–1401 (1997)
3. Kobayashi, Y.: Mesh-independent ray-trace algorithm for concrete structures. *Constr. Build. Mater.* **48**, 1309–1317 (2012)
4. Kobayashi, Y., Shiotani, T.: Seismic tomography with estimation of source location for concrete structures. *Struct. Faults Repair* (2012)
5. Kobayashi, Y., Shiotani, T., Oda, K.: Three-dimensional AE-Tomography with accurate source location technique. *Struct. Faults Repair* (2014)
6. Momoki, S., Chai, H.K., Yorikawa, M., Mochizuki, Y., Shiotani, T., Kobayashi, Y.: Development of one side placement model-elastic Tomography by characteristic of surface wave. *Tobishima Technical Report*, no. 61, pp. 41–46 (2012). (in Japanese)
7. Osawa, S., Shiotani, T., Momoki, S., Kobayashi, Y.: Damage visualization or rock material in triaxial compression test with 3D AE tomography. *JSNDI Prog. Acoust. Emission XVII*, 157–163 (2014)
8. Schubert, F.: Basic principles of acoustic emission tomography. *J. Acoust. Emission* **22**, 147–158 (2004)
9. Schubert, F.: Tomography techniques of acoustic emission monitoring. *ECNDT* (2006). (We. 3.6.2.)
10. Shinomiya, T., Morishima, H., Nakanishi, Y., Shiotani, T.: Damage diagnosis technique for brick structures using acoustic emission. *6th World Congress on Railway Record*, Edinburgh (2003)
11. Shiotani, T., Nakanishi, Y., Luo, X., Haya, H., Inaba, T.: Damage evaluation for railway structures by means of acoustic emission. *Trans. Tech. Publ. Key Eng. Mater.* **270–273**, 1622–1630 (2004)
12. Shiotani, T., Osawa, S., Momoki, S., Ohtsu, H.: Visualization of damage in RC bridge deck for bullet trains with AE tomography. *Adv. Acoust. Emission Technol.* 357–368 (2014)

Chapter 5

Acoustic Emission Analysis for NDE in Concrete

Dimtrios G. Aggelis

Abstract Acoustic emission (AE) is one of the promising techniques for structural health monitoring (SHM) purposes in concrete structures. Due to its passive and non-invasive nature, it can be applied without disturbing the operation while it provides information that no other monitoring technique can. During the last decades great developments have taken place in the technical equipment and the analysis tools. The present chapter intents to summarize the recent trends in AE parameter analysis mainly related to fracture mode identification. This issue carries high importance since fracture of concrete materials and structures includes shifts between different modes. Therefore, its identification supplies information on the damage status. However, the characterization should remain as simple as possible in order to have the potential to be implemented in situ.

Keywords AE • Concrete • Structural health monitoring • Parameter analysis

5.1 Introduction

Structural safety of civil structures is of great concern to the engineering world. Operational load, environmental effects and random events like earthquakes may accumulate serious damage compromising the durability of the structures. With the aim of avoiding loss of lives and capital, structural health monitoring (SHM) procedures are implemented. These concern the detection, localization and characterization of damage which will enable the proper maintenance action through repair. The reality that a large percentage of infrastructures are more than 50 years old highlights the need for suitable monitoring and maintenance [38]. Acoustic emission (AE), among other monitoring techniques, is a valuable tool for SHM purposes in concrete structures and materials. It can be applied in specific

D.G. Aggelis (✉)

Department of Mechanics of Materials and Constructions, Vrije Universiteit Brussel,
Brussels, Belgium
e-mail: daggelis@vub.ac.be

intervals or even in continuous monitoring schemes to supply real time information and reliable assessment on the damage status of the target component [86].

The AE technique detects and records the elastic waves after irreversible processes in the material. These processes include damage propagation in any form (mainly cracking, delaminations, fiber pull-out etc.), development of corrosion or other specific irreversible processes. Usually piezoelectric transducers are applied, placed on the surface of the material with suitable coupling. These transducers transform any transient pressure change reaching their surface into an electric waveform. After amplification, the signals are fed to the acquisition board where digitization takes place, while the main waveform parameters are measured in real time [40, 53]. A representation of an AE setup is given in Fig. 5.1, while the main parameters of an AE waveform are depicted in Fig. 5.2.

Apart from the use of the total AE activity which is indicative of the process of failure, the waveform shape offers important information on the sources. Therefore, several descriptors are used to quantify the waveform characteristics. Intensity related parameters include Amplitude (A) which is the highest voltage of the

Fig. 5.1 Typical AE setup in laboratory and in situ

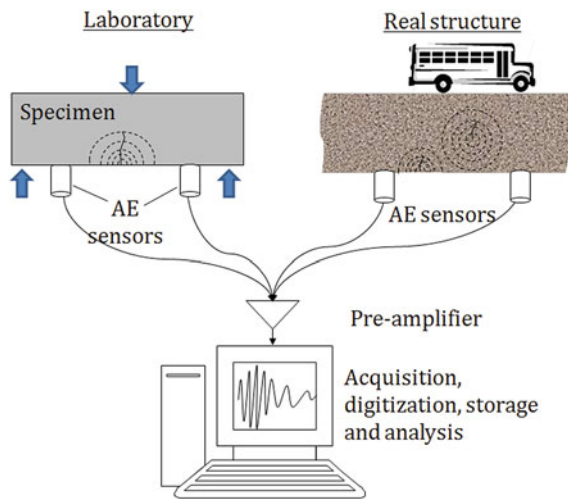
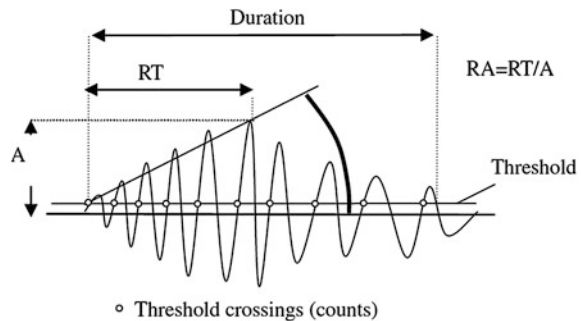


Fig. 5.2 Typical AE waveform



waveform. Additionally, energy (MARSE, measured area under the rectified signal envelope) takes into account the content of the whole waveform. The time between the first threshold crossing of the signal and the time of the maximum peak is called Rise time (RT). Similarly duration (Dur) is defined as the time between the first and last threshold crossings. Based on the shape of the first part of the signal, the RA value (RT over A) or the inverse of the rising angle has been introduced. The frequency content is also important. Several parameters are used to exploit the frequency information. The simplest is the “average frequency” (AF) which is calculated in time domain as the ratio of the total number of threshold crossings over the duration of the waveform in kHz. Additionally, the peak frequency (PF) is defined as the frequency with the highest magnitude in the FFT domain, while central frequency (CF) is the centroid of the spectrum. Additionally more specific parameters can be applied like the “partial power” of specific frequency bands over the total spectrum. In order to measure frequency domain parameters, the whole waveform must be recorded and FFT conducted in real time [39]. This may cause acquisition delays and loss of information especially during moments of high activity (e.g., fracturing moments). On the other hand, recording of the whole waveform enables the usually referred to as “signal based” analysis and offers more possibilities for feature extraction like the aforementioned frequency domain parameters, moment tensor analysis (MTA) and filtering of noise [14, 37, 40, 59, 60, 64]. Going back to the waveform shape, features like the RT and Duration occupy higher values for shear type of sources, while frequency ones are higher for tension as will be extensively discussed.

The way that information is extracted by AE measurements depends on the targeted application, the layout of the experiment and the preference of the user. Different approaches have been used quite successfully. Some are based on the total AE activity in relation to load. Others utilize the amplitude and the amplitude distribution of the waveforms, while others utilize the waveform parameters using simple or more sophisticated analysis tools to unlock the hidden information from the damage sources. The present chapter intends to highlight the recent developments in waveform parameter analysis and cover a—hopefully—indicative part of the relevant literature.

5.2 Analysis Based on the Total Activity

The AE activity is closely related to the cracking process. Therefore, only the number of the cumulative AE signals received during a period of time has great potential for characterization. The total activity of AE has been utilized numerous times in order to produce correlations with sustained load and damage as measured for example by the crack opening displacement in notched specimens [27]. Similarly, the number of AE events has been related to the depth of notch and the type of concrete [24]. In studies related to chemical degradation, AE activity attributed to micro-cracking and infiltration of the contaminated water into concrete

pores exhibited strong correlation to the carbonation process and the thermal cycles [16]. In other studies the development of corrosion of reinforced concrete in accelerated experiments was followed by AE. The different stages of corrosion (dormant, initiation, acceleration) were identified by the cumulative events, while the measurements were complimented by AF and RA shifts and Moment Tensor Analysis (MTA) or principal component analysis for identification of the mode of crack and corrosion stage [20, 46]. The number of events has been utilized in the form of the rate process theory in the estimation of damage of samples taken from concrete structures with a recent example related to the great East Japan earthquake of 2011 in the Tohoku area where the probability of AE event occurrence was related to the stress level in concrete compression testing [84]. The increase in the rate of recorded AE events was used to indicate the start of the serious cracking in notched concrete beams under bending [42]. The cumulative number of AE counts has shown good correlation to the curing behavior and the mix design in fresh concrete [88], the content of steel fibers, and the resulted toughness [82].

The study of the received AE in relation to load produces very interesting characterization results. In case of cyclic loading, when an unloading phase is part of the protocol, the activity received during the decreasing phase of loading is indicative of damage. This is quantified by the Calm Ratio which is defined as the total activity during the unloading phase over the total activity of the whole loading—unloading cycle. For intact material this parameter obtains values close to zero due to the negligible activity at unloading. However, when considerable damage is accumulated, serious AE activity is recorded during unloading increasing this ratio even to values higher than 0.5 meaning that most of the activity occurs after the peak load [61]. The “threshold” value between minor and serious damage is defined in conjunction with other observations like visual assessment and may differ according to the conditions. It is the incremental trend of Calm Ratio that alerts for development of serious damage. In the recent literature Calm Ratio has been used to assess the condition of reinforced concrete beams under bending. High values of calm ratio have been related to poor condition in pre-stressed concrete bridges [65, 77]. In another case the limit between moderate and serious damage was set to 0.5 in monitoring of railway substructures [51, 79], or higher in bending of reinforced concrete beams [25], and in laboratory experiments of reinforced concrete beams under bending [90]. The decrease of calm ratio after repair has been used to evaluate the repair effectiveness in concrete piers of a water intake facility [75]. This parameter is usually combined with the so called “Load ratio” which is similar to the well known “Felicity ratio” [34]. It is based on the Kaiser effect [44, 85] or more accurately in the absence of it. When damage has accumulated in a material, acoustic emission activity may be recorded even at stress levels lower than previously sustained. The Load ratio (ratio of the load when AE is recorded during reloading over the previous maximum load) obtains values close to one for intact material but decreases for serious damage [81]. The extent of distributed damage during compression of concrete cubes has been assessed based on the cumulative number of events as well as the Felicity ratio, which showed a monotonic decrease for increasing stress level [72]. Calm and load ratio have been utilized for the

assessment of reinforced concrete slabs during central monotonic loading after being exposed to rockfall impact [48]. Other examples can be found in the aforementioned literature for calm ratio, since these indices are usually applied in combination. When both these damage indices are used, the combination of high calm ratio and low load ratio is a strong indication of poor structural condition and it is a way of quantification of damage status [61].

Apart from the number of emission, energy and amplitude have also been used for more accurate characterization of the fracture process or the damage condition of structures [36]. This chapter focuses more on other waveform parameters, as will be discussed, but some examples of the benefit of energy-related parameters are included. Specifically the AE energy has been shown indicative of the interface quality between different layers of concrete mixes used for repair purposes [73], while it has been used for comparison of crack arrest mechanisms of different shear reinforcing jackets [87]. It was also correlated to the fracture energy of concrete and toughness of steel fiber reinforced concrete, SFRC [8, 21, 45, 56, 91]. Energy has been used to distinguish between emissions of wire breakage and other sources in continuous monitoring of a pre-stressed concrete bridge [35], while it was indicative of peeling of the cover concrete in torsion-bending experiments [57].

The amplitude distribution of the incoming hits offers reliable information on the fracture scale. Minor damage consists of many and low amplitude events, while macro-cracking usually propagates with less but stronger events. This information is quantified by the b -value or the improved b -value (ib -value), which stands for the grade of the cumulative amplitude distribution [78]. Due to the sensitivity of the distribution of AE amplitudes on the fracturing events, the ib -value exhibits strong drops prior to macro-fracture acting in essence as a warning [11, 17, 26, 29, 49].

5.3 AE Parameter Analysis

5.3.1 Relation of AE Waveform to Fracture Process

A specific kind of information which is crucial for the structural behavior of a component during any type of loading is the fracture pattern. In most of the cases, engineering materials are composites including possibly aggregates, fibers, bars or reinforcing patches applied on a basic cementitious matrix. Due to their complexity, their fracture includes different mechanisms. A usual example from concrete is the initial matrix cracking that occurs at load much lower than the ultimate, while phenomena that develop later are possibly the detachment of the rebars, pull-out of fibers and debonding of external patches. The latter phenomena include strong shearing action in the sense that the sides of the fractured area move in a parallel planes but opposite direction (see Fig. 5.3 right). Since these shearing phenomena tend to separate the weaker concrete matrix from the reinforcement (rebars, fibers, patches), they are regarded quite critical for the mechanical performance. It is

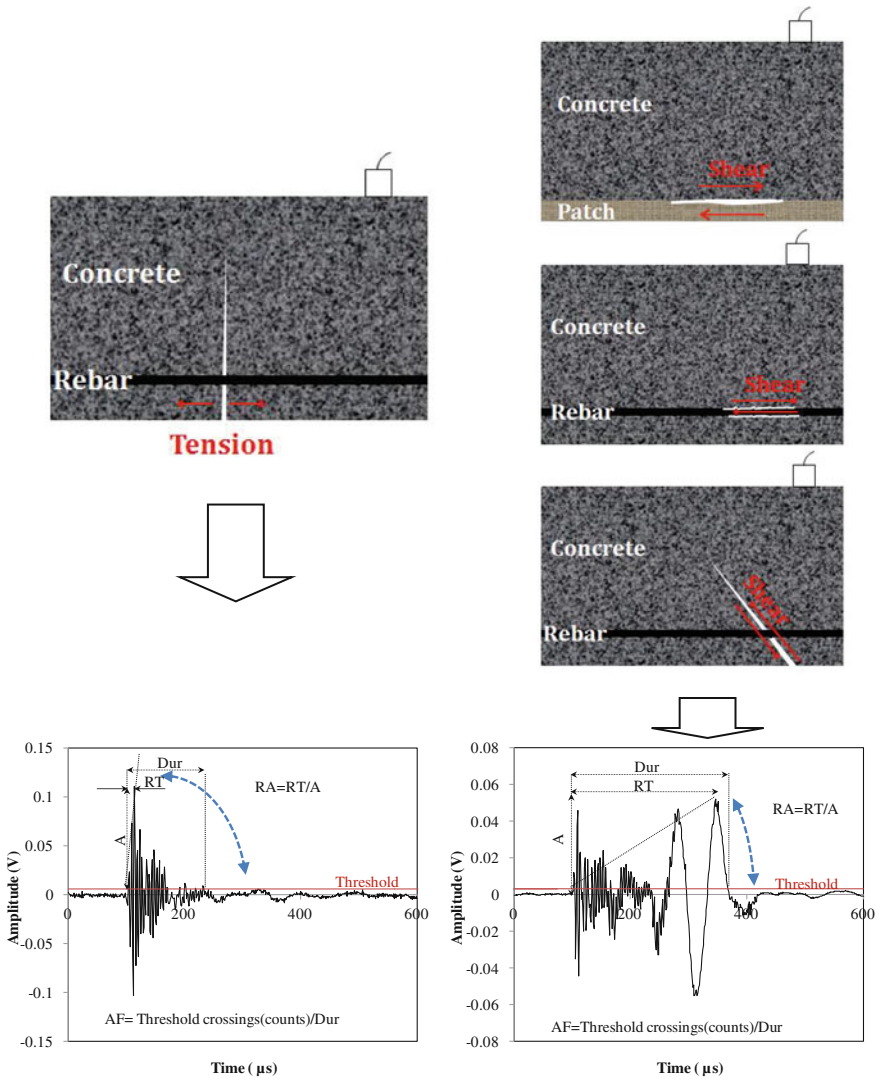


Fig. 5.3 Typical fracture modes in concrete and corresponding AE waveforms

widely accepted that these phenomena occur at high loads and lead to ultimate fracture, while tensile phenomena are typically noted at lower loads while the component or specimen is still stable. Therefore, characterization of the dominant fracture mechanism may provide necessary information on the status of the component. This can be part of a SHM procedure in real structures but also can be very helpful in the laboratory in the framework of material fracture studies. The research in the area for several decades has reached to the publication of numerous studies and a set of recommendations for practical use [62].

5.4 AE Waveform Parameter Analysis

In this paragraph, the waveform parameters that lead to fracture mode identification are discussed. As an introduction to this discussion, phenomena related to tensile cracking emit signals of higher frequency content and shorter duration (see Fig. 5.3 left). Therefore, parameters like AF or PF mentioned above, obtain higher values in general for tension rather than shear processes. Reversely, parameters like the DUR, RT, RA are typically higher for shear. The studies based on AE waveform parameters recently gain ground due to their efficiency as well as their simplicity. The frequency indicator “average frequency” (see Fig. 5.3) despite its threshold dependent nature has proven to be very sensitive to the fracture mode. Indeed, concerning the usual levels of threshold that can be used in practice (roughly 35–45 dB) the average frequency does not change noticeably. Additionally, the RA value which exploits the initial rising angle of the waveform seems to improve the classification. As prescribed in the relevant recommendation [62], the RA should be evaluated in units of time over voltage (ms/V or μ s/V). Therefore, if the amplitude is given in logarithmic scale (e.g., dB) it should be transformed back to original voltage.

The amplitude A, in dB format is expressed as

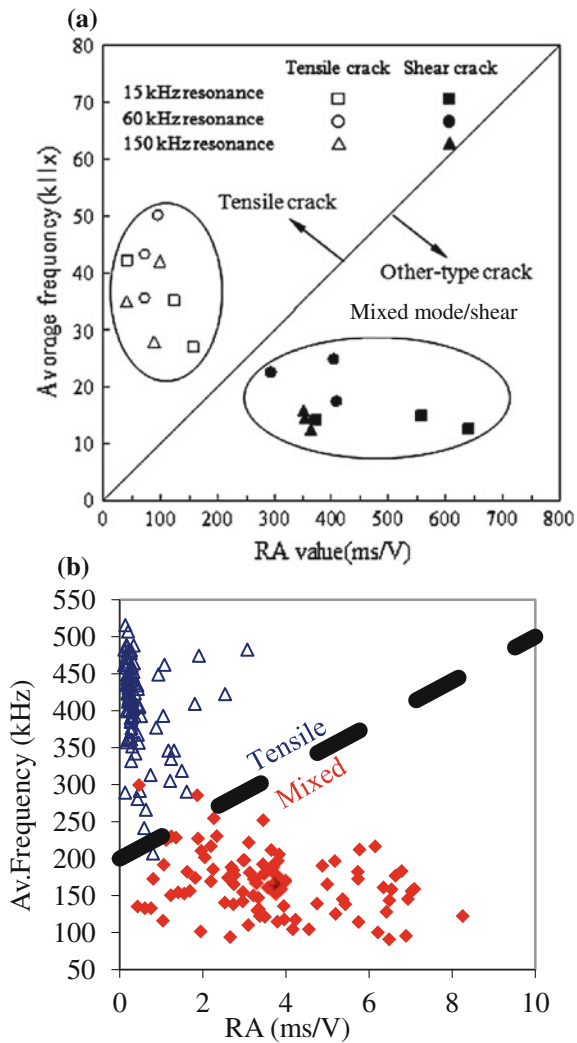
$$A(\text{dB}) = 20 \cdot \log\left(\frac{V}{V_{\text{ref}}}\right) - G \quad (5.1)$$

where G is the pre-amplifier gain and V_{ref} the reference value used in the AE software (usually 1 μ V). The above equation should be solved for V so that the result is expressed in Volts.

In general, as the relevant recommendations describe, the populations of AE is plotted in vertical axes of AF and RA. In simple cases of laboratory experiments, the populations due to tensile loading and shear can be separated by a single diagonal line. The top-left domain hosts the tension-related signals and the bottom-right the shearing ones, as seen in Fig. 5.4a [62, 63]. Still, the threshold line should be adjusted depending on the experimental conditions, including the material, the type of sensors and the geometric parameters as seen in the example of Fig. 5.4b [7].

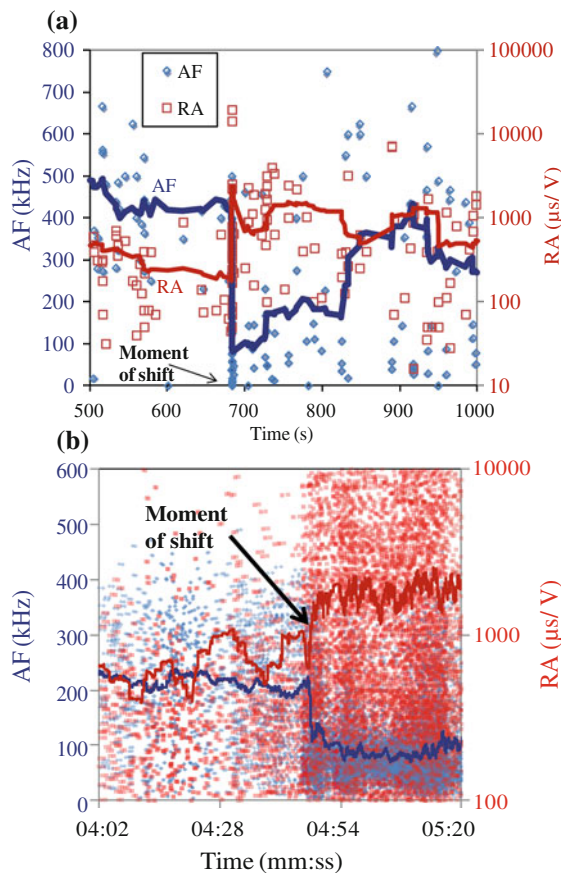
Plenty of studies in laboratory scale have demonstrated the effectiveness of this approach as will be discussed. In any case the selection of the most appropriate parameters is done after careful examination of the total set of data. Usually, the parameters that exhibit the strongest change as the fracture evolves should be targeted due to higher sensitivity. It is highly possible that the same set of data does not exhibit the same sensitivity in all different kinds of studies. Therefore, although some parameters may be more widely used than others, as will also be shown below, still all the data should be evaluated in a set of experiments that is conducted on different geometries, materials or sensor types. In the following, some indicative recent studies are mentioned as representative examples of this approach.

Fig. 5.4 Classification of cracking mode based on **a** resonant sensors in concrete [62], **b** broadband sensors in steel fiber reinforced concrete (SFRC) [7]



Decreasing trend of AF and increase of RA has been noted after the major fracture event in SFRC beams, attributed to the shearing action of pull-out of fibers which are bridging the main cracks [7]. These parameters have shown sensitivity on the chemical coating of the fibers which promotes fiber-matrix bonding and therefore, deflects cracking away from the fiber-concrete interphase into the matrix [8]. An example is shown in Fig. 5.5a that clearly shows the strong sensitivity of the specific features in the damage process. From the moment on that fiber pull-out starts to contribute after the main fracture incident (shown by the arrow), frequency characteristics decrease and features related to the duration of the signal increase. Although it is a possibility, in most cases, complete separation of different

Fig. 5.5 Time histories of AF and RA for **a** an SFRC beam under bending, **b** TRC beam under bending



populations is not an issue of concern; the overlap is great mainly due to the actual coincidence or overlap of the mechanisms. However, the sliding average line is very helpful just to demonstrate the crucial shifting moments, since the information of a “cloud” of points is not easily perceived by the human brain. Depending on the total number of points, the sliding window could be from several tens of points up to hundreds. The same behavior has been reported in textile reinforced cement beams, which fracture in a similar way under bending load. The brittle matrix is initially cracked followed by fiber pull-out and delamination events between successive plies. This transition is registered in a very vivid way introducing a drop of AF by approximately 50 % and an increase in RA of more than 200 % in average [18], see Fig. 5.5b. Additionally, the same parameters may well distinguish the behavior of straight and arch beams. In straight beams the load is vertical to the reinforcing layers and the emissions have higher frequency and shorter duration throughout loading. On the contrary, the curved geometry imposes compression-shear forces aligned with the layers substantially decreasing the AE frequencies even for slight curvatures [19].

Similar trends can be seen when the shearing is not due to debonding or pull-out but is just due to the pure shear stresses acting on a concrete matrix. The difference between compressive and pull-out forces on the AE signals as well as the resulted stress field in concrete were recently examined in a mixed experimental-numerical study [54, 55]. The stress field during the pull-out experiment has strong shear components when using a confinement ring and the AE received is of notably lower frequency and higher RA level compared to a similar cube under compression. The differences are more pronounced by broadband sensors (approximately 100 kHz for pull-out and 200 kHz for compression) but resonant sensors can still record a difference (approx. 75 kHz for pull-out and 120 kHz for compression). The distinction between bending and shear has also been examined in concrete and mortar matrices. When mortar prisms were fractured in three-point bending, due to the absence of strong shear in the middle of the span, frequencies above 110 kHz and RA values less than 500 $\mu\text{s}/\text{V}$ were obtained. In the case of shear fracture experiments, frequencies notably dropped and RA increased [10]. Another relevant study, concerning concrete specimens in an up-scale of 2.5 times resulted in similar trends though there was some overlap attributed to non-uniform propagation wave paths [1]. The behavior of concrete prismatic beams with and without vinyl fiber reinforcement layer was examined in bending and considerable changes in the waveform parameters were shown in the “grade” of the AE waveform, which is the inverse of RA (A/RT). Here the comparison showed that the vinyl fiber layer restrained shear cracking that becomes dominant in the plain specimens [3]. Cylindrical concrete specimens in compression showed a gradual decrease of AF during failure and a more pronounced increase of RA and energy indicating that shear cracks lead the damage evolution to the final collapse [22]. In an earlier study conducted with resonant sensors, the same transition was noted in compression of recycled aggregate concrete [94]. Specimens that, based on the AF-RA parameters, did not exhibit shear mode of cracking up to 2/3 of the maximum stress, were considered to have good adhesion in the aggregate-matrix interphase. For better characterization results different pattern recognition algorithms have been used and the effect of the propagation path on the success of the classification has been quantified [32]. It was seen that the results are improved when the data are treated separately according to the receiving sensor, rather than as a unified set.

The same analysis proved successful in the case of large beams, where it was shown that as the material was increasingly loaded up to failure, the population of AE shifted to lower frequencies and higher RA values [74]. Tests were conducted for fatigue loading as well, for the successive phases of which, the shift in the AF-RA plane was evident, corresponding to the development of the shear diagonal cracks [52]. The conclusions from reinforced concrete frames under seismic loading were similar. It was reported that for higher acceleration loading, shear cracks identified by lower AE frequency centroid and higher RA values were developed, in contrast to low acceleration load when no shear cracks were found [50]. Still in large scale, and specifically in cyclic testing of reinforced concrete shear walls pattern recognition algorithms like the k-means and the Gaussian mixture model

were applied to automatically separate tensile and shear cracks in the AF-RA plane [31, 33].

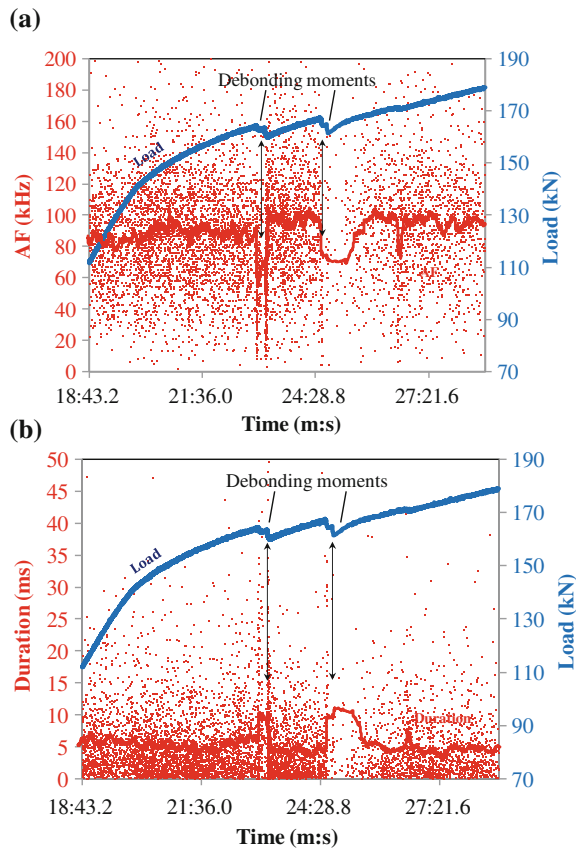
The parameter AF has been solely used as a criterion to distinguish between cracking and friction of cables in post-tensioned concrete members. The threshold between the two types of emission was defined at 50 kHz in this study, using resonant sensors at 60 kHz [80]. The maximum RA value and frequency (in the form of central frequency this time) produced good correlations to the heterogeneity content of mortar prism specimens, while energy related parameters exhibited strong correlation to the ultimate load in three point bending [54, 55]. In similar fashion in bending experiments of concrete beams, the classification between tensile and shear cracks was in good agreement with moment tensor analysis. In this study, it is mentioned, that the first hits of each AE event should be taken into account, something quite reasonable since shorter propagation times (and distances) do not accumulate much distortion on the waveform shape [58]. Differences induced in the fracture behavior by fly ash and variable curing conditions were also examined by these waveform parameters [41]. The relation between AF and RA has been used to characterize the cracking mode in prestressed concrete experiments simulating water transport pipes [30] while the shift of the AE population to lower AF and higher RA followed well the damage by increased load level. The same analysis produced good preliminary results in bending of pre-stressed railway concrete sleepers, showing that for incremental loading conditions the average values of AF decreased and RA increased indicating the development of damage from concrete cracking to friction of the rebar [66].

In externally repaired concrete beams during bending, the debonding of the reinforcing patches pushes the population of the AE hits at lower frequencies and longer duration regimes as shown in Fig. 5.6a and b. In a real time monitoring case, these changes would be registered as strong spikes in the time history plots. Therefore, the shift in the mechanisms would be evident even in real time, as shown in Fig. 5.6 for a relevant case of carbon fiber reinforced polymer (CFRP) patch debonding [89]. These transitions can be used in order to detect critical moments in the loading history of a structure. Later it was confirmed by the surface strain field, as measured by digital image correlation (DIC), that at those specific moments debonding events actually occurred between the reinforcing patch and the concrete substrate, which were the reason for the transient load drops.

Still, it is highlighted that although in each one of the studies classification results may be successful this does not mean that there is a unified and global treatment of the data that would facilitate all the different cases. So far, the methodology is case-specific depending on the type of sensors, the size of the member and the location of the sensors [95]. However, at the time of writing of this text efforts are continued for establishment of standardization procedures by the relevant Scientific Committee [69].

As the scale of the experiment increases, the overlap between points of different origin will certainly increase due to the combined effect of damping and scattering that attenuate elastic signals and distort the waveforms [27]. Generally, the frequency characteristics will decrease while up to a distance, characteristics like

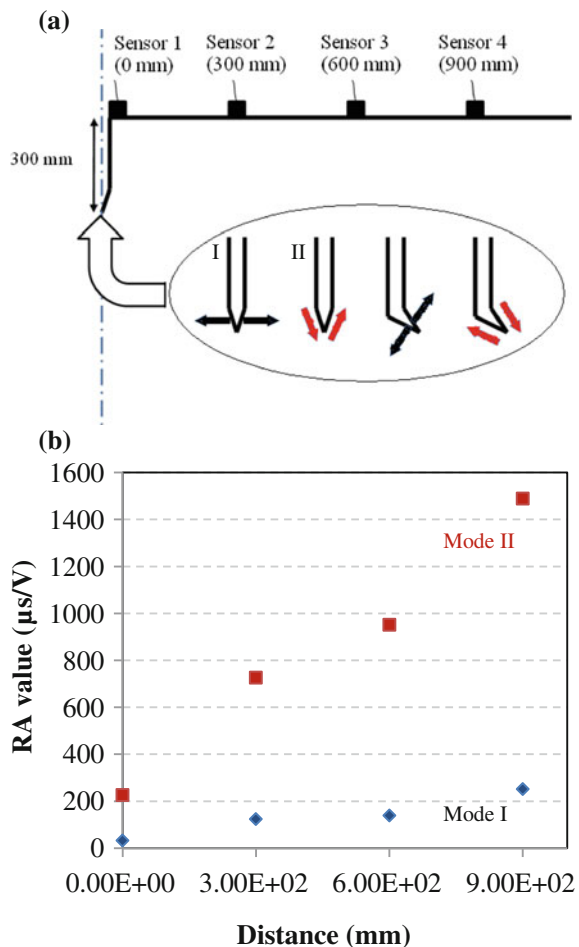
Fig. 5.6 Load and **a** AF, **b** AE duration histories for a beam with external reinforcing CFRP strip. The AF and duration *solid lines* are sliding averages of recent 200 points



duration and rise time will increase as a typical effect of scattering [6, 23]. For longer distances, duration may also decrease due to excessive attenuation. It is mentioned that although AF and RA have been used extensively, other features may perform similarly well, like duration and energy in cases. Additionally, according to the type of sensor (resonant vs. broadband) the classification boundaries will have to be modified in order to result in acceptable classification [2].

Numerical simulations using the boundary element method (BEM) were conducted on the waveforms received by sensors at different distances from a surface breaking crack, as seen in Fig. 5.7. They showed that the RA value of the waveform is higher for parallel movement in opposite directions of the sides of the crack tip (shear, II) compared to movement away from each other (tension, I), see again Fig. 5.7a. This is attributed to the different amount of elastic energy that forms longitudinal or shear waves. For the shear type of crack opening, the percentage of shear wave energy is higher than in the tensile mode, resulting in waveforms with most of their energy well after the fast initial longitudinal arrivals. Therefore, duration and rise time are increased with a corresponding drop of frequency content. In addition, the values had strong increasing tendency for longer propagation,

Fig. 5.7 **a** BEM geometric model for wave emission after movement of a surface crack tip, **b** waveform RA value for different sensors and straight crack tip movements [68]



which was attributed to the separation of the different wave modes (longitudinal, shear and Rayleigh) which run on different velocities. The study included also inclined crack tips showing approximately the same trends while the result did not change much even for different threshold levels of 2 and 5 % of the maximum amplitude, which are anyway high for practical use [68]. Additionally, simulations have shown the strong effect of scattering on the (micro-)structure in relation to propagation of AE waves [9, 71]. Even an additional propagation distance of cm induces strong distortion on the AE waveforms, as shown in mortar specimens during bending in a mixed experimental-numerical study [4]. In large scale the effect is so strong that it should be taken into account for the proper placement of the sensors [15, 76].

5.5 Combination of NDT Techniques

It should be mentioned that the combined use of different techniques along with AE monitoring benchmarks the results and helps to define exactly the cause of AE, which would else carry a degree of uncertainty. In that respect X-ray tomography has been used to compliment AE results from freezing-thawing and cracking due to compression in concrete specimens [28, 83]. Acoustic emission has been well combined with digital image correlation (DIC) in concrete studies [12, 13, 70, 89, 92]. DIC provides accurate information on the surface crack patterns, while it particularly helps to identify moments of debonding of external patches that are commonly used for repair purposes. Therefore, the shift of the populations of AE points can safely be attributed to the correct process without the risk of faulty assumptions. Figure 5.8a shows the population of cracking AE signals received during stable load increase in four-point bending of a concrete beam, and during a load drop. Despite the strong overlap, the change of the average values is evident.

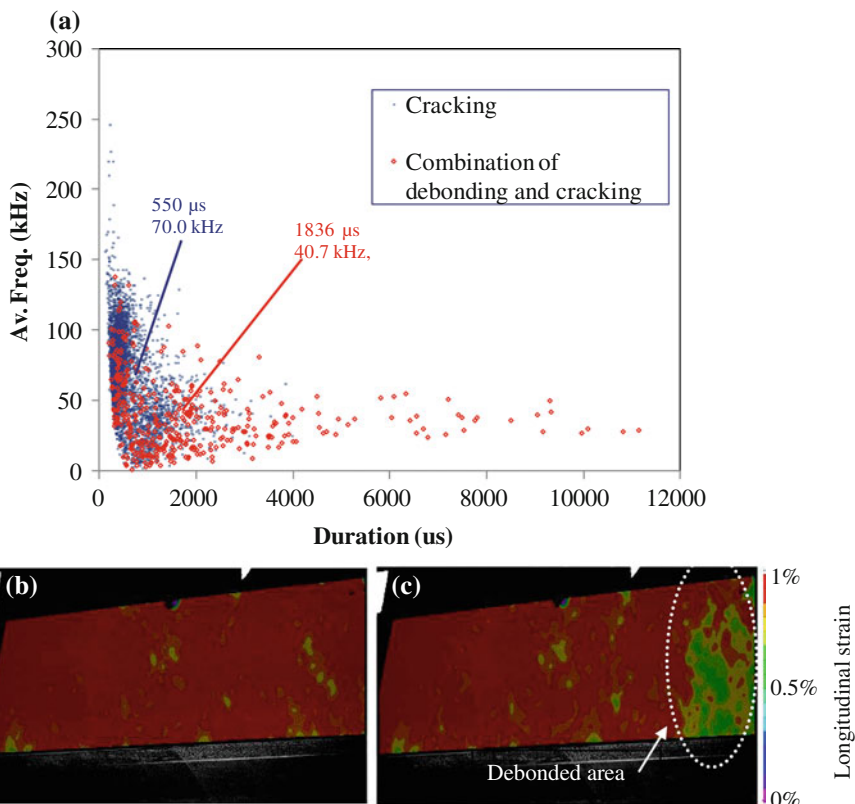


Fig. 5.8 a AE population recorded from concrete cracking and CFRP debonding moments, longitudinal strain (b) before load drop, c after load drop

Figure 5.8b shows the corresponding strain fields on the external layer of textile reinforced concrete before and after this particular load drop moment. The strain reduction in the right end area signifies debonding and confirms that the shift in the parameters of AE received during the load drop are due to debonding action in addition to the cracking that continues.

AE has been combined with ultrasound in order to correlate the AE activity with the stiffness degradation in mortar prisms and concrete beams (Mpalaskas et al. [43, 54, 55]). Additionally, ultrasonic pulse velocity (UPV) measurements have been complementarily used with AE during four point bending in composite concrete specimens. AE event locations coincided to low pulse velocity areas and both agreed well to the visual observation of cracks [3]. This proved the reliability of both methods, which can be used in large scale where visual observation may not always be possible and certainly for the interior of the structure. AE and UPV work complementary since small cracks that cannot influence pulse velocity can be identified by AE during their propagation. On the other hand, inactive cracks that show no AE activity may influence UPV. It was concluded that simultaneous application of stress wave techniques (AE and UT) shows the capacity to detect the time and location of damage and gives a good assessment for the status of the material [5, 81]. Nonlinear ultrasonic amplitude has been related to the Felicity ratio and cumulative emissions from concrete compression tests [72]. Linear and non-linear wave parameters (pulse velocity and quadratic second harmonic amplitude respectively) have been used in combination to AE activity and counts for characterization of the hydration of fresh concrete mixes [88].

Vibration has also been used to correlate damage information with the AE results in reinforced concrete beams [93]. In a study concerning the frost behavior of concrete mixes, acoustic emission monitoring showed much less activity for specimens with high frost resistance after several freezing cycles. The results were benchmarked by visual inspection of the surface crack pattern as well as impact-echo which showed a substantial decrease of resonant frequency for the low resistant mixture [67]. Additionally, infrared thermography and ultrasonics complimented AE in detecting of flaws in concrete masonry walls [47].

5.6 Conclusions

The present chapter wishes to contribute to the review of recent trends in parameter analysis of AE waveform for fracture characterization. The sensitivity of different AE parameters to the mode is reported with numerous experimental examples. It is shown that several AE waveform parameters are sensitive to the fracture mode. Processes like debonding of external patches, pull-out of fibers or reinforcing bars give distinct AE signatures than cracking and can be used for study and monitoring of the fracture process. Additionally, cracks triggered by shear stresses in concrete also show different characteristics (mainly in terms of frequency and duration) than tensile cracks. While the capability of recording full waveform exists in most of

contemporary acquisition systems, extraction of classical parameters remains a very effective way to characterize fracture, enhanced when necessary by features of frequency domain and other NDT monitoring techniques.

References

1. Aggelis, D.G., Mpalkas, A.C., Matikas, T. E., Van Hemelrijck, D.: Acoustic emission signatures of damage modes in concrete. In: Proceedings of SPIE 9062, Smart Sensor Phenomena, Technology, Networks, and Systems Integration 2014, p. 90620P (2014a). doi:[10.1117/12.2044750](https://doi.org/10.1117/12.2044750). ISBN 9780819499882
2. Aggelis, D.G., Ohtsu, M.: Qualitative AE Indices for Characterization of Concrete Damage Status. pp. 185–214, In: Burnett J.K. (ed.) Theory and Uses of Acoustic Emissions. Nova Science Publishers (2012)
3. Aggelis, D.G., Shiotani, T., Momoki, S., Hirama, A.: Acoustic emission and ultrasound for damage characterization of concrete elements. *Am. Concr. Inst. Mater. J.* **106**(6), 509–514 (2009)
4. Aggelis, D.G., Shiotani, T., Papacharalampopoulos, A., Polyzos, D.: The influence of propagation path on acoustic emission monitoring of concrete. *Struct. Health Monit.* **11**(3), 359–366 (2012b)
5. Aggelis, D.G., Shiotani, T., Terazawa, M.: Assessment of construction joint effect in full-scale concrete beams by acoustic emission activity. *J. Eng. Mech.* **136**(7), 906–912 (2010)
6. Aggelis, D.G., Tsangouri, E., Van Hemelrijck D.: Influence of propagation distance on cracking and debonding acoustic emissions in externally reinforced concrete beams, *Mecanica* (2014b). doi:[10.1007/s11012-014-9900-6](https://doi.org/10.1007/s11012-014-9900-6) (in press)
7. Aggelis, D.G.: Classification of cracking mode in concrete by acoustic emission parameters. *Mech. Res. Commun.* **38**, 153–157 (2011)
8. Aggelis, D.G., Mpalkas, A.C., Matikas, T.E.: Investigation of different fracture modes in cement-based materials by acoustic emission. *Cem. Concr. Res.* **48**, 1–8 (2013b)
9. Aggelis, D.G., Mpalkas, A.C., Ntalakas, D., Matikas, T.E.: Effect of wave distortion on acoustic emission characterization of cementitious materials. *Constr. Build. Mater.* **35**, 183–190 (2012a)
10. Aggelis, D.G., Soulioti, D.V., Gatselou, E.A., Barkoula, N.-M., Matikas, T.E.: Monitoring of the mechanical behavior of concrete with chemically treated steel fibers by acoustic emission. *Constr. Build. Mater.* **48**, 1255–1260 (2013a)
11. Aggelis, D.G., Soulioti, D.V., Sapouridis, N., Barkoula, N.M., Paipetis, A.S., Matikas, T.E.: Acoustic emission characterization of the fracture process in fibre reinforced concrete. *Constr. Build. Mater.* **25**, 4126–4131 (2011)
12. Aggelis, D.G., Verbruggen, S., Tsangouri, E., Tysmans, T., Van Hemelrijck, D.: Characterization of mechanical performance of concrete beams with external reinforcement by acoustic emission and digital image correlation. *Constr. Build. Mater.* **47**, 1037–1045 (2013)
13. Alam, S.Y., Saliba, J., Loukili, A.: Fracture examination in concrete through combined digital image correlation and acoustic emission techniques. *Constr. Build. Mater.* **69**, 232–242 (2014)
14. Alver, N., Murat, T.H., Yasin, S.Ö., Ercan, E., Karcili, M., Selman, E., Ohno, K.: Effect of CFRP-spacing on fracture mechanism of CFRP-strengthened reinforced concrete beam identified by AE-SiGMA. *Constr. Build. Mater.* **67**, 146–156 (2014)
15. Anastopoulos, A., Bousias, S., Toutountzakis, T.: Acoustic emission monitoring of reinforced concrete frame during seismic loading. *J. Acoust. Emission* **25**, 33–41 (2007)

16. Assouli, B., Simescu, F., Debicki, G., Idrissi, H.: Detection and identification of concrete cracking during corrosion of reinforced concrete by acoustic emission coupled to the electrochemical techniques. *NDT&E Int.* **38**, 682–689 (2005)
17. Behnia, A., Chai, H.K., Shiotani, T.: Advanced structural health monitoring of concrete structures with the aid of acoustic emission. *Constr. Build. Mater.* **65**, 282–302 (2014)
18. Blom, J., El Kadi, M., Wastiels, J., Aggelis, D.G.: Bending fracture of textile reinforced cement laminates monitored by acoustic emission: Influence of aspect ratio. *Constr. Build. Mater.* **70**, 370–378 (2014a)
19. Blom, J., Wastiels, J., Aggelis, D.G.: Application of acoustic emission on the characterization of fracture in textile reinforced cement laminates. *Sci. World J.* **2014**(178020), 7 (2014b). <http://dx.doi.org/10.1155/2014/178020>
20. Calabrese, L., Campanella, G., Proverbio, E.: Identification of corrosion mechanisms by univariate and multivariate statistical analysis during long term acoustic emission monitoring on a pre-stressed concrete beam. *Corros. Sci.* **73**, 161–171 (2013)
21. Carpinteri, A., Cardone, F., Lacidogna, G.: Energy emissions from failure, phenomena: mechanical, electromagnetic, nuclear. *Exp. Mech.* **50**, 1235–1243 (2010)
22. Carpinteri, A., Corrado, M., Lacidogna, G.: Heterogeneous materials in compression: Correlations between absorbed, released and acoustic emission energies. *Eng. Fail. Anal.* **33**, 236–250 (2013a)
23. Carpinteri, A., Lacidogna, G., Accornero, F., Mpalkas, A., Matikas, T.E., Aggelis, D.G.: Influence of damage in the acoustic emission parameters. *Cem. Concr. Compos.* **44**, 9–16 (2013b)
24. Chen, B., Liu, J.: Experimental study on AE characteristics of three-point-bending concrete beams. *Cem. Concr. Res.* **34**, 391–397 (2004)
25. Colombo, S., Forde, M.C., Main, I.G., Shigeishi, M.: Predicting the ultimate bending capacity of concrete beams from the “relaxation ratio” analysis of AE signals. *Constr. Build. Mater.* **19**, 746–754 (2005)
26. Colombo, S., Main, I.G., Forde, M.C.: Assessing damage of reinforced concrete beam using “b-value” analysis of acoustic emission signals. *J. Mater. Civil Eng.* **15**, 280–286 (2003)
27. Dai, Q., Ng, K., Zhou, J., Kreiger, E.L., Ahlborn, T.M.: Damage investigation of single-edge notched beam tests with normal strength concrete and ultra high performance concrete specimens using acoustic emission techniques. *Constr. Build. Mater.* **31**, 231–242 (2012)
28. Elaqua, H., Godin, N., Peix, G., R'Mili, M., Fantozzi, G.: Damage evolution analysis in mortar, during compressive loading using acoustic emission and X-ray tomography: effects of the sand/cement ratio. *Cem. Concr. Res.* **37**, 703–713 (2007)
29. ElBatanouny, M.K., Ziehl, P.H., Larosche, A., Mangual, J., Matta, F., Nanni, A.: Acoustic emission monitoring for assessment of prestressed concrete beams. *Constr. Build. Mater.* **58**, 46–53 (2014)
30. Elfergani, H.A., Pullin, R., Holford, K.M.: Damage assessment of corrosion in prestressed concrete by acoustic emission. *Constr. Build. Mater.* **40**, 925–933 (2013)
31. Farhidzadeh, A., Dehghan-Niri, E., Salamone, S., Luna, B., Whittaker, A.: Monitoring Crack propagation in reinforced concrete shear walls by acoustic emission. *J. Struct. Eng.* **139**(12), 04013010 (2013a). doi:[10.1061/\(ASCE\)ST.1943-541X.0000781](https://doi.org/10.1061/(ASCE)ST.1943-541X.0000781)
32. Farhidzadeh, A., Mpalkas, A.C., Matikas, T.E., Farhidzadeh, H., Aggelis, D.G.: Fracture mode identification in cementitious materials using supervised pattern recognition of acoustic emission features: part B. *Const. Build. Mater.* **67**, 129–138 (2014)
33. Farhidzadeh, A., Salamone, S., Singla, P.: A probabilistic approach for damage identification and crack mode classification in reinforced concrete structures. *J. Intell. Mater. Syst. Struct.* **24** (14), 1722–1735 (2013b)
34. Fowler, T.J.: Experience with acoustic emission monitoring of chemical process industry vessels. In: *Progress in AE III*, pp. 150–162 (1986)
35. Fricker, S., Vogel, T.: Site installation and testing of a continuous acoustic monitoring. *Constr. Build. Mater.* **21**, 501–510 (2007)

36. Golaski, L., Gebski, P., Ono, K.: Diagnostics of reinforced concrete bridges by acoustic emission. *J. Acoust. Emission* **20**, 83–98 (2002)
37. Grosse, C.U., Finck, F.: Quantitative evaluation of fracture processes in concrete using signal-based acoustic emission techniques. *Cem. Concr. Compos.* **28**, 330–336 (2006)
38. Grosse C.U.: Wireless sensing and acoustic emission array techniques, chapter 15. In: Grosse, C.U., Ohtsu, M. (eds.), *Acoustic Emission Testing*, pp. 367–381. Springer, Berlin (2008a)
39. Grosse, C.U.: Chapter 5: signal-based AE analysis. In: Grosse C.U., Ohtsu M. (eds.) *Acoustic emission testing*, pp. 53–99. Springer, Berlin (2008b)
40. Grosse, C.U., Ohtsu, M.: *Acoustic Emission Testing*. Springer, Berlin (2008)
41. Haneef, T.K., Kumari, K., Mukhopadhyay, C.K., Venkatachalapathy Rao, B.P., Jayakumar, T.: Influence of fly ash and curing on cracking behavior of concrete by acoustic emission technique. *Constr. Build. Mater.* **44**, 342–350 (2013)
42. Hu, S., Lu, J., Xiao, F.: Evaluation of concrete fracture procedure based on acoustic emission parameters. *Constr. Build. Mater.* **47**, 1249–1256 (2013)
43. Iliopoulos, S., Iliopoulos, A., Pyl, L., Sol, H., Aggelis, D.G.: A qualitative and quantitative investigation of the uncracked and cracked condition of concrete beams using impulse excitation, acoustic emission, and ultrasonic pulse velocity techniques, Volume 9062, 2014, Article number 90620Q, Smart Sensor Phenomena, Technology, Networks, and Systems Integration 2014; San Diego, CA; U.S.A (2014)
44. Kaiser J.: Untersuchung über das Auftreten von Geräuschen beim Zugversuch. Ph.D. thesis, Technische Hochschule Munich (1950)
45. Karihaloo, B.L., Ramachandra, Murthy A., Iyer, N.R.: Determination of size-independent specific fracture energy of concrete mixes by the tri-linear model. *Cem. Concr. Res.* **49**, 82–88 (2013)
46. Kawasaki, Y., Wakuda, T., Kobarai, T., Ohtsu, M.: Corrosion mechanisms in reinforced concrete by acoustic emission. *Constr. Build. Mater.* **48**, 1240–1247 (2013)
47. Khan, F., Bartoli, I., Rajaram, S., Vanniamparambil, P.A., Kontsos, A., Bolhassani, M., Hamid, A.: Acoustics and temperature based NDT for damage assessment of concrete masonry system subjected to cyclic loading. In: Proceedings of SPIE 9063, Nondestructive Characterization for Composite Materials, Aerospace Engineering, Civil Infrastructure, and Homeland Security 2014, p. 90630B. doi:[10.1117/12.2045129](https://doi.org/10.1117/12.2045129) (2014)
48. Kocur, G.K., Vogel, T.: Classification of the damage condition of preloaded reinforced concrete slabs using parameter-based acoustic emission analysis. *Constr. Build. Mater.* **24**, 2332–2338 (2010)
49. Kurz, J.H., Finck, F., Grosse, C.U., Reinhardt, H.-W.: Stress drop and stress redistribution in concrete quantified over time by the b-value analysis. *Struct. Health Monit.* **5**(1), 69–81 (2006)
50. Lu, Y., Li, Z., Liao, W.: Damage monitoring of reinforced concrete frames under seismic loading using cement-based piezoelectric sensor. *Mater. Struct.* **44**(7), 1273–1285 (2011)
51. Luo, X., Haya, H., Inaba, T., Shiotani, T., Nakanishi, Y.: Damage evaluation of railway structures by using train-induced AE. *Constr. Build. Mater.* **18**, 215–223 (2004)
52. Md, Nor N., Ibrahim, A., Bunnori, N.M., Saman, H.M.: Acoustic emission signal for fatigue crack classification on reinforced concrete beam. *Constr. Build. Mater.* **49**, 583–590 (2013)
53. Mindess, S.: Acoustic emission methods. In: Malhotra, V.M., Carino, N.J. (eds.) CRC handbook of nondestructive testing of concrete. Boca Raton (FL), CRC (2004)
54. Mpalkas, A.C., Thanasia, O.V., Matikas, T.E., Aggelis, D.G.: Mechanical and fracture behavior of cement-based materials characterized by combined elastic wave approaches. *Constr. Build. Mater.* **50**, 649–656 (2014)
55. Mpalkas, A.C., Vasilakos, I., Matikas, T.E., Chai, H.K., Aggelis, D.G.: Monitoring of the fracture mechanisms induced by pull-out and compression in concrete. *Eng. Fract. Mech.* **128**, 219–230 (2014)
56. Muralidhara, S., Raghu Prasad, B.K., Eskandari, H., Karihaloo, B.L.: Fracture process zone size and true fracture energy of concrete using acoustic emission. *Construct. Build. Mater.* **24**, 479–486 (2010)

57. Ogawa, Y., Kawasaki, Y., Okamoto, T.: Fracture behavior of RC members subjected to bending shear and torsion using acoustic emission method. *Constr. Build. Mater.* **67**, 165–169 (2014)
58. Ohno, K., Ohtsu, M.: Crack classification in concrete based on acoustic emission. *Constr. Build. Mater.* **24**, 2339–2346 (2010)
59. Ohno, K., Uji, K., Ueno, A., Ohtsu, M.: Fracture process zone in notched concrete beam under three-point bending by acoustic emission. *Constr. Build. Mater.* **67**, 139–145 (2014)
60. Ohtsu, M.: Simplified moment tensor analysis and unified decomposition of AE source: application in situ hydrofracturing test. *J. Geophys. Res.* **96**(B4):6211–6221 (1991)
61. Ohtsu, M.: Recommendation of RILEM TC 212-ACD: acoustic emission and related NDE techniques for crack detection and damage evaluation in concrete, Test method for damage qualification of reinforced concrete beams by acoustic emission, *Mater. Struct.* **43**(9), 1183–1186 (2010a)
62. Ohtsu, M.: Recommendations of RILEM Technical Committee 212-ACD: acoustic emission and related NDE techniques for crack detection and damage evaluation in concrete: 3. Test method for classification of active cracks in concrete structures by acoustic emission. *Mater. Struct.* **43**(9), 1187–1189 (2010b)
63. Ohtsu, M., Isoda, T., Tomoda, Y.: Acoustic emission techniques standardized for concrete structures. *J. Acoust. Emission* **25**, 21–32 (2007)
64. Ohtsu, M., Okamoto, T., Yuyama, S.: Moment tensor analysis of AE for cracking mechanisms in concrete. *ACI Struct. J.* **95**(2), 87–95 (1998)
65. Ohtsu, M., Uchida, M., Okamoto, T., Yuyama, S.: Damage assessment of reinforced concrete beams qualified by acoustic emission. *ACI Struct. J.* **99**(4), 411–417 (2002)
66. Omundi, B., Aggelis, D.G., Sol, H., Sitters, C.: Acoustic emission behaviour of prestressed concrete sleepers under Quasi-Static homologation testing. In: Proceedings of the 31st Conference of the European Working Group on Acoustic Emission, Dresden, Germany, 3–5 Sept 2014. <http://www.ewgae2014.com/portals/131/bb/we3a2.pdf>
67. Pazdera, L., Topolar, L.: Application acoustic emission method during concrete frost resistance. *Russ. J. Nondestr. Test.* **50**(2), 127–131 (2014)
68. Polyzos, D., Papacharalampopoulos, A., Shiotani, T., Aggelis, D.G.: Dependence of AE parameters on the propagation distance. *J. Acoust. Emission* **29**, 57–67 (2011)
69. Rilem (2014) http://rilem.net/gene/main.php?base=8750&gp_id=252
70. Rouchier, S., Foray, G., Godin, N., Woloszyn, M., Roux, J.-J.: Damage monitoring in fibre reinforced mortar by combined digital image correlation and acoustic emission. *Constr. Build. Mater.* **38**, 371–380 (2013)
71. Schechinger, B., Vogel, T.: Acoustic emission for monitoring a reinforced concrete beam subject to four-point-bending. *Constr. Build. Mater.* **21**, 483–490 (2007)
72. Shah, A.A., Ribakov, Y.: Effectiveness of nonlinear ultrasonic and acoustic emission evaluation of concrete with distributed damages. *Mater. Des.* **31**, 3777–3784 (2010)
73. Shah, S.G., Chandra Kishen, J.M.: Fracture behavior of concrete–concrete interface using acoustic emission technique. *Eng. Fract. Mech.* **77**, 908–924 (2010)
74. Shahidan, S., Pulin, R., Muhamad Bunnori, N., Holford, K.M.: Damage classification in reinforced concrete beam by acoustic emission signal analysis. *Constr. Build. Mater.* **45**, 78–86 (2013)
75. Shiotani, T., Aggelis, D.G.: Evaluation of repair effect for deteriorated concrete piers of intake dam using AE activity. *J. Acoust. Emission* **25**, 69–79 (2007)
76. Shiotani, T., Aggelis, D.G., Makishima, O.: Global monitoring of large concrete structures using acoustic emission and ultrasonic techniques. *J. Bridge Eng. ASCE* **14**(3), 188–192 (2009)
77. Shiotani, T., Aggelis, D.G., Makishima, O.: Global monitoring of concrete bridge using acoustic emission. *J. Acoust. Emission* **25**, 308–315 (2007)
78. Shiotani, T., Fujii, K., Aoki, T., Amou, K.: Evaluation of progressive failure using AE sources and improved b-value on slope model tests. *Prog. Acoust. Emission* **7**, 529–534 (1994)

79. Shiotani, T., Nakanishi, Y., Luo, X., Haya, H., Inaba, T.: Damage evaluation for railway structures by means of acoustic emission. *Key Eng. Mater.* **270–273**, 1622–1630 (2004)
80. Shiotani, T., Oshima, Y., Goto, M., Momoki, S.: Temporal and spatial evaluation of grout failure process with PC cable breakage by means of acoustic emission. *Constr. Build. Mater.* **48**, 1286–1292 (2013)
81. Shiotani, T., Shigeishi, M., Ohtsu, M.: Acoustic emission characteristics of concrete-piles. *Constr. Build. Mater.* **13**, 73–85 (1999)
82. Soulioti, D., Barkoula, N.M., Paipetis, A., Matikas, T.E., Shiotani, T., Aggelis, D.G.: Acoustic emission behavior of steel fibre reinforced concrete under bending. *Constr. Build. Mater.* **23**, 3532–3536 (2009)
83. Suzuki, T., Ogata, H., Takada, R., Aoki, M., Ohtsu, M.: Use of acoustic emission and X-ray computed tomography for damage evaluation of freeze-thawed concrete. *Constr. Build. Mater.* **24**, 2347–2352 (2010)
84. Suzuki, T., Ohtsu, M.: Damage estimation of concrete canal due to earthquake effects by acoustic emission method. *Constr. Build. Mater.* **67**, 186–191 (2014)
85. Tensi, H.M.: The Kaiser-effect and its scientific background. *J. Acoust. Emission* **22**, S1–S16 (2004)
86. Torres Arredondo M.-A.: Acoustic Emission Testing and Acousto-Ultrasonics for Structural Health Monitoring. Ph.D. thesis, Universitat Siegen (2013). ISSN 2191-5601
87. Triantafillou, T.C., Papanicolaou, C.G.: Shear strengthening of reinforced concrete members with textile reinforced mortar (TRM) jackets. *Mater. Struct.* **39**, 93–103 (2006)
88. Van Den Abeele, K., Desadeler, W., De Schutter, G., Wevers, M.: Active and passive monitoring of the early hydration process in concrete using linear and nonlinear acoustics. *Cem. Concr. Res.* **39**, 426–432 (2009)
89. Verbruggen, S., Aggelis, D.G., Tysmans, T., Wastiels, J.: Bending of beams externally reinforced with TRC and CFRP monitored by DIC and AE. *Compos. Struct.* **112**, 113–121 (2014)
90. Vidya Sagar, R., Raghu Prasad, B.K.: A review of recent developments in parametric based acoustic emission techniques applied to concrete structures. *Nondestr. Test. Eval.* **27**(1), 47–68 (2012)
91. Vidya, Sagar R., Raghu Prasad, B.K.: An experimental study on acoustic emission energy as a quantitative measure of size independent specific fracture energy of concrete beams. *Constr. Build. Mater.* **25**, 2349–2357 (2011)
92. Vidya Sagar, R., Raghu Prasad, B.K.: Damage limit states of reinforced concrete beams subjected to incremental cyclic loading using relaxation ratio analysis of AE parameters. *Constr. Build. Mater.* **35**, 139–148 (2012)
93. Wang, Y., Hao, H.: Integrated health monitoring for reinforced concrete beams: an experimental study. *Aust. J. Mech. Eng.* **8**(2), 207–217 (2011)
94. Watanabe, T., Nishibata, S., Hashimoto, C., Ohtsu, M.: Compressive failure in concrete of recycled aggregate by acoustic emission. *Constr. Build. Mater.* **21**, 470–476 (2007)
95. Ziehl, P., Pollock, A.: (2012) Acoustic emission for civil structures. In: Sikorski W. (ed.) *Acoustic Emission*, InTech. doi:[10.5772/32652](https://doi.org/10.5772/32652). <http://www.intechopen.com/books/acoustic-emission/acoustic-emission-for-civil-structures>. ISBN: 978-953-51-0056-0

Chapter 6

Cross-Sectional Visualization of Defects by SIBIE

Takeshi Watanabe, Ninel Alver and Masayasu Ohtsu

Abstract For nondestructive evaluation (NDE) of concrete structures, the impact-echo method has been successfully applied to locate defects and voids in concrete. To compensate the difficulty in selecting the resonant frequency and to visually locate a defect, an imaging procedure named SIBIE (Stack Imaging of spectral amplitude Based on Impact-Echo) has been developed. This is an imaging technique for visualizing defects of which locations are known or identified. Following the basic concept and procedure, applications to concrete structures are discussed. The presence of the ungrouted duct can be visually identified by the SIBIE procedure in both the cases of plastic sheath and metal sheath. In addition, the depth of the surface crack is visually evaluated.

Keywords Impact-echo • Visualization of defects • Concrete • Grout • SIBIE

6.1 Introduction

The impact-echo method is well known as a non-destructive testing method for concrete structures [8]. The method has been applied to such types of defects in concrete as thickness measurement of a slab, grouting performance and void detection in a post-tensioning tendon duct, identification of surface-opening crack depth, and so forth. In principle, the location of a defect or a void is estimated by identifying the resonant (peak) frequency in the frequency spectrum, which is

T. Watanabe

Department of Civil Engineering, The University of Tokushima, Tokushima, Japan
e-mail: watanabe@ce.tokushima-u.ac.jp

N. Alver

Ege University, Bornova, Izmir, Turkey

M. Ohtsu (✉)

Graduate School of Engineering, Kyoto University, Kyoto, Japan
e-mail: ohtsu.masayasu.4v@kyoto-u.ac.jp

associated with a travel path from an impact point to a detection point via the defect due to reflection or diffraction.

Development of the impact-echo method has been summarized [9], referring to four major breakthroughs. The first is numerical analysis by the finite element method (FEM), which eventually leads to a theoretical background on the shape factors. The second is the use of steel balls as the impact, which enables to apply Hertz's theory to determine frequency bounds in the analysis. The third is the use of the displacement sensor, and the forth is the use of frequency spectra. Although the method has been successfully applied to practical inspections, there exist still several limitations in applications to concrete members and structures in service.

The shape factor is one critical issue to properly estimate the location of the defect, because the location is only calculated from the peak frequency. However, one essential drawback is the identification of peak frequencies, because it is sometimes not easy to determine the peak frequency correctly, which is particularly associated with the presence of defects. The frequency spectrum cannot always be interpreted successfully, because many peaks are often observed in the spectrum. Stack Imaging of Spectral Amplitudes Based on Impact-Echo (SIBIE) procedure has been developed to improve the impact-echo method, applying an imaging procedure to the impact-echo data [3].

6.2 Impact-Echo and Key Issues Associated

The impact-echo method consists of such three stages as applying the impact, detecting waves, and identifying peak frequencies after FFT (Fast Fourier Transform) analysis of detected waves. Concerning the frequency spectrum analyzed, each stage has a key issue.

According to Hertz's theory, the impact due to the steel-ball drop has a particular contact time T_c , primarily depending on the radius, D , of the steel ball. Sansalone presented a simplified equation [8],

$$T_c = 0.0043D. \quad (6.1)$$

Examples of the upper-bound frequencies f_c covered by the contact times of the impactor are illustrated in Fig. 6.1a, which are calculated from,

$$f_c = 1.25/T_c = 1.25/(0.0043D). \quad (6.2)$$

Since the impact-echo requires picking up the peak frequency resonated with the location of a defect, the upper-bound frequency f_c should be higher than the resonant frequency. Otherwise, as illustrated, the peak frequency might disappear. From Eq. 6.2, the upper-bound frequency f_c is inversely proportional to the radius of a steel ball. The larger the diameter of a steel ball becomes, the lower the upper-bound frequency shifts. In order to generate impact energy sufficient enough

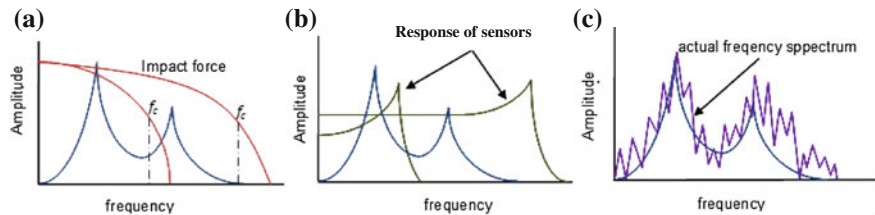


Fig. 6.1 Key issues in impact-echo. **a** Impact response. **b** Response of sensor detection. **c** Frequency spectrum

to drive elastic waves which can propagate more than 1 m with little attenuation in concrete, a steel ball of at least 10 mm diameter is often necessary. According to Eqs. 6.1 and 6.2, such a ball could generate frequency contents up to only 29 kHz. In Fig. 6.1a, two examples of the frequency spectra driven by the impacts are denoted. Because the spectrum to be detected contains two peak frequencies, the upper-bound frequency f_c should be higher than these peak frequencies to identify both of them. In the case of the spectrum plotted with the lower f_c , the higher peak frequency cannot be detected even though this peak frequency is associated with the defect. This is occasionally the case where the impact is driven by such as a hammer and a pendulum impact tester. The resonance frequency f_r due to thickness H is obtained from,

$$f_r = Cv_p/2H. \quad (6.3)$$

Here C is the shape factor and v_p is the velocity of P wave. In the case of normal concrete, v_p is approximately 4000 m/s. Then, $f_r = 33.3$ kHz in the case that $H = 6$ cm and $C = 1$. This implies that the resonance frequency f_r may not be identified in the case where the steel ball of 10 mm in diameter is used to detect the thickness of 6 cm, because the frequency range generated is limited to 29 kHz. Thus, the impact which could generate higher frequency components is desirable, although the impact energy driven by a smaller steel ball is not so high. It is suggested that the impactor device has to be properly developed, so that the impact frequency content is so known as to cover the resonance frequencies to be identified.

The frequency response of the receiving device, in particular, of sensors should also cover the frequency range. As an example, two frequency spectra of the receiving devices are denoted by broken curves in Fig. 6.1b. Again, in the case of the device with the lower resonance frequency, the higher peak frequency of the spectrum plotted cannot be detected in the system. Consequently, the detection system with a proper range of frequency response has to be equipped.

As one example, the detection device in the impact-echo commercially available is shown in Fig. 6.2a. A frequency spectrum obtained by the system is presented in Fig. 6.2b. Frequency response over 5 kHz is so low that defects shallower than 400 mm might not be able to be detected, according to Eq. 6.3.

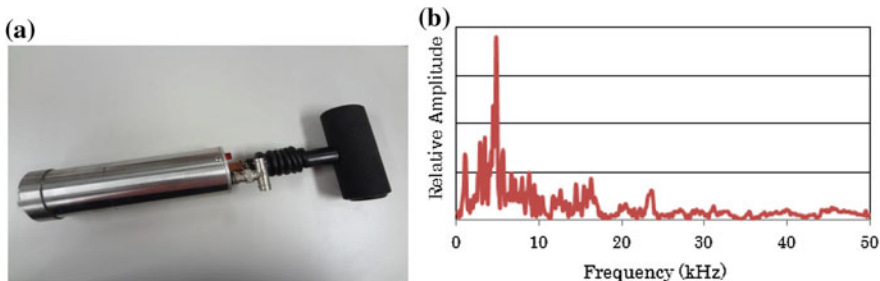


Fig. 6.2 Example of the detection system and its frequency response. **a** Impact-echo device. **b** Frequency spectrum obtained

As shown in Fig. 6.1c, frequency spectrum analyzed by FFT usually contains many peak frequencies. Thus, it might be not easy to identify particular peaks in the frequency spectra. In addition, it is sometimes uncertain whether the amplitude variation of the relevant peaks is due to coupling problems or to changes in the structural conditions. In this respect, SIBIE procedure has been developed as a visualized technique.

6.3 Development of Impactors

6.3.1 Impactors

A standard impactor in the impact-echo is the steel-ball drop. As given in Eq. 6.2, the upper-bound frequency f_c , which is known a corner frequency in seismology, is inversely proportional to the diameter of the steel-ball. The higher the corner frequency is driven, the smaller ball is to be employed. This implies that the impactor of the higher frequency content can only drive the low energy impact.

To generate elastic waves of higher frequency content and good impact energy, a shooting device of an aluminum bullet has been developed. The aluminum bullet of 8 mm diameter in Fig. 6.3a is shot by driving compressed air with 0.05 MPa pressure. A portable compressor employed is shown in Fig. 6.3b along with a projector device. Frequency components of the device are compared with those of the steel-ball drop.

Two issues are raised on the shooting device: (1) Devices are of large-scale, and (2) In the case of testing many points, measurement takes time. Therefore, in order to miniaturize the input device and to be available for on-site measurement, a titanium head shown in Fig. 6.4b is directly attached to an impactor device equipped with a spring system shown in Fig. 6.4b. Frequency components of titanium heads of two sizes in the figure are compared with those of aluminum heads.

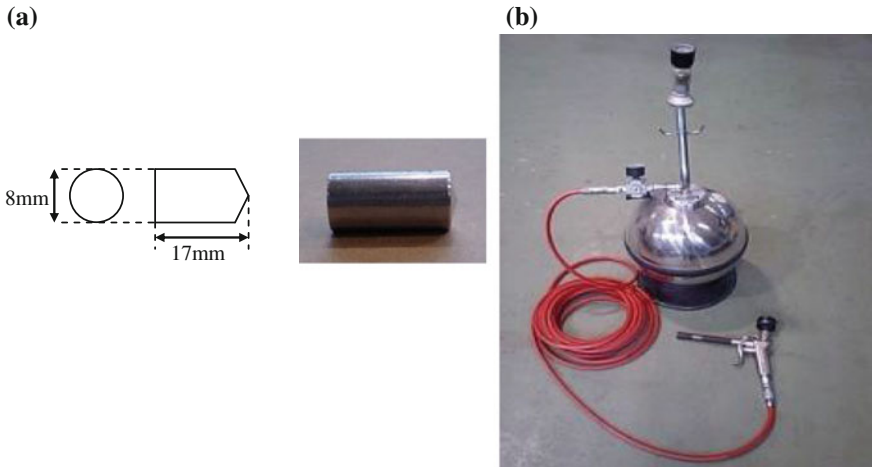


Fig. 6.3 Impactor developed, shooting an aluminum bullet with compressed air. **a** Aluminum bullet. **b** Portable compressor with a projector

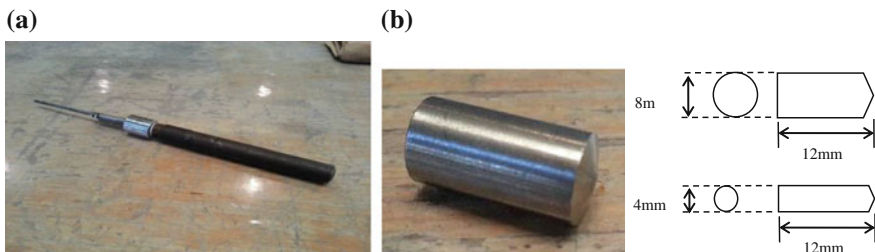


Fig. 6.4 Impact device for on-site measurement. **a** Impact device with spring. **b** Titanium head and sizes

6.3.2 Impact Test

To evaluate response of the device, the specimen of dimensions $400 \times 400 \times 100$ mm was employed. P-wave velocity of the specimen was obtained as 4040 m/s by the velocity measurement. The impact was applied to the specimen as shown in Fig. 6.5a and elastic waves of output were detected by using the laser vibrometer shown in Fig. 6.5b, and recorded in the oscilloscope. Here, sampling time was 0.1 μ s and the number of digitized data for each waveform was 2048. This is because the first arrival waves from the impact point are only detected, so that the reflection waves from the bottom of the specimen are not recorded.

An impact response of the shooting device was compared with those of steel balls. Steel balls of 8 and 20 mm diameter were dropped from 100 mm height. Concerning the spring device, titanium and aluminum heads of 4 and 8 mm diameters were tested as shown in Fig. 6.4b. Detected waves by the laser

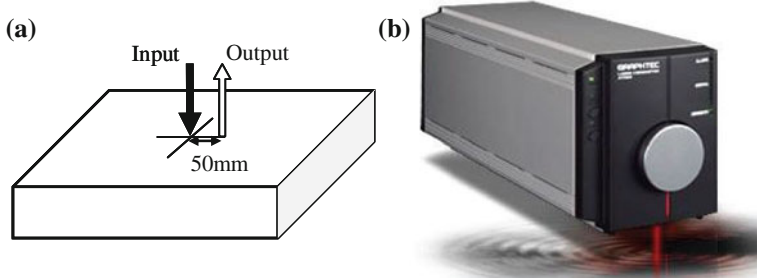


Fig. 6.5 Test set-up and vibrometer for output. **a** Set-up for the impact test. **b** Laser vibrometer

vibrometer were analyzed by the Fast Fourier Transform (FFT), and Fourier spectra were obtained.

6.3.3 Theory for Analysis

In elastodynamics, a problem to compute elastic waves at the surface, resulting from a point force in a half space is known as Lamb's problem [6]. The impact (input) illustrated in Fig. 6.5a could generate wave motions known as Lamb's solutions for a surface pulse, in the case that the pulse is applied as a step-function. Introducing the solution $G(x, y, t)$ of Lamb's problem, dynamic displacement $u(x, t)$ in the vertical direction at location x (center in Fig. 6.5a) due to impact force $f(y, t)$ at location y (50 mm apart in Fig. 6.5a) is formulated as,

$$u(x, t) = dG(x, y, t)/dt * f(y, t). \quad (6.4)$$

Here symbol $*$ means the convolution integral. A numerical program $G(x, y, t)$ of by Fortran has been published elsewhere [5]. Because it is known that the laser vibrometer employed detects velocity components of waves $v(x, t)$ and has a flat response up to 50 kHz, Eq. 6.4 is modified as,

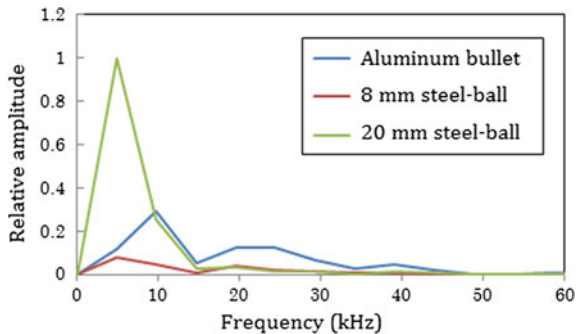
$$v(x, t) = d^2G(x, y, t)/dt^2 * f(y, t). \quad (6.5)$$

Converting functions in Eq. 6.5 into the frequency domain by Fourier transform, frequency response of the impact is obtained as,

$$F(f) = G(f)/([i2\pi f]^2 V(f)). \quad (6.6)$$

Here $V(f)$, $G(f)$ and $F(f)$ are absolute values of Fourier transforms of $v(t)$, $G(t)$ and $f(t)$, respectively.

Fig. 6.6 Frequency contents of the impactors

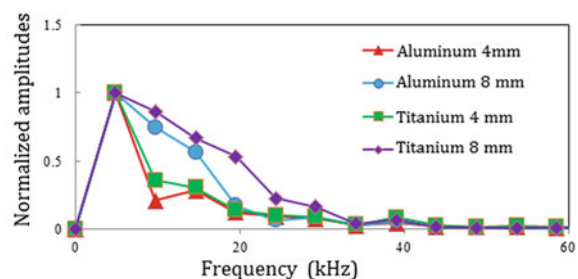


6.3.4 Evaluation of Impactor Response

In the impact test, the aluminum bullet of 8 mm diameter was shot by driving compressed air with 0.05 MPa pressure at the center (input point in Fig. 6.5a). Steel balls of 8 and 20 mm diameter were also dropped from 100 mm height at the center of the specimen. After recording detected waves, these were analyzed by Eq. 6.6. The frequency responses of these impactors analyzed are compared in Fig. 6.6. It is observed that the steel-ball drop of 20 mm diameter has the highest amplitude, but the frequency content is limited to around 15 kHz. From Eq. 6.2, it is estimated as 14.53 kHz. In contrast, the steel-ball of 8 mm generates the lowest amplitude and the corner frequency is estimated as 36.33 kHz from Eq. 6.2. The shooting device has the moderate amplitude and good response up to 35 kHz.

Frequency responses of impacts by the spring device are shown in Fig. 6.7. Dominant frequency ranges of aluminum of 4 mm diameter and 8 mm diameter, and titanium of 4 mm, and 8 mm are found as 0–10, 0–20, 0–20, and 0–30 kHz, respectively. Compared with the others, the titanium head of 8 mm has high frequency components and good amplitudes. Compared with the aluminum bullet by using the compressed air in Fig. 6.6, it is observed that the spring device with the titanium head of 8 mm diameter has comparable frequency components and amplitudes.

Fig. 6.7 Frequency responses of the spring device



6.4 Selection of the Sensor

In the impact-echo method established by Sansalone [9], the displacement transducer (sensor) was employed. The sensor was originally developed for acoustic emission (AE) testing [7]. It consists of a small conical piezoelectric element and a large brass backing. It was confirmed that a flat response up to MHz range can be achieved, but the sensitivity was not good enough for AE measurement in metal. Consequently, it has been applied to sensor calibration in AE research.

One example of commercially available devices in the impact-echo is shown in Fig. 6.2a. Although the displacement sensor originally has a flat response, the device has a particular frequency range up to 10 kHz as shown in Fig. 6.2b. Probably, this is because the sensor is equipped with the built-in impactor in the case.

An accelerometer has been applied at Kumamoto University for detection of elastic waves. It is known that the accelerometer has a flat response up to its resonant frequency. So, the nominal frequency range is set to lower than the resonance. A wide-band accelerometer of the nominal frequency up to 30 kHz was employed, which is of 5 mm diameter and shown in Fig. 6.8a. In order to confirm the response, a calibration test was performed.

By employing the experimental set-up in Fig. 6.5, the accelerometer was placed in the opposite direction to the laser vibrometer, 50 mm apart from the center. The aluminum bullet was shot at the center. A frequency spectrum of detected waves by the accelerometer was divided by that of the laser vibrometer. A result is shown in Fig. 6.8b. It is confirmed that the accelerometer has a fairly flat response up to 35 kHz, and the sensitivity increases over 35 kHz due to the effect of the resonance. Thus, by employing either the shooting device with the aluminum bullet or the spring device with titanium head, the use of the accelerometer confirms that the frequency spectra could obtain without the effects of the impactor and the sensor up to 30 kHz.

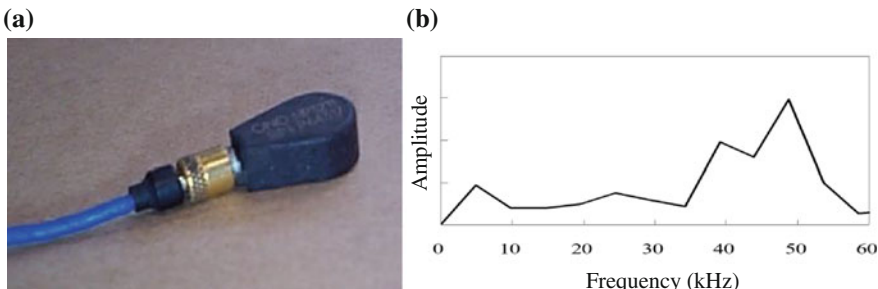


Fig. 6.8 Accelerometer system for detection. **a** Accelerometer. **b** Frequency response of the accelerometer

6.5 SIBIE Procedure

In the impact-echo method, a cross-section of the specimen with a cavity is illustrated in Fig. 6.9a. When the elastic wave is driven to the specimen, the paths of the elastic wave are shown. As shown in Fig. 6.9b, frequency spectrum is obtained by applying the fast Fourier transform (FFT) analysis to a detected wave at an output point in the figure. Here, peak frequencies appear at f_T and f_{void} , which are calculated as,

$$f_T = 0.96 \frac{v_p}{2T}, \quad (6.7)$$

$$f_{void} = 0.96 \frac{v_p}{2d}, \quad (6.8)$$

where f_T is the resonance frequency of a plate thickness T , f_{void} is the resonance frequency of a void in depth d , and 0.96 is a shape factor determined from geometry [9].

SIBIE procedure is a post-processing technique of impact-echo data. This is an imaging technique for detected waveforms in the frequency domain. In the procedure, first, a cross-section of concrete is divided into square elements as shown in Fig. 6.10a.

Then, resonance frequencies due to reflections at each element are computed. The travel distance from the input location to the output via the element is calculated as,

$$R = r_1 + r_2. \quad (6.9)$$

Resonance frequencies due to reflections or diffractions at each element are calculated from,

$$f_R = v_p/R, \quad (6.10)$$

$$fr_2 = v_p/r_2. \quad (6.11)$$

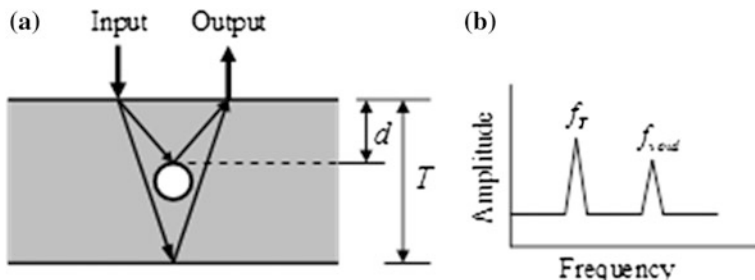


Fig. 6.9 Principle of void detection by the impact-echo. **a** Cross-section of the member with a cavity. **b** Frequency spectrum obtained

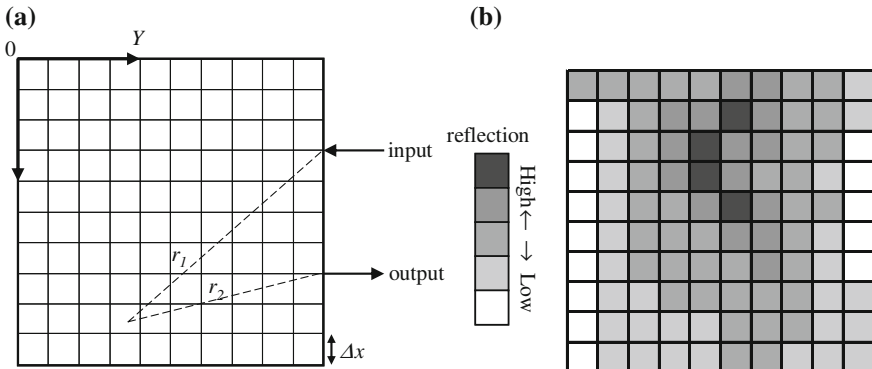


Fig. 6.10 Concept of SIBIE analysis. **a** Cross-section of an imaging model. **b** Stacking of spectral amplitudes

Spectral amplitudes corresponding to these two resonant frequencies in the frequency spectrum are summed up. Thus, an intensity of spectral amplitudes at each element is estimated as a stacked image as shown in Fig. 6.10b. As seen in Eqs. 6.10 and 6.11, the shape factors are neglected, because intensities of the image are obtained as a zone and the precise determination of the location is out of the scope. The minimum size of the square mesh Δ for the SIBIE analysis should be approximately equal to $v_p\Delta t/2$. Employing two accelerometers at two detection points during the impact test improves the SIBIE results [1]. Numerous researches have been conducted both in laboratory and on site and different variables have been examined to study the effectiveness of SIBIE procedure [1–5].

6.6 On-site Applications

6.6.1 Imperfectly Grouted Sheath in Prestressed Concrete

(a) Specimen

In order to study an applicability of SIBIE procedure to on-site measurement in prestressed concrete (PC), a model test was performed. A model specimen with imperfectly grouted ducts is illustrated in Fig. 6.11. The specimen is of dimensions $500 \times 1000 \times 2000$ mm, which corresponds to a web portion of a box-girder bridge. The velocity of P-wave measured was 4300 m/s. As shown in Fig. 6.12, it contains a grouted duct, a partially grouted duct, and an ungrouted duct. The diameter of each sheath is 70 mm, and pictures of all ducts are given in Fig. 6.12b. To take into account the cases that ducts are arranged in parallel, the resonant frequencies corresponding the distances from the sides are calculated.

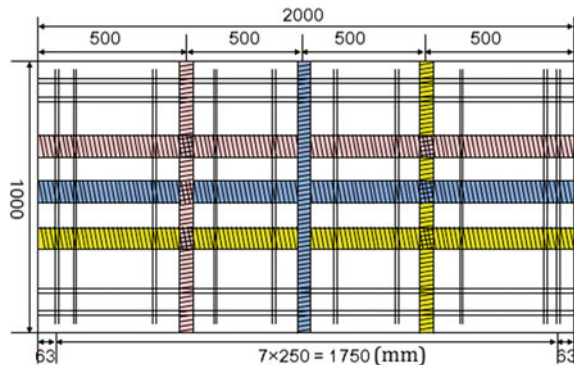


Fig. 6.11 Model specimen with ungrouted ducts

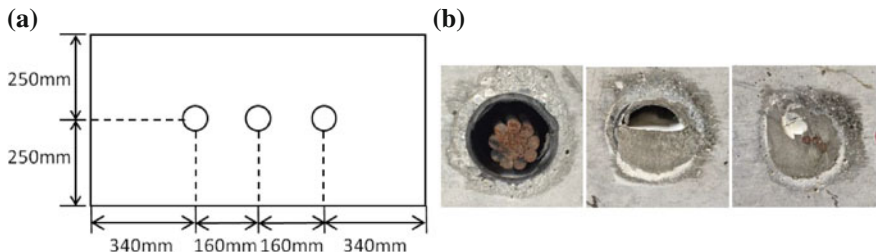


Fig. 6.12 Cross-section of model specimen. **a** Three ducts at cross-section. **b** Cross-sectional views of three ducts

From Eq. 6.11, it is found that the upper limit frequencies in the SIBIE analysis should be set to 5 kHz for the depth of 500 mm ($340 + 160$ mm) and 7 kHz for the depth of 340 mm, respectively. The impact by the spring device was given right over the duct, and elastic waves were detected by the accelerometers at two opposite locations apart from 50 mm from the impact location.

(b) SIBIE Results

SIBIE results are given in Fig. 6.13. For the case of left-side input in Fig. 6.13a, the higher reflection is observed only at the ungrouted duct. In contrast, for the case of right-side input, a weak reflection is observed at the grouted duct, and the higher reflection is observed at the partially grouted and ungrouted ducts.

In Fig. 6.13b, results of 5 kHz upper limit frequency are shown. For the case of the left-side input, the partially grouted duct is clearly identified without the effect of ungrouted duct located at the shallower depth. In the case of the left-side input, the partially grouted and the ungrouted ducts are visually identified. Thus, it is confirmed that the grouting condition of the ducts arranged in parallel can be estimated.

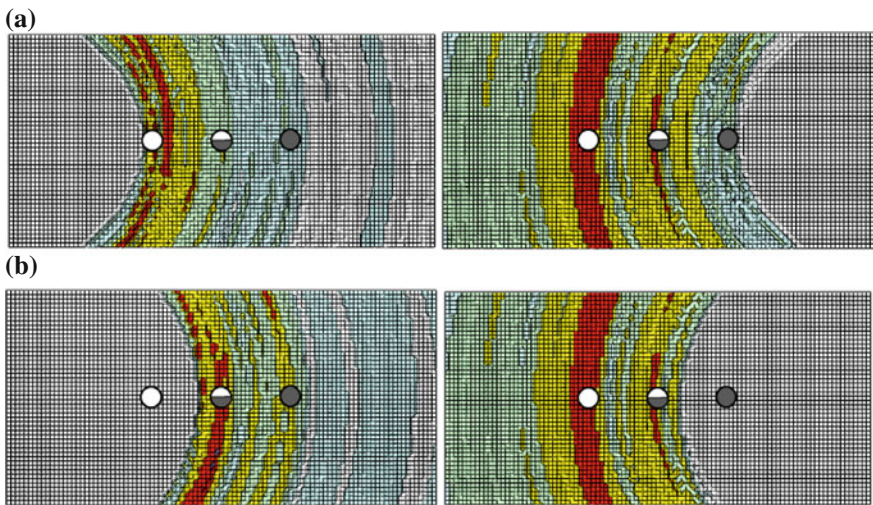


Fig. 6.13 Results of SIBIE analysis in PC ducts. **a** 7 kHz upper limit frequency. **b** 5 kHz upper limit frequency

6.6.2 Depth of Surface Crack

(a) Test Site

At a construction site of a highway bridge, surface cracks were found in the back side of one abutment at early ages as shown in Fig. 6.14a. The abutment is 4.47 m high and 12.65 m wide. The widths of these cracks varied from 0.1 to 2 mm. Since the area was very cold during winter, the cause of cracking was considered to be internal constraint due to thermal expansion of mass concrete. For maintenance and repair, at three cracks as shown in Fig. 6.14a as Nos. 9 to 11, the depths of cracks were measured by the ultrasonic test. Results are given in Table 6.1. It is found the depths are varied from 50 to 70 mm. Since these values are shallower than the cover thickness (90 mm) of reinforcement, it was decided that only the surface was sealed by mortar as shown in Fig. 6.13b, without injecting grout. This is because the abutment is going to be completely filled with soil and no particular damage might be expected except further water penetration.

In order to investigate the effect of repair at the locations of these cracks, the SIBIE measurement and analysis were conducted after repair. P-wave velocity was measured at the site and was determined as 4400 m/s. The impact was applied horizontally 50 mm apart from the crack (marked at repair), and elastic waves were detected at locations 50 mm apart in the opposite direction horizontally from the crack. The cross-section analyzed was 50 mm wide and 100 mm deep. This is because the thickness of the abutment is over 300 mm, and we were interested in the depths of surface cracks.

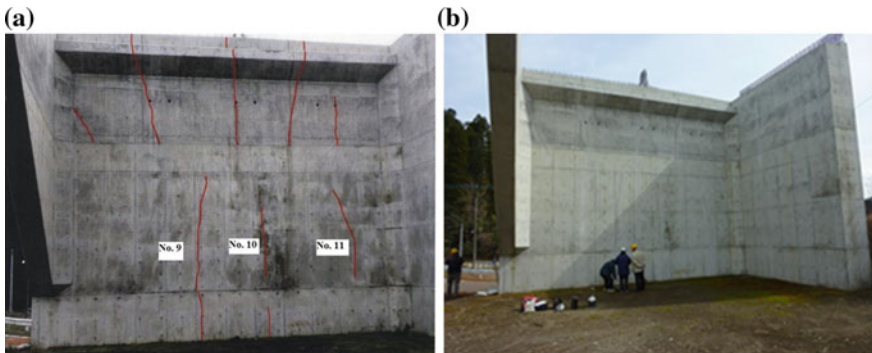


Fig. 6.14 **a** Bridge abutment with surface cracks and **b** a view after repair

Table 6.1 NDT results of the depths of surface cracks

Crack number	Crack depth by UT (mm)	Crack depth by SIBIE (mm): average	Repaired depth by SIBIE (mm)
No. 9	70	76.6	15
No. 10	50	60	5
No. 11	60	90	15–20

(b) Results of SIBIE analysis

In Fig. 6.15a, one crack estimated at No. 9 is illustrated. The reflection intensity at each mesh was graded with 5 colors from high to low. The figure denotes the cross-section of 50 mm width and 100 mm depth with milli-meter unit. Because the crack should exist inside concrete, a solid line is placed, drawing from the high intensity region of the top portion to that of the bottom. From the figure, it is realized that an opening crack is really present. According to the SIBIE analysis, the surface area is coated up to 15 mm depth, and the crack extends to 85 mm depth. In the test, three points along the crack were selected for the measurement. An average depth estimated from the SIBIE analysis was 76.6 mm.

A result at a crack of No. 10 is shown in Fig. 6.15b. It is observed that the depth of surface coating is around 5 mm and the crack extends up to 70 mm. In the case of a crack of No. 11 in Fig. 6.14c, the depth of surface coating is 10 mm and the crack extends up to 90 mm. At these cracks, the tests were also conducted at three locations. All results are summarized in Table 6.1, comparing with results of UT.

Thus, it is confirmed that the SIBIE results are comparable to those of UT. Since the SIBIE results are visually obtained, the technique is practical and no experts are required. In addition to the depth of the surface crack, it is demonstrated that a repaired depth could be estimated.

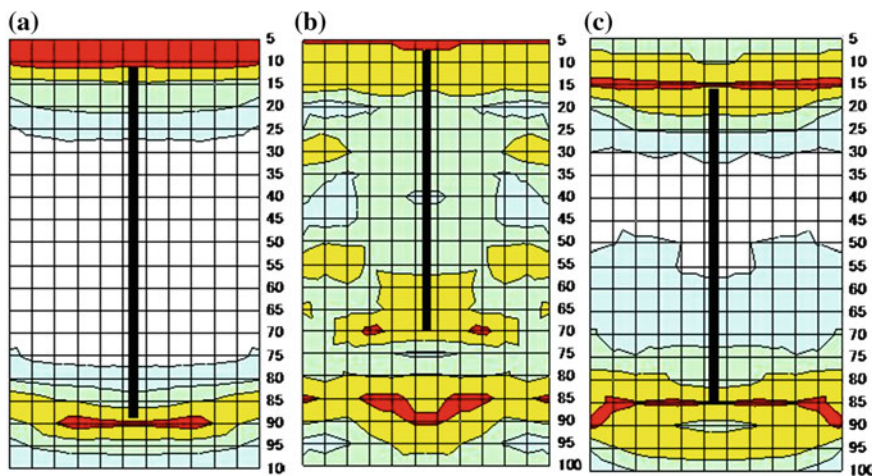


Fig. 6.15 SIBIE results at cracks of Nos. 9 to 11 after repair. **a** SIBIE result at no. 9. **b** SIBIE result at no. 10. **c** SIBIE results at no. 11

6.7 Concluding Remarks

As shown in on-site applications, the SIBIE procedure has been developed as an NDE technique to identify defects at known locations. In the case of PC ducts, locations of the ducts are known in the design documents or could be identified by a radar system. The issue is to discriminate ungrouted ducts and grouted ducts. In the case of the surface crack, the location is known, and we are interested in the depth. So far, detecting defects of unknown depth and unknown location is out of the scope. The technique is developed as given here. Henceforth, the standardization is in progress.

References

1. Ata, N., Mihara, S., Ohtsu, M.: Imaging of ungrouted tendon ducts in prestressed concrete by improved SIBIE. *NDT & E Int.* **40**(3), 258–264 (2007)
2. Alver, N., Ohtsu, M.: BEM analysis of dynamic behavior of concrete in impact-echo test. *Constr. Build. Mater.* **21**(3), 519–526 (2007)
3. Ohtsu, M., Watanabe, T.: Stack imaging of spectral amplitudes based on impact-echo for flaw detection. *NDT & E Int.* **35**, 189–196 (2002)
4. Ohtsu, M., Alver, N.: Development of non-contact SIBIE procedure for identifying ungrouted tendon duct. *NDT & E Int.* **42**(2), 120–127 (2009)
5. Ohtsu, M., Ono, K.: A Generalized Theory of Acoustic Emission and Green's Functions in a Half Space. *J. Acoustic Emission*, **3**(1), 124–133 (1984)
6. Ohtsu, M., Yamada, M., Sonoda, T.: Quantitative evaluation of SIBIE procedure and case studies. *Constr. Build. Mater.* **48**, 1248–1254 (2013)

7. Perkeris, C.L.: The seismic surface pulse. Proc. Natl. Acad. Sci. **41**, 469–480 (1955)
8. Proctor, T.M.: Some details on the NBS conical transducer. J. Acoustic Emission **1**(3), 173–178 (1982)
9. Sansalone, M.J., Streett, W.B.: Impact-echo. NY Bullbrier Press, Ithaca (1997)
10. Sansalone, M.J.: Impact-echo: the complete story. ACI Struct. J. **94**(6), 777–786 (1997)

Chapter 7

3D Visualization of Crack Kinematics by AE-SiGMA

Kentaro Ohno and Masayasu Ohtsu

Abstract Kinematics of crack nucleation is physically associated with acoustic emission (AE) source mechanisms. Mathematically, kinematical information on cracking is represented by the moment tensor. In quantitative AE waveform analysis, one powerful technique for three-dimensional (3D) visualization of AE source has been developed as SiGMA (Simplified Green's functions for Moment tensor Analysis), where crack kinematics of locations, types and orientations of AE source is quantitatively analyzed. Starting with theoretical background and principle, the procedure is explained with a sample code.

Keywords Crack kinematics • Concrete • Sigma

7.1 Introduction

The generalized theory of acoustic emission (AE) has been established on the basis of elastodynamics and the dislocation model for crack motion [2]. Theoretical treatment of crack motion leads to the moment tensor analysis for source kinematics on AE waves. In order to perform the moment tensor analysis, one quantitative technique for AE waveform analysis has been developed as SiGMA (Simplified Green's functions for Moment tensor Analysis) [3]. Crack kinematics on locations, types and orientations are quantitatively determined.

K. Ohno
Tokyo Metropolitan University, Tokyo, Japan
e-mail: ohno@tmu.ac.jp

M. Ohtsu (✉)
Graduate School of Engineering, Kyoto University, Kyoto, Japan
e-mail: ohtsu.masayasu.4v@kyoto-u.ac.jp

7.2 Theoretical Background and Principle

In order to model a crack as an AE source, the discontinuity of the displacements (dislocation), virtual two surfaces F^+ and F^- are considered as shown in Fig. 7.1. Before a crack is nucleated, these two surfaces make a coincident motion. Due to cracking, the discontinuity of displacement $\mathbf{b}(\mathbf{y}, t)$ is nucleated between the two surfaces and denoted by using superscripts + and - on surface F^+ and F^- ,

$$\mathbf{b}_i(\mathbf{y}, t) = \mathbf{u}_i^+(\mathbf{y}, t) - \mathbf{u}_i^-(\mathbf{y}, t). \quad (7.1)$$

Vector $\mathbf{b}(\mathbf{y}, t)$ is called the dislocation and is identical to Burgers vector in crystallography. Introducing Green's functions $G_{ip}(\mathbf{x}, \mathbf{y}, t)$ in elastodynamics, eventually the following basic equation is derived,

$$\mathbf{u}_k(\mathbf{x}, t) = G_{kp,q}(\mathbf{x}, \mathbf{y}, t) * S(t) C_{pqij} n_j l_i \Delta V, \quad (7.2)$$

where vector $\mathbf{u}(\mathbf{x}, t)$ represents the displacement of the elastic wave detected, C_{pqij} are the material constants, \mathbf{l} is the unit direction vector and $S(t)$ is the source-time function of crack motion. ΔV is the crack volume, and \mathbf{n} is the outward normal vector to the crack surface. It is noted that the amplitude of AE wave, $\mathbf{u}(\mathbf{x}, t)$, is explicitly associated with the crack volume, neither simply with the crack area nor with crack opening.

Equation 7.2 contains two vectors \mathbf{l} and \mathbf{n} , and thus moment tensor M_{pq} is introduced for an inverse problem,

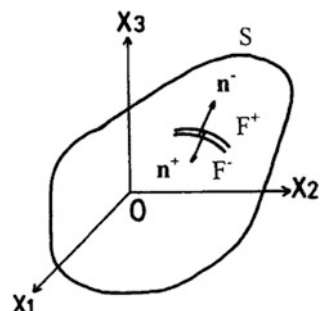
$$M_{pq} = C_{pqkl} l_k n_l \Delta V. \quad (7.3)$$

Now, we have the following equation,

$$\mathbf{u}_k(\mathbf{x}, t) = G_{kp,q}(\mathbf{x}, \mathbf{y}, t) M_{pq} * S(t). \quad (7.4)$$

The moment tensor, M_{pq} , is defined by the product of the elastic constants [N/m^2] and the crack volume [m^3], which leads to the moment of physical unit

Fig. 7.1 Crack (dislocation) surfaces F^+ and F^-



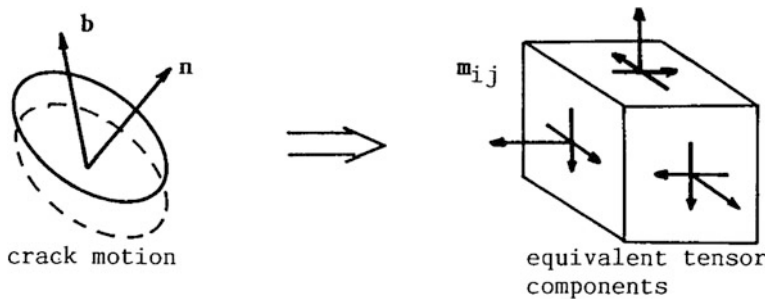


Fig. 7.2 Modeling crack motion by the moment tensor

[Nm]. The moment tensor is a symmetric tensor of the 2nd-order and is comparable to a stress tensor, as shown in Fig. 7.2.

Mathematically, the dipole forces and the double-couple forces in seismic motions correspond to particular components of the tensor. Normal components of the moment tensor are identical to the dipole forces, while couple forces correspond to tangential (shear) components.

7.3 Simplified Procedure

In order to be readily applicable to processing a large amount of AE waves. Based on the far-field term of P wave, a simplified procedure has been developed as a SiGMA (Simplified Green's functions for Moment tensor Analysis) code, which is suitable for a PC-based processor and robust in computation. By taking into account only P wave motion of the far field ($1/R$ term) of Green's function in an infinite space, the displacement $U_i(x, t)$ of P wave motion is obtained from Eq. 7.4 as,

$$U_i(x, t) = -1/(4\pi\rho v_p^3) r_i r_p r_q / R dS(t)/dt M_{pq}. \quad (7.5)$$

Here ρ is the density of the material and v_p is the velocity of P wave. R is the distance between the source y and the observation point x , of which direction cosine is $r = (r_1, r_2, r_3)$. Considering the effect of reflection at the surface and neglecting the source-time function, amplitude $A(x)$ of the first motion is represented,

$$A(x) = C_s \text{Ref}(t, r) / R r_i M_{ij} r_j \quad (7.6)$$

where C_s is the calibration coefficient including material constants. t is the direction of the sensor sensitivity. $\text{Ref}(t, r)$ is the reflection coefficient at the observation location x , which is obtained as,

$$\text{Ref}(\mathbf{t}, \mathbf{r}) = \frac{2k^2 a (k^2 - 2[1 - a^2])}{(k^2 - 2[1 - a^2])^2 + 4a[1 - a^2]\sqrt{k^2 - 1 + a^2}} \quad (7.7)$$

Here \mathbf{t} is the orientation vector of sensor sensitivity and $k = v_p/v_s$ and a is the scalar product of vector \mathbf{r} and vector \mathbf{t} . In the case that P wave is incident vertically to the surface ($a = 1$), $\text{Ref}(\mathbf{t}, \mathbf{r}) = 2$. In the case that the sensors are absolutely calibrated, the coefficients C_s are known. In a general case, relative coefficients are readily obtained by a pencil-lead break test. After the sensors are attached onto a specimen, a test is conducted as illustrated in Fig. 7.3. AE waves are recorded due to a pencil-lead break and then relative coefficients C_s are obtained from,

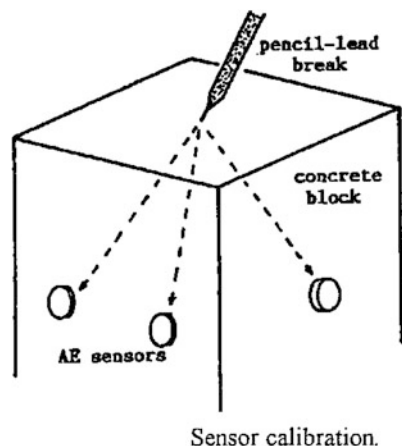
$$C_s = AoR/\text{Ref}(\mathbf{t}, \mathbf{r}) \quad (7.8)$$

Thus, the relative calibration coefficient C_s of equivalent sensitivity is obtained for each sensor. Since absolutely calibrated sensors are seldom available in AE measurement, the moment tensor analysis (SiGMA) to determine the relative tensor components is preferable in practical applications. Since the moment tensor is symmetric, the number of independent unknowns M_{ij} to be solved is six. Thus, multi-channel observation of the first motions at more than six channels is required to determine the moment tensor components.

Displaying AE waveform on CRT screen, two parameters of the arrival time (P1) and the amplitude of the first motion (P2) in Fig. 7.4 are determined. In the location procedure, source location \mathbf{y} is determined from the arrival time differences. AE source (crack) location x' is determined from the arrival time differences t_i between the observation point x_i and x_{i+1} , by solving equations,

$$R_i - R_{i+1} = |x_i - x'| - |x_{i+1} - x'| = v_p t_i \quad (7.9)$$

Fig. 7.3 Experiment for relative sensor calibration



Sensor calibration.

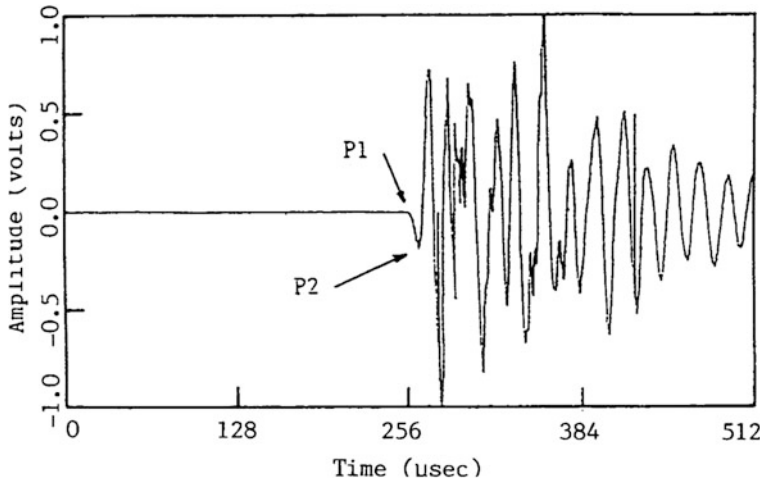


Fig. 7.4 Detected AE wave and two parameters P1 and P2

Then, distance R and its direction vector \mathbf{r} are determined. The amplitudes of the first motions at more than 6 channels are substituted into Eq. 7.6, and the components of the moment tensor M_{ij} are determined.

7.4 First-Motion Detection

Determination of the two parameters of P1 and P2 has been carried out manually via a software package named “wave-monitor”. In order to process a lot of AE waveforms, easy and quick determination of the first motion is in great demand. Focusing on the intervals before and after the onset of seismic signal, autoregressive (AR) techniques has been developed [1]. A direct AIC method is applied to determination of the arrival time for the SiGMA analysis. As the number of amplitudes of a digitized AE wave is N and values of amplitudes are X_i ($i = 1, 2, \dots, N$), AIC_k at point $i = k$ is represented as,

$$AIC_k = k \cdot \log\{\text{var}(X[1, k])\} + (N - k) \cdot \log\{\text{var}(X[k, N])\}, \quad (7.10)$$

where $\text{var}(X[1, k])$ indicate the variance between X_1 and X_k , and $\text{var}(X[k, N])$ is also the variance between X_k and X_N . The AIC method defines the onset point as the global minimum.

The AIC function was applied to AE waveforms detected. One example is shown in Fig. 7.5. A portion of the first motion enlarged is given in Fig. 7.5b. In the case, the arrival time was determined at $k = 251$ manually. In the figure, the minimum value of AIC is observed at $k = 252$. In the automated detection of the

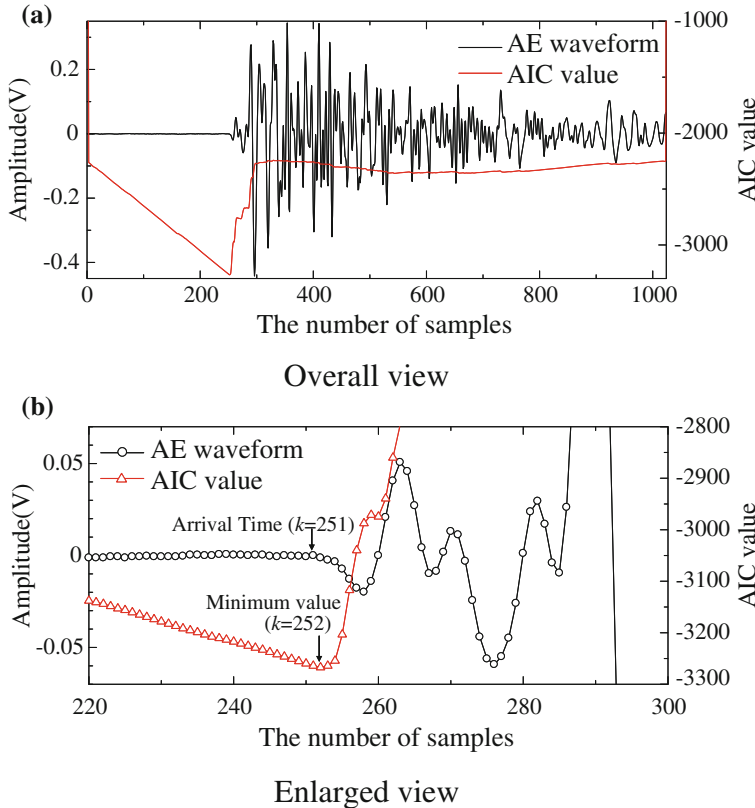


Fig. 7.5 Calculated AIC function for a waveform with high S/N ratio

first motion (auto-picker), this value was adopted. Then, the parameter P1 of arrival time is determined by applying the following equation,

$$P1 = [T_k \{Min(AIC_k)\} - 1] \times \Delta t, \quad (7.11)$$

where $T_k[Min(AIC_k)]$ represents the sampling-time number when AIC_k becomes the minimum value at $i = k$ and Δt is sampling time which is set to $1 \mu s$ in our experiments. As for the determination of the parameter P2, amplitude X_i which satisfies the following condition is adopted, increasing the sampling-time number from k in Eq. 7.9,

$$P2 = X_i, \quad \text{If } \begin{array}{l} X_{i+1} - X_i < 0 \quad \text{when } X_{k+1} > X_k \\ \text{or} \\ X_{i+1} - X_i > 0 \quad \text{when } X_{k+1} < X_k \end{array} \quad (7.12)$$

Where the index i represents the sampling-time number between $k + 1$ and N . A sample program for automatically picking the first arrival and the amplitude of the first motion is listed in Appendix.

7.5 Implementation of SiGMA Code

Since the SiGMA code requires only relative values of the moment tensor components, the relative calibration of the sensors is sufficient enough. A series of algebraic equations on unknown moment-tensor components M_{pq} is derived. The procedure to solve Eq. 7.6 is named SiGMA (Simplified Green's function for Moment tensor Analysis) [3, 4]. It is obtained as,

$$A(\mathbf{x}) = Cs \frac{\text{Re}(\mathbf{t}, \mathbf{r})}{R} (r_1 \quad r_2 \quad r_3) \begin{pmatrix} m_{11} & m_{12} & m_{13} \\ m_{12} & m_{22} & m_{23} \\ m_{13} & m_{23} & m_{33} \end{pmatrix} \begin{pmatrix} r_1 \\ r_2 \\ r_3 \end{pmatrix} \quad (7.13)$$

These components can be determined from the observation of the first motions at more than six sensor locations. To solve Eq. 7.13 the coefficient Cs , the reflection coefficient $\text{Re}(\mathbf{t}, \mathbf{r})$, the distance R , and its direction cosine vector \mathbf{r} are necessary. The coefficients Cs and $\text{Re}(\mathbf{t}, \mathbf{r})$ are obtained from Eqs. 7.7 and 7.8. Other values can be obtained from the source (flaw) location analysis. Thus, the location analysis is essential to perform the moment tensor analysis.

The classification of a crack is performed by the eigenvalue analysis of the moment tensor. From Eq. 7.3, a moment tensor for a pure shear crack is obtained as,

$$M_{pq} = \begin{pmatrix} 0 & 0 & \mu\Delta V \\ 0 & 0 & 0 \\ \mu\Delta V & 0 & 0 \end{pmatrix} \quad (7.14)$$

From the eigenvalue analysis, three eigenvalues are obtained as $\mu\Delta V$, 0, and $-\mu\Delta V$. Setting the ratio of the maximum shear contribution as X , three eigenvalues for the shear crack are represented as X , 0, $-X$. In the case of a pure tensile crack, the moment tensor is represented,

$$M_{pq} = \begin{pmatrix} \lambda\Delta V & 0 & 0 \\ 0 & \lambda\Delta V & 0 \\ 0 & 0 & (\lambda + 2\mu)\Delta V \end{pmatrix} \quad (7.15)$$

Because this is the case where the direction of crack motion is parallel to the coordinate axis, the matrix is already diagonalized, and diagonal components are identical to three eigenvalues: $\lambda\Delta V$, $\lambda\Delta V$, $(\lambda + 2\mu)\Delta V$. In the case of the shear crack, the components of the tensor are deviatoric, as the sum of all components is equal to

zero (non-volumetric). Accordingly, the components in Eq. 7.13 can be decomposed into the deviatoric (non-volumetric) components and the isotropic components as,

$$\begin{pmatrix} \lambda\Delta V \\ \lambda\Delta V \\ (\lambda+2\mu)\Delta V \end{pmatrix} = \begin{pmatrix} -\frac{2\mu\Delta V}{3} \\ -\frac{2\mu\Delta V}{3} \\ \frac{4\mu\Delta V}{3} \end{pmatrix} + \begin{pmatrix} (\lambda + \frac{2\mu}{3})\Delta V \\ (\lambda + \frac{2\mu}{3})\Delta V \\ (\lambda + \frac{2\mu}{3})\Delta V \end{pmatrix} \quad (7.16)$$

Setting the ratio of the maximum deviatoric tensile component as Y and the isotropic tensile as Z, three eigenvalues are denoted as $-Y/2 + Z$, $-Y/2 + Z$ and $Y + Z$. Then, it is assumed that the principal axes of the shear crack are identical to those of the tensile crack. As a result, the eigenvalues of the moment tensor for a general case are represented by the combination of the shear crack and the tensile crack. The following decomposition is obtained as the relative ratios X, Y and Z,

$$\begin{array}{rcl} 1.0 & = & X + Y + Z, \\ \text{the intermediate eigenvalue/the maximum eigenvalue} & = & 0 -Y/2 + Z, \\ \text{the minimum eigenvalue/the maximum eigenvalue} & = & -X -Y/2 + Z, \end{array} \quad (7.17)$$

where X, Y, and Z denote the shear ratio, the deviatoric tensile ratio, and the isotropic tensile ratio, respectively.

These are schematically shown in Fig. 7.6. It should be pointed out that the ratio X becomes larger than 1.0 in the case that both the ratios Y and Z are negative [5]. The case happens only if the scalar product $l_k n_k$ is negative, because the eigenvalues are determined from relative tensor components. Re-correcting the value of the scalar product, the three ratios are determined as well-posed.

In the present SiGMA code, AE sources of which the shear ratios are less than 40 % are classified into tensile cracks. The sources of $X > 60\%$ are classified into shear cracks. In between 40 and 60 %, cracks are referred to as mixed mode. In the eigenvalue analysis, three eigenvectors $\mathbf{e1}$, $\mathbf{e2}$, and $\mathbf{e3}$,

$$\begin{aligned} \mathbf{e1} &= \mathbf{l} + \mathbf{n} \\ \mathbf{e2} &= \mathbf{l} \times \mathbf{n} \\ \mathbf{e3} &= \mathbf{l} - \mathbf{n}, \end{aligned} \quad (7.18)$$

are also determined. Vectors \mathbf{l} and \mathbf{n} , which are interchangeable, are recovered. Thus orientations of crack motion \mathbf{l} and crack plane \mathbf{n} are obtained.

An example of results analyzed by SiGMA is listed in Table 7.1. Location coordinates of the source are given, following moment tensor components. Then, results of the eigenvalue analysis are presented. Since the shear ratio X is lower than

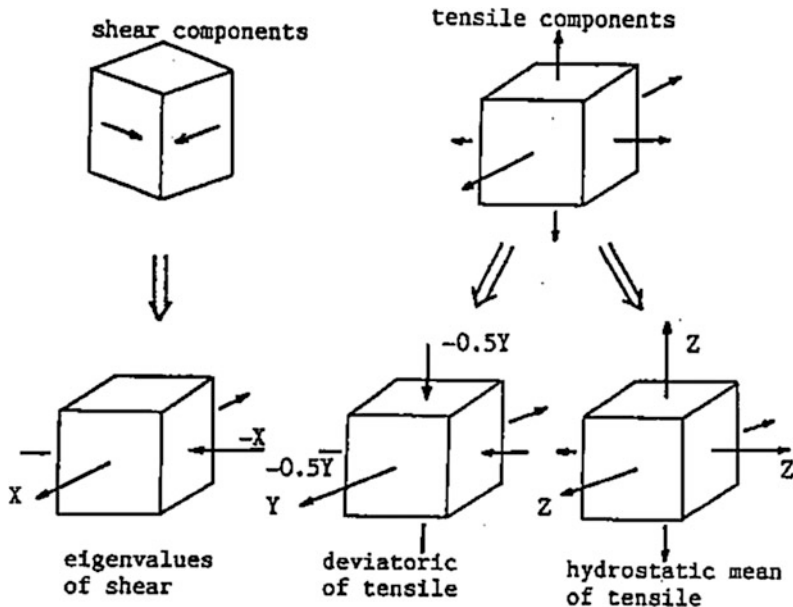


Fig. 7.6 Unified decomposition of eigenvalues of the moment tensor

30 %, the source is classified as a tensile crack. At the bottom, two vectors of crack normal are given. A sample program for SiGMA procedure is given at Appendix, following the determination of the first motions.

7.6 Visualization of SiGMA Results

Numerical results on AE source kinematics are listed in Table 7.1. In order to visualize these data, many graphic software are commercially available. Here, the Light Wave 3D software (New Tek) is applied. Crack models for AE sources are shown in Fig. 7.7. Here, an arrow vector indicates a crack motion vector, and a circular plate corresponds to a crack surface, which is perpendicular to a crack normal vector.

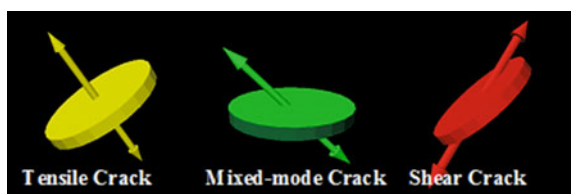
By using these models, crack generation process in a reinforced concrete beam is shown in Fig. 7.8. Shifting from Stage 1 to Stage 3, AE sources coalesce around a final diagonal failure plane. AE sources seem to propagate from the center to the upper and the bottom zones. It is interesting that tensile cracks always proceed to the zones.

Table 7.1 Listed results of SiGMA analysis

[--]	Event Number : 25						
[--]	Moment Tensor Solution						

	-0.4526	-0.1073	0.0543				
	0.1151		0.5543				
		1.0000					

[--]	Source Location Solution						
	X	Y	Z				
	-0.015	-0.029	0.012				
[--]	Eigen Values & Vectors Solution						
		maximum	midiate	minimum			
Eigen Value		1.0000	-0.0865	-0.3905			
Eigen Vector X		-0.0014	0.3308	-0.9437			
Eigen Vector Y		-0.4336	-0.8506	-0.2975			
Eigen Vector Z		-0.9011	0.4088	0.1446			
Composition Ratio of Eigen Value (%)							
Shear :	30.40		CLVD :	52.16		Mean :	17.43
[--]	Crack Motion & Crack Surface Normal Directions						
	X	Y	Z				
Motion	-0.443	-0.522	-0.729				
Normal	0.440	-0.244	-0.864				

Fig. 7.7 Crack models for AE sources

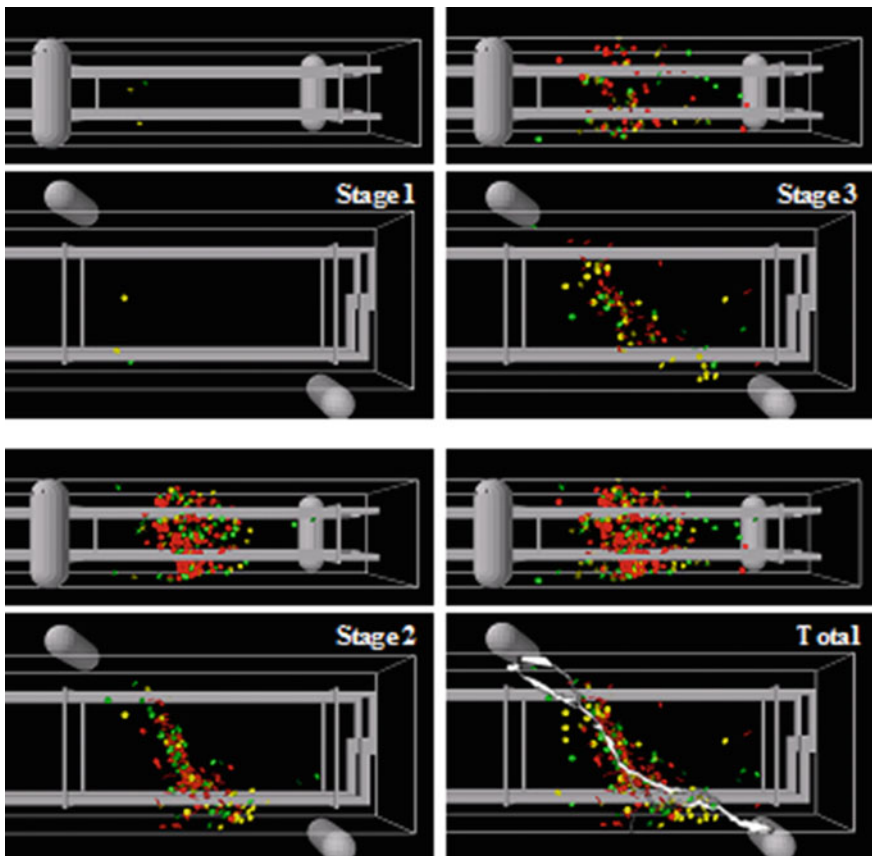


Fig. 7.8 SiGMA results visualized

7.7 Concluding Remarks

By applying the sample code in the appendix, kinematics of AE sources are obtained on source location, source (crack) type and crack motion vectors including the crack normal to the crack plane. To perform the analysis, multi-channel AE system more than 6 channels is necessary. In addition, waveforms of all the channels are to be recorded digitally. In the case, all arrivals of the first motions are simultaneously to be recorded with the aid of proper threshold. It is often encountered that the noise level is too high for the first motion to be properly detected, and sometimes so high as to be smeared. Although the location procedure is usually conducted by triggering at the threshold, the arrival times of all the waveforms are to be derived. Following the arrival times of the first motions, the amplitudes of the first motions not the peak amplitudes are to be recorded to solve the moment tensor.

Appendix: Sample Program of SiGMA

```

C ****
C          6CH-AutoSiGMA Analysis Program Code
C          made by Dr. Kentaro OHNO
C          Tokyo Metropolitan Univ., 2009/12/12
C ..... Input Data .....
C The number of channels: MAXCH and NCH
C The difference of detection time:ST
C Wave data:WA
C Variance of wave data:V
C The difference of variance:AC
C Rank of algebraic equation for source location:NRANK
C The number of moment tensor elements: NMTS
C Coordinates of sensors (x,y,z) in unit [m]: TDX(I),TDY(I),TDZ(I)
C Arrival time: ATM(I)
C Amplitude of the first motion: AMP(I)
C Outward normal of sensor orientation(Nx,Ny,Nz):BNX(I),BNY(I),BNZ(I)
C Velocity of P wave in unit [m/s]: VP
C Poisson's ratio : PO
C ****
PARAMETER(MAXCH=6,NUM=1024,NRANK=3,NCH=6,NMTS=6)
DOUBLE PRECISION ST(NCH)
DOUBLE PRECISION SEC(MAXCH*NUM,NCH),WA(MAXCH*NUM,NCH)
DOUBLE PRECISION WA1(MAXCH*NUM,NCH),AVR 1(MAXCH*NUM,NCH)
DOUBLE PRECISION WW1(MAXCH*NUM,NCH)
DOUBLE PRECISION WA2(MAXCH*NUM,NCH),AVR2(MAXCH*NUM,NCH)
DOUBLE PRECISION WW2(MAXCH*NUM,NCH)
DOUBLE PRECISION AC(MAXCH*NUM,NCH),AMIN(NCH),JMIN(NCH)
DOUBLE PRECISION ALPHA(1:N RANK,1:NRANK+1),ESTIM(1:NRANK)
DOUBLE PRECISION BEHTA(1:NRANK,1:NRANK+1),SIGMA(1:NRANK)
DOUBLE PRECISION MTALP(1:NMTS,1:NMTS+1),MTBHT(1:NMTS,1:NMTS+1)
DOUBLE PRECISION MTEST(1:NMTS),MTSGM(1:NMTS)
DOUBLE PRECISION STSEC(6),STMIN,DW(6),WD(6),JAMP(6)
DOUBLE PRECISION RAI(0:MAXCH-1),LAI(0:MAXCH-1)
DOUBLE PRECISION MAI(0:MAXCH-1),NAI(0:MAXCH-1)
DOUBLE PRECISION XA,YA,ZA,SOURCEX,SOURCEY,SOURCEZ
REAL V1(MAXCH*NUM,NCH),V2(MAXCH*NUM,NCH)
REAL MTMAT(1:NRANK,1:NRANK),MEMAT(1:NRANK,1:NRANK)
REAL EIMAT(1:NRANK,1:NRANK)
REAL EQUAT(1:MAXCH,1:NRANK+1),TRANS(1:NRANK,1:MAXCH)
REAL ATM(1:MAXCH)
REAL TDX(1:MAXCH),TDY(1:MAXCH),TDZ(1:MAXCH)
REAL T(0:MAXCH-1),A(0:MAXCH-1),B(0:MAXCH-1),C(0:MAXCH-1)
REAL AIJ(1:MAXCH-2),BIJ(1:MAXCH-2),CIJ(1:MAXCH-2)
REAL DIJ(1:MAXCH-2),EIJ(1:MAXCH-2)
REAL VP,TMIN,AJI
REAL MTEQT(1:MAXCH,1:NMTS+1),MTTRS(1:NMTS,1:MAXCH),AMP(1:MAXCH)
REAL BNX(6),BNY(6),BNZ(6),STX(6),STY(6),STZ(6),MEAN
REAL CCC(6),MTS(6),RT(6),MTSMAX
REAL EVALU(3),EVCTR(3,3),SSS(6),COEF(6)
REAL EN1,ENX1,ENY1,ENZ1,EN2,ENX2,ENY2,ENZ2,FAY,THETA,THE1
INTEGER H,I,II,J,K,L,P,Q,R,S,IMIN,F1,F2,ID(6),SENSOR(6)
CHARACTER INPUT*20,OUTFILE*20,SUMOUT*20, MODE*10
CHARACTER CHK*3,OK*2,CHA*1,CHB*1,CHC*1,CHD*1,CHE*1
C

```

```

C =====
C
C           AUTO READING
C           (ARRIVAL TIME AND THE AMPLITUDE OF THE FIRST MOTION)
C
C =====
C =====
C           DATA INPUT
C =====
C
OPEN(UNIT=3,FILE='SENSORARRAY.TXT')
READ(3,*) (ID(I),TDX(I),TDY(I),TDZ(I),I=1,NCH)
READ(3,*) (ID(I),BNX(I),BNY(I),BNZ(I),I=1,NCH)
READ(3,*) VP
C
SUMOUT='SUMMARYOUT.TXT'
OPEN(UNIT=8,FILE=SUMOUT)
WRITE(8,5000)
5000 FORMAT('-- AE SENSOR COORDINATE --')
WRITE(8,5001)
5001 FORMAT('CH',3X,' TDX ',2X,' TDY ',2X,' TDZ ')
WRITE(8,5002)(ID(I),TDX(I),TDY(I),TDZ(I),I=1,NCH)
5002 FORMAT(I1,1X,F6.3,1X,F6.3,1X,F6.3)
WRITE(8,5003)
5003 FORMAT('-- AE SENSOR NORMAL VECTOR --')
WRITE(8,5004)
5004 FORMAT('CH',3X,' BNX ',2X,' BNY ',2X,' BNZ ')
WRITE(8,5005)(ID(I),BNX(I),BNY(I),BNZ(I),I=1,NCH)
5005 FORMAT(I1,1X,F6.3,1X,F6.3,1X,F6.3)
WRITE(8,5006)VP
5006 FORMAT('VP=',F6.1)
WRITE(8,5007)
5007 FORMAT(3X,'No.',3X,'Time(s)',3X,'x',3X,'y',3X,'z',3X,'Ratio',3X,
'/MODE',3X,'THETA1',1X,'FAY1',2X,'THETA2',1X,'FAY2')
C
WRITE(*,*) 'WHAT IS YOUR FILE RANGE?'
READ(*,*) F1,F2
DO 4000 II=F1,F2
WRITE(*,*) II,'/',F2
C
L=II/10000
P=(II-L*10000)/1000
Q=(II-L*10000-P*1000)/100
R=(II-L*10000-P*1000-Q*100)/10
S=II-L*10000-P*1000-Q*100-R*10
C
CALLITOC(L,CHA)
CALLITOC(P,CHB)
CALLITOC(Q,CHC)
CALLITOC(R,CHD)
CALLITOC(S,CHE)
C
IF (II.GE.10000) THEN
INPUT='sample_//CHA//CHB//CHC//CHD//CHE//'.TXT'
ELSE IF ((II.LT.10000).AND.(II.GE.1000)) THEN
INPUT='sample_//CHB//CHC//CHD//CHE//'.TXT'
ELSE IF ((II.LT.1000).AND.(II.GE.100)) THEN

```

```

INPUT='sample_//CHC//CHD//CHE//.TXT'
ELSE IF ((I1.LT.100).AND.(I1.GE.10)) THEN
INPUT='sample_//CHD//CHE//.TXT'
ELSE
INPUT='sample_//CHE//.TXT'
END IF

C
OPEN(UNIT=4,FILE=INPUT)
C
DT=0.000001
DO 10 I=1,NCH
  READ(4,*)SENSOR(I),ST(I)
10 CONTINUE
C
STMIN=1.0E10
DO 11 I=1,NCH
  IF(ST(I).LE.STMIN) THEN
    STMIN=ST(I)
  END IF
11 CONTINUE
DO 12 I=1,NCH
  STSEC(I)=ST(I)-STMIN
12 CONTINUE
DO 13 I=1,NCH
  DO 14 J=1,NUM
    READ(4,*) WA(J,I)
14 CONTINUE
13 CONTINUE
DO 15 I=1,NCH
  SEC(1,I)=-2.56E-04+STSEC(I)
15 CONTINUE
DO 20 I=1,NCH
  DO 21 J=2,NUM
    SEC(J,I)=SEC(J-1,I)+DT
21 CONTINUE
20 CONTINUE
C
C.....VARIANCE CALCULATION
C
DO 30 I=1,NCH
  DO 31 J=1,512
    NUMBER=NUMBER + 1.
    WA1(J,I)=WA1(J-1,I)+WA(J,I)
    AVR1(J,I)=REAL(WA1(J,I))/J
    WW1(J,I)=WW1(J-1,I)+(WA(J,I))**2
    V1(J,I)=REAL(WW1(J,I))/J-(AVR1(J,I))**2
31 CONTINUE
30 CONTINUE
  DO 40 I=1,NCH
    DO 41 J=0,511
      WA2(512-J,I)=WA2(512-J+1,I)+WA(512-J,I)
      AVR2(512-J,I)=REAL(WA2(512-J,I))/(J+1)
      WW2(512-J,I)=WW2(512-J+1,I)+WA(512-J,I)**2
      V2(512-J,I)=REAL(WW2(512-J,I))/(J+1)-(AVR2(512-J,I))**2
41 CONTINUE
40 CONTINUE
C

```

```

C.....AC CALCULATION FOR ARRIVAL TIME
C
  DO 50 I=1,NCH
    DO 51 J=1,25
      AC(J,I)=0.
  51 CONTINUE
  50 CONTINUE
    DO 60 I=1,NCH
      DO 61 J=21,512
        AC(J,I)=J*ALOG10(V1(J,I))+(512-J)* ALOG10(V2(J,I))
  61 CONTINUE
  60 CONTINUE
    DO 62 I=1,NCH
      DO 63 J=315,NUM
        AC(J,I)=0.
  63 CONTINUE
  62 CONTINUE
    DO 64 I=1,NCH
      AMIN(I)=1.0E10
      DO 65 J=25,315
        IF(AC(J,I).LE.AMIN(I)) THEN
          AMIN(I)=AC(J,I)
          JMIN(I)=J-1
        END IF
  65 CONTINUE
  64 CONTINUE
C
  DO 27 I=1,NCH
    ATM(I)=SEC(JMIN(I),I)
  27 CONTINUE
C
C..... AMPLITUDE OF THE FIRST MOTION
C
  DO 80 I=1,NCH
    DO 81 J=JMIN(I),NUM
      IF(WA(J+1,I).GT.WA(J,I)) THEN
        DW(I)=WA(J+2,I)-WA(J+1,I)
        IF(DW(I).LE.0.0) THEN
          JAMP(I)=J+1
          GOTO 84
        END IF
      ELSE IF (WA(J+1,I).LT.WA(J,I)) THEN
        WD(I)=WA(J+2,I)-WA(J+1,I)
        IF(WD(I).GE.0.0) THEN
          JAMP(I)=J+1
          GOTO 84
        END IF
      END IF
  81 CONTINUE
  84 AMP(I)=WA(JAMP(I),I)
  80 CONTINUE
  34 FORMAT(8E14.5)
  CLOSE(4)
C
C =====
C           SiGMA PROCEDURE

```

```

C
C =====
C
C      MATERIAL DATA
C =====
C
C      PO=0.2
C =====
C      OUTPUT FILE
C =====
C
C      IF (II.GE.1000) THEN
C      OUTFILE=CHA//CHB//CHC//CHD//'.OUT'
C      ELSE IF ((II.LT.1000).AND.(II.GE.100)) THEN
C      OUTFILE=CHB//CHC//CHD//'.OUT'
C      ELSE IF ((II.LT.100).AND.(II.GE.10)) THEN
C      OUTFILE=CHC//CHD//'.OUT'
C      ELSE
C      OUTFILE=CHD//'.OUT'
C      END IF
C
C      ****
C      *      3-D SOURCE LOCATION      *
C      ****
C
C..... THE NEAREST TRANSDUCER CH. FROM AE SOURCE
C
C      TMIN=1.0E10
C      DO 200 I=1,NCH
C      IF (ATM(I).LE.TMIN) THEN
C          TMIN=ATM(I)
C          IMIN=I
C      END IF
C      200 CONTINUE
C
C..... RELATIVE POSITIONS OF TRANSDUCERS, ARRIVAL TIME OF P-WAVE
C
C      CHK='ON'
C      J=0
C      DO 215 I=1,NCH
C      IF (I.NE.IMIN) THEN
C          J=J+1
C          T(J)=ATM(I)-ATM(IMIN)
C          A(J)=TDX(I)-TDX(IMIN)
C          B(J)=TDY(I)-TDY(IMIN)
C          C(J)=TDZ(I)-TDZ(IMIN)
C      ELSE
C          T(0)=ATM(I)-ATM(IMIN)
C          A(0)=TDX(I)-TDX(IMIN)
C          B(0)=TDY(I)-TDY(IMIN)
C          C(0)=TDZ(I)-TDZ(IMIN)
C      END IF
C      215 CONTINUE
C
C..... INITIAL SOURCE LOCATION BY LEAST SQUARE METHOD
C

```

```

DO 300 I=1,NCH-2
J=+1
AIJ(I)=2.* (A(I)*T(J)-A(J)*T(I))
BIJ(I)=2.* (B(I)*T(J)-B(J)*T(I))
CIJ(I)=2.* (C(I)*T(J)-C(J)*T(I))
DIJ(I)=T(I)*T(J)*(T(I)-T(J))
EIJ(I)=T(J)*(A(I)**2.+B(I)**2.+C(I)**2.)
>           -T(I)*(A(J)**2.+B(J)**2.+C(J)**2.)
300 CONTINUE
C
DO 410 I=1,3
DO 400 J=1,4
ALPHA(I,J)=0.
BEHTA(I,J)=0.
400   CONTINUE
ESTIM(I)=0.
SIGMA(I)=0.
410 CONTINUE
C
DO 420 I=1,NCH-2
EQUAT(I,1)=AIJ(I)
EQUAT(I,2)=BIJ(I)
EQUAT(I,3)=CIJ(I)
EQUAT(I,4)=EIJ(I)-DIJ(I)*(VP**2)
TRANS(1,I)=AIJ(I)
TRANS(2,I)=BIJ(I)
TRANS(3,I)=CIJ(I)
420 CONTINUE
C
DO 540 I=1,4
DO 530 J=1,3
AJI=0.
DO 520 K=1,NCH-2
AJI=TRANS(J,K)*EQUAT(K,I)+AJI
520   CONTINUE
ALPHA(J,I)=DBLE(AJI)
530   CONTINUE
540 CONTINUE
C -----
CALL SIMEQ3(ALPHA,BEHTA,ESTIM,SIGMA,NRANK,OK,CHK)
C -----
IF (OK.EQ.'NO') GO TO 9000
XA=SNGL(ALPHA(1,4))
YA=SNGL(ALPHA(2,4))
ZA=SNGL(ALPHA(3,4))
C..... TAYLOR'S DEVELOPMENT SOURCE LOCATION BY LEAST SQUARE METHOD
C
H=0
600 H=H+1
DO 605 I=0,NCH-1
RAI(I)=SQRT((XA-A(I))**2.+(YA-B(I))**2.+(ZA-C(I))**2.)
LAI(I)=(XA-A(I))/RAI(I)
MAI(I)=(YA-B(I))/RAI(I)
NAI(I)=(ZA-C(I))/RAI(I)
605   CONTINUE
C

```

```

DO 660 I=1,3
  DO 650 J=1,4
    ALPHA(I,J)=0.
    BEHTA(I,J)=0.
650    CONTINUE
    ESTIM(I)=0.
    SIGMA(I)=0.
660    CONTINUE
C
  DO 670 I=1,NCH-1
    EQUAT(I,1)=LAI(I)-LAI(0)
    EQUAT(I,2)=MAI(I)-MAI(0)
    EQUAT(I,3)=NAI(I)-NAI(0)
    EQUAT(I,4)=VP*T(I)-RAI(I)+RAI(0)
    TRANS(1,I)=LAI(I)-LAI(0)
    TRANS(2,I)=MAI(I)-MAI(0)
    TRANS(3,I)=NAI(I)-NAI(0)
670    CONTINUE
C
  DO 940 I=1,4
    DO 930 J=1,3
      AJI=0.
      DO 920 K=1,NCH-1
        AJI=TRANS(J,K)*EQUAT(K,I)+AJI
920      CONTINUE
        ALPHA(J,I)=DBLE(AJI)
930      CONTINUE
940    CONTINUE
C
-----  

C      CALL SIMEQ3(ALPHA,BEHTA,ESTIM,SIGMA,NRANK,OK,CHK)
C
-----  

C      IF (OK.EQ.'NO') GO TO 965
XA=XAXA+SNGL(ALPHA(1,4))
YA=YA+SNGL(ALPHA(2,4))
ZA=ZA+SNGL(ALPHA(3,4))
C
IF (DABS(ALPHA(1,4)).LE.1.0D-6) THEN
  IF (DABS(ALPHA(2,4)).LE.1.0D-6) THEN
    IF (DABS(ALPHA(3,4)).LE.1.0D-6) THEN
      GO TO 965
    END IF
  END IF
END IF
IF (H.LT.101) GO TO 600
C
965 CONTINUE
  SOURCEX=XA+TDX(IMIN)
  SOURCEY=YA+TDY(IMIN)
  SOURCEZ=ZA+TDZ(IMIN)
C
*****  

C      * 3-D MOMENT TENSOR SOLUTION      *
*****  

C
C..... ELEMENTS OF MOMENT TENSOR
C
  VPS=SQRT(2.*(1.-PO)/(1.-2.*PO))

```

```

DO 999 I=1,NCH
  RT(I)=SQRT((TDX(I)-SOURCEX)**2+(TDY(I)-SOURCEY)**2
  1+(TDZ(I)-SOURCEZ)**2)
    STX(I)=(TDX(I)-SOURCEX)/RT(I)
    STY(I)=(TDY(I)-SOURCEY)/RT(I)
    STZ(I)=(TDZ(I)-SOURCEZ)/RT(I)
999 CONTINUE
DO 1000 I=1,NCH
  CCC(I)=STX(I)*BNX(I)+STY(I)*BNY(I)+STZ(I)*BNZ(I)
  SSS(I)=SQRT(1.-CCC(I)**2)
  COEF(I)=(2.*VPS**2*CCC(I)*(VPS**2-2.*SSS(I)**2))/(
  1.((VPS**2-2.*SSS(I)**2)**2
  2.+4.*SSS(I)**2*CCC(I)*SQRT(VPS**2-SSS(I)**2)))
1000 CONTINUE
C
C..... MOMENT TENSOR SOLUTION BY LEAST SQUARE METHOD
C
DO 1110 I=1,6
  DO 1100 J=1,7
    MTALP(I,J)=0.
    MTBHT(I,J)=0.
1100 CONTINUE
  MTEST(I)=0.
  MTSGM(I)=0.
1110 CONTINUE
C
DO 1120 I=1,NCH
  MTEQT(I,1)=   STX(I)*STX(I)
  MTEQT(I,2)=2.*STX(I)*STY(I)
  MTEQT(I,3)=2.*STX(I)*STZ(I)
  MTEQT(I,4)=   STY(I)*STY(I)
  MTEQT(I,5)=2.*STY(I)*STZ(I)
  MTEQT(I,6)=   STZ(I)*STZ(I)
  MTEQT(I,7)=RT(I)*AMP(I)/COEF(I)
  MTTRS(1,I)=   STX(I)*STX(I)
  MTTRS(2,I)=2.*STX(I)*STY(I)
  MTTRS(3,I)=2.*STX(I)*STZ(I)
  MTTRS(4,I)=   STY(I)*STY(I)
  MTTRS(5,I)=2.*STY(I)*STZ(I)
  MTTRS(6,I)=   STZ(I)*STZ(I)
1120 CONTINUE
C
DO 1185 I=1,7
  DO 1180 J=1,6
    AJI=0.
    DO 1175 K=1,NCH
      AJI=MTTRS(J,K)*MTEQT(K,I)+AJI
1175 CONTINUE
    MTALP(J,I)=AJI
1180 CONTINUE
1185 CONTINUE
  OK='OK'
  CHK='ON'
C -----
----- CALL SIMEQ3(MTALP,MTBHT,MTEST,MTSGM,NMTS,OK,CHK)
C -----

```

```

IF(OK.EQ.'NO') GO TO 9000
C
DO 1190 I=1,NMTS
MTS(I)=MTALP(I,7)*1.0E10
1190 CONTINUE
C
C..... NORMALIZATION OF MOMENT TENSOR ELEMENTS
C
MTSMAX=MTS(1)
DO 1200 I=1,6
IF (ABS(MTSMAX).LT.ABS(MTS(I))) THEN
MTSMAX=MTS(I)
END IF
1200 CONTINUE
DO 1205 I=1,6
MTS(I)=MTS(I)/MTSMAX
1205 CONTINUE
C
C ****
C * EIGEN VALUE & VECTOR ANALYSIS *
C ****
C
C..... EIGEN VALUES & VECTORS BY JACOBI'S METHOD
C
EA=0.0000001
N=3
DO 2000 I=0,N
DO 1995 J=1,N
MTMAT(I,J)=0.
IF(I.EQ.0) GO TO 1995
MEMAT(I,J)=0.
EIMAT(I,J)=0.
1995 CONTINUE
2000 CONTINUE
C
MTMAT(1,1)=MTS(1)
MTMAT(1,2)=MTS(2)
MTMAT(1,3)=MTS(3)
MTMAT(2,1)=MTS(2)
MTMAT(2,2)=MTS(4)
MTMAT(2,3)=MTS(5)
MTMAT(3,1)=MTS(3)
MTMAT(3,2)=MTS(5)
MTMAT(3,3)=MTS(6)
C
MEMAT(1,1)=MTS(1)
MEMAT(1,2)=MTS(2)
MEMAT(1,3)=MTS(3)
MEMAT(2,1)=MTS(2)
MEMAT(2,2)=MTS(4)
MEMAT(2,3)=MTS(5)
MEMAT(3,1)=MTS(3)
MEMAT(3,2)=MTS(5)
MEMAT(3,3)=MTS(6)
C
-----
CALL JACOBI(MEMAT,EIMAT,N,EA)

```

```

C -----
C
DO 2095 K=1,N
MTMAT(0,K)=0.
DO 2090 I=1,N
  W=MEMAT(K,K)*EIMAT(I,K)
  DO 2085 J=1,N
    W=W-MTMAT(I,J)*EIMAT(J,K)
2085   CONTINUE
    MTMAT(0,K)=MTMAT(0,K)+W*W
2090   CONTINUE
2095 CONTINUE
C
DO 2117 I=1,3
  EVALU(I)=MEMAT(I,I)
  DO 2116 J=1,3
    EVCTR(I,J)=EIMAT(I,J)
2116   CONTINUE
2117 CONTINUE
C
IF (EVALU(1).LT.0.) THEN
  EVALU(1)=EVALU(1)*(-1.)
  EVALU(2)=EVALU(2)*(-1.)
  EVALU(3)=EVALU(3)*(-1.)
END IF
C
C..... PRINT OUT EIGEN VALUES & VECTORS
C
DO 2166 I=2,3
  EVALU(I)=EVALU(I)/EVALU(1)
2166 CONTINUE
  EVALU(1)=EVALU(1)/EVALU(1)
  DO 2169 I=1,3
    IF(EVALU(I).LT.-1.0) EVALU(I)=-1.0
2169 CONTINUE
C
C..... DECOMPOSITION OF EIGEN VALUE & PRINT OUT
C
MEAN=(1./3.)*(EVALU(1)+EVALU(3)+EVALU(2))
CLVD=2.*(MEAN-EVALU(2))
IF(CLVD.LT.0.) CLVD=0.
SHER=EVALU(1)-CLVD-MEAN
IF(SHER.LT.0.) SHER=0.
TOTAL=SHER+CLVD+MEAN
SHER=SHER/TOTAL
CLVD=CLVD/TOTAL
MEAN=MEAN/TOTAL
TENS=CLVD+MEAN
C
C..... CRACK TYPE DECISION & PRINT OUT
C
C.....[ Case of Tensile Motion ]
PI=3.1416
IF (TENS.GE.0.60) THEN
  ENX1=EVCTR(1,1)+EVCTR(1,3)
  ENY1=EVCTR(2,1)+EVCTR(2,3)
  ENZ1=EVCTR(3,1)+EVCTR(3,3)

```

```

EN1=SQRT(ENX1**2+ENY1**2+ENZ1**2)
FAY=ACOS(ENZ1/EN1)/PI*180.
SINF=SIN(ACOS(ENZ1/EN1))
THE1=(ENY1/EN1)/SINF
THETA=ASIN(THE1)/PI*180.
WRITE(8,5008) II,ST(1),SOURCEX,SOURCEY,SOURCEZ,SHER*100.,
/THETA,FAY
5008 FORMAT(1X,I4,4X,F13.7,4X,F7.3,4X,F7.3,4X,F7.3,5X,F5.2,3X,
/TENSILE',3X,F7.2,3X,F7.2)
END IF
C
C.....[ Case of Shear Motion ]
C
IF(SHER.LE.0.4) GO TO 9000
IF (TENS.LE.0.40) THEN
ENX1=EVCTR(1,1)+EVCTR(1,3)
ENY1=EVCTR(2,1)+EVCTR(2,3)
ENZ1=EVCTR(3,1)+EVCTR(3,3)
ENX2=EVCTR(1,1)-EVCTR(1,3)
ENY2=EVCTR(2,1)-EVCTR(2,3)
ENZ2=EVCTR(3,1)-EVCTR(3,3)
EN1=SQRT(ENX1**2+ENY1**2+ENZ1**2)
EN2=SQRT(ENX2**2+ENY2**2+ENZ2**2)
FAY1=ACOS(ENZ1/EN1)/PI*180.
SINF1=SIN(ACOS(ENZ1/EN1))
THE1=(ENY1/EN1)/SINF1
THETA1=ASIN(THE1)/PI*180.
FAY2=ACOS(ENZ2/EN2)/PI*180.
SINF2=SIN(ACOS(ENZ2/EN2))
THE2=(ENY2/EN2)/SINF2
THETA2=ASIN(THE2)/PI*180.
WRITE(8,5009) II,ST(1),SOURCEX,SOURCEY,SOURCEZ,SHER*100.,
/THETA1,FAY1,THETA2,FAY2
5009 FORMAT(1X,I4,4X,F13.7,4X,F7.3,4X,F7.3,4X,F7.3,5X,F5.2,3X,
/SHEAR',3X,F7.2,3X,F7.2,3X,F7.2)
END IF
C
C.....[ Case of Mixed Motion ]
C
IF ((TENS.LT.0.60).AND.(TENS.GT.0.40)) THEN
ENX1=EVCTR(1,1)+EVCTR(1,3)
ENY1=EVCTR(2,1)+EVCTR(2,3)
ENZ1=EVCTR(3,1)+EVCTR(3,3)
ENX2=EVCTR(1,1)+EVCTR(1,3)
ENY2=EVCTR(2,1)-EVCTR(2,3)
ENZ2=EVCTR(3,1)-EVCTR(3,3)
EN1=SQRT(ENX1**2+ENY1**2+ENZ1**2)
EN2=SQRT(ENX2**2+ENY2**2+ENZ2**2)
FAY1=ACOS(ENZ1/EN1)/PI*180.
SINF1=SIN(ACOS(ENZ1/EN1))
THE1=(ENY1/EN1)/SINF1
THETA1=ASIN(THE1)/PI*180.
FAY2=ACOS(ENZ2/EN2)/PI*180.
SINF2=SIN(ACOS(ENZ2/EN2))
THE2=(ENY2/EN2)/SINF2
THETA2=ASIN(THE2)/PI*180.
WRITE(8,5010) II,ST(1),SOURCEX,SOURCEY,SOURCEZ,SHER*100.,

```

```

/THTA1,FAY1,THTA2,FAY2
5010 FORMAT(1X,I4,4X,F13.7,4X,F7.3,4X,F7.3,4X,F7.3,5X,F5.2,3X,
  /'MIXED-MODE',3X,
  /F7.2,3X,F7.2,3X,F7.2,3X,F7.2)
  END IF
C
C.....C
9000 CONTINUE
C      CLOSE(7)
4000 CONTINUE
      CLOSE(8)
      STOP
      END
C =====
C           Subroutines ITOC
C =====
C
SUBROUTINE ITOC(N,IC)
CHARACTER IC(*)*
C
M=N
L=LEN(IC)
DO 10 I=1,L
IC(I:I)='0'
10 CONTINUE
C
K=1
1   M=M/100
IF(M.LE.0) GO TO 2
K=K+1
GO TO 1
2 CONTINUE
C
M=N
DO 20 I=1,K
ID=10** (K-I)
IN=M/ID
M=MOD(M,ID)
IC(L-K+I:L-K+1)=CHAR(IN+48)
20 CONTINUE
C
RETURN
END
C =====
C           Subroutines Simultaneous Equations for The Least Square Method
C =====
C
C..... SUBROUTINE SIMULTANEOUS EQUATION FOR 'N' RANK MATRIX
C           * sweep out method, full pivot *
C
SUBROUTINE SIMEQ3(A,B,E,S,N,OK,CHK)
DOUBLE PRECISION A(N,N+1),B(N,N+1),E(N),S(N)
CHARACTER OK*2,CHK*3
C
DO 10 I=1,N
DO 5 J=1,N+1
B(I,J)=A(I,J)

```

```

      5   CONTINUE
10  CONTINUE
C
C     IF (CHK.EQ.'ON ') THEN
C       WRITE(6,25)
C       25  FORMAT(1H0,'== Sweep Out Method, Full Pivot Selection ==/')
C         >           * simultaneous equations matrix [ ALPHA ] *)
DO 45 I=1,N
C           WRITE(6,30) I,A(I,1),A(I,2),A(I,3)
C       30  FORMAT(1H ,I2,5X,E15.3,2X,E15.3,2X,E15.3)
45  CONTINUE
END IF
C
C     IF (N.LT.1) THEN
D=0.
C       WRITE(6,50)
C       50  FORMAT(1H ,6X,'>> This problem can not be done in '
C         >           , 'Determine simultaneous equation matrix. <<<')
C         OK='NO'
C         GO TO 230
END IF
C
C     IF (N.EQ.1) THEN
D=A(1,1)
IF (D.EQ.0.) THEN
C       WRITE(6,50)
C         OK='NO'
C         GO TO 230
END IF
DO 55 J=1,N+1
  A(1,J)=A(1,J)/D
55  CONTINUE
GO TO 170
END IF
C
D=1.
DO 150 J=1,N
  KM=J
  LM=J
  AM=ABS(A(J,J))
  DO 70 K=J+1,N
    DO 60 L=J+1,N
      AX=ABS(A(K,L))
      IF (AX.GT.AM) THEN
        KM=K
        LM=L
        AM=AX
      END IF
60    CONTINUE
70    CONTINUE
    IF (AM.EQ.0.) THEN
      D=0.
C       WRITE(6,50)
C         OK='NO'
C         GO TO 230
    END IF
C

```

```

IF (KM.EQ.J) GO TO 90
DO 80 K=J,N+1
  AX=A(J,K)
  A(J,K)=A(KM,K)
  A(KM,K)=AX
80  CONTINUE
D=-D
90  IF (LM.EQ.J) GO TO 110
DO 100 K=1,N
  AX=A(K,J)
  A(K,J)=A(K,LM)
  A(K,LM)=AX
100 CONTINUE
D=D
110 AX=A(J,J)
D=AX*D
A(J,J)=LM
DO 120 K=J+1,N+1
  A(J,K)=A(J,K)/AX
120 CONTINUE
DO 140 K=1,N
  IF (J.EQ.K) GO TO 140
  AX=A(K,J)
  A(K,J)=0.
  DO 130 L=J+1,N+1
    A(K,L)=A(K,L)-A(J,L)*AX
130 CONTINUE
140 CONTINUE
150 CONTINUE
C
DO 165 J=N,1,-1
  K=A(J,J)
  IF (K.EQ.J) GO TO 160
  DO 155 L=N+1,N+1
    AX=A(J,L)
    A(J,L)=A(K,L)
    A(K,L)=AX
155  CONTINUE
160  A(J,J)=1.
165 CONTINUE
C
170 IF (CHK.EQ.'ON ') THEN
C           WRITE(6,180)
C 180  FORMAT(1H0,* solution *)
  DO 190 I=1,N
C           WRITE(6,185) I,A(I,N+1)
C 185  FORMAT(1H ,S('I2,' ) = ',E22.10E3)
  190 CONTINUE
C           WRITE(6,200)
C 200  FORMAT(1H0,* estimation of solution *)
  DO 220 I=1,N
    S(I)=0.
    DO 210 J=1,N
      S(I)=S(I)+B(I,J)*A(J,N+1)
210  CONTINUE
    E(I)=ABS(S(I)-B(I,N+1))
C           WRITE(6,215) I,E(I)
  
```

```

C 215      FORMAT(1H ,'E(',I2,' ) = ',E22.10E3)
220      CONTINUE
      END IF
C
230 CONTINUE
      RETURN
      END
C
C =====
C      Subroutines Eigen Values & Vectors Analysis
C =====
C..... SUBROUTINE Eigen Value & Eigen Vectors for 'N' Rank Matrix
C           *      estimation [ EA ]      *
C           *      Yacobi's threshould method  *
C
SUBROUTINE JACOBI(A,U,N,EPSL)
DIMENSION A(N,N),U(N,N)
AMAX=0.
DO 20 I=1,N
    DO 10 J=1,N
        U(I,J)=0.
10   CONTINUE
        U(I,I)=1.
20   CONTINUE
    DO 40 I=1,N-1
        DO 30 J=I+1,N
            IF(AMAX.GE.ABS(A(I,J))) GO TO 30
            AMAX=ABS(A(I,J)))
30   CONTINUE
40   CONTINUE
    EPST=.01*AMAX
    DO 45 I=1,N
        DO 44 J=1,N
            IF (I.NE.J) THEN
                IF (A(I,J).NE.0.) GO TO 100
            END IF
44   CONTINUE
45   CONTINUE
        GO TO 200
100  CONTINUE
    DO 70 MP=1,N-1
        DO 60 NQ=MP+1,N
            IF(ABS(A(MP,NQ)).LT.EPST) GO TO 60
            IP=MP
            IQ=NQ
            APQ=A(IP,IP)-A(IQ,IQ)
            TA=-2.*A(IP,IQ)/(APQ+SQRT(APQ**2+4.*A(IP,IQ)**2))
            CO=1./SQRT(1.+TA**2)
            SI=CO*TA
            DO 50 I=1,N
                UIP=U(I,IP)*CO-U(I,IQ)*SI
                U(I,IQ)=U(I,IP)*SI+U(I,IQ)*CO
                U(I,IP)=UIP
                IF((I.EQ.IP).OR.(I.EQ.IQ)) GO TO 50
                AIP=A(I,IP)*CO-A(I,IQ)*SI

```

```

A(I,IQ)=A(I,IP)*SI+A(I,IQ)*CO
A(I,IP)=AIP
A(IQ,I)=A(I,IQ)
A(IP,I)=AIP
50   CONTINUE
APP=A(IP,IP)*CO**2-2.*A(IP,IQ)*SI*CO+A(IQ,IQ)*SI**2
A(IQ,IQ)=A(IP,IP)*SI**2+2.*A(IP,IQ)*SI*CO+A(IQ,IQ)*CO**2
A(IP,IP)=APP
A(IP,IQ)=0.
A(IQ,IP)=0.
60   CONTINUE
70 CONTINUE
IF(EPST.LT.EPSL) GO TO 200
EPST=.01*EPST
GO TO 100
200 CONTINUE
RETURN
END

```

References

1. Ohno, K., Shimozono, S., Sawada, Y., Ohtsu, M.: Mechanisms of diagonal-shear failure in reinforced concrete beams analyzed by AE-sigma. *J. Solid Mech. and Mater. Eng.* **2**(4), 462–472 (2008)
2. Ohtsu, M., Ono, K.: A generalized theory of acoustic emission and green's functions in a half space. *J. of AE* **3**(1), 124–133 (1984)
3. Ohtsu, M.: Simplified moment tensor analysis and unified decomposition of acoustic emission source: application to in situ hydrofracturing test. *J. Geophys. Res.* **96**(B4), 6211–6221 (1991)
4. Ohtsu, M., Okamoto, T., Yuyama, S.: Moment tensor analysis of AE for cracking mechanisms in concrete. *ACI Struct. J.* **95**(2), 87–95 (1998)
5. Suaris, W., van Mier, J.G.M.: AE source characterization in concrete under biaxial loading. *Mater. Struct.* **28**, 444–449 (1995)

Chapter 8

Hybrid NDE for Rebar Corrosion in Concrete

Yuma Kawasaki, Yuichi Tomoda and Masayasu Ohtsu

Abstract Corrosion of reinforcing steel-bar (rebar) is modelled phenomenologically as corrosion losses of three phases. Corresponding to these phases, high AE activities are characteristically observed twice during the corrosion process. It is shown that the 1st AE activity corresponds to the onset of the corrosion in rebar and at the 2nd period of high activity AE events result from concrete cracking due to the expansion of rebar caused by corrosion products. The expansion caused by corrosion products generates micro-cracks in concrete as corrosion-induced cracks, of which mechanisms can be investigated experimentally by AE. To this end, SiGMA (Simplified Green's functions for Moment tensor Analysis) is applied to the corrosion process in reinforced concrete. To compare with cracking mechanisms identified by SiGMA, a numerical analysis by the two-dimensional boundary element method (BEM) is performed for stress analysis and applied boundary nodes were determined from a diffusion analysis of chloride contents by the finite element method (FEM). Thus, fracture mechanisms of corrosion-induced cracks are quantitatively evaluated by AE-SiGMA and BEM. For on-site measurement of the corrosion in reinforced concrete, hybrid nondestructive evaluation (NDE) is going to be developed. Here, acoustic emission (AE) measurement is conducted, along with measuring half-cell potentials and polarization resistances at the surface of concrete. In order to identify the corroded area along rebar, the potential inversion by BEM (PiBEM) analysis is applied. Thus, plausible areas of the corrosion in rebar are identified.

Keywords Corrosion of rebar · AE · BEM · Half-cell potential

Y. Kawasaki · Y. Tomoda

Graduate School of Science and Technology, Kumamoto University, Kumamoto, Japan

Y. Tomoda

Faculty of Engineering, Kumamoto University, Kumamoto, Japan

M. Ohtsu (✉)

Graduate School of Engineering, Kyoto University, Kyoto, Japan

e-mail: ohtsu.masayasu.4v@kyoto-u.ac.jp

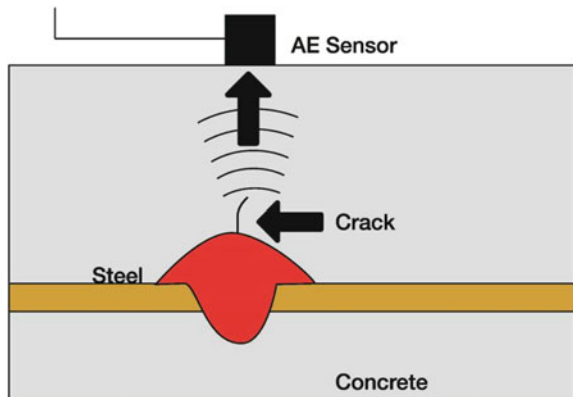
8.1 Introduction

Corrosion of a reinforcing steel-bar (rebar) is known to be one of critical deteriorations in reinforced concrete. When chloride concentration at the level of rebar in concrete exceeds a range of values with the probability for onset of corrosion, a passive layer on the surface of rebar is destroyed and corrosion is initiated. Then electrochemical reaction continues with available oxygen and water. In order to maintain concrete structures in healthy and safe conditions, an early warning of the corrosion by nondestructive evaluation (NDE) is in practical demand. Inspection methods for NDE currently available, however, might lack such a function as to provide precise information prior to the critical corrosion.

Development of a reliable NDE method for early warning is of significant importance for monitoring rebar corrosion. By applying acoustic emission (AE) techniques, it has been reported that concrete cracking due to rebar corrosion is effectively detected [3, 12, 14]. In ferrous metals, in addition, it is recently reported that the onset of corrosion is readily detected by AE measurement [2]. Thus, AE events are readily detected during the corrosion process of rebar in concrete as shown in Fig. 8.1.

In recent years, early degradation by reinforcement corrosion has been reported in many RC structures. For NDE of rebar corrosion, half-cell potentials and the polarization resistance are currently available. Since these are based on electric parameters at the concrete surface, results are considerably affected by the environmental conditions. To improve this issue, it is suggested to evaluate electric parameters not at the concrete surface but on the rebar surface. Recently, to determine half-cell potentials on the rebar surface, the potential inversion by the boundary element method (PiBEM) is proposed [6].

Fig. 8.1 AE detection due to rebar corrosion



8.2 Phenomenological Model of Corrosion Process and AE Observation

8.2.1 The Model of Corrosion Process

In the Japanese standard specifications for maintenance of concrete structures [4], a deterioration process due to corrosion in reinforced concrete is postulated. The titles of the stages or the phases during the process are modified and shown in Fig. 8.2. Here, two transition periods are defined at the onset of corrosion and at the nucleation of cracking. The former is associated with the transition period from the dormant stage (phase I) to the initiation stage (phase II). Because the corrosion-related damage could begin during phase II, it is desirable to effectively identify this period. This implies that the target of inspection was to identify the time of nucleation of concrete cracking from the initiation stage (phase II) to the accelerated stage (phase III) in the figure.

Practically, identification of this transition period is of importance to assess the durability of reinforced concrete structures, because cracks actively occur in concrete due to the expansion of corrosive product during phase III. Still, earlier warning or information of the corrosion is desirable, which could be associated with the transition from phase I to phase II.

According to a phenomenological model of reinforcement corrosion in marine environments [7], a typical corrosion loss is illustrated as shown in Fig. 8.3. At phase 1, the corrosion is initiated. The rate of the corrosion process is controlled by the rate of transport of oxygen. As the corrosion products build up on the corroding surface of rebar, the flow of oxygen is eventually inhibited and the rate of the corrosion loss decreases at phase 2. This is a nonlinear corrosion-loss-time relationship for corrosion under aerobic conditions, although a monotonous increase of corrosion loss is assumed in Fig. 8.1. The corrosion process involves further corrosion loss as phases 3 and 4 due to anaerobic corrosion. Thus, two-step corrosion losses are modeled, instead of the monotonous deterioration in Fig. 8.2.

Fig. 8.2 Deterioration process due to corrosion

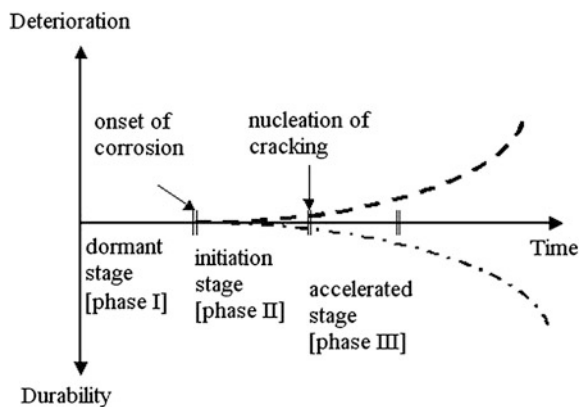
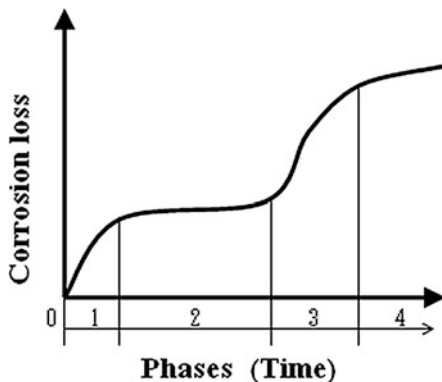


Fig. 8.3 Typical corrosion loss for steel in seawater immersion [7]



8.2.2 Accelerated Corrosion Experiments

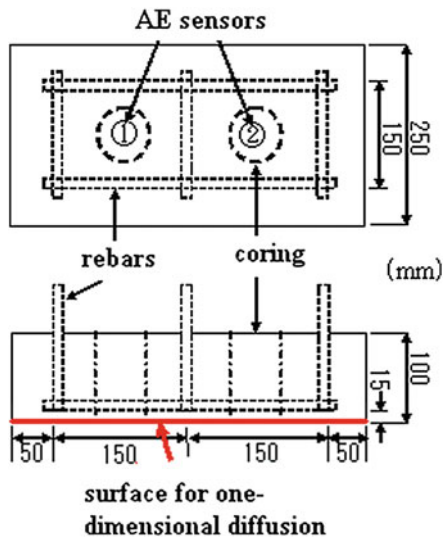
Reinforced concrete specimens tested were of dimensions $300 \times 300 \times 100$ mm. Deformed steel-bars (rebars) of 13 mm (0.51 in.) nominal diameter were embedded with 15 mm (0.59 in.) cover-thicknesses for longitudinal reinforcement. Configuration of the specimen is illustrated in Fig. 8.4. When making specimens, concrete was mixed with NaCl solution. In order to investigate the threshold limit of chloride concentration for the corrosion, the lower-bound threshold value (chloride amount 0.3 kg/m^3 of concrete volume; 0.093 % mass of cement) prescribed in the code [4] was taken into account. After the standard curing for 28 days in 20°C water, chloride content was measured and found to be 0.125 kg/m^3 (0.039 % mass of cement) in concrete as lower than 0.3 kg/m^3 in volume. The compressive strength at 28 days of the standard curing was 35.0 MPa. Following the standard curing, all surfaces of the specimen were coated by epoxy, except the bottom surface for one-directional diffusion as illustrated in Fig. 8.4.

An accelerated corrosion test and a cyclic wet-dry test were conducted. In the accelerated corrosion test, the specimen was placed on a copper plate in a container filled with 3 % NaCl solution. Between rebars and the copper plate, 100 mA electric current (0.754 mA/mm^2) was continuously charged. In the cyclic wet-dry test, the specimens were cyclically put into the container in the figure without charge for a week and subsequently dried under ambient temperature for another week.

AE measurement was continuously conducted, by using AE analyzer. Two broadband-type AE sensors of 1 MHz resonance were attached to the upper surface of the specimen at the center of coring locations shown in Fig. 8.4. Frequency range of the measurement was 10 kHz–1 MHz and total amplification was 60 dB gain. For event counting, the dead-time was set to 2 ms and the threshold level was 40 dB gain.

Half-cell potentials at the surface of the specimen were measured by a portable corrosion-meter. In the accelerated corrosion test, the measurement was conducted twice a day, right after discontinuing the current. When the average potentials reached to -350 mV (C.S.E.), which gives more than 90 % probability of

Fig. 8.4 Sketch of reinforced concrete specimen



corrosion [1], the test was terminated. In the cyclic test, the specimen was weekly measured until the average potentials in dry condition reached to -350 mV (C.S.E.). During the half-cell potential measurement, AE measurement was discontinued in both tests.

Chloride concentrations were measured at several periods. At first, the initial concentration was measured by using a standard cylinder sample after 28-day moisture-curing as an initial value. At other periods, two core samples of 5 cm diameter were taken from the specimens, of which locations are also illustrated in Fig. 8.4. Slicing the core into 5 mm-thick disks and crushing them, concentrations of total chloride ions were determined by the potentiometric titration method. At two stages during the cyclic test, rebars were taken out of the specimen. Then, they were cut into 10 mm portions, and then ferrous ions on their surface-layers were examined by the scanning electron microscope.

8.2.3 AE Observation

A relation between AE activity and half-cell potentials measured are shown in Fig. 8.5. The number of AE events is plotted as a total of two channels counted for one hour. Two periods of high AE activities are clearly observed around at 3 days elapsed and at 7 days elapsed. The activity at the 1st period is even higher than the 2nd. It is noted that the half-cell potentials start to decrease after the 1st high activity. This may suggest the onset of corrosion in rebars, although the potential are still less negative than -350 mV (ASTM criterion denoted in the graph) at the 2nd high activity. It is known that the half-cell potential lower than -350 mV is

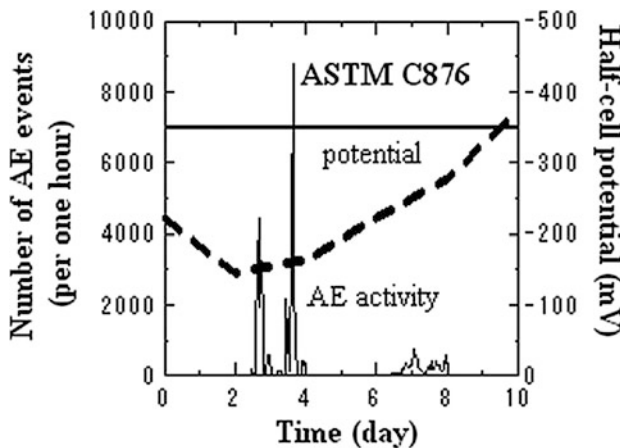


Fig. 8.5 AE activities and half-cell potentials in the accelerated corrosion test

prescribed as more than 90 % probability of the corrosion and the probability is uncertain between -200 and -350 mV by ASTM C876 [1]. This implies that the corrosion could be monitored from AE activities more confidently than the half-cell potentials, if the 1st high AE activity is associated with the corrosion activity.

Following two periods of high AE activities and at the final stage, cores were taken. Thus, total chloride ions were determined in depths. Based on chloride concentrations at the initial and after the 1st high AE activity, chloride concentration at the cover thickness was analytically estimated by the error function formula. Results are plotted in Fig. 8.6. A broken curve shows analytical values, which are compared with measured values (open circles in the figure) at the cover thickness in the tests. Agreement between analyzed and measured values after the 2nd high activity and at the final stage is reasonable. In the figure, two horizontal lines are denoted. One is the lower bound of threshold value for onset of corrosion (0.3 kg/m^3 in volume, 0.093% mass of cement volume) and the other is the threshold value (1.2 kg/m^3 in volume) for performance-based design [4]. In this design code, concrete with chloride content over 1.2 kg/m^3 (0.068 lb/ft^3 in volume, 0.372% mass of cement) is not allowed in construction for preventing the corrosion. In the figure, the total number of AE hits observed during the acceleration test is also given by a solid curve. It is interesting that the curve of the total number of AE hits is in remarkable agreement with the typical corrosion loss in the phenomenological model in Fig. 8.2. This could suggest that AE activity observed could phenomenologically corresponds to the corrosion activity in rebar. Comparing AE activity with chloride concentration, it is found that chloride concentration becomes higher than 0.3 kg/m^3 around at the 1st AE activity, and it reaches higher than 1.2 kg/m^3 , resulting in the 2nd AE activity. Consequently, it might be summarized that two high AE activities reasonably correspond to two periods of the onset of corrosion and the nucleation of cracking.

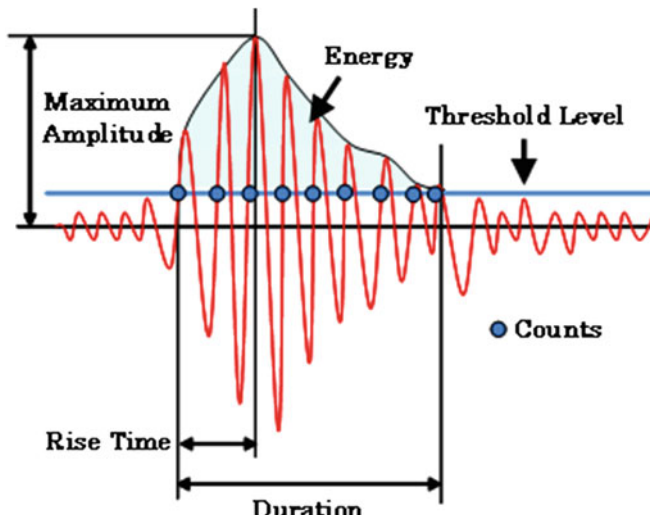


Fig. 8.6 AE waveform parameters

In the cyclic wet and dry test, the RA values and the average frequency of AE waves illustrated in Fig. 8.6 were determined from the following equations [10], by averaging the data in two weeks of wet and dry,

$$\text{RA} = \text{Rise time}/\text{Maximum amplitude}, \quad (8.1)$$

$$\text{Average frequency} = \text{Counts}/\text{Duration}. \quad (8.2)$$

Results are shown in Fig. 8.7 Corresponding to the 1st period, the RA value becomes large and the average frequency is low, which implies that AE sources are classified as other-type cracks [10]. After 100 days elapsed, a slight increase of the RA values is observed. Still, identification of the 2nd high activity seems to be difficult. In the test, the 2nd period was identified around at 100 days elapsed, where the RA values are low and the average frequencies are fairly high. It is suggested from Fig. 8.7 that tensile cracks were nucleated at this period.

In addition, the b-values calculated from Eq. 8.3 were determined during each wet-dry cycle as the average values.

$$\log_{10} N = \alpha - b \log_{10} A, \quad (8.3)$$

A relationship between the number of AE events, N , and the amplitudes, A , is statistically represented, where α and b are empirical constants. In the case that the b -value is large, small AE events are mostly generated. In contrast, the case where the b -values become small implies nucleation of large AE events. Results are shown in Fig. 8.7. It is observed that b -value becomes high at the 1st period and then b -values keep fairly low. Results suggest generation of small other-type cracks at

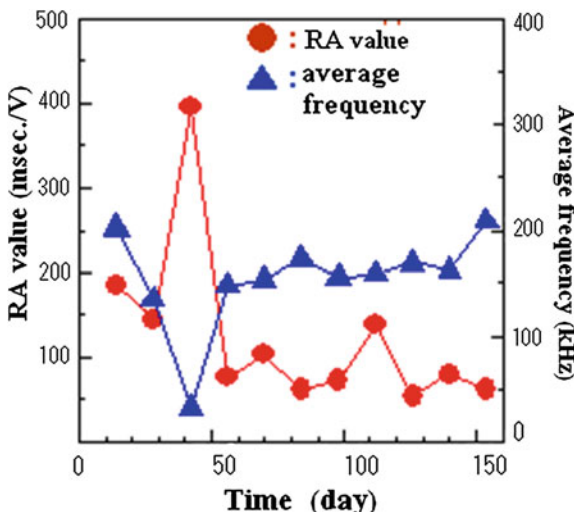


Fig. 8.7 The RA values and the average frequencies in the cyclic wet-dry test

the 1st period and nucleation of fairly large tensile cracks at the 2nd period. Combining the results of the accelerated test, it may be concluded that the 1st high AE activity is associated with generation of small other-type cracks and could be related with the onset of corrosion in reinforcement. The 2nd high AE activity results from the nucleation of fairly large tensile cracks, which could be generated due to the expansion of rebar caused by corrosion product.

8.2.4 Visual Confirmation

In the cyclic wet-dry test, it is found that chloride concentration at rebar reaches to the lower-bound threshold of 0.3 kg/m^3 after 40 days. At around 100 days elapsed, the concentration becomes higher than 1.2 kg/m^3 . Accordingly, at 42 days elapsed and 126 days elapsed, rebars were removed and visually inspected. No corrosion was observed on rebar surface after 42 days, while rebar was fully corroded after 126 days. These results imply that rebars could corrode after chloride concentration reaches over 1.2 kg/m^3 in concrete. AE activities after 100 days could reasonably result from concrete cracking due to the expansion of corrosive products in rebars.

In order to investigate the condition of rebar at the 1st AE activity, the surface of rebar was examined by the scanning electron micrograph (SEM). Distributions of ferrous ions at the initial of as-received condition and at 42 days elapsed are compared in Fig. 8.8. In the as-received condition, a reinforcing steel bar was cut into a fragment around 10 mm long and then the cross-section of the rebar fragment was examined. In Fig. 8.8a, from the left, white, gray and black zones are observed. The white zone is observed inside steel and the gray zone corresponds to the surface

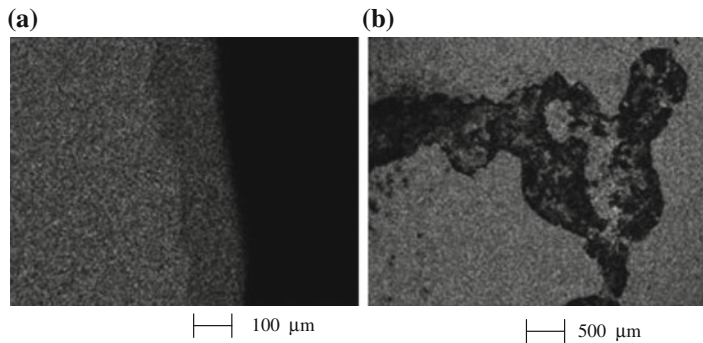


Fig. 8.8 Distributions of ferrous ions on rebar surface. **a** Distribution of ferrous ions (grey region) prior to the test. **b** Distribution of ferrous ions after the 1st period

layer. As shown, homogeneous distribution of ferrous ions is observed at the surface as the gray zone. At 42 days elapsed, rebars removed were cut into 10 mm fragments, and the circumferential surfaces were examined. In Fig. 8.8b, it is shown that at some portions of the surface layer, ferrous ions (grey) vanish and black areas appear as non-ferrous zones. This demonstrates that the onset of corrosion occurs in rebars at the 1st period of AE activities (Ohtsu and Tomoda 2008).

8.3 Mechanisms of Corrosion-Induced Cracks

AE activities under cyclic wet and dry test are investigated. In order to study fracture mechanisms of corrosion-induced cracks, SiGMA (Simplified Green's functions for Moment tensor Analysis) [9, 11] is applied to the corrosion process in reinforced concrete. To compare with cracking mechanisms identified by SiGMA, a numerical analysis by the two-dimensional boundary element method (BEM) is performed for stress analysis and applied boundary nodes were determined from a diffusion analysis of chloride contents by the finite element method (FEM). Thus, fracture mechanisms of corrosion-induced cracks are quantitatively evaluated by AE-SiGMA and BEM.

8.3.1 Cyclic Wet-Dry Tests

RC specimens of dimensions $75 \times 100 \times 400$ mm were made. Configuration of the specimen is illustrated in Fig. 8.9. A rebar of 13 mm diameter was embedded with 20 mm cover-thickness for longitudinal arrangement. To promote the corrosion, a notch of dimensions of $150 \times 10 \times 1$ mm was set at the bottom of the mold. Here,

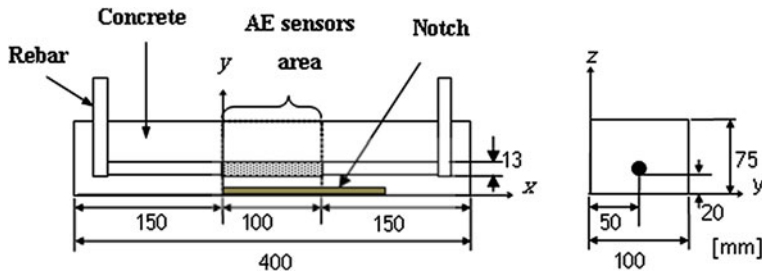


Fig. 8.9 RC specimen tested

NaCl solution is employed as mixing water. The compressive strength and the velocity of P-wave of hardened concrete at 28 day of moisture curing are 36.1 MPa and 4500 m/s. Following the standard curing for 28 days, corrosion process under salt attack was simulated by cyclic wet and dry condition, where the specimens were cyclically put into the container filled with 3 % NaCl solution for a week and subsequently taken out of the container to dry under ambient temperature for another week.

AE measurement was continuously conducted, by using AE measurement system. Six AE sensors (R15) of 150 kHz resonance were attached to the surface of the specimen at the area in Fig. 8.9. The frequency range of the measurement was 10 kHz–2 MHz and total amplification was 60 dB gain. For event counting, the dead-time was set to 2 ms and the threshold level was set to 40 dB gain. Every week, AE measurement was temporarily interrupted for the electrochemical measurement.

Half-cell potentials at the surface on the bottom of the specimen were measured by a portable corrosion meter, SRI-CM-II [13] every week. Results of the half-cell potentials were converted to the probability of corrosion on the basis of ASTM C876 standard.

8.3.2 Numerical Analysis

Ingress of chloride ions is governed by the diffusion equation. The diffusion equation was solved by using 2-D FEM in order to clarify chloride concentration at a cross-section. As for analytical parameters, the chloride initial contents is 0.047 kg/m^3 and diffusion coefficient is $6.05 \times 10^{-8} \text{ cm}^2/\text{s}$ and the corresponding value of the surface chloride contents is set to 18.2 kg/m^3 .

A BEM model is made, which corresponds to a half portion of a cross-section in RC beam. The boundary corresponding to the notch is set to be stress free from constraints. Expansive pressure due to corrosion products was applied at the cavity, corresponding to the rebar. The pressure was assumed as 1 MPa, which were applied to boundary nodes determined from chloride concentration analyzed by FEM. Poisson's ratio and Young's modulus was set to 0.22 and 27 GPa, respectively.

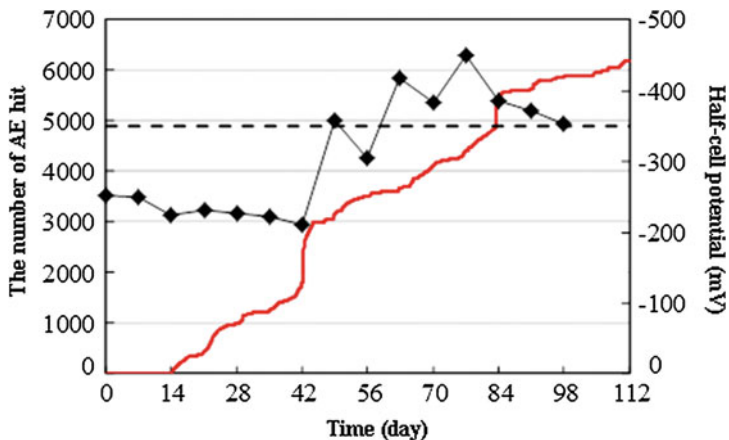


Fig. 8.10 Cumulative AE hits and half-cell potentials

8.3.3 AE Activity and Half-Cell Potential

Cumulative AE hits of all 6 channels are compared with half-cell potentials in Fig. 8.10. The half-cell potentials start to decrease after 42 days. After 56 days elapsed, the potentials became more negative than -350 mV. From these results, the corrosion-induced cracks occurred from 42 days. Thus, after 42 days, rust breaking and other internal cracks around rebar could occur. Then, corrosion-induced cracks in concrete must be nucleated due to expansion of corrosion products in rebar.

8.3.4 Numerical Analysis by FEM and BEM

Results of FEM of a half portion of a cross-section at 42 days are shown in Fig. 8.11. It is confirmed that chloride contents exceed 1.2 kg/m^3 at -33.75° orientation. Thus, expansive pressure (1 MPa) was applied to these boundary nodes points. From BEM analysis, the stress distribution in the horizontal direction at 42 days elapsed, which corresponds to the opening mode, is plotted in Fig. 8.12. The highest stress and the second highest stress are observed toward -78.75° and -45° orientations, respectively. It may suggest the case that the spalling cracks (-45°) propagates following the surface cracks (-78.75°). These results imply that the expansive pressure due to the corrosion products could generate the surface crack, and then generate the spalling crack.

Fig. 8.11 Chloride concentration

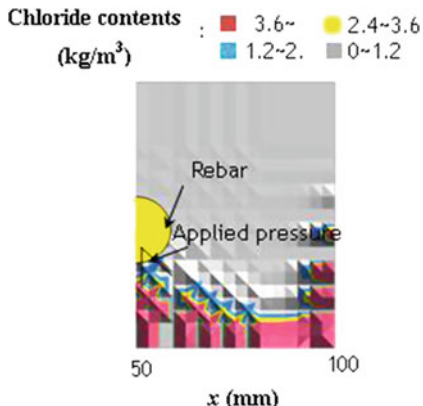
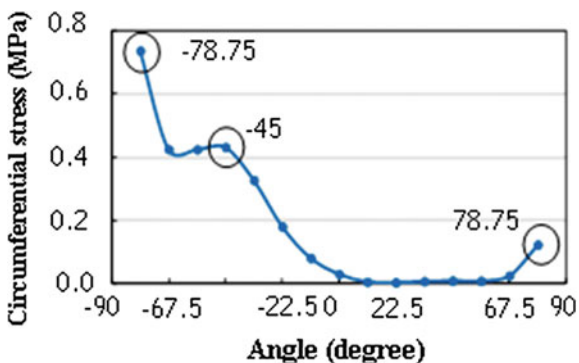


Fig. 8.12 Distribution of stress



8.3.5 SiGMA Analysis and Visual Observation

Results of the SiGMA analysis at 42 days elapsed are shown in Fig. 8.13. Mostly events are located surrounding the rebar. The events which are located at -78.75° orientation are mostly classified into tensile (opening) cracks. Thus, the surface crack is initiated as tensile cracks, whereas mixed-mode and shear cracks are less active. Additionally, shear cracks (sliding) are observed at 78.75° orientation, after tensile cracks observed. Referring to Fig. 8.12, this result clarifies why the spalling cracks were generated, following the surface cracks in the experiment.

Results of the stereo-microscope of cross-section at 56 days are shown in Fig. 8.14. Three micro-cracks were observed at the cross section toward the bottom of RC beam. Orientation of these cracks is about -78.75° . Thus, it is confirmed that

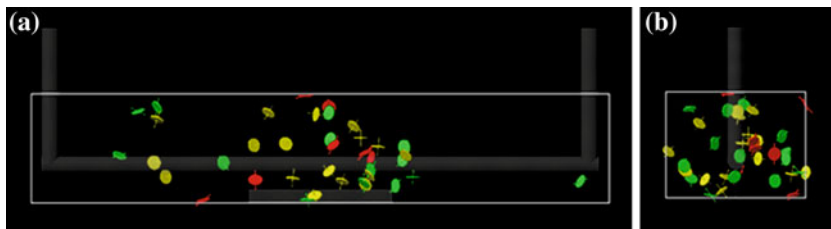
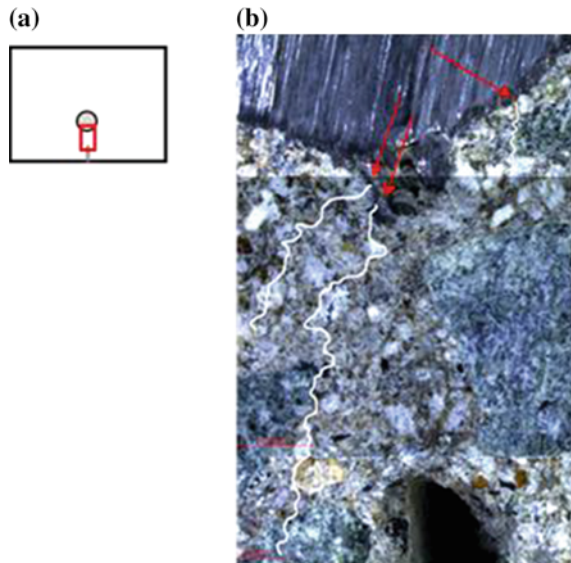


Fig. 8.13 Results of SiGMA analysis. **a** Side view. **b** Cross section

Fig. 8.14 Micrograph observation. **a** Observed location. **b** Cross section



tensile cracks are observed at around -80° orientation as the surface cracks and the spalling cracks [5].

$$\nabla^2 u(x) = 0$$

8.4 Electro-Chemical Measurement and PiBEM Analysis

As given the results, for NDE of rebar corrosion, half-cell potentials and the polarization resistance are available. Since these are based on electric parameters at the concrete surface, results are considerably affected by the environmental conditions. To improve this issue, the potential inversion by the boundary element method (PiBEM) is proposed [6].

8.4.1 PiBEM Analysis

Electrical potential $u(x)$ in concrete satisfies the Laplace equation,

$$\nabla^2 u(x) = 0 \quad (8.4)$$

In the boundary element method (BEM), the solution is formulated as,

$$u(x) = \int_S \left\{ G(x, y) \frac{\partial u}{\partial n}(y) - \frac{\partial G}{\partial n}(x, y) \cdot u(y) \right\} dS \quad (8.5)$$

Here, $G(x, y)$ is an elementary solution. Equation 8.5 is digitized by the BEM method, as follows;

$$u(x) = \sum_{j=1}^N G(x, y_j) \frac{\partial u}{\partial n}(y_j) S_j - \sum_{j=1}^N \frac{\partial G}{\partial n}(x, y_j) u(j) S_j$$

The concrete surface S_h is divided into the element S_j . Setting the electrode of the internal point (point on a rebar) x_i as u_i , we have,

$$u_i = C_1 \left(\sum_{j=1}^1 \frac{\partial G_{ij}}{\partial n} u_j S_j \right) + C_2 \left(\sum_{j=1}^1 G_{ij} \frac{1}{I_j} S_j \right) \quad (8.6)$$

Here, u_i and S_j are the half-cell potential at x_i on the surface of concrete, and the surface area at x_j , respectively. Here, the current $\partial u / \partial x_j$ is correlated with the polarization resistance I_j as,

$$\frac{\partial u}{\partial n_j} \propto \frac{B}{I_j}$$

Substituting two coefficients C_1 and C_2 into the potential term and the current term for compensation in Eq. 8.6, we have,

$$\begin{aligned} u_1 &= C_1 \left(\sum_{j=1}^N \frac{\partial G(x_1, y_j)}{\partial n} u_j S_j \right) + C_2 \left(\sum_{j=1}^N G(x_1, y_j) \frac{1}{I_j} S_j \right) \\ u_2 &= C_1 \left(\sum_{j=1}^N \frac{\partial G(x_2, y_j)}{\partial n} u_j S_j \right) + C_2 \left(\sum_{j=1}^N G(x_2, y_j) \frac{1}{I_j} S_j \right) \end{aligned} \quad (8.7)$$

In the experiment, potentials u_j and resistances I_j were measured at the surface locations y_j , and also by embedded sensors. Substituting the half-cell potential u_j at two locations x_1 and x_2 of embedded sensors into Eq. 8.7, the coefficients C_1 and C_2 are determined. Then the half-cell potentials at the rebar surface at nay locations can be calculated from Eq. 8.6. A Fortran program for the PiBEM analysis is given in the appendix.

8.4.2 Experiments for Hybrid NDE

Four specimens NC1, NC2, NC3 and FA1 are illustrated in Fig. 8.15. In one specimen (FA1), 20 % of cement by weight was replaced by fly ash (FA). Four RC specimens of dimensions $1100 \times 150 \times 75$ mm were made. A deformed rebar of 10 mm nominal diameter is embedded with 20 mm cover-thickness. The test specimen was coated at all the side except the bottom with the waterproofing paint after water-curing for 28 days.

Then, a corrosion process due to salt attack was simulated by a cyclic wet and dry test. The specimen was cyclically placed into a container filled with 3 % NaCl solution for a week and subsequently taken out of the container to dry under ambient temperature for another week.

On the basis of results of the half-cell potential and polarization resistance measurement, later AE sensors were attached at selected positions as indicated in Fig. 8.15. Continuation monitoring was initiated at the time judged as reinforcement corrosion began.

AE measuring system (DiSP) is employed. 6 AE sensors of 150 kHz resonance (R15) is attached to the surface of the specimen as shown in Fig. 8.15. The

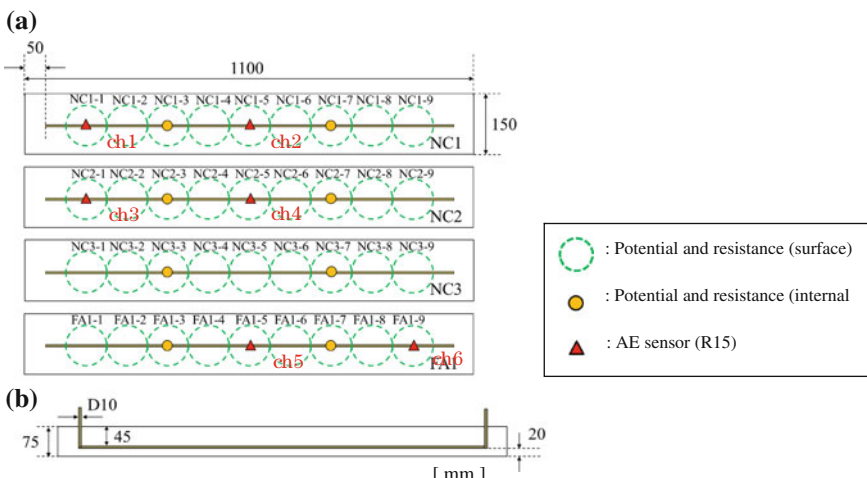


Fig. 8.15 RC specimens tested and the locations measured. **a** Top view. **b** Cross-section

frequency range of the measurement was 10 kHz–2 MHz. AE signals were amplified with 40 dB gain in a pre-amplifier and 20 dB gain in a main amplifier. For ringdown-counting, the dead-time was set to 2 ms and the threshold level to 40 dB gain. Moreover, the sampling frequency was 1 MHz, the A/D conversion of the signal waveform was carried out, and one waveform was recorded as data of 1024 amplitude values. The potentials at the surface of the specimen were measured by using a portable corrosion meter, (SRI-CM-II) [13], and C.S.E. values were estimated on the basis of ASTM C876 standard [1].

8.4.3 AE Activities

Results of AE activities are shown in Fig. 8.16. It is realized that active corrosion seems to start from 56 days, and thus the corrosion-induced cracks could be initiated. In the specimen NC1, the rapid increase of AE hits are observed at 63 days and the 77 days elapsed. In contrast, in the specimen FA1, AE hits are increasing rapidly at 84 days elapsed. Thus, it is considered that active corrosion start at 63 days in NC1, while it delays until 84 days in FA1.

8.4.4 Potential Analysis

Results of PiBEM in NC1 and FA1 are shown in Fig. 8.17. When the potentials become lower than -350 mV, it indicates the possibility of 90 % corrosion possibility. In the case of NC1, fluctuations of the analytical values are large while the fluctuations of that are little in FA1. It is clearly observed that NC1 must be corroded after 63 days elapsed. In contrast, it is estimated that no corrosion occurs

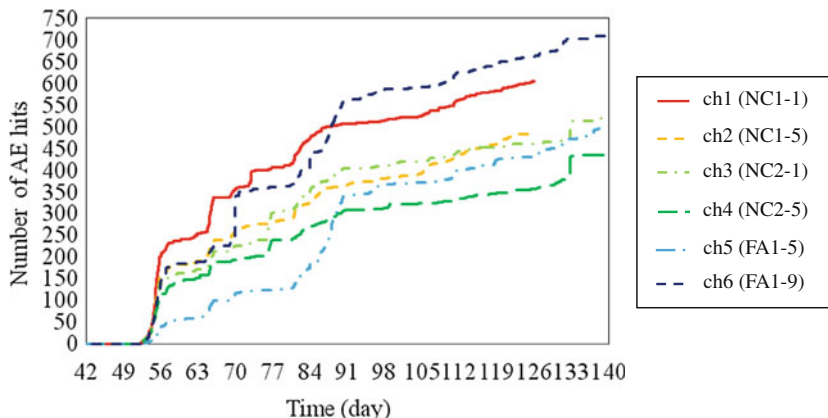


Fig. 8.16 AE activities at all channels

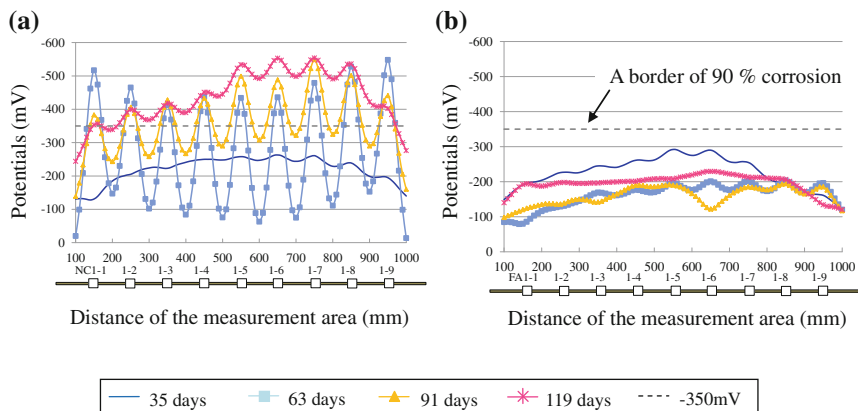


Fig. 8.17 Potential values analyzed. **a** NC1. **b** FA1

in FA1 even after 119 days elapsed. It is noted that the half-cell potentials of NC1 become more negative at the right part. The increase in AE activity from 63 days is considered to be verified from the potential distribution of NC1 in Fig. 8.16. It is realized that the corrosion process at NC1 is more active than that of FA1.

8.4.5 Confirmation by Micrograph Observation

All rebars were removed to observe visually the corrosion state after the cyclic test. Surface observation of rebar and the cross-sectional observation of the test specimen were performed using the micrograph. The observed position of a micrograph is indicated in Fig. 8.18, and the result of observation is shown in Fig. 8.19. From a cross-sectional observation of rebar in Fig. 8.19a, it is found that rebar on the osmosis side is exfoliated, generating corrosion products. As seen in Fig. 8.19b, progress of a crack is confirmed at -45° direction.

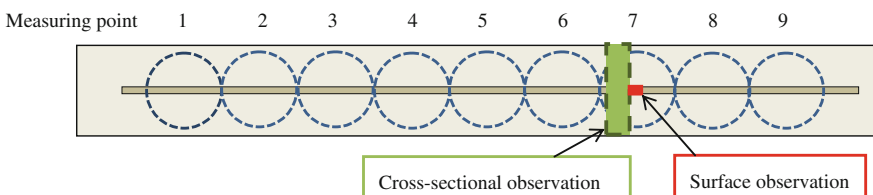


Fig. 8.18 Position of micrograph observation

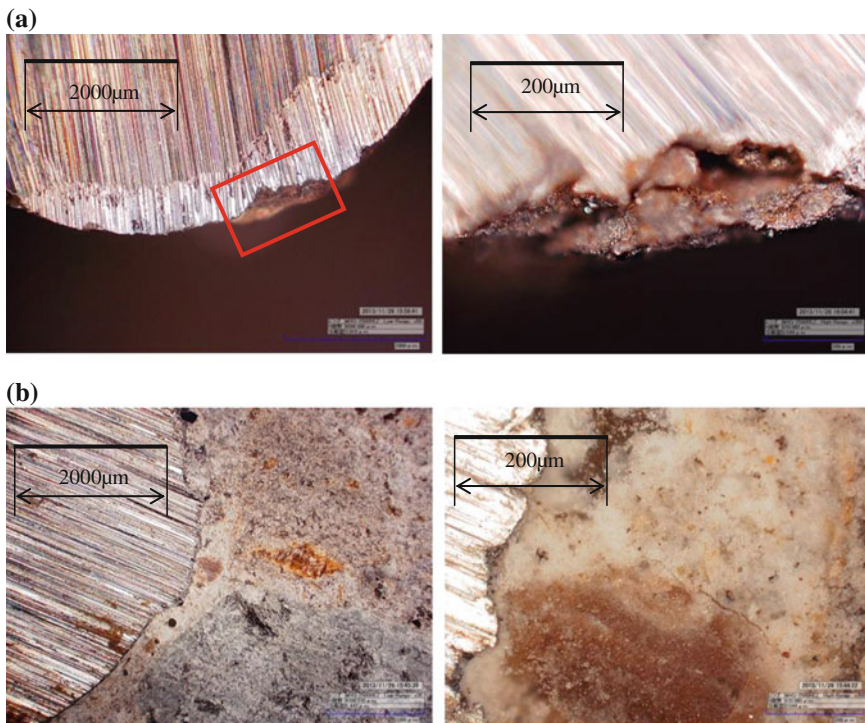


Fig. 8.19 Result of the micrograph observation. **a** Cross-sectional observation of rebar. **b** Crack observation

8.5 Concluding Remarks

Results obtained are summarized as follows.

- (1) By combining AE technique with PiBEM analysis, the onset of reinforcement corrosion is readily estimated.
- (2) From the result of the PiBEM analysis, it is promising to precisely identify the corroded area in rebar.
- (3) From the result of the stress analysis by the BEM analysis, it is predicted that the crack progresses at 45° inclined toward the bottom. The fact is in remarkable agreement with visual observation by the micrograph. Thus, the effectiveness of hybrid NDE is confirmed by these experimental results.

Appendix: Program for PiBEM Aanalysis

Appendix: Program for PiBEM analysis

```

C..... **** BEM SOLUTION FOR HALF-CELL POTENTIAL IN REBAR *****
C..... .
C..... .
C..... DIMENSION U(500),V(500),X(500),Y(500),Z(500),XN(500),YN(500)
C..... 1,ZN(500),DS(500),R(500),T(500,500),G(500,500),NOD(2)
C..... .
C..... ***** INPUT DATA *****
C..... .
C..... OPEN(3,FILE='Test.dat')
C..... OPEN(5,FILE='Poten.out')
C..... READ(3,110) NB,NI
C..... 110 FORMAT(2I6)
C..... .
C..... NT=NB+NI
C..... CALL INPUT(NB,NI,X,Y,Z,V,R,DS,NOD)
C..... CLOSE(3)
C..... Outward Normal
C..... DO 250 I=1,NB
C..... XN(I)=0.
C..... YN(I)=0.
C..... ZN(I)=1.0
C..... 250 CONTINUE
C..... .
C..... ***** BOUNDARY CONDITION *****
C..... .
C..... DO 17 I=1,NB
C..... U(I)=V(I)
C..... 17 CONTINUE
C..... VA=-273.8*0.001
C..... VB=-292.3*0.001
C..... WRITE(5,16) NOD(1),VA,NOD(2),VB
C..... 16 FORMAT(1H ,I5,F10.3,3X,I5,F10.3)
C..... .
C..... ***** PREPARATION *****
C..... .

```

```

T(II,J)=0.
G(II,J)=0.
21 CONTINUE
20 CONTINUE
C
C-----***** G & T-MATRIX *****
C
DO 35 I=1,NI
II=NB+I
XI=X(II)
YI=Y(II)
ZI=Z(II)
DO 36 J=1,NB
XK=XN(J)
YK=YN(J)
ZK=ZN(J)
XJ=X(J)
YJ=Y(J)
ZJ=Z(J)
CALL GIJ(XI,YI,ZI,XJ,YJ,ZJ,GG)
CALL TIJ(XI,YI,ZI,XJ,YJ,ZJ,XK,YK,ZK,TT)
G(II,J)=GG
T(II,J)=TT
36 CONTINUE
35 CONTINUE
C
C.....***** SOLUTION *****
A3=VA
B3=VB
A1=0.
A2=0.
B1=0.
B2=0.
DO 61 J=1,NB
A1=G(NOD(1,J)/R(J)*DS(J)+A1
A2=T(NOD(1,J)*U(J)*DS(J)+A2
B1=G(NOD(2,J)/R(J)*DS(J)+B1
B2=T(NOD(2,J)*U(J)*DS(J)+B2
61 CONTINUE
CO1=(A3*B2-A2*B3)/(A1*B2-A2*B1)

```

```

CO2=(A1*B3-A3*B1)/(A1*B2-A2*B1)
WRITE(6,66) CO1,CO2
WRITE(5,66) CO1,CO2
66 FORMAT(1H ,'CO1=',E12.3,3X,'CO2=',E12.3)

C
C.....***** INTERNAL POTENTIALS *****
C
DO 71 I=1,NI
K=NB+I
U(K)=0.
DO 72 J=1,NB
U(K)=U(K)+CO2*T(K,J)*U(J)*DS(J)+CO1*G(K,J)*DS(J)/R(J)
72    CONTINUE
71 CONTINUE
UU=(VA-U(NOD(1))+VB-U(NOD(2)))/2.
DO 73 I=NB+1,NT
U(I)=UU+U(I)
73 CONTINUE
WRITE(5,79) UU
79 FORMAT(1H ,'Hosei Po=',F10.3)

C
C.....***** RESULTS OUTPUT *****
C
WRITE(5,300) (I,X(I),Y(I),Z(I),U(I),I=1,NT)
300 FORMAT(1H ,NO.='I3,2X,'X='F8.1,2X,'Y='F8.1,2X
      , 'Z='F8.1,2X,'U=',E12.3)
END
C-----
SUBROUTINE INPUT(NB,NI,X,Y,Z,V,R,DS,NOD)
DIMENSION X(500),Y(500),Z(500),V(500),R(500)
1,DS(500),NOD(2)
C
C
C    *** X-Y-Z COORDINATES *****
C    All Points  (mm)
NT=NB+NI
READ(3,210)(X(I),I=1,NT)
210 FORMAT(10F6.1)
DO 200 I=1,NT
Y(I)=0.

```

```

Z(I)=0.

200 CONTINUE
C      Internal points
C      COVERTHICKNESS
      READ(3,205) COV
205 FORMAT(F5.1)
      DO 240 I=1,NI
      Z(NB+I)=-COV
240 CONTINUE
C      ***HALF-CELL POTENTIAL and POLARIZATION RESISTANCE***
C
      READ(3,220)(V(I),R(I),I=1,NB)
220 FORMAT(2F6.1)
      DO 221 I=1,NB
      V(I)=V(I)*0.001
221 CONTINUE
C
C      *** AREA OF MEASUREMENT *****
C
      DO 230 I=1,NB
      DS(I)=6360.
230 CONTINUE
C      **** Mini-Sensor location *****
      READ(3,320) NOD(1),NOD(2)
320 FORMAT(2I5)
      RETURN
      END
C-----
      SUBROUTINE TIJ(XI,YI,ZI,XJ,YJ,ZJ,XK,YK,ZK,TT)
      RS=SQRT((XI-XJ)**2+(YI-YJ)**2+(ZI-ZJ)**2)
      RN=((XI-XJ)*XK+(YI-YJ)*YK+(ZI-ZJ)*ZK)/RS
      TT=RN/(4.*3.1416*RS*RS)
      RETURN
      END
C-----
      SUBROUTINE GIJ(XI,YI,ZI,XJ,YJ,ZJ,GG)
      RS=SQRT((XI-XJ)**2+(YI-YJ)**2+(ZI-ZJ)**2)
      GG=-1./(4.*3.1416*RS)
      RETURN
      END

```

References

1. ASTM C876.: Standard test method for half-cell potentials of uncoated reinforcing steel in concrete, ASTM (1991)
2. Cho, H., Takemoto, M.: Acoustic emission from rust in stress corrosion cracking, In: Proceedings of the European Working Group of AE, BB 90-CD, 503–510 (2004)
3. Idrissi, H., Liman, A.: Study and characterization by acoustic emission and electrochemical measurements of concrete deterioration caused by reinforcement steel corrosion. NDT and E Int. **36**, 563–569 (2003)
4. JSCE.: Standard specifications for concrete structures “Version of Maintenance” (2001)
5. Kawasaki, Y., Kobayai, T., Ohtsu, M.: Kinematics of corrosion damage monitored by acoustic emission techniques and based on a phenomenological model. Adv. Concr. Technol. **10**, 160–169 (2012)
6. Kobayai, T., Wakuda, T., Tomoda, Y., Ohtsu, M.: Hybrid-NDT for evaluation of rebar corrosion in RC by AE, In: Proceedings of Concrete Structure Scenarios, JSMS, vol. 12, 55–62 (2012)
7. Melchers, R.E., Li, C.Q.: Phenomenological modeling of reinforcement corrosion in marine environments. ACI Mater. J. **103**(1), 25–32 (2006)
8. Ohtsu, M., Tomoda, Y. : Phenomenological model of corrosion process in reinforced concrete identified by AE. ACI Mater. J. **105**(2), 194–199 (2008)
9. Ohtsu, M.: Simplified moment tensor analysis and unified decomposition of acoustic emission source : Application to in situ hydrofracturing test, J. Geophys. Res., **96**(B4), 6211–6221 (1991)
10. Ohtsu, M.: Test method for classification of active cracks in concrete structures by AE, Mater. Struct. **43**, 1187–1189 (2010)
11. Ohtsu, M., Okamoto, T., Yuyama, S.: Moment tensor analysis of acoustic emission for cracking mechanisms in concrete. ACI Struct. J. **95**(2), 87–95 (1998)
12. Ohtsu, M., Tomoda, Y., Sakata, Y., Murata, M., Matsushita, H.: In situ monitoring and diagnosis of RC members in an exposure test against salt attack, In: Proceedings of the 10th International Conference on Structural Faults and Repair, CD-ROM (2003)
13. Yokota, M.: Study on corrosion monitoring of reinforcing steel bars in 36 years-old actual concrete structures. Concr. Libr. JSCE **33**, 155–164 (1999)
14. Yoon, D.J., Weiss, W.J., Shah, S.P.: Assessing damage in corroded reinforced concrete using acoustic emission. J. Eng. Mech. ASCE **126**(3), 273–283 (2000)

Chapter 9

On-Site Damage Evaluation by AE and CT in Concrete

Tetsuya Suzuki and Masayasu Ohtsu

Abstract For detailed inspections of concrete structures, non-destructive tests (NDT) are often conducted and then mechanical properties are compared with detected NDT parameters. In this chapter, damage evaluation of concrete by AE and X-ray computerized tomography (CT) tests are presented. The concrete damage is visualized by X-ray CT. Since nucleation of AE events in damaged concrete is affected by crack distribution, the damage parameter estimated is correlated with the dynamic modulus of elasticity E_d which is calculated from P-wave velocity. The results confirm that the damage of concrete could be estimated by applying AE measurement, damage parameter in damage mechanics, CT images and modulus E_d . It is also shown that the static modulus E_0 is closely correlated with the dynamic modulus E_d . Based on a relation between AE rate and the damage parameter, the damage of concrete is quantitatively estimated.

Keywords Acoustic emission • X-ray CT • Concrete damage • Damage mechanics • DeCAT • Dynamic modulus of elasticity

9.1 Introduction

The durability of concrete structure is found to decrease drastically due to the effects of environmental effects. One particular example is associated with seismic wave-motions (earthquake). Recently, the Great East-Japan Earthquake hit Tohoku area in Japan on March 11, 2011 [2]. As a result, damage evaluation techniques for diagnostic inspection are in great demand in concrete engineering. The degree of

T. Suzuki (✉)

Faculty of Agriculture, Department of Agricultural and Environmental Engineering, Niigata University, Niigata, Japan
e-mail: suzuki@agr.niigata-u.ac.jp

M. Ohtsu

Graduate School of Engineering, Kyoto University, Kyoto, Japan
e-mail: ohtsu.masayasu.4v@kyoto-u.ac.jp

damage in concrete structures is, in most cases, evaluated only from the decrease in concrete strength. For effective damage estimation of concrete, it is necessary to evaluate not only the mechanical properties but also directly the degree of damage.

We have proposed quantitative damage evaluation of concrete, by applying acoustic emission (AE) and X-ray CT in the core test [9, 11]. The procedure is named DeCAT (Damage Estimation of Concrete by Acoustic Emission Technique), which is based on estimating the intact modulus of elasticity in concrete. To inspect existing structures for maintenance, AE techniques draw a great attention [1]. This is because crack nucleation and extension are readily detected and monitored. In this respect, the measurement of AE activity in the compression test of core samples is established. By applying DeCAT, the intact modulus of elasticity in concrete is estimated on the basis of damage mechanics. The estimated damage parameter is correlated with the dynamic modulus of elasticity E_d calculated from P-wave velocity [5].

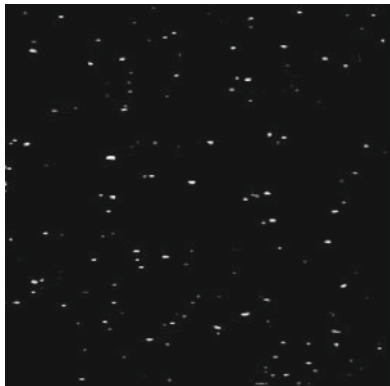
In this chapter, damage estimation of concrete is investigated applying AE and X-ray CT. Test samples were taken from existing reinforced concrete structures, which were subjected to such environmental effects as freeze-thawed process and earthquakes. Crack distribution in concrete was inspected with helical CT scans, which were performed at one-millimeter intervals. After helical CT scan, concrete damage was evaluated by AE parameters and dynamic modulus of elasticity E_d . Thus, the decreases in mechanical properties in service concrete structures are quantitatively evaluated.

9.2 Crack Evolution in Concrete Structures In-Service

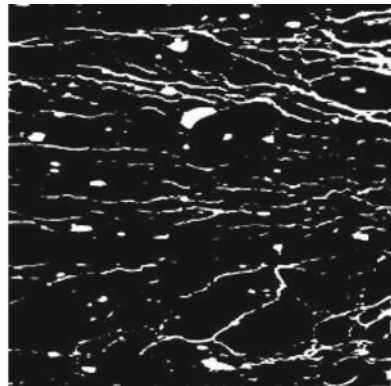
9.2.1 Concrete Damage in Damage Mechanics

The concrete damage is accumulated by evolution of cracks. Continuous damage mechanics (CDM) describes the influence of accumulation of material damage such as micro-cracks on mechanical response of a solid. The concept of damage mechanics was proposed by Kachanov [3]. Since then, various damage mechanics models have been developed. Loland [4] developed a scalar damage parameter to describe fracture of concrete under stress-strain condition. The physical meaning of the scalar damage parameter is demonstrated by considering a representative volume element in a material [7], as shown in Fig. 9.1. The element has a gross cross-sectional area A , which could results from initial material flaws and load-induced cracks. Here, the net cross-sectional area of the element A^* excludes the area of the defects, which corresponds to $A^* - A$. Thus, the damage parameter Ω is defined as,

$$\Omega = \frac{A^* - A}{A^*} = 1 - \frac{A}{A^*}. \quad (9.1)$$



**Concrete cross-section "A"
(gross area) in non-damage
condition.**



**Concrete cross-section "A*"
(effective area) in damaged
(cracked) condition.**

Fig. 9.1 Illustration of concrete cross-sections in non-damaged and damaged conditions

Based on the parameter Ω , Otsu [6] developed an evaluation method for quantification of concrete damage using AE. AE generation behavior in core test is associated with inner crack development which is evaluated by the parameter Ω . Suzuki [11] evaluated the damage degree in freeze-thawed concrete using AE and X-ray CT. Suzuki [9] found the decrease in CT values in deteriorated concrete samples due to earthquake motion.

9.2.2 *Visualization and Quantification of Cracks in Concrete Using X-ray CT*

Cylindrical samples were taken from an existing structure which has been affected by the freezing and thawing effect in Hokkaido, Japan. The structure was constructed about 40 years ago and was heavily cracked. Core-drilled samples were inspected with a helical CT scan system shown in Fig. 9.2. CT scans were performed at one-millimeter intervals before the compression test. The measurement conditions are shown in Table 9.1.

In Fig. 9.3, a heavily cracked core-sample is named “Type A”. A little cracked core-sample is named “Type B”, and a non-cracked sample is named “Type C”. Output images are visualized in gray scale, where air appears as a dark area and the densest portions appear as white. The exact positioning was ensured using a laser positioning device. In this experiment, samples were scanned constantly at 0.5 mm pitch overlapping. A total of 200–400 two-dimensional (2D) images were obtained from each specimen depending on the specimen length.

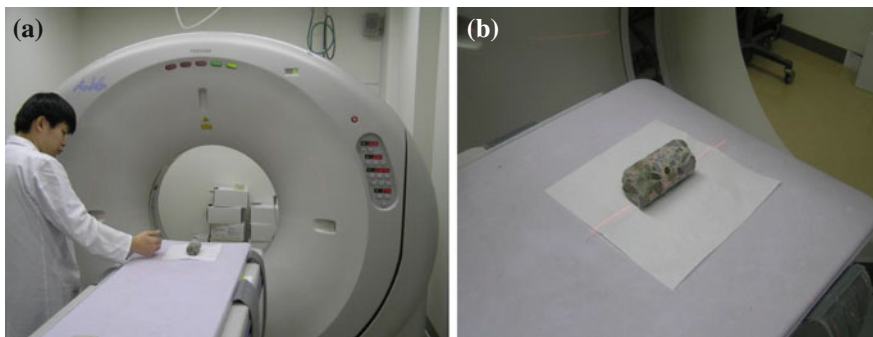


Fig. 9.2 A general view of CT machine during concrete-core scanning. **a** X-ray CT machine. **b** Testing concrete-core

Table 9.1 Setting used for helical CT scan

Helical pitch	15.0
Slice thickness	0.5 mm
Speed	7.5 mm/rotation
Exposure	120 kW and 300 mA
Recon matrix	512 × 512
Field of view	100–200 mm

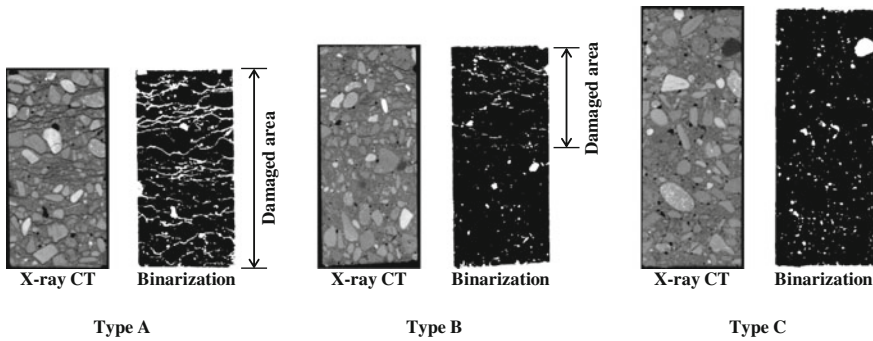


Fig. 9.3 Characteristics of concrete damage in tested samples

From results of the CT scans, the probability density function (PDF) of perimeter of pores and cracks was estimated as shown in Fig. 9.4. The perimeters over 10 mm are compared among Type A, B and C. Large pores and cracks over 20 mm are dominantly observed in Type A, while those of smaller than 10 mm are only observed in Type C. The concentration index I_δ is compared with perimeter of pore and cracks as shown in Fig. 9.5. The concentration index I_δ is defined as,

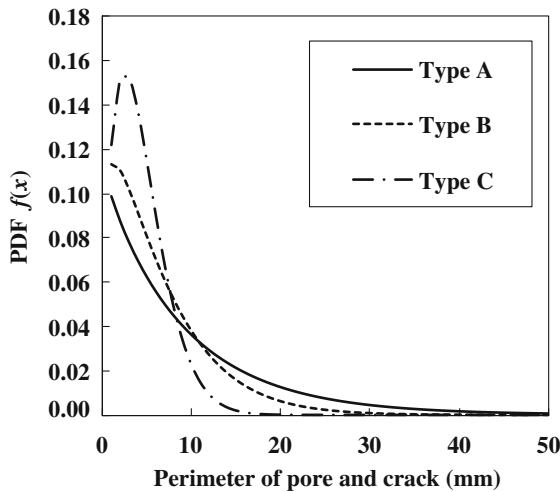


Fig. 9.4 Results of pore and crack distribution

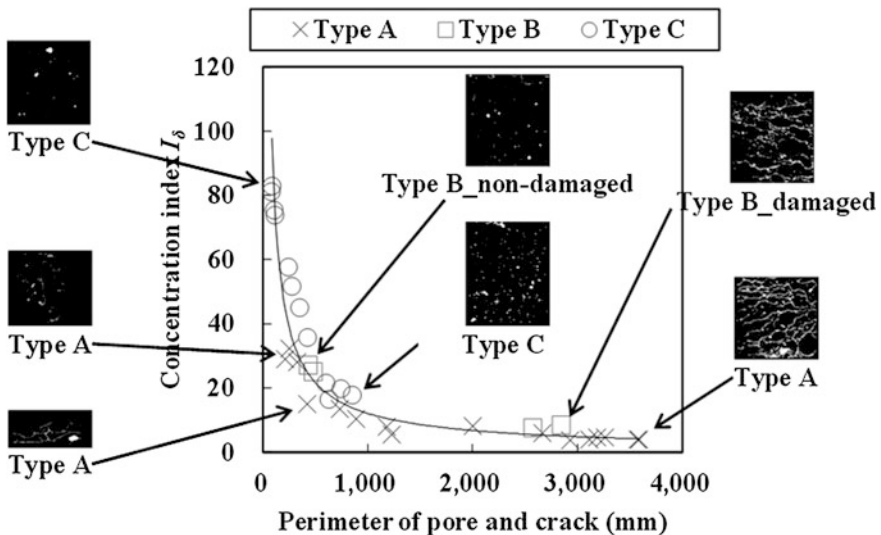


Fig. 9.5 Comparison of concentration index I_δ and perimeter of cracks

$$I_\delta = m \sum_{i=1}^m \{x_i (x_i - 1)\} \left/ \sum_{i=1}^m x_i (\sum_{i=1}^m x_i - 1)\right., \quad (9.2)$$

where x_i is the number of points in the compartment, m is the number of compartment.

It is considered that the volume of crack is closely associated with deterioration of concrete. These results confirm that the relation between characteristics of X-ray image and crack volume is to be useful for the damage evaluation in concrete.

9.3 Evaluation of Mechanical Properties in Cracked Concrete by AE

9.3.1 Characteristics of AE Generation Behavior in Core Test

After X-ray CT tests, uniaxial compression tests of core samples were conducted, measuring AE activities along with strains as shown in Fig. 9.6. AE monitoring was carried out by employing AE sensor of 150 kHz resonance (R15a, PAC) which was attached at 6 locations of the specimen. Amplification was 60 dB gains in total. The frequency range was set from 60 kHz to 1 MHz. AE hits were detected at threshold level 42 dB by AE system (SAMOS-AE, PAC).

The averaged compressive strength of Types A and B is 8.5 N/mm^2 , as 14.9 N/mm^2 at the maximum, and 4.2 N/mm^2 at the minimum. In Types A and B, particular differences in mechanical properties are not observed. On the other hand, the strength of Type C is 32.9 N/mm^2 on the average, which is 3.87 times higher than Types A and B.

Results of AE tests are shown in Fig. 9.7. In the cracked samples (Type A and B), low amplitude AE events (42–59 dB) are observed at the middle height of the specimen. In Type C, in contrast, high amplitude AE events frequently appear. This is because AE generation behaviors in Types A and B are mostly affected by friction of existing cracks.

Distributions of AE events detected are analyzed by the Weibull distribution, as shown in Fig. 9.8. It is found an amplitude distribution by the power-density function (PDF) is concentrated in low values (40–50 dB) in Type A.

Therefore, it is found that the strengths may not be explicitly associated with the damages defined by the pore volumes in the case of freezing-thawing damages. Even though the damage is minor, the durability of concrete definitely decreases. These results suggest that AE parameters are quite sensitive to it.

9.4 On-site Damage Evaluation Using DeCAT

9.4.1 DeCAT Procedure

Loland [4] assumed that the relationship between damage parameter Ω and strain ε under uniaxial compression as,

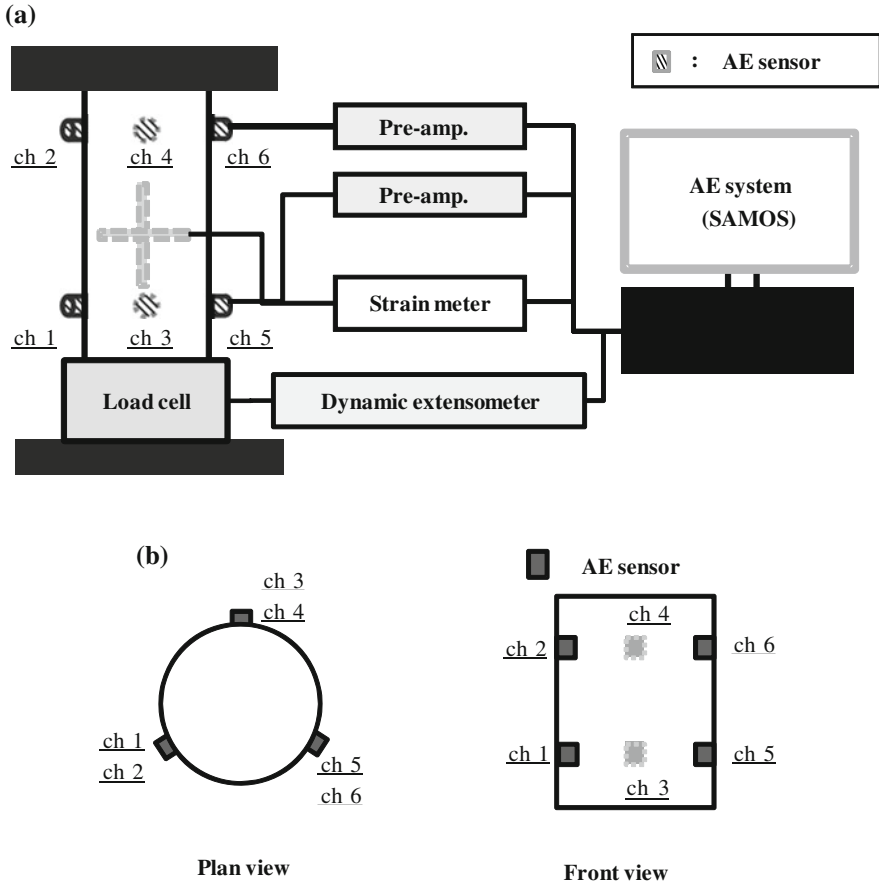


Fig. 9.6 Test setup for AE monitoring system in compression test. **a** Compression test with AE. **b** AE sensor arrangement

$$\Omega = \Omega_0 + A_0 \varepsilon^\lambda, \quad (9.3)$$

where Ω_0 is the initial damage at the onset of the uniaxial compression test, and A_0 and λ are empirical constants of concrete. The following equation is derived from Eqs. 9.1 and 9.3,

$$\sigma = (E_0 - E * A_0 \varepsilon^\lambda) \varepsilon, \quad (9.4)$$

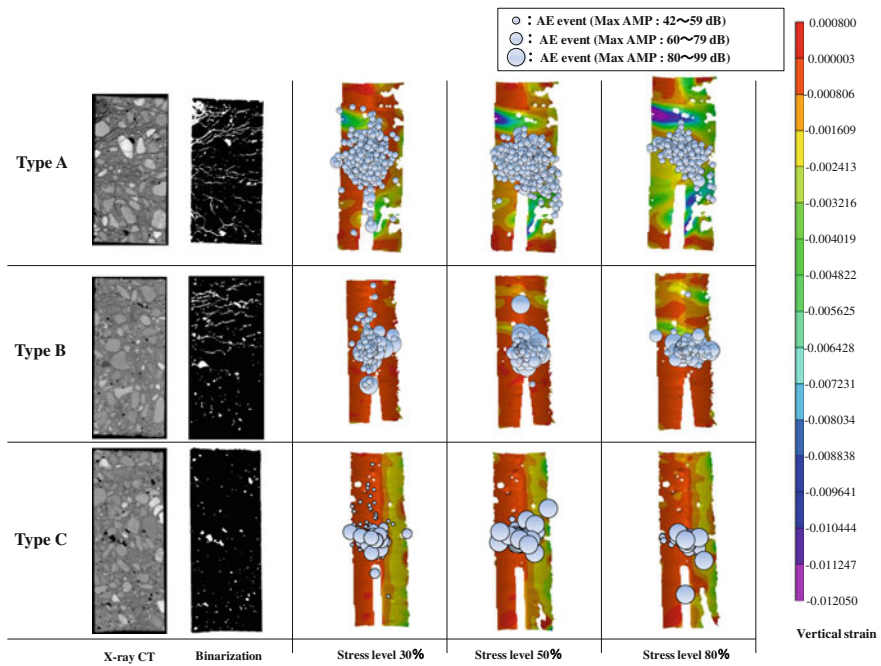


Fig. 9.7 AE generation behavior in compression test

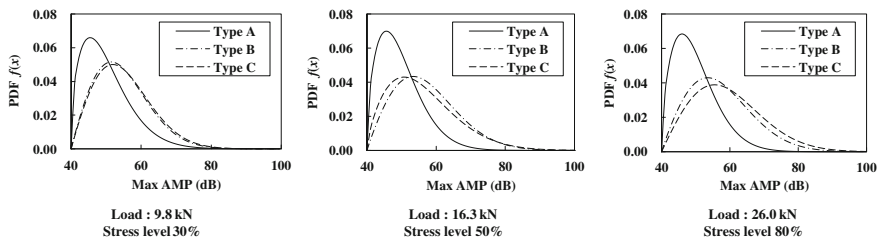


Fig. 9.8 Characteristics of detected AE events by the Weibull analysis

here,

$$E_0 = E * (1 - \Omega_0), \quad (9.5)$$

$$E_c = E_0 - E * A_0 e^{\lambda}, \quad (9.6)$$

From Eq. 9.5, to estimate the initial damage Ω_0 , it is essential to obtain the modulus of intact concrete E^* . However, it is not feasible to determine E^* of

concrete in an existing structure. To estimate E^* from AE measurement, the relation between the total number of AE events and the stress level in Eq. 9.7 is correlated with Loland model [8].

$$f(V) = \frac{a}{V} + b, \quad (9.7)$$

where a and b are empirical constants. Here, the value ‘ a ’ is named the rate.

The static initial modulus of elasticity E_0 is to be quantitatively determined as a tangential gradient of the stress-strain curve in compression test. From Eq. 9.4,

$$\sigma = E_0\varepsilon - E^*A_0\varepsilon^{\lambda+1}, \quad (9.8)$$

Thus, the static modulus, E_0 , is uniquely determined as a tangential modulus: $d\sigma/d\varepsilon$ at $\varepsilon = 0$.

We have found the highest correlation between the damage parameter ‘ λ ’ and the rate ‘ a ’ (AE database; [8]). AE database consists of 200 samples tested in the Kumamoto University from 1988 to 2013. A linear correlation between ‘ λ ’ and the rate ‘ a ’ value is reasonably assumed. Thus, the equation of λ' is expressed,

$$\begin{aligned} \lambda' &= a'X + Y, \\ \lambda + (a \times 100) &= (a \times 100)X + Y. \end{aligned} \quad (9.9)$$

where

$$\lambda = \frac{E_c}{E_0 - E_c}. \quad (9.10)$$

Here, it is assumed that $E_0 = E^*$ when $a = 0.0$. This allows us to estimate Young’s modulus of intact concrete E^* from AE database as,

$$E^* = E_c + \frac{E_c}{Y}. \quad (9.11)$$

In this procedure, the damage of concrete is evaluated by relative moduli E' as presented,

$$E' = \frac{E^*}{E_0} \times 100. \quad (9.12)$$

Here E_0 is the tangent modulus of elasticity in the compression test. The procedure to estimate the relative moduli E' is named DeCAT (Damage Estimation of Concrete by Acoustic Emission Technique; see Fig. 9.9).

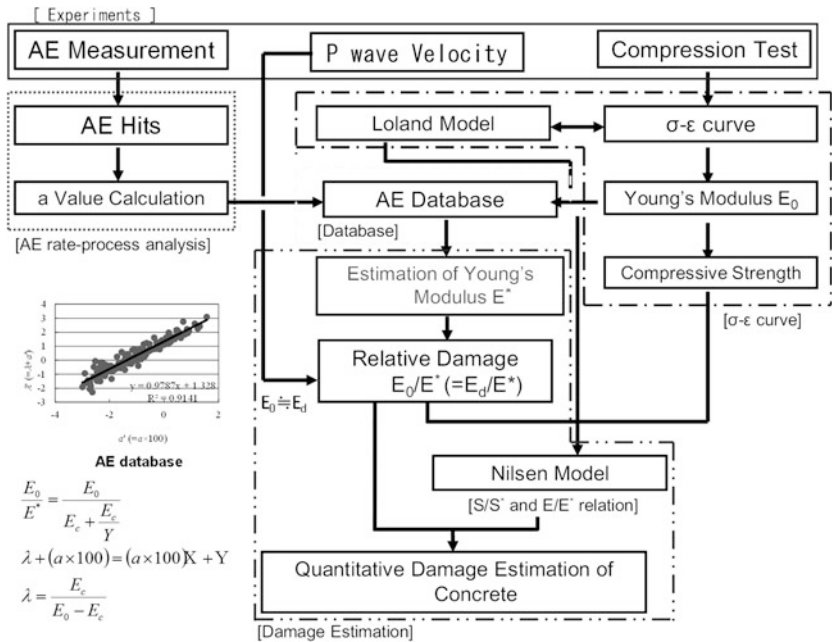


Fig. 9.9 DeCAT procedure

9.4.2 Damage Estimation of Concrete by DeCAT and Dynamic Modulus of Elasticity E_d

The dynamic modulus of elasticity E_d is a useful mechanical parameter for damage evaluation of concrete [5]. This parameter is closely related to the relative moduli calculated by DeCAT [5, 10].

Elastic waves are generated and propagate in concrete due to either a dynamic force or crack development. In an isotropic elastic body, the primary wave (P-wave) propagates with the velocity V_p ,

$$V_p = \sqrt{\frac{E_d(1-\nu)}{\rho(1-2\nu)(1+\nu)}} \quad (9.13)$$

where E_d is the dynamic modulus of elasticity, ν is Poisson's ratio and ρ is the density of concrete. In concrete engineering, the static modulus of elasticity is normally obtained as a secant modulus in the compression test, while the dynamic modulus of elasticity is determined from the velocity estimated by the ultrasonic test. In the case that the static modulus is determined from a tangential modulus, it is reported that no difference is found between the static and the dynamic modulus [5].

So, relative moduli determined from the dynamic modulus are compared with results of AE rate process analysis [8].

9.4.3 Case Study: Damage Evaluation of RC Arch Member in Service for 87 Years

Core samples were drilled and collected from an arch portion of a reinforced concrete road-bridge shown in Fig. 9.10 that had been in service for 87 years. Using concrete-cores, the damage are estimated from a relation between dynamic modulus of elasticity E_d and static modulus of elasticity E_0 . AE measurement in a compression test was conducted. MISTRAS-AE system (manufactured by PAC) was employed to count AE hits. AE hits were detected by using an AE sensor UT-1000 (resonance frequency: approx. 1 MHz).

Results of mechanical properties, compressive strength of core-samples are 25.3 N/mm² on the average, 32.4 N/mm² at the maximum, and 20.1 N/mm² at the minimum. Initial modulus of elasticity E_0 is 21.2GPa on the average, 27.9GPa at the maximum, and 16.8GPa at the minimum. Dynamic modulus of elasticity E_d is calculated from Eq. 9.13. The longitudinal wave velocity of concrete V_p are 3,207 m/s on the average, 3,770 m/s at the maximum, and 2,600 m/s at the minimum. Young's moduli E_d are 22.1 GPa on average, 29.7 GPa at the maximum, and 14.8 GPa at the minimum. Relative moduli (E_0/E^*) are compared with compressive strengths (f'_c) as shown in Fig. 9.11. It is clearly observed that relative modulus estimated show a similar trend to the compression strengths. Because the



Fig. 9.10 Concrete arch member of the Gion Bridge

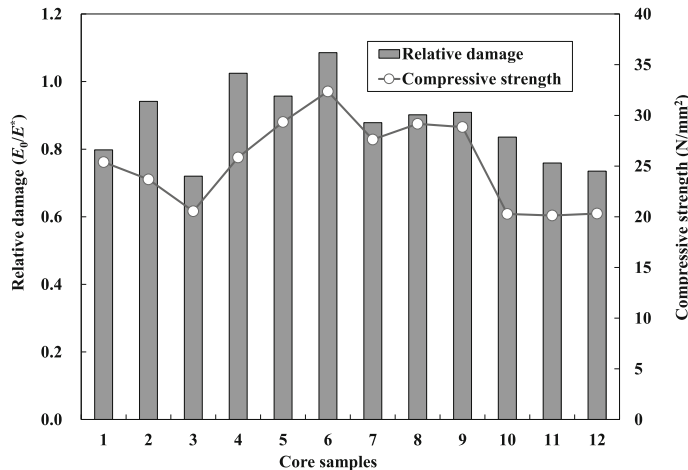


Fig. 9.11 Comparison of relative moduli and compressive strength

relative moduli of all specimens are almost 1.0 or below, it is considered that they are fairly damaged.

According to Fig. 9.12, Initial modulus E_0 and dynamic modulus E_d are almost identical. It is experimentally confirmed that there exists little difference between initial Young's modulus and dynamic Young's modulus. As in the case of frost damage, relative damages are normally estimated from dynamic Young's modulus [5]. The dynamic modulus is physically identical to static modulus in core test. Therefore, the dynamic modulus is most useful damage parameter for on-site non-destructive damage evaluation of concrete structure.

9.4.4 Case Study: Concrete Canal Structure Affected by Earthquake

The testing structure was selected in the Tohoku region, where the damage evaluation was carried out using AE in the core test. Core samples of 10 cm in diameter and about 20 cm in height were taken from a concrete open-canal wall (Fig. 9.13) in Miyagi prefecture, Japan. The concrete wall of the canal was subjected to the Great East Japan Earthquake which was constructed 8 years ago.

Core samples were drilled out from pre- and post- the Great East Japan Earthquake conditions. In addition, the ultrasonic test was conducted in the same canal walls in the conditions of post-earthquake. After longitudinal wave velocity was determined, dynamic modulus of elasticity E_d was calculated from P wave velocity. AE monitoring in the core test was conducted at the same conditions of concrete road bridge.

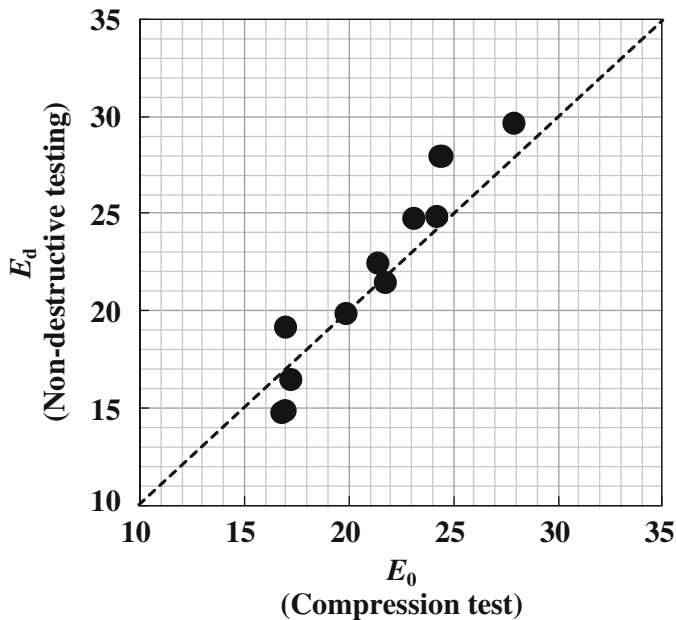


Fig. 9.12 Comparison of Young's modulus E_d and E_0 in concrete bridge



Fig. 9.13 Location of sampling site in concrete canal (Photo Head works)

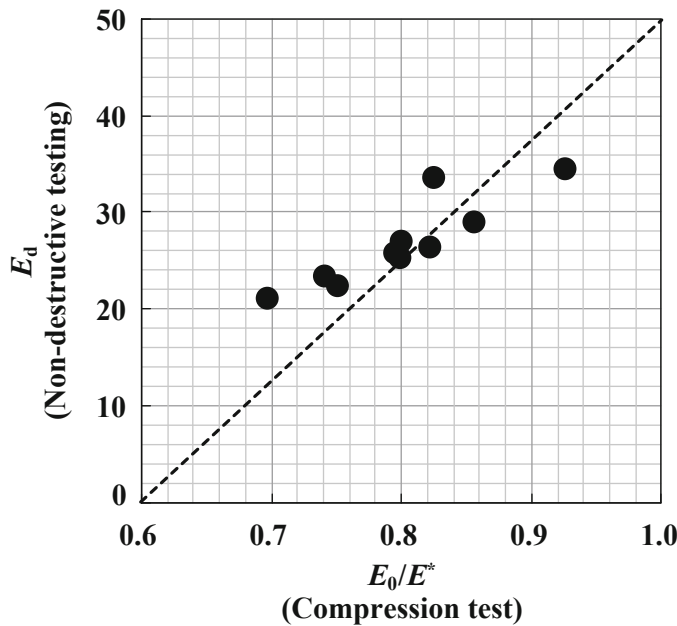


Fig. 9.14 Comparison of dynamic modulus of elasticity E_d and relative moduli E_0/E^* in concrete canal structure

Results of mechanical properties, the compressive strength is 25.0 N/mm² as the average (max: 30.1 N/mm², min: 18.5 N/mm²) in the pre-earthquake condition, while that of the post-earthquake condition is 24.8 N/mm² (max: 31.5 N/mm², min: 20.5 N/mm²). Thus, the decrease in the mechanical properties is not clearly observed. On the other hand, the CT value and relative damage E_0/E^* are lower than those of pre-earthquake samples [9]. These results indicate that the CT and relative damage are effective for quantitative evaluation of concrete damage. In Fig. 9.14, these dynamic modulus of elasticity E_d are compared with the relative damage E_0/E^* which is defined as damage parameter [11]. It is clearly observed that the relative damages are in reasonable agreement with dynamic modulus of elasticity E_d after the earthquake.

9.5 Conclusion

For on-site damage evaluation of concrete, AE and X-ray CT methods were applied to the experiments of core samples. The crack distributions of concrete-core were inspected with X-ray CT method. The damage of concrete due to crack progressive conditions was evaluated by AE parameter in compression test. AE generation behavior is closely associated with the concrete damage, which can be quantitatively

evaluated by the relation between the dynamic modulus of elasticity E_d and the static modulus E_0 . The concrete damage is associated with statistical properties of CT data. Thus, the damage of concrete is quantitatively estimated as damage parameters by AE and X-ray CT.

References

1. Grosse, C. U. and Ohtsu, M. (eds.) Acoustic Emission Testing, Berlin, Springer, 3–10 (2008)
2. Kazama, M., Noda, T.: Damage Statics (Summary of the 2011 off the Pacific Coast of Tohoku Earthquake damage). *Soils Found.* **52**(5), 780–792 (2012)
3. Kochanov, D.: Time of rupture process under creep conditions. *Izvestia Akademii Nauk, USSR* **8**, 26–31 (1958)
4. Loland, K.E.: Continuous damage model for load—response estimation of concrete. *Cem. Concr. Res.* **10**, 395–402 (1989)
5. Ohtsu, M.: Damage evaluation in freezing and thawing test of concrete by elastic-wave methods. *Mater. Struct.* **44**, 1725–1734 (2011)
6. Ohtsu, M., Kawai, Y., Yuji, S.: Evaluation of deterioration in concrete by acoustic emission activity. *Proc. of the Japan Concrete Institute* **10**(2), 849–854 (1988)
7. Ouyang, C.: Fracture mechanics of concrete, Wiley International Science, 454–456 (1995)
8. Suzuki, T., Ohtsu, M.: Damage evaluation of core concrete by AE. *Concr. Res. Lett.* **2**(3), 275–279 (2011)
9. Suzuki, T., Ohtsu, M.: Use of acoustic emission for damage evaluation of concrete structure hit by the Great East Japan earthquake. *Constr. Build. Mater.* **67**, 186–191 (2014)
10. Suzuki, T., Shigeishi, M., Ohtsu, M.: Relative damage evaluation of concrete in a road bridge by AE rate—process analysis, *Mater. Struct.* **40**(2), 221–227 (2007)
11. Suzuki, T., Ogata, H., Takada, R., Aoki, M., Ohtsu, M.: Use of acoustic emission and X-ray computed tomography for damage evaluation of freeze-thawed concrete. *Constr. Build. Mater.* **24**, 2347–2352 (2010)

Chapter 10

Overview of Visualized NDE for On-Site Measurement

Masayasu Ohtsu

Abstract Toward the sustainable society, long service life of infrastructure is going to be an evolutional target in the world. Aging and disastrous damage in concrete structures have updated the urgent demand for continuing maintenance of the structures in service. To this end, a variety of non-destructive testing (NDT) techniques and evaluation methods for diagnosis and prognosis are surveyed. Thus, visualized non-destructive evaluation (NDE) for on-site measurement is overviewed.

Keyword Concrete structures • Masonry structures • Acoustic emission (AE) • AE tomography • SIBIE • SiGMA • Rebar corrosion

10.1 Introduction

In medical and diagnostic inspections for human body, the ultrasonography is well known as a visualized technique. In a similar manner to the ultrasonic testing in structures, the ultrasonic waves (volumetric or P wave) are produced by electrically stimulating a crystal called a transducer. As it strikes an interface or boundary between tissues of varying density (e.g., muscle and blood), some of the waves are reflected back to the transducer as echoes. The echoes are then converted into electrical impulses that are displayed on an oscilloscope, presenting a “picture” of the tissues under examination.

Because the human body consists mostly of moisture, only P waves can propagate and reflect. Thus, the ultrasonography is readily applied to examination of such organs as heart, aorta, blood vessels, and abdominopelvic cavity. In contrast, both elastic waves of P wave and S wave could propagate in such solid materials as concrete and rock. Therefore, visualization of echoes is not easy without particular technics and to be developed by sophisticated procedures as discussed in Chaps. 4, 6 and 7.

M. Ohtsu (✉)

Graduate School of Engineering, Kyoto University, Kyoto, Japan
e-mail: ohtsu.masayasu.4v@kyoto-u.ac.jp

As other visualized techniques in civil engineering, infra-red thermography and X-ray inspection are commercially available. Except a few applications to concrete structures in Chap. 2, they are not discussed in detail. This is because no extensive survey has been made in the committee, except for the X-ray computer tomography in Chap. 9. As a result, development of advanced elastic-wave methods is comprehensively stated with emphasis on acoustic emission (AE), as the follow-up committee of the previous technical committee, TC 212-ACD (acoustic emission and related NDE techniques for crack detection and damage evaluation in concrete).

10.2 Overview and Achievements

In Chap. 2, issues related to the NDE monitoring of concrete structures are addressed. The importance and special characteristics of concrete make it a challenging material for the usual NDE techniques. Because of the advancement of technologies, the capabilities of testing continuously increase as discussed.

Improvement of devices and new technologies like wireless sensors simplify monitoring, while tomography algorithms enable accurate visualization of the damage pattern within the structure. The developments in NDE are matching the increased needs of contemporary construction, like better control during manufacturing and operation, as well as reliable condition assessment when is judged necessary. These hopefully meet the highest quality standards, satisfy the requirements of the stakeholders and ensure a safe management of the infrastructure for the public namely infra-asset management.

Concerning AE applications to masonry structures in Chap. 3, three case studies have been presented to show the capability on damage assessment of historical structures. The collected data were analyzed in order to interpret the evolution of damage.

One case study focused on the structural stability of three medieval towers rising in the center of Alba, a characteristic town in Piedmont. The evolution of damage in a pillar, that is a part of the vertical bearing structure of the Syracuse Cathedral, is evaluated. From AE observation, it is found these structures are subjected to a damage process mainly due to the seismic actions. This suggests that AE structural monitoring coupled to the analysis of local earthquake activity can be a tool of crucial importance in earthquake damage mitigation.

The case of Chapel XVII of the Sacred Mountain of Varallo has been presented. It shows some structural concern due to large cracks and a degradation of the high valuable frescos, which tend to detach from the masonry support. In order to assess the evolution of those phenomena, the results of the AE monitoring program have been provided. The monitoring results show that the large cracks are stable, while the process of detachment of the frescos is evolving cyclically.

The proposed non-destructive monitoring approach allows for analyze cracks evolution, and in general damage propagation. Therefore it is useful to derive the optimal priority for interventions directed to preservation, safeguard and valorization of the masonry architectural heritage.

In Chap. 4, theory of AE tomography is briefly reviewed. This is a novel procedure as the advanced computerized tomography of the elastic-wave measurement. As discussed here, both the velocity distribution of elastic waves and the source locations of AE events are simultaneously obtained. Starting with two-dimensional cases, the capability of AE Tomography is discussed by performing a series of numerical investigations. Furthermore, in the three-dimensional problems, AE Tomography is applied to evaluation of existing structures as well as laboratory tests to verify an applicability of AE Tomography.

In Chap. 5, recent trends in parameter analysis of AE waveform for fracture characterization is reviewed. The sensitivity of different AE parameters to the mode is reported with numerous experimental examples. It is shown that several AE waveform parameters are sensitive to the fracture mode. Processes like debonding of external patches, pull-out of fibers or reinforcing bars give distinct AE signatures than cracking and can be used for study and monitoring of the fracture process.

Additionally, cracks triggered by shear stresses in concrete also show different characteristics (mainly in terms of frequency and duration) than tensile cracks. While the capability of recording full waveform exists in most of contemporary acquisition systems, extraction of classical parameters remains a very effective way to characterize fracture, enhanced when necessary by features of frequency domain and other NDT monitoring techniques.

As shown in Chap. 6, on-site applications of the SIBIE procedure are stated as an NDE technique to identify defects at known locations. In the case of prestressed concrete (PC) ducts, locations of the ducts are known in the design documents or could be identified by a radar system. The issue is to discriminate ungrouted ducts and grouted ducts.

In the case of the surface crack, the location is known, and we are interested in the depth. So far, detecting defects of unknown depth and unknown location is out of the scope. The technique is developed as given here. Henceforth, the standardization is in progress.

In Chap. 7, by applying the sample code in the appendix, kinematics of AE sources are obtained on source location, source (crack) type and crack motion vectors including the crack normal to the crack plane. To perform the analysis, multi-channel AE system more than 6 channels is necessary. In addition, waveforms of all the channels are to be recorded digitally. In the case, all arrivals of the first motions are simultaneously to be recorded with the aid of proper threshold. It is often encountered that the noise level is too high for the first motion to be properly detected, and sometimes so high as to be smeared. Although the location procedure is usually conducted by triggering at the threshold, the arrival times of all the waveforms are to be derived. Following the arrival times of the first motions, the amplitudes of the first motions not the peak amplitudes are to be recorded to solve the moment tensor.

In Chap. 8, a hybrid NDE for early and quantitative detection of rebar corrosion in reinforced concrete is proposed. By combining AE technique with electro-chemical analysis, the onset of reinforcement corrosion is readily estimated. It is promising to precisely identify the corroded area in rebar.

From the result of the stress analysis by the boundary element method (BEM), it is predicted that the crack progresses with an inclined angle to the bottom. The fact is in remarkable agreement with visual observation by the micrograph. Thus, the effectiveness of hybrid NDE is confirmed by these experimental results.

In Chap. 9, for on-site damage evaluation of concrete, AE and X-ray CT methods were applied to the experiments of core samples. The crack distributions of concrete-core were inspected with X-ray CT method. The damage of concrete due to crack progressive conditions was evaluated by AE parameter in compression test. AE generation behavior is closely associated with the concrete damage, which can be quantitatively evaluated by the relation between the dynamic modulus of elasticity E_d and the static modulus E_0 . The concrete damage is associated with statistical properties of CT data. Thus, the damage of concrete is quantitatively estimated as damage parameters by AE and X-ray CT.

10.3 Concluding Remarks

Toward the sustainable society, long service life of infrastructure is going to be an evolutional target in the world. Aging and disastrous damages due to recent earthquakes in concrete structures have updated the urgent demand for continuing maintenance of the structures in service. This is a critical demand for the sustainable infrastructure. To this end, a variety of NDT techniques and evaluation methods for diagnosis are under development.

With respect to human body, the medical dock is systematized in Japan as the medical dock similar to the ship dry-dock. In order to extend the service life of the concrete structure, an “infra-dock”, referring to the medical dock for human body, is to be established. Thus, the technical committee “JCI-TC-125FS: establishment of infra-dock for concrete structures” has been set up in the Japan Concrete Institute (JCI). As basic constituents of the infra-dock, inspection techniques for on-site measurements should be synthesized as the prognosis procedure. For prognosis of structures, visualization and imaging of NDT results are in great demand for practitioners and engineers for inspection. In collaboration with JIC-TC-125FS, on-site measurements of concrete and masonry structures by NDT techniques are comprehensively surveyed in TC TC-239 MCM, “On-Site Measurement of Concrete and Masonry Structures by Visualized NDT”, focussing on visualization procedures and prognostic techniques for the infra-dock.

Based on these researches, it is confirmed found that the elastic-wave methods shall play a key role for nondestructive evaluation (NDE) of concrete structures. Consequently, theoretical bases of the elastic-wave methods are clarified and reviewed. Then, successful results on applications to NDE in concrete structures are presented discussed, which could be useful for establishment of infra-dock. It is expected that the achievement could constitute the infra-dock programs and courses.